Design of broadband antireflective layer stacks with low surface energy prepared by sol-gel method on glass for photovoltaic application

Cecilia Agustín Sáenz

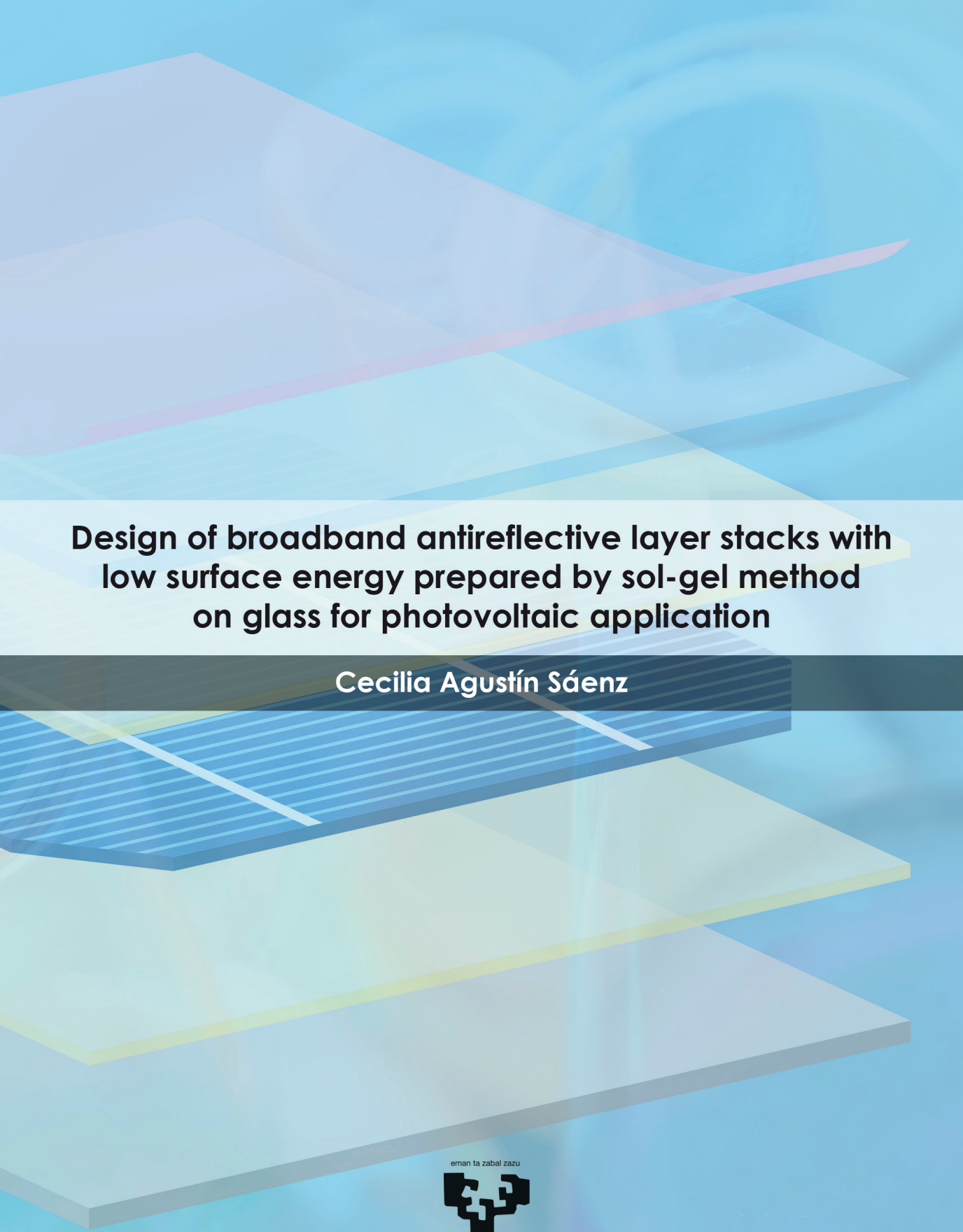

eman ta zabal zazu

Universidad del País Vasco

Euskal Herriko Unibertsitatea

Donostia-San Sebastián 2019

eman ta zabal zazu

Universidad del País Vasco

Euskal Herriko Unibertsitatea

tecnalia

Design of broadband antireflective layer stacks with low surface energy prepared by sol-gel method on glass for photovoltaic application

Cecilia Agustín Sáenz

PhD Program Renewable Materials Engineering

Thesis Supervisors: Dr. Maider Machado García and Dr. Agnieszka Tercjak

Department of Chemical and Environmental Engineering

Faculty of Engineering, Gipuzkoa

Donostia-San Sebastián, 2019

Table of contents

Summary

The main objective of this investigation work has been the achievement of antireflective (AR) coating materials for the glass-air interface, and the searching of the most rational design which provides a proper trade-off between optical properties, cost-efficiency, processability, enhancement of the electrical performance of solar cells and reliability during real life operation.

As shown in the scheme in Figure I this dissertation consists of 6 Chapters. The Chapter 1 introduces the relevant aspects of the photovoltaic technology, such as the types of solar cells related to their efficiency and spectral response, the way that these cells are assembled into a module, and requirements for the front cover sheet. The most promising materials and technologies for depositing antireflective coatings with antisoiling (AS) capabilities are also addressed. The experimental techniques and their fundamental bases as well as equipment used for the characterization of the developed coating materials are described in the Chapter 2. The Chapter 3 presents the theoretical optical design of the antireflective coating materials which maximizes light transmittance matched with spectral response of multi-junction solar cells, considering that outstanding durability in terms of antireflective stability are also required. The experimental deposition of the antireflective coating materials is approached combining acid-catalyzed sol-gel route and evaporation induced self-assembly (EISA) method. The scanning of four types of organic/inorganic systems and the optimization of the water/alkoxide ratio allows to select the coatings that fulfils specific thickness value, porosity and optical constants combined with excellent results on sol stability. The Chapter 4 focuses on the chemical modification of the surface to obtain coatings capable to contribute against soiling adherence, without losing the AR properties, also considering the mechanical robustness required to withstand outdoors exposure. This Chapter presents a comparative study of two parallel approaches optimized to obtain low surface free energy coating materials. The Chapter 5 deals with reliability tests applied to the most promising coatings under accelerated aging tests following photovoltaics standards. The enhancement of electrical response of silicon and multi-junction cells provided by the interposed antireflective coatings is theoretically and experimentally assessed. Finally, a general overview, conclusions, prospect and future work coming from this investigation work are summarized in the Chapter 6.

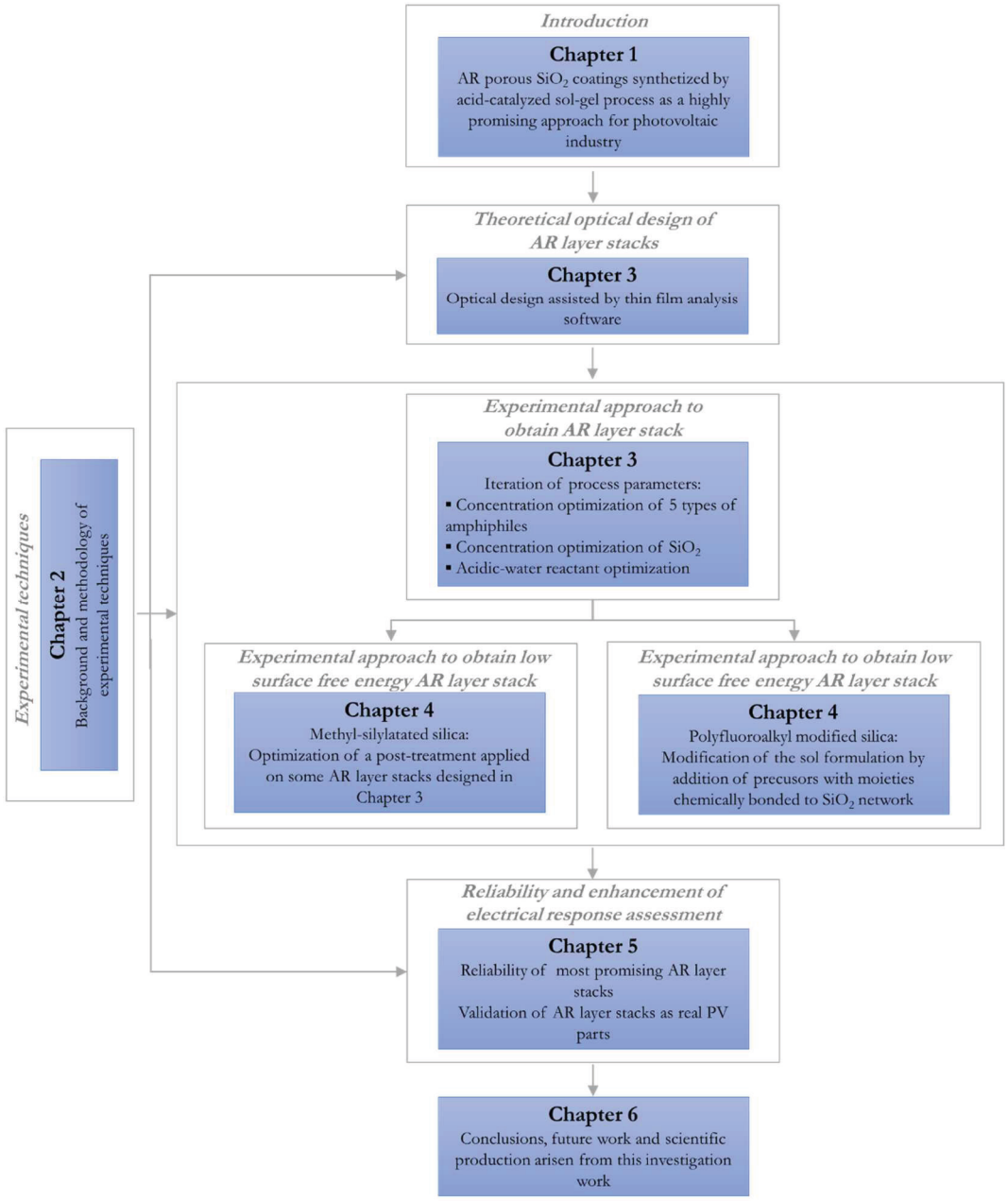

Figure I. Outline of the investigation work.

Motivation and objectives

Glass is the most dominant material used in current solar energy modules to provide protection and insulation due to its optical, thermal and mechanical properties. However, Fresnel reflection in the glass-air interface induces optical losses that become in power losses when the solar cells are integrated in the photovoltaic modules. Minimizing the optical and electrical losses during module production is essential to transfer the cell efficiency to the module. Photovoltaic electricity has become one central pillar for the renewable energy transition triggered by the tremendous progress in cost reduction. In such a highly cost-sensitive industry, the solar electricity cost must compete with conventionally generated electricity through continuous updating of high energy yield, low cost systems with long lifetime and reduced maintenance.

The motivation of this work has consisted of the design of a feasible antireflective coating system applied in the glass-air interfaces of the photovoltaic and concentrated photovoltaic modules. With the aim to reduce the cell to module losses, an antireflective coating system must be capable to provide increased energy harvesting to the module through the maximization of light transmittance impinging solar cell. Apart from optical properties, the mechanical and chemical properties of the surface must be envisaged to provide long durability performance and low soiling adherence to the photovoltaic modules.

Taking above into account the objectives of this research work are listed below:

- Calculation of the antireflective coating properties that theoretically provide the optical design that better matches to spectral response of solar cells,
- Development of an environmental-friendly, cost-effective and easy up-scaling process that allows to grow coatings that meet the optical theoretical targets,
- Development and comparison between different surface functionalization processes to obtain low surface free energy without detrimental effect on optical properties,
- Evaluation of the correlation between the coating process parameters, optical, mechanical and chemical properties and the results obtained in reliability tests,
- Assessment of how the improved optical performance provided by the antireflective coating system contributes to the enhancement of the electrical performance of different types of solar cells.

The work developed in this investigation work has been done in the framework of the European projects entitled: *Elevated concentration photovoltaic solar energy generator and fully automated machinery for high throughput manufacturing and testing* (ECOSOLE), *Concentrating photovoltaic modules using advanced technologies and cells for highest efficiencies* (CPVMatch) and *Global optimization of integrated photovoltaics system for low electricity cost* (GoPV). Those projects have motivated the collaboration with relevant international research institutes and companies of the photovoltaic and concentrated photovoltaic field such as Instituto de energía solar (Universidad Politécnica de Madrid), Fraunhofer Institute for solar energy systems, Ricerca sul sistema energetico (RSE SpA), Italian national agency for new technologies, energy and sustainable economic development (ENEA), BECAR Srl (Gruppo Beghelli), GXC Coatings GmbH and others.

Chapter 1

Introduction

This Chapter introduces the main motivation for the development of antireflective coatings by sol-gel technology in solar energy applications. For this, a general overview of solar energy applications, more particularly focused on photovoltaics is presented. The solar cells evolution from silicon cells to multi-junction solar cells, the subsequent broadening of their spectral response and the optical elements used to increase the concentration factor of solar irradiance on the linear or point collectors are revised.

The requirement of glass covers for module protection and electrical insulation, given its mechanical rigidity and thermal stability properties, introduces optical losses in the system. Therefore, antireflective layer systems are potentially required in solar energy applications to minimize Fresnel reflection losses at glass-air interfaces during long-term operation at harsh conditions.

In such a highly cost-sensitive industry, the required low costs per square meter support the development of cost-effective antireflective coatings. In this context the sol-gel method is among the most attractive processes. Sol-gel is a low-cost, low-temperature and simple operation deposition process that offers a vast range of opportunities for material design with a very precise control of microstructure.

1.1. Solar energy

Renewable solar energy is currently the fastest growing power generation source worldwide [1]. Solar energy can be exploited to produce thermal energy through solar thermal collectors, and to produce electrical energy through photovoltaic (PV) collectors [2]. Particularly PV technology has experienced a nearly exponential increase since 1992, reaching almost the 100 GW installed only in 2017 and again about 100 GW in 2018 [3], surpassing half a TW-peak (TWp) of cumulative worldwide installed power. This implies a higher deployment than fossil fuels and nuclear energy combined. Currently, PV installations are able to power around 3% of global electricity demand, with all renewables already contributing to 12.1% of total global power output in 2017. Although developing estimations for the following years is complex, several sources as the European Technology and Innovation Platform for Photovoltaics, predict that the cumulative global PV capacity would reach about 3 TWp by 2030 and 20 TWp by 2050 [4] which will make solar power the largest electricity source worldwide.

Crystalline silicon (c-Si) is the most mature PV material and the long-term market leader [5]. This material is abundant and low-cost; however, its theoretical conversion efficiency limit is 29.1% [6]. Recently, Yoshikawa et al. [7] from Kaneka Corp. attained the highest efficiency equal to 26.3% (0.7% increase over the previous record) in a silicon solar cell combining interdigitated back contacts and amorphous silicon/crystalline silicon heterojunction.

Whereas the evolution of the efficiency of silicon solar cells has arrived at an almost asymptotic maximum, the efficiency of multi-junction (MJ) solar cells has shown remarkable improvements in the last years. Spectral response of silicon solar cells is between 300-1100 nm, while the III-V multi-junction solar cells are active in a larger part of the solar spectrum, over the broad wavelength range of 300-2000 nm.

This technology is based on expensive high efficient solar cells made up of several p-n junctions (subcells) of III-V semiconductor alloys that can currently yield up to ~46% conversion efficiency at cell level [8] and 38.9% at module level [8][9], operating at light concentration levels up to 1000X thanks to refractive or reflective cost-effective optical elements, which permit to reduce the area of the expensive MJ cells. These PV module configurations are particularly known as concentrated photovoltaic (CPV) or high concentrated photovoltaic (HCPV), depending on the light concentration factor.

Efficiencies of over 40% under concentrated air mass 1.5 direct reference (AM1.5D, ASTM G-173-03 [10]) have been experimentally demonstrated for the triple-junction solar cell structures: lattice-matched (LM), metamorphic-mismatched (MM) and inverted metamorphic mismatched (IMM) [11].

Nowadays, the most industrially available MJ solar cell is still the lattice-matched GaInP/GaInAs/Ge triple-junction solar cell [12], as similar structures have been successfully employed for space applications [13][14][15]. These devices have reached conversions efficiencies of 44% at 942 suns and have demonstrated a long-term reliability under real operation conditions [12]. In these devices, materials with the same lattice constant must be combined, and therefore it is not possible to select the best semiconductor materials that would better suit to the solar spectrum.

Therefore, different approaches to achieve current-matching conditions have been proposed [16][17] and metamorphic-mismatched GaInP/GaInAs/Ge solar cells is the most emerged one since a wide window of semiconductors can be prepared. Whereas LM is based on lattice-matched semiconductors, MM cells are composed by stacking active semiconductors layers of different lattice constants, separated by compositionally graded buffer layers. Both LM and MM solar cells are grown on a single-crystal Ge substrate which forms the bottom junction [18]. MM solar cells have higher theoretical conversion efficiency than LM solar cells and have reached a record efficiency of 44.4% at 500 suns [19].

However, Ge bottom cell generates an excess current under the solar spectrum, and in practice, current matching of the cell in the module is necessary only in the spectral range of 300-910 nm [8]. In the IMM solar cells, the strategy is inverting the direction of grown: the top cell GaInP is firstly grown lattice matched to the substrate, followed by middle cell, matched if it is GaAs; or minimally mismatched if it is GaInAs; and the bottom cell InGaAs which is most highly lattice mismatched. This direction of growth helps to prevent threading dislocations from degrading the higher band gap cells where most of the power is generated. Finally, current matching of the cell must be optimized over the full wavelength range of 300-1800 nm.

MJ solar cells with three p-n junctions based on MM or IMM structures have not been still produced in large quantities [11], while on the other hand, the development of MJ solar cells with four p-n junctions based on LM, MM and IMM structures is being approached [20]. The efficiency target for 4-junction cells is 50% [21], and the current world record for cell efficiency

under concentrated light factor around 500X [22] of 46.0% was achieved with a wafer bonding technology that also combined lattice-mismatched materials (GaInP/GaAs//GaInAsP/GaInAs) [22].

In parallel, research efforts are focused on increasing the concentration factor in order to reduce the size of expensive but high-efficient solar cells, which lead to enhancement of the efficiency of the whole system. Indeed, the cost per watt-peak of a CPV system is drastically reduced as a function of the concentration [20] and CPV has the potential of becoming the large-scale generation of PV energy with competitive costs [23] specially in the sunniest regions.

Concentrator photovoltaic systems can be classified as a function of their strategy for concentrating sunrays as presented in Figure 1-1.

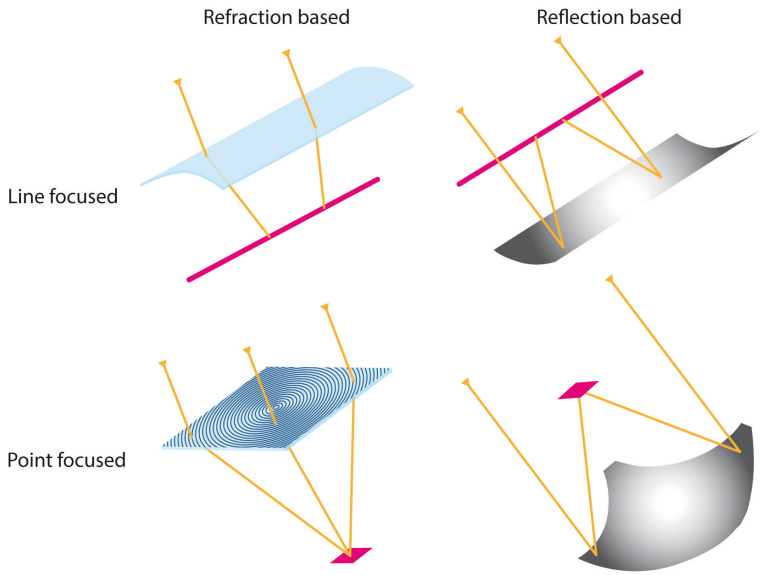

Figure 1-1. Schematic CPV systems according to their concentration strategy.

The most typical configurations are point-focused, commonly, Fresnel-based lens for refractive strategy and Cassegrain reflector for reflective strategy [38]. Moreover, the concentration on the solar cell can be improved with a homogenizer prism, that can be also refractive or reflective. The schematic diagrams of incident light tracks in both configurations are shown in Figure 1-2.

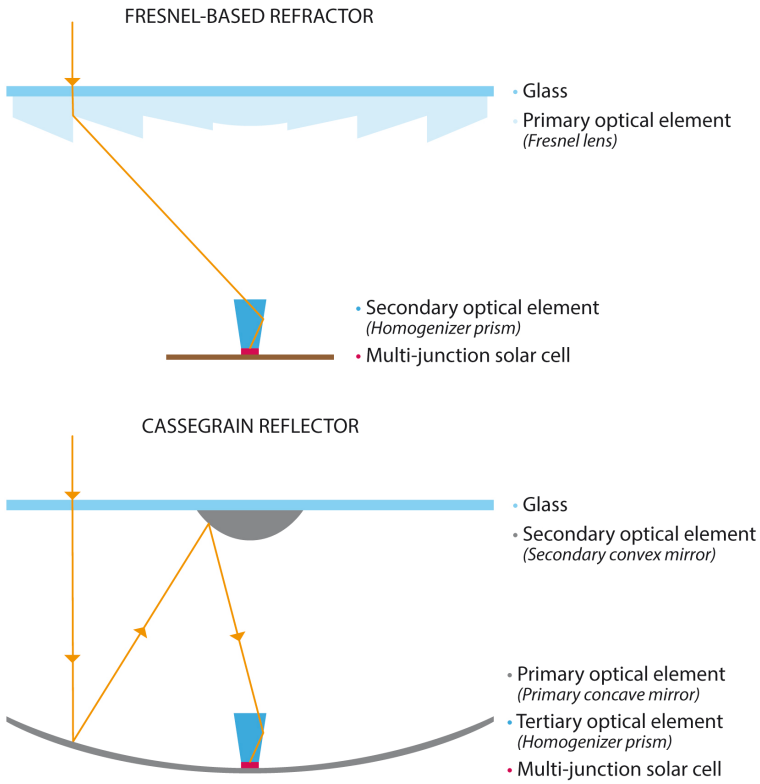

Figure 1-2. CPV modules based on point-focus optical elements.

Nowadays, most of the commercially available CPV are based on silicone on glass (SoG) Fresnel lenses. The most industrially available process is based on injection of silicone, due to the cost-effectiveness and high scalability. In order to produce the optical silicone with the Fresnel facets, a mold with the designed faceted domes is pressed against the glass and then the silicone is injected in between. Once the mold is embossed to the silicone, a heating process at temperatures below 200 ºC promotes the curing of the silicone, and its bonding to the supporting glass [24].

1.2. Glass-air interface in solar energy

Both PV and CPV modules need to be protected and isolated from harsh environmental conditions (such as heat, ultraviolet radiation and corrosive media) that can affect their performance. Regardless module or configuration design, the role of the outside protection can be performed by a front cover sheet, providing also the needed mechanical rigidity, thermal stability and electrical insulation. This front cover sheet should interfere as little as possible with the optical requirements of the PV cells and the module. At the same time, it should be

robust enough to withstand itself the harsh conditions during operating life cycle without being damaged. Additionally, this cover sheet must offer a high optical transmission in a wide wavelength range of the solar spectrum which maximizes the solar radiation flux impinging on the cells, with a spectral distribution matching the cells response.

Among the most used materials for the front cover sheet are those of polymeric nature such as polymethyl methacrylate and polycarbonate, or inorganic nature such as glasses of different compositions. Although the mechanical and thermal stability properties of glass are unquestionably higher, in the recent past, cost-effectiveness justified in some cases the use of polymers in PV applications. Nowadays, the cost production of glass has become more competitive and it is the most used material for module cover sheets [25].

There are three types of industrially produced flat glass: float glass, rolled glass and drawn glass. However, the most extended industrial process (~90% market share) is float glass since on a large-scale it offers the best quality, highest yields, and the lowest price.

The float glass process, pioneered by Alastair Pilkington in the 50s, meant a relatively low-cost process to produce high-quality flat sheet glass. This process consists of the pouring of molten glass on a bed of molten tin in nitrogen atmosphere, thus creating a uniform glass sheet with a highly smooth and flat surface. Rolled glass process is used for patterned-glass and wired-glass since they cannot be produced on totally flat surfaces. The process consists of laminating soften glass between two rollers, some of them being patterned. Drawn glass consists of continuous drawing of the molten glass by a series of rolls. However, its use is marginal in large-scale production.

Most of flat glass is also known, in terms of its composition, as soda-lime glass. The presence of silica, sodium and calcium oxides is indispensable, and it usually also contains magnesium oxide, iron, titanium, potassium and aluminum. Whereas the softening temperature of SiO_2 is 1500-1670 °C, sodium oxide in the composition allows to drop this temperature to 550-750 °C, what turns it into a cost-competitive process. In addition, other components must be added to lend chemical resistance to the material. However, the addition of these compounds, have a detrimental effect on its optical properties.

The most commonly used glass for PV modules protection is float glass with low iron content. The iron content in this type of glass is around 100 ppm, in comparison to the 1000 usually contained in the classic soda-lime. The lower the iron content, the better the provided solar

transmittance is. Whereas the solar transmittance of soda-lime glass (300-2500 nm) is ~85%, low iron float glass can offer up to ~91%. Therefore, these types of glass are used when the operational requirements justify the production cost increase.

On the other side, the alkali and alkaline-earth metals (sodium, calcium, potassium, magnesium) can diffuse out of the glass (particularly under thermal load or applied voltage) thus forming precipitates on the surface, such as $CaCO_3$ crystals thus spoiling the optical properties. In fact, borosilicate glass and fused quartz contain low or null alkali and alkaline-earth elements and are used in applications where high operational temperatures are required since their softening temperature is around 820 ºC. Borosilicate is used in applications where a high thermal resistance is required, such as thermal absorbers in concentrated solar power (CSP) configurations and fused quartz is commonly used for the homogenizer prism in CPV modules.

However, although glass composition can be optimized to improve the optical properties of standard soda-lime glass, Fresnel reflections are produced at the interface in any case, due to the difference between the refractive indexes of glass and the surrounding medium, generally air. Even the most optimized glass composition can present reflection losses up to 8% [25].

Antireflective (AR) effect between two media with different refractive indexes can be achieved by several approaches such as surface texturing [26][27], interference-type layer stacks by destructive interference of light reflected at different interfaces [28] and multi-layer stacks with graded refractive index structure (GRIN) [29]. The total reflection of the system can be minimized by adjusting the refractive index and thickness of each layer. In fact, patterned-glass can be used as cover glass in PV modules with a very light pattern acting as antireflective coating [25].

In order to harvest the full potential of photovoltaic cells, the antireflection effect needs to maximize the optical transmission in the wavelength range that matches the spectral response of the solar cells (i.e., the ratio between the produced current and the incoming power). In the case of MJ solar cells, their broad wavelength range of operation, approximately ranging between 300-2000 nm, requires an antireflection broadband performance.

Therefore, AR layer systems are a key requirement in solar energy applications in order to minimize Fresnel reflection losses in the glass-air interfaces. Some examples are presented in the Figure 1-3. Depending on the module configuration, the AR layer is needed on one or

both sides of the cover glass, and even in the homogenizer refractive prism.

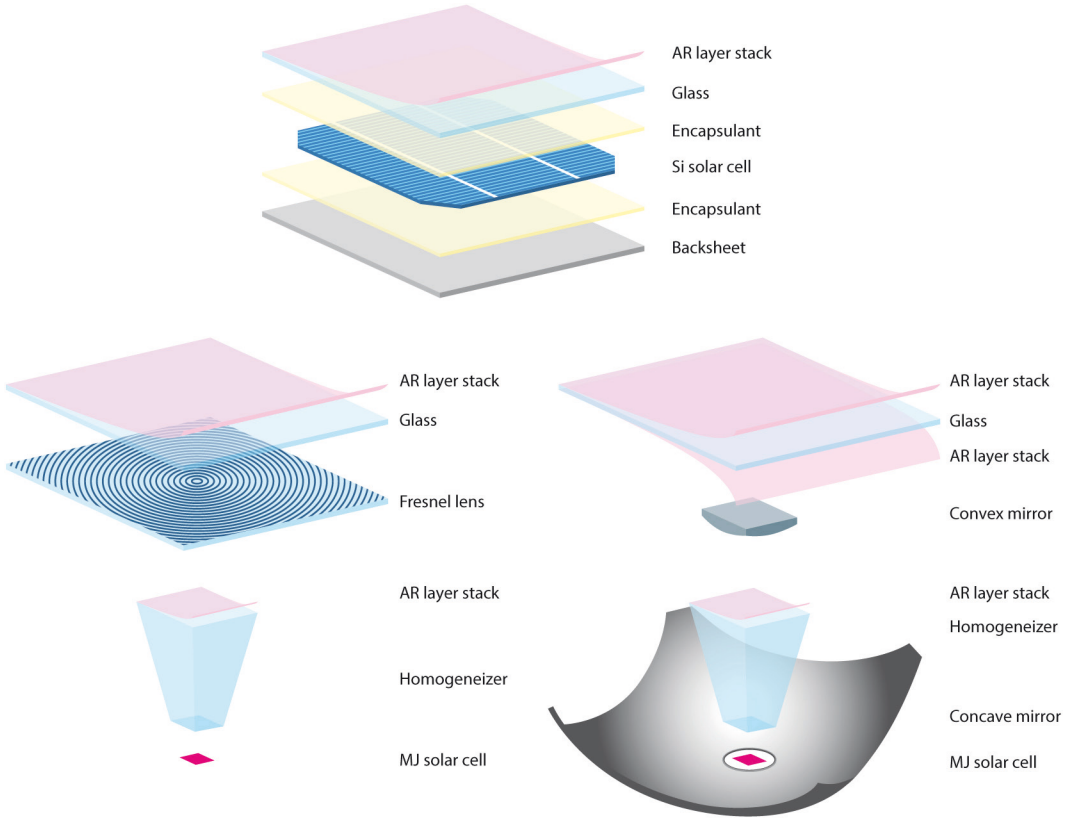

Figure 1-3. AR layer systems on PV and CPV modules.

1.3. Antireflective coatings by sol-gel method

PV is a highly cost-sensitive industry and the required low costs per square meter support the development of highly cost-effective AR coatings. The concept of levelized cost of energy (LCOE) is used to fairly compare electricity prices and costs among diverse power generation technologies. According to the SunShot Initiative, LCOE should reach a cost of 0.03 $/kWh for utility-scale PV, 0.04 $/kWh for commercial, and 0.05 $/kWh for residential rooftop PV systems by 2030 [30][31] and power purchase agreements below 0.02 €/kWh have been signed in several countries according to European Technology & Innovation Platform PV [4]. They indicate that LCOE for utility-scale PV in Malaga with 7% nominal weighted average costs of capital is currently 0.023 €/kWh and is decreasing to 0.014 €/kWh by 2030. In high direct irradiation conditions, CPV has the potential to provide electricity at competitive costs. While CPV modules allow to achieve efficiencies far beyond flat-plate c-Si technology, the main challenge is the difficulty of CPV to compete with flat-plate modules on cost. Fraunhofer

Institute for solar energy systems and the Department of Energy of the United States, using technical and financial assumptions have calculated LCOE for large scale CPV ranging from 0.10 to 0.15 €/kWh for locations with direct normal irradiance (DNI) of 2000 kWh/m²a and from 0.08 to 0.12 €/kWh for 2500 kWh/m²a DNI [32] and depending on installations growth, it could reach 0.045-0.075 €/kWh by 2030. One of the possibilities to reduce LCOE for both CPV and flat-panel c-Si technology is to improve the optical performance at module level. AR coating system will be feasible depending on the ratio between the coating processing cost and enhanced efficiency of the photovoltaic system.

In a GRIN structure AR system, depending on the application, the AR multi-layer stack may consist of an only single layer covering a narrow spectral bandwidth or multiple layers permitting to achieve a broadband optical performance [29]. The required value of refractive index of some of the layers partaking in an AR multi-layer stack with GRIN structure needs to be very low and bulk materials cannot meet this criterion. The lowest refractive index that can be achieved by dense material is about 1.38 for MgF_2 [33] followed by 1.50 for SiO_2. However, regarding mechanical properties, SiO_2 is harder and more resistant to abrasion [34][35]. An alternative way to attain the required refractive index is based on the introduction of voids into the bulk coating materials. Most studies regarding AR coatings following this strategy are based on porous SiO_2 material [36–61].

Sol-gel method is one of the most attractive processes, as it offers a vast range of opportunities for material design with a very precise control of microstructure [62][63] and homogeneity of the fabricated material by governing features such as volume and size of pores, besides being a low-cost, low-temperature and simple operation process. The synthesis route for the creation of inorganic oxides consists of the admixture of chemical precursors, generally metal alkoxides, that are hydrolyzed with acidic or basic water in alcohol media as homogenizing agent, obtaining an inorganic network. Depending on the process parameters, the same starting precursors can result in very different structures with only small changes in preparation conditions [64]. The resultant stable sol is then deposited through any of the common methods that let to grow a homogeneous coating from a liquid on a substrate, such as dip coating, spray coating, spin coating, roll coating, flow coating. During evaporation of solvent, the gel is formed and finally, a thermal treatment is needed to promote the elimination of unreacted compounds as well as physiosorbed water and solvent, thus allowing to attain a consolidated inorganic network. In order to effectively contribute to LCOE reduction, the AR layer system

should be deposited by means of a cost-competitive, easy up-scaling, highly efficient as well as environmental-friendly process.

Although sol-gel is an intrinsically low-cost technology, the chemical process can be precisely optimized in terms of finding the synthesis conditions that lead to very stable sols with extended pot life that permits to deposit mechanically stable coatings with durable AR properties, and a high repeatability over time.

All these features are important advantages over vacuum deposition techniques that had been previously used for growing the AR coatings [65]. These techniques such as magnetron sputtering or physical vapor deposition permitted to obtain high-quality coatings. However, they are very expensive and present some limitations regarding material structure and porosity required for this application.

1.3.1. Acid and basic catalysis

As mentioned, porous SiO_2 prepared by sol-gel method is one of the most suitable materials for solar energy AR applications.

Sol-gel process consists of the preparation of inorganic polymers or ceramics from solution through a transformation from liquid precursors to a sol and finally to a network structure of inorganic oxide in the form of glasses, glass ceramics, and ceramics. Most common synthesis is based on metal alkoxides route. The control of the hydrolysis and condensation reaction of these organometallics leads to the desired formation of the material during the sol-gel-glass processes. The key to mastering sol-gel chemistry is based on the proper management of the hydrolysis and condensation of the alkoxides, that strongly depends on the electronegativity of its metal central atom (M). For a specific $M(OR)_4$ alkoxide, the reaction parameters that must be considered are the nature of the R-group, the ratio of water to alkoxide, the ratio of solvent to alkoxide (alkoxide concentration) and the presence and concentration of catalysts. Taking into account the silicon electronegativity that affects the ionic character of the M-O bond, the chemistry of the silicon alkoxides is very slow, and its hydrolysis and condensation must be trigger by either acid or base catalysts. The pH of the media affects the relative rates of the hydrolysis and condensation reactions of the silicon alkoxide [66][67], and therefore, the structure and porosity of the processed material [68].

When the hydrolysis reaction of monomeric alkoxysilanes is approached under acidic

conditions (see Figure 1-4), the alkoxide group is protonated in a first step and electron density is withdrawn from silicon making it more electrophilic and susceptible to water attack [69]. Under basic conditions (see Figure 1-4), the water dissociation takes place producing nucleophilic hydroxyl anions, which react with silicon.

Successive hydrolysis steps get progressively slower under acidic conditions and faster under basic conditions [70][71] provoking a remarkable difference in the obtained sol and therefore in the structure of the coating material.

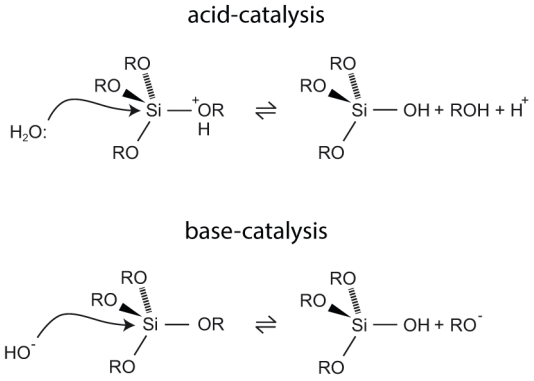

Figure 1-4. Hydrolysis of monomeric alkoxysilane under acidic and basic conditions.

Furthermore, under basic conditions, hydrolysis kinetics are more strongly affected by other parameters like the concentration of alkoxide and nature of the solvent. The triggering of condensation reactions depends on the degree of hydrolysis that has already occurred as a silanol group is required. In basic conditions, since hydrolysis steps get progressively faster, all the alkoxide groups are likely hydrolyzed before the first condensation step occurs, then condensation steps result in small, highly branched agglomerates which eventually crosslink to form a colloidal sol. The processed coating results in a particulate and porous material [72], but with weak bindings between particles and poor abrasion resistance.

In acidic conditions, condensation begins before hydrolysis is complete, and it takes place on terminal silanols, resulting in chain-like structures in the sol. The processed coating results in a network-like dense material [68][72] with strong adherence to the substrate and high mechanical properties.

The gel is an intermediate state of matter between a solid and a liquid formed by polymers or long chain molecules crosslinked to create a tangled network which extends through (thus incorporating) a liquid. In this case, the gel is formed by the polymerization of hydrolyzed

silicon alkoxides that finally entrap the alcoholic solution. These processes are necessarily accompanied by drastic changes of the viscosity behavior of the reaction mixture as long as polymer size increase, provoked by the crosslinking of polymeric species. Since viscosity is an important parameter that contributes to the coating formation, [73], the reaction parameters must be controlled in order to obtain long stable sols that evolves slowly and grow repeatable coatings. The chemistry in acid-catalyzed sols usually lets to obtain more stable sols than those prepared in basic conditions.

Regarding porous silica developed by sol-gel process for AR applications, most of the reported research work is focused on the design of mono-layer materials and studies their optical properties only in narrow wavelength band reporting transmission value at a single wavelength.

The majority of these studies are based on glass dipping in sols prepared with tetraethyl orthosilicate (TEOS) [38–40,48,50,54,55,58–61,74–76] and mixture of TEOS and methyl triethoxysilane (MTES) [43–47,49,51,52,57], or even in commercial colloidal silica solution [36][37]. In this research field, Liu et al. [48] have worked with base-catalyzed sol-gel synthesis as well as Li et al. [55], who used the silica coating as part of a multi-layer stack. Other research works [54,56–59] have combined base and acid-catalyzed conditions of sol-gel synthesis in order to reach a tradeoff between optical and mechanical properties. Another strategy to improve mechanical properties has been focused on the deposition of an inner coating using acid-catalyzed sol and an external coating from a base-catalyzed sol [60][61].

The strategy followed on this research work is addressed to the attainment of a porous structure through acid-catalysis approach. Apart from the optical properties, the main challenge is to obtain robust and mechanically stable coatings as well as long stable sols that permits to deposit homogeneous and repeatable coatings for a long time, by means of a highly efficient and a cost-competitive process.

1.3.2. Evaporation induced self-assembly (EISA) method

In order to obtain porosity in acid-catalyzed synthesis route, an extensive approach first reported by Asefa et al. [77] and Brinker et al. [78] consists of combining sol-gel precursors and amphiphilic molecules or surfactants. Since then the combination of various sol-gel precursors (alkoxides with Si, Ti, Zr as central atom) and various surfactants allows to obtain a large number of coating mesostructures with pore dimension range from 2 to 20 nm [79][80], and it is known as EISA method.

Amphiphiles are chained molecules that have one moiety that dislike the solvent, and other moiety that favours it [81]. If water is the solvent these moieties are called hydrophobic and hydrophilic, respectively. Therefore, amphiphile behavior cannot be explain without explicit reference to the solvent. When the amphiphiles are dispersed in a solution, they self-assemble into micelle structures, above a certain critical concentration known as critical micellar concentration (CMC) [82]. They can organize into a variety of shapes such as spherical or cylindrical micelles that maintain the solvophilic parts of the surfactant in contact with solvent while shielding the solvophobic parts within the micellar interior [78]. Therefore, in order to have stable micellar structures, the solvent should be selective in the sense that it should show affinity to one part of the molecule and rejection to the other.

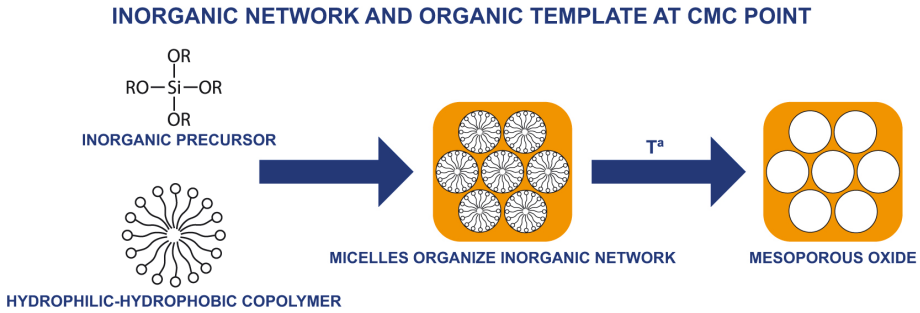

Figure 1-5. Gel and final mesoporous structure from starting organic phases and inorganic precursors.

These amphiphiles can be from different nature, depending on the hydrophilic moiety, and therefore on its dissociation way in aqueous media. They can be sub-divided as i) non-ionic surfactants, if they are molecules such as copolymers that have n-alkyl chain as hydrocarbon tail and a hydrophilic polar moiety and ii) as ionic surfactants if they dissociate in water solution. Ionic surfactants are further classified as anionic surfactants, if dissociate into an amphiphilic anion or as cationic surfactant if dissociate into an amphiphilic cation. Another particular sub-division are the amphoteric surfactants, whose dissociation depends on the pH. They are anionic at high pH or cationic at low pH.

In order to obtain an effective organization of the mesostructure of the grown layer, the inorganic polymerization during the coating deposition must be avoided. In silica chemistry, this is achieved under acidic conditions. At hydronium ion concentration close to the isoelectric point of colloidal silica, the siloxane chain condensation is paralyzed, and the silica-amphiphile self-assembly can take place in the resulting deposited films. Therefore, EISA procedure is a combined method in which both the chemical parameters in the sol formulation

and the deposition process influences the obtained material [79]. When the sol is deposited on the substrate and the alcohol evaporation rapidly starts at the interface film/air, an inhomogeneous evaporation would lead to differences in the film composition along its depth profile, due to concentration gradients. For example, a rapid evaporation provokes enrichment of oxide groups and amphiphile molecules in the surface. Environmental conditions during coating deposition such as temperature and relative humidity are also key factors to control during deposition to achieve homogenous mesostructured coatings.

Through the preparation of an acid-catalyzed sol, containing an inorganic precursor and an amphiphile in alcohol medium, the micelles formed by the amphiphile act as structure directing agent (SDA) as shown in Figure 1-5. The homogenous sol that contains amphiphiles in alcohol and water media is used for deposition of the coating, and the preferential evaporation of alcohol concentrates the gel film in water, amphiphiles and silica species [78]. The increasing of amphiphile above its CMC drives self-assembly of the formed micelles and silica polymers. The outcome is the formation of thin film mesostructures that depends on the physic-chemical properties of the amphiphiles and are oriented with respect the substrate plane. The differences in the alcohol/water/silica monomer/amphiphile system lead to different morphologies in space [83]. After the elimination of amphiphile compounds through thermal treatment or solvent extraction, the porous structure is obtained. The dip coating process of a sol containing inorganic precursor and amphiphile, and its self-assembly lead by controlled solvent evaporation up to CMC is schematized in the Figure 1-6.

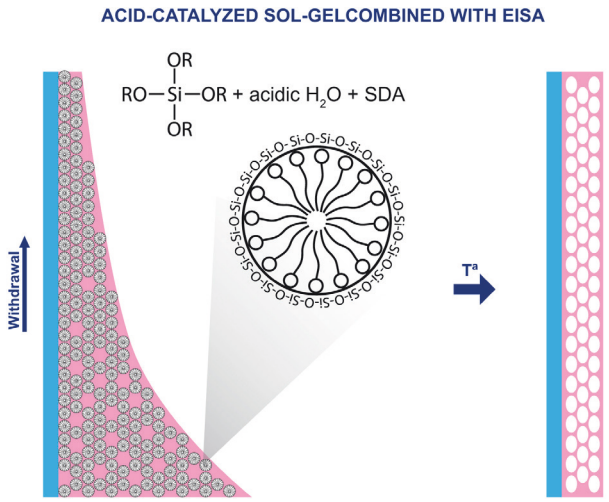

Figure 1-6. Acid-catalyzed silica species and amphiphile micelles self-assembly during withdrawal step.

1.3.3. Water content as structure regulating tool

As explained, inorganic network synthetized by acid-catalyzed, unlike the base-catalyzed one, leads to the formation of a material with an extended linear or randomly poor branched structure. The advantage is that coatings with robust mechanical properties and good adhesion are derived from this route, as well as sols with long-term stability [68]. Base-catalyzed synthesis leads to formation of highly crosslinked discrete polymeric clusters that promote a porous structure with poorer mechanical properties and more instable sols, whereas colloidal suspensions are formed by highly crosslinked dense particles that may also be built by base-catalysis [84]. The polymer growth along sol-gel processes is observed in the Figure 1-7. By adjustment and selection of the synthesis parameters and amphiphiles as structure directing agents, acid-catalyzed sol-gel approach combined with EISA result in a proper method to control the microstructure, the pore volume and pore size of the coating, while obtaining highly stable sols and materials.

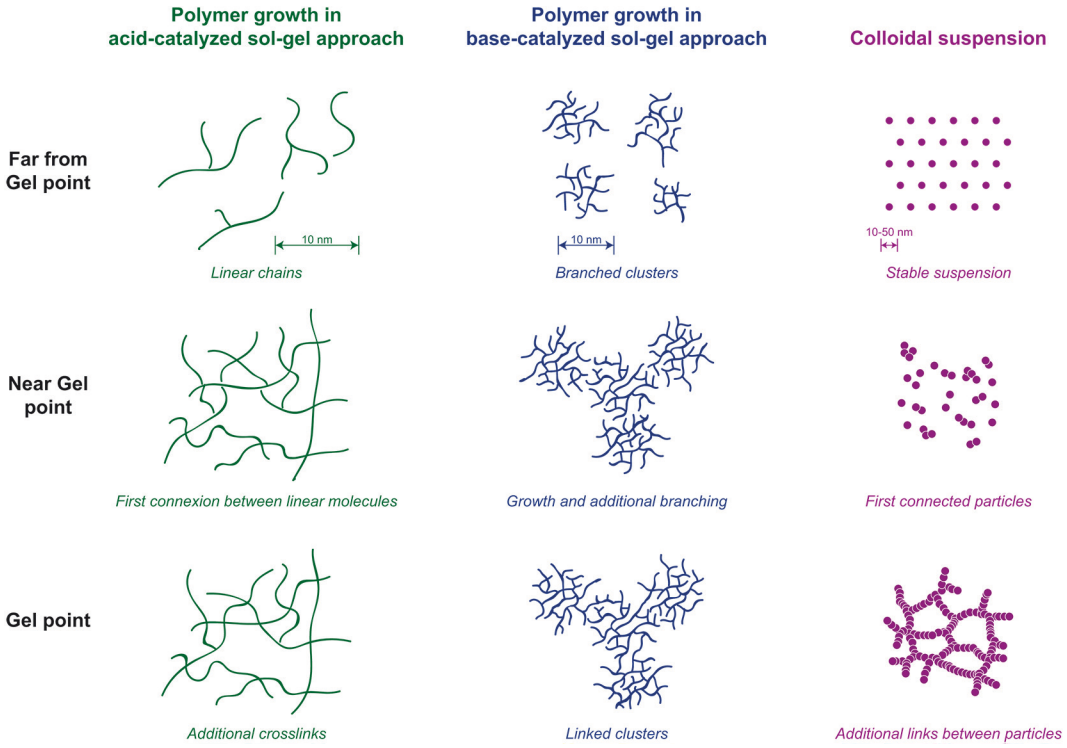

Figure 1-7. Structure evolution in acid-catalyzed, base-catalyzed and colloidal sols adapted from [85] with permission of Elsevier.

However, due to the extensive range of possibilities that this technique offers, improved approach can be tailored by adjusting other parameters in order to obtain further accurate

structures. Apart from catalyst and pH, the structural properties of the sol-gel prepared materials are strongly affected by other process parameters and, particularly, by the water/alkoxide molar ratio (R_w), which is an important structure regulating tool [86].

In the acid-catalyzed approach, low R_w conditions lead to the beginning of the condensation of siloxane bonds prior to the completion of the hydrolysis. This condensation takes place on terminal silanols, thus leading to the formation of weakly branched chain-like networks. High R_w conditions (>> 4) foster a hydrolysis step which can be fully completed before condensation [62], which, in turn, is favored through the water producing reaction rather than the alcohol producing one, according to Figure 1-8. The water produced by condensation causes a complete hydrolysis and enhances the depolymerization rate that occurs preferentially at less stable sites [68]. Subsequent repolymerization forms stable configurations at the expense of unstable ones, which finally leads to the increase of branching in chains whose structure may be closer to that of discrete colloidal particles from base-catalysis. The silicate condensation sequences from atomic or molecular scale (monomer, dimer, linear or cyclic trimer, cyclic tetramer, and higher order generation of discrete colloidal particles) obtained from acid-catalyzed TEOS has been widely investigated by Engelhardt et al. [87] using ^{29}Si nuclear magnetic resonance for characterization. By further connection of the single rings and chains, two-dimensional single layers are first formed that subsequently leads to three-dimensional frameworks [88]. The coatings processed with such acid-catalyzed TEOS in high R_w conditions results in a more branched network with respect to the low R_w cases. Thus, higher porosity structures closer to base-catalyzed processing can be provided but simultaneously maintaining a strong adherence and good mechanical properties associated to the acid-catalyzed process. Based upon this theoretical background, Collina et at. [72] demonstrated that the surface area of acid-catalyzed TEOS porous gels strongly increased for R_w values raising up to ten.

$$\equiv Si - OR + H_2O \underset{\text{esterification}}{\overset{\text{hydrolysis}}{\rightleftharpoons}} \equiv Si - OH + ROH$$

$$\equiv Si - OR + HO - Si \equiv \underset{\text{alcoholic depolymerization}}{\overset{\text{alcohol condensation}}{\rightleftharpoons}} \equiv Si - O - Si + ROH$$

$$\equiv Si - OH + HO - Si \equiv \underset{\text{hydrolytic depolymerization}}{\overset{\text{water condensation}}{\rightleftharpoons}} \equiv Si - O - Si \equiv + H_2O$$

Figure 1-8. Hydrolysis, condensation and reversed reactions of Si alkoxide.

The R_w must be used as structure regulating tool in order to obtain the most efficient approach for the deposition of highly performing AR layer systems for CPV applications. It can offer an important role considering the desired environmental-friendliness, cost-effectiveness and easy up-scaling characteristics of the process and envisaging the good sol stability and durability of designed in this way coatings.

1.4. Antisoiling and durability properties

AR coatings applied on photovoltaic modules operating outdoors must assure an in-service long-term high optical performance. In order to achieve this target, they must exhibit inherent properties such as mechanical robustness, excellent adhesion and cohesion. They must guarantee a high performance in a variety of climates and also be capable to mitigate the impact of external factors such as dust and dirt adherence, that can reduce the optical performance of the glass cover and therefore, PV modules. The soling is an important problem in large-scale ground PV power plants (of 10-20 MW) or in very large-scale PV power generation systems (200 MW-1GW) covering areas of several km^2 or tens of km^2, respectively, and in particular is more severe for the CPV solar technologies which use lenses or mirrors to concentrate the solar light. Up to a 26% decrease in produced electrical power due to soling has been measured for the CPV technology [89], because it mainly collects the direct solar radiation, in contrast to flat panels [90]. When the collector surface is soiled, the dust produces diffused solar radiation and a significant part of the incoming light is scattered and thus, lost. In order to cope with the impact of soiling in solar energy installations, oversized plants or the periodic cleaning of the modules are generally considered, which in turn increase the solar technologies costs in terms of the capital or operating expenditures (CAPEX or OPEX, respectively). Additionally, the solar power plant cleaning is not an environment-friendly operation, since water is wasted for cleaning in areas which suffer from water short-age (which usually have also high solar irradiation), also becoming more expensive. Therefore, technical efforts in order to provide electrical energy at a more competitive cost through environment-friendly installations must be addressed towards the development and assessment of durable AR coating systems for cover glass of solar modules. The double purpose of minimizing Fresnel losses (thus increasing energy generation) and achieving soling repellence in the external glass-air interface has become of crucial importance to reduce the capital expenditure and solar power plant maintenance.

The power loss due to soiling varies depending on physical and chemical properties of dust particles as well as on geographic locations [91]. Dust can comprise small amounts of organic material (pollen, vegetation, fungi, bacteria, bird droppings), and, most commonly, inorganic minerals from geomorphic fallout such as sand, clay, or eroded limestone. The particle size, constituents and shape of the dust vary from region to region throughout the world, as well as the deposition behavior and accumulation rates. The surface energy of the coatings is an important property that influences their wettability, adhesion and friction properties and therefore it may be modulated to contribute against soiling adherence. In particular, the wetting behavior of a surface by a liquid is governed by both the surface free energy and its structure [92]. Perfluorinated polymers are known for being materials with extremely low surface free energy (SFE), which results in an antiadhesive behavior for polar and non-polar substances [93]. Shafrin et al. [94] reviewed the critical surface tension exhibited by low energy surfaces obtaining the following order for those constituted by $–CF_3$ < $–CF_2H$ < $–CF_2$- < $–CH_2$-CF_3 < $–CF_2$-CFH- < $–CH_3$ < $–CF_2$-CH_2- < –CFH-CH_2- < $–CH_2$-. Chlorocarbon or nitrated hydrocarbon surfaces were subsequent ranked after those fluoro and hydrofluoro-carbon based materials. Furthermore, the high strength of the C-F bond grants high thermal, chemical, photochemical and hydrolytic stability, which are relevant features for outdoor application and weathering resistance.

In a porous silica material, residual silanol groups (Si-OH) stand on the surface, being capable to promote the adsorption of moisture or contaminants in outdoor exposure. This phenomenon could affect the optical properties of AR coatings, as the air into the pores is replaced by water vapor and contaminants [45][46].

In order to undertake one of the external factors that may alter the optical properties of the system when operating outdoors, such as soiling, several approaches can be envisaged, taking into account their cost-competitiveness.

The first way may consist in the post-treatment of a finally sintered porous silica coating with the aim to reduce the number of free silanol groups (Si-OH) on the surface by replacing them with other moieties with antiadhesive behavior. A widely studied approach has been the replacement of the active hydroxyl groups by inert organosilyl groups by methyl-silylating processes that would turn the surface to hydrophobic [45][46]. Several methyl-silylating agents have been studied in the literature as candidates for replacement of hydroxyl groups to trimethylsilyl (–Si-$(CH_3)_3$), obtaining inert hydrophobic surfaces. Particularly hexamethyl

disilazane (HMDS) has been used as methyl-silyating agent to functionalize porous silica coatings through several approaches such as contact with HMDS vapor [43,95,96], or immersion in solutions with different organic solvents (hexane [45,46,58,97], toluene [98–100], alcohol [101]). The searched effect of the methyl-silylating post-treatment is the achievement of hydrophobic surfaces that contribute to the reduction in the adsorption of soiling accompanied by slightly or negligible decrease of transmittance. Ideally free silanol groups standing in both internal and external surface are prone to be replaced by $–Si-(CH_3)_3$ groups as shown in Figure 1-9.

An alternative way may be approached through the addition of low contents of components with hydrophobic moieties during sol synthesis, that interfere as less as possible in the optical properties. The best way is the incorporation of these moieties covalently bonded to porous silica backbone what can be done by adding organoalkoxides with non-hydrolizable groups linked to silicon central atoms as a Si-C bond. For example, polyfluoroalkyl alkoxysilanes (FAS) can be used as fluorocarbon moiety carrier in a sol-gel synthetized material. Voorhoeve [102] had proved that organohalosilanes with fluorine in the α- and β-carbon positions to silicon hydrolyzed very easily at the –C-Si≡ bond. For that reason, polyfluoroalkyl with hydrogen in α- and β-carbon and fully fluorinated carbon from γ-position to the end of the chain should be more suitable for the synthesis of a covalently bonded organic-inorganic hybrid material. There are several works that have combined FAS in sol-gel matrixes with the purpose to obtain super-liquid-repellent surfaces [103–105]. However, these works do not balance the repellence property with the AR behavior of the coating and some of them also tailor the surface roughness.

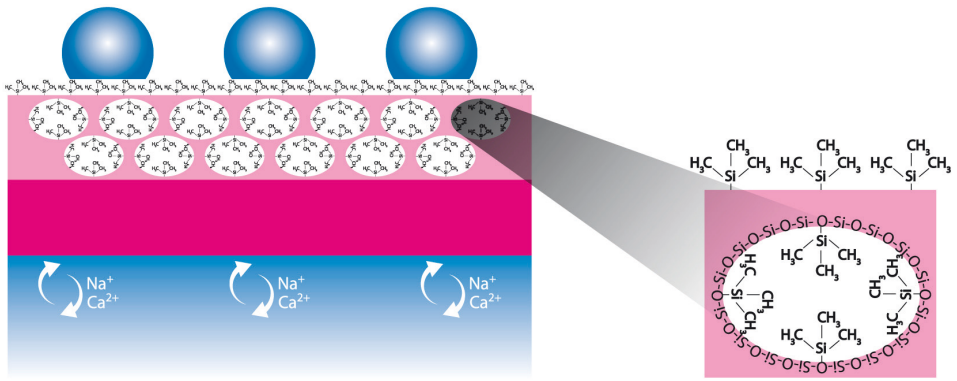

Figure 1-9. Effect of methyl-silylating post-treatment on porous coating.

It is well known that the wetting of a surface by a liquid is affected by the roughness of the surface [106–108]. Indeed, an effective way to enhance the hydrophobic properties of a coating is to increase its surface roughness, as corroborated by Miller et al. [109] on polytetrafluroethylene (PTFE) thin films. In this work, the smoother PTFE surface exhibited hydrophobic behavior (90-100º) while superhydrofobic properties (150º) where achieved by the roughest surface. However, surface roughness has a remarkable effect on the specular and diffuse components of reflectance. It is known that a smooth surface reflects most part of the incident light in the specular direction, whereas a rough surface reflects it in a lobe around the specular direction [110]. As previously mentioned, CPV technology uses only the direct beam component of the incident light. Thus, diffuse reflection should be avoided.

Substantial differences exist among both mentioned routes (methyl-silylation and polyfluoroalkyl doping) from the point of view of production cost, time, and energy consumption, mainly linked to required production steps and sintering temperatures. Focusing on the cost-effectiveness of hydrophobic porous coating processes, it can be first underlined that whereas the first approach requires two steps the second one is a one-step process to achieve final properties (AR and low surface energy). The second aspect of the process is related to applied temperature treatment needed to consolidate the coating, and therefore the energy consumption. The first approach consists of a first deposition of a totally inorganic porous SiO_2, that can be treated at any required temperature for consolidation. However, the second approach contains organic derivatives in their initial formulation, and consequently present temperature restrictions in order not to degrade that moieties. A trade-off between cost-effectiveness and the mechanical properties derived from thermal treatment to assure robustness must be achieved.

Another issue concerning the modification of optical properties over time is related to glass composition. As explained before, the float glass used in solar energy applications presents a low iron content aiming to improve solar transmittance. However, despite its higher production cost, sodium, calcium, potassium, and magnesium content is not avoided in the glass formulation with the related threat of their potential diffusion out of the glass when it is used for an extended period of time [111]. The ions of those alkali and alkaline-earth metals (alkali) diffusing from the glass substrate to the porous coating tend to form carbonate species in contact with the atmosphere. In fact, Helsch et al. [112] observed the formation of $CaCO_3$ crystals in a porous silica coating, reducing the optical transmission at 500 nm from 99% to

94% after aging of the coated float glass in ambient atmosphere for a few weeks. An effective way to prevent alkali diffusion is by means of an inner diffusion-preventing layer as part of the AR layer stack [111].

References

[1] Solar Power Europe, Global market outlook for solar power 2018-2022, Brussels, Belgium, 2018.

[2] Y. Jia, G. Alva, G. Fang, Development and applications of photovoltaic-thermal systems: A review, Renew. Sustain. Energy Rev. 102 (2019) 249–265.

[3] International Energy Agency - Photovoltaic Power Systems Technology Collaboration Programme, 2019 Snapshot of Global PV Markets, 2019.

[4] European Technology & Innovation Platform PV, PV the cheapest electricity source almost everywhere, 2019.

[5] M.A. Green, High-efficiency silicon solar cell concepts, McEvoy's Handb. Photovoltaics Fundam. Appl. 33 (2017) 95–128.

[6] W. Shockley, H.J. Queisser, Detailed balance limit of efficiency of p-n junction solar cells, J. Appl. Phys. 32 (1961) 510–519.

[7] H. Kawasaki, K. Konishi, D. Adachi, H. Uzu, T. Irie, K. Yoshikawa, K. Nakano, T. Uto, W. Yoshida, K. Yamamoto, M. Kanematsu, Silicon heterojunction solar cell with interdigitated back contacts for a photoconversion efficiency over 26%, Nat. Energy. 2 (2017) 17032.

[8] S. van Riesen, M. Neubauer, A. Boos, M.M. Rico, C. Gourdel, S. Wanka, R. Krause, P. Guernard, A. Gombert, New module design with 4-junction solar cells for high efficiencies, AIP Conf. Proc. 1679 (2015).

[9] M.A. Green, K. Emery, Y. Hishikawa, W. Warta, E.D. Dunlop, Solar cell efficiency tables (version 47), Prog. Photovoltaics Res. Appl. 24 (2016) 3–11.

[10] ASTM G173-03, Standard tables for reference solar spectral irradiances: direct normal and hemispherical on 37º tilted surface, 2013.

[11] S.P. Phillipps, W. Guter, E. Welser, J. Schöone, M. Steiner, F. Dimroth, A.W. Bett, Present status in the development of III–V multi-junction solar cells, in: Next Gener. Photovoltaics, 2012: pp. 1689–1699.

[12] E.F. Fernández, F. Almonacid, A.J. Garcia-Loureiro, Multi-junction solar cells electrical characterization by neuronal networks under different irradiance, spectrum and cell temperature, Energy. 90 (2015) 846–856.

[13] R.R. King, C.M. Fetzer, D.C. Law, K.M. Edmondson, H. Yoon, G.S. Kinsey, D.D. Krut, J.H. Ermer, P. Hebert, B.T. Cavicchi, N.H. Karam, Conference Record, in: IEEE 4th World Conf. Photovolt. Energy Conversion, Waikoloa, HI, 17–12 May, 2006: pp. 1757–1762.

[14] P.R. Sharps, A. Comfeld, M. Stan, A. Korostyshevsky, V. Ley, B. Cho, T. Varghese, J. Diaz, D. Aiken, Conference Record, in: 33rd IEEE Photovolt. Spec. Conf. San Diego, USA, 11–16 May, 2008: pp. 2046–2051.

[15] A.W. Bett, F. Dimroth, W. Guter, R. Hoheisel, E. Oliva, S.P. Philipps, J. Schöne, G. Siefer, M. Steiner, A.Wekkeli, E.Welser, M.Meusel, W. Köstler, G. Strobl, Conference Record, in: 24th Eur. Photovolt. Sol. Energy Conf. Exhib. Hamburg, Ger. 21–25 Sep, 2009: pp. 1–6.

[16] D.J. Friedman, J.F. Geisz, S.R. Kurtz, J.M. Olson, 1-eV solar cells with GaInNAs active layer, J. Cryst. Growth. 195 (1998) 409–415.

[17] K.W.J. Barnham, I. Ballard, J.P. Connolly, N.J. Ekins-Daukes, B.G. Kluftinger, J. Nelson, C. Rohr, Quantum well solar cells, Phys. E. 14 (2002) 27–36.

[18] J.F. Geisz, D.J. Friedman, J.S. Ward, A. Duda, W.J. Olavarria, T.E. Moriarty, J.T. Kiehl, M.J. Romero, A.G. Norman, K.M. Jones, 40.8% Efficient inverted triple-junction solar cell with two independently metamorphic junctions, Appl. Phys. Lett. 93 (2008).

[19] R.R. King, D. Bhusari, D. Larrabee, X.-Q. Liu, E. Rehder, K. Edmondson, H. Cotal, R.K. Jones, J.H. Ermer, C.M. Fetzer, D.C. Law, N.H. Karam, Solar cell generations over 40% efficiency, Prog. Photovoltaics Res. Appl. 20 (2012) 801–815.

[20] E.F. Fernández, F. Almonacid, P.M. Rodrigo, P.J. Pérez-higueras, CPV Systems, in: McEvoy's Handb. Photovoltaics, Elsevier Ltd, 2018: pp. 929–986.

[21] T.N.D. Tibbits, P. Beutel, M. Grave, C. Karcher, E. Oliva, G. Siefer, A. Wekkeli, M. Schachtner, F. Dimroth, A.W. Bett, R. Krause, M. Piccin, N. Blanc, M. Muñoz-Rico, C. Arena, E. Guiot,

C. Charles-Alfred, C. Drazek, F. Janin, L. Farrugia, B. Hoarau, J. Wasselin, A. Tauzin, T. Signamarcheix, T. Hannappel, K. Schwarzburg, A. Dobrich, New efficiency frontiers with wafer-bonded multi-junction solar cells, 29Th Eur. PV Sol. Energy Conf. (2014) 4.

[22] E. Gerster, T. Gerstmaier, A. Gombert, R. Krause, S. Van Riesen, S. Wanka, T. Zech, SOITEC's 4 junction solar cell module one year on sun, AIP Conf. Proc. 1679 (2015).

[23] P. Rodrigo, E.F. Fernández, F. Almonacid, P.J. Pérez-Higueras, Models for the electrical characterization of high concentration photovoltaic cells and modules: A review, Renew. Sustain. Energy Rev. 26 (2013) 752–760.

[24] C. Algora, I. Rey-Stolle, Handbook of concentrator photovoltaic technology, John Wiley and Sons Ltd., 2016.

[25] K. Burrows, V. Fthenakis, Glass needs for a growing photovoltaics industry, Sol. Energy Mater. Sol. Cells. 132 (2015) 455–459.

[26] Y.H. Kang, S.S. Oh, Y.S. Kim, C.G. Choi, Fabrication of antireflection nanostructures by hybrid nano-patterning lithography, Microelectron. Eng. 87 (2010) 125–128.

[27] C.J. Ting, C.F. Chen, C.P. Chou, Subwavelength structures for broadband antireflection application, Opt. Commun. 282 (2009) 434–438.

[28] Y. Li, K. Yang, B. Xia, B. Yang, L. Yan, M. He, H. Yan, B. Jiang, Preparation of mechanically stable triple-layer interference broadband antireflective coatings with self-cleaning property by sol-gel technique, RSC Adv. 7 (2017) 14660–14668.

[29] D. Chen, Anti-reflection (AR) coatings made by sol gel processes : A review, Sol. Energy Mater. Sol. Cells. 68 (2001) 313–336.

[30] The SunShot Initiative's 2030 Goal: 3¢ per Kilowatt Hour for Solar Electricity New Solar Opportunities for a New Decade, U.S. Department of Energy, 2016.

[31] W. Cole, B. Frew, P. Gagnon, J. Richards, Y. Sun, J. Zuboy, M. Woodhouse, R. Margolis, SunShot 2030 for Photovoltaics (PV): Envisioning a Low-cost PV Future, U.S. Department of Energy, 2017.

[32] M. Wiesenfarth, S.P. Philipps, A.W. Bett, K. Horowitz, S. Kurtz, Current status of concentrator photovoltaic (CPV) technology, U.S. Department of Energy Office of Scientific and Technical Information, 2017.

[33] L. Dumas, E. Quesnel, F. Pierre, F. Bertin, Optical properties of magnesium fluoride thin films produced by argon ion-beam assisted deposition, J. Vac. Sci. Technol. A Vacuum, Surfaces, Film. 20 (2002) 102–106.

[34] H.K. Pulker, Coatings on glass, Elsevier, 1999.

[35] V. Hody-Le Caër, E. De Chambrier, S. Mertin, M. Joly, M. Schaer, J.L. Scartezzini, A. Schüler, Optical and morphological characterisation of low refractive index materials for coatings on solar collector glazing, Renew. Energy. 53 (2013) 27–34.

[36] M. Manca, A. Cannavale, L. De Marco, A.S. Aricò, R. Cingolani, G. Gigli, Durable superhydrophobic and antireflective surfaces by trimethylsilanized silica nanoparticles-based sol-gel processing, Langmuir. 25 (2009) 6357–6362.

[37] G. Helsch, A. Mös, J. Deubener, M. Höland, Thermal resistance of nanoporous antireflective coatings on silica glass for solar tower receivers, Sol. Energy Mater. Sol. Cells. 94 (2010) 2191–2196.

[38] J.H. Rouse, B.A. MacNeill, G.S. Ferguson, Sol-gel processing of ordered multilayers to produce composite films of controlled thickness, Chem. Mater. 12 (2000) 2502–2507.

[39] H.K. Raut, A.S. Nair, S.S. Dinachali, V.A. Ganesh, T.M. Walsh, S. Ramakrishna, Porous SiO_2 anti-reflective coatings on large-area substrates by electrospinning and their application to solar modules, Sol. Energy Mater. Sol. Cells. 111 (2013) 9–15.

[40] X. Meng, Y. Wang, H. Wang, J. Zhong, R. Chen, Preparation of hydrophobic and abrasion-resistant silica antireflective coatings by using a cationic surfactant to regulate surface morphologies, Sol. Energy. 101 (2014) 283–290.

[41] Y. Xu, C. Peng, C. Xin, J. Wu, Preparation of silica antireflective films for solar energy application, Mater. Lett. 94 (2013) 89–91.

[42] Y. Li, H. Lv, L. Ye, L. Yan, Y. Zhang, B. Xia, H. Yan, B. Jiang, Preparation of porous silica films in a binary template system for double-layer broadband antireflective coatings, RSC Adv. 5 (2015) 20365–20370.

[43] T.-J. Ha, H.-H. Park, S.-B. Jung, H. Ryu, B.-G. Yu, Investigation of the effect of calcination temperature on HMDS-treated ordered mesoporous silica film., J. Colloid Interface Sci. 326 (2008) 186–190.

[44] G.S. Vicente, R. Bayón, A. Morales, Effect of additives on the durability and properties of antireflective films for solar glass covers, J. Sol. Energy Eng. 130 (2008) 011007.

[45] G. San Vicente, R. Bayón, N. Germán, A. Morales, Surface modification of porous antireflective coatings for solar glass covers, Sol. Energy. 85 (2011) 676–680.

[46] G. San Vicente, R. Bayón, N. Germán, A. Morales, Long-term durability of sol-gel porous coatings for solar glass covers, Thin Solid Films. 517 (2009) 3157–3160.

[47] H.L. Yang, L. Hao, J.N. Wang, Z.N. Zhang, X.P. Liu, L.J. Jiang, Self-cleaning and antireflective films for all-glass evacuated tube solar collectors, Energy Procedia. (2015) 226–232.

[48] B.T. Liu, W. De Yeh, Antireflective surface fabricated from colloidal silica nanoparticles, Colloids Surf. A Physicochem. Eng. Asp. 356 (2010) 145–149.

[49] D.B. Mahadik, R.V. Lakshmi, H.C. Barshilia, High performance single layer nano-porous antireflection coatings on glass by sol-gel process for solar energy applications, Sol. Energy Mater. Sol. Cells. 140 (2015) 61–68.

[50] R. Prado, G. Beobide, A. Marcaide, J. Goikoetxea, A. Aranzabe, Development of multifunctional sol-gel coatings: Anti-reflection coatings with enhanced self-cleaning capacity, Sol. Energy Mater. Sol. Cells. 94 (2010) 1081–1088.

[51] M. Faustini, L. Nicole, C. Boissière, P. Innocenzi, C. Sanchez, D. Grosso, Hydrophobic, antireflective, self-cleaning, and antifogging sol-gel coatings: An example of multifunctional nanostructured materials for photovoltaic cells, Chem. Mater. 22 (2010) 4406–4413.

[52] L. Miao, L.F. Su, S. Tanemura, C.A.J. Fisher, L.L. Zhao, Q. Liang, G. Xu, Cost-effective nanoporous SiO_2-TiO_2 coatings on glass substrates with antireflective and self-cleaning properties, Appl. Energy. 112 (2013) 1198–1205.

[53] Y. Li, H. Lv, L. Ye, L. Yan, Y. Zhang, B. Xia, H. Yan, B. Jiang, Preparation of porous silica films in a binary template system for double-layer broadband antireflective coatings, RSC Adv. 5 (2015) 20365–20370.

[54] A. Vincent, S. Babu, E. Brinley, A. Karakoti, S. Deshpande, S. Seal, Role of catalyst on refractive index tunability of porous silica antireflective coatings by sol-gel technique, J. Phys. Chem. C. 111 (2007) 8291–8298.

[55] D. Li, F. Huang, S. Ding, Sol-gel preparation and characterization of nanoporous ZnO/SiO2 coatings with broadband antireflection properties, Appl. Surf. Sci. 257 (2011) 9110–9119.

[56] H.M. Shang, Y. Wang, S.J. Limmer, T.P. Chou, K. Takahashi, G.Z. Cao, Optically transparent superhydrophobic silica-based films, Thin Solid Films. 472 (2005) 37–43.

[57] S. Cai, Y. Zhang, H. Zhang, H. Yan, H. Lv, B. Jiang, Sol-gel preparation of hydrophobic silica antireflective coatings with low refractive index by base/acid two-step catalysis, ACS Appl. Mater. Interfaces. (2014) 8–13.

[58] H. Ye, X. Zhang, Y. Zhang, L. Ye, B. Xiao, H. Lv, B. Jiang, Preparation of antireflective coatings with high transmittance and enhanced abrasion-resistance by a base/acid two-step catalyzed sol-gel process, Sol. Energy Mater. Sol. Cells. 95 (2011) 2347–2351.

[59] G. Wu, J. Wang, J. Shen, T. Yang, Q. Zhang, B. Zhou, Z. Deng, B. Fan, D. Zhou, F. Zhang, A new method to control nano-porous structure of sol-gel-derived silica films and their properties, Mater. Res. Bull. 36 (2001) 2127–2139.

[60] Y. Zhang, F. Gao, L. Gao, L. Hou, Y. Jia, Study of tri-layer antireflection coatings prepared by sol-gel method, J. Sol-Gel Sci. Technol. 62 (2012) 134–139.

[61] X. Li, J. Shen, A scratch-resistant and hydrophobic broadband antireflective coating by sol-gel method, Thin Solid Films. 519 (2011) 6236–6240.

[62] J.C. Pouxviel, J.P. Boilot, J.C. Beloeil, J.Y. Lallemand, NMR study of the sol/gel polymerization, J. Non. Cryst. Solids. 89 (1987) 345–360.

[63] K.C. Chen, T. Tsuchiya, J.D. Mackenzie, Sol-gel processing of silica. I. The role of the starting compounds, J. Non. Cryst. Solids. 81 (1986) 227–237.
[64] A.E. Danks, S.R. Hall, Z. Schnepp, The evolution of 'sol-gel' chemistry as a technique for materials synthesis, Mater. Horizons. 3 (2016) 91–112.
[65] J. Moghal, J. Kobler, J. Sauer, J. Best, M. Gardener, A.A.R. Watt, G. Wakefield, High-Performance, Single-Layer Antireflective Optical Coatings Comprising Mesoporous Silica Nanoparticles, ACS Appl. Mater. Interfaces. 4 (2012) 854–859.
[66] E.J.A. Pope, J.D. Mackenzie, Sol-gel processing of silica. II. The role of the catalyst, J. Non. Cryst. Solids. 87 (1986) 185–198.
[67] M.A. Fardad, Catalysts and the structure of SiO_2 sol-gel films, J. Mater. Sci. 35 (2000) 1835–1841.
[68] J.C. Brinker, Hydrolysis and condensation of silicates: effects on structure, J. Non. Cryst. Solids. 100 (1988) 31–50.
[69] J.C. Brinker, G.W. Scherer, Sol-gel science: the physics and chemistry of sol-gel processing, Academic press, inc, 1990.
[70] R. Aelion, A. Loebel, F. Eirich, The hydrolysis and polycondensation of tetra alkoxysilanes, Recl. Des Trav. Chim. Des Pays-Bas. 69 (2010) 61–75.
[71] R. Aelion, A. Loebel, F. Eirich, Hydrolysis of ethyl silicate, J. Am. Chem. Soc. 72 (1950) 5705–5712.
[72] D. Collina, G. Fornasari, A. Rinaldo, F. Trifirò, G. Leofanti, G. Paparatto, G. Petrini, Silica preparation via sol-gel method: A comparison with ammoximation activity, Stud. Surf. Sci. Catal. 91 (1995) 401–410.
[73] L. Scriven, Physics and applications of dip coating and spin coating, MRS Proceedings, 121. (1988).
[74] A. Schüler, D. Dutta, E. De Chambrier, C. Roecker, G. De Temmerman, P. Oelhafen, J.-L. Scartezzini, Sol-gel deposition and optical characterization of multilayered $SiO_2/Ti_{1-x}Si_xO_2$ coatings on solar collector glasses, Sol. Energy Mater. Sol. Cells. 90 (2006) 2894–2907.
[75] X. Wang, J. Shen, Sol-gel derived durable antireflective coating for solar glass, J. Sol-Gel Sci. Technol. 53 (2010) 322–327.
[76] N. Lari, S. Ahangarani, A. Shanaghi, Stable multilayer TiO_2-SiO_2 coatings for antireflection applications, Glas. Phys. Chem. 42 (2016) 70–77.
[77] T. Asefa, M.J. MacLachlan, N. Coombs, G.A. Ozin, Periodic mesoporous organosilicas with organic groups inside the channel walls, Nature. 402 (1999) 867–871.
[78] J.C. Brinker, Y. Lu, A. Sellinger, H. Fan, Evaporation-induced self-assembly: nanostructures made easy, Adv. Mater. 11 (1999) 579–585.
[79] D. Grosso, F. Cagnol, G.J.D.A.A. Soler-Illia, E.L. Crepaldi, H. Amenitsch, A. Brunet-Bruneau, A. Bourgeois, C. Sanchez, Fundamentals of mesostructuring through evaporation-induced self-assembly, Adv. Funct. Mater. 14 (2004) 309–322.
[80] N. Arconada, Y. Castro, A. Durán, Photocatalytic properties in aqueous solution of porous TiO_2-anatase films prepared by sol-gel process, Appl. Catal. A Gen. 385 (2010) 101–107.
[81] F. Leermakers, J.C. Eriksson, H. Lyklema, Association colloids and their equilibrium modelling, in: Fundam. Interface Colloid Sci., 2005: pp. 1–123.
[82] H. Demissie, R. Duraisamy, Effects of electrolytes on the surface and micellar characteristics of sodium dodecyl sulphate surfactant solution, J. Sci. Innov. Res. 5 (2016) 208–214.
[83] A.E.C. Palmqvist, Synthesis of ordered mesoporous materials using surfactant liquid crystals or micellar solutions, Curr. Opin. Colloid Interface Sci. 8 (2003) 145–155.
[84] F. Orgaz-Orgaz, Gel to glass conversion: densification kinetics and controlling mechanisms, J. Non. Cryst. Solids. 100 (1988) 115–141.
[85] J.C. Brinker, G.W. Scherer, Sol-gel-glass: I. Gelation and gel structure, J. Non. Cryst. Solids. 70 (1985) 301–322.
[86] J.J. van Beek, D. Seykens, J.B.H. Jansen, R.D. Schuiling, Incipient polymerization of SiO_2 in acid-catalyzed TMOS sol-gel systems with molar water/alkoxide ratio between 0.5 and 32, J. Non. Cryst. Solids. 134 (1991) 14–22.

[87] G. Engelhardt, W. Altenburg, D. Hoebbel, W. Wieker, ^{29}Si-NMR-Spektroskopie an Silicatlösungen. IV. Untersuchungen zur Kondensation der Monokieselsäure, ZAAC - J. Inorg. Gen. Chem. 428 (1977) 43–52.
[88] G. Engelhardt, Silicon-29 NMR of solid silicates, Encycl. Magn. Reson. (2007).
[89] M. Vivar, R. Herrero, I. Antón, F. Martínez-Moreno, R. Moretón, G. Sala, A.W. Blakers, J. Smeltink, Effect of soiling in CPV systems, Sol. Energy. 84 (2010) 1327–1335.
[90] A. Grosjean, A. Soum-Glaude, P. Neveu, L. Thomas, Comprehensive simulation and optimization of porous SiO_2 antireflective coating to improve glass solar transmittance for solar energy applications, Sol. Energy Mater. Sol. Cells. 182 (2018) 166–177.
[91] E.Y.T. Chen, L. Ma, Y. Yue, B. Guo, H. Liang, Measurement of dust sweeping force for cleaning solar panels, Sol. Energy Mater. Sol. Cells. 179 (2018) 247–253.
[92] W. Tang, Y. Huang, W. Meng, F. Qing, Synthesis of fluorinated hyperbranched polymers capable as highly hydrophobic and oleophobic coating materials, Eur. Polym. J. 46 (2010) 506–518.
[93] R. Kaseman, S. Brück, H. Schmith, Fluorine modification of ORMOCER (ORganically MOdified CERamics)-coating materials, Eurogel 91. (1992) 353–360.
[94] E.G. Shafrin, W.A. Zisman, Constitutive relations in the wetting of low energy surfaces and the theory of the retraction method of preparing monolayers, J Phys Chem. 1046 (1957) 519–524.
[95] K.C. Hsu, K.J. Chao, S.F. Chen, H.K. Li, P.Y. Wu, The effect of surfactant removal on continuous mesoporous ultra-thin silica films-A study by X-ray reflectivity, X-ray diffraction and Kr adsorption, Thin Solid Films. 517 (2008) 686–690.
[96] C. Himcinschi, M. Friedrich, S. Frühauf, I. Streiter, S.E. Schulz, T. Gessner, M.R. Baklanov, K.P. Mogilnikov, D.R.T. Zahn, Ellipsometric study of the change in the porosity of silica xerogels after chemical modification of the surface with hexamethyldisilazane, Anal. Bioanal. Chem. 374 (2002) 654–657.
[97] Y. Yuan, Y. Chen, W.L. Chen, R.J. Hong, Preparation, durability and thermostability of hydrophobic antireflective coatings for solar glass covers, Sol. Energy. 118 (2015) 222–231.
[98] Y.-K. Chen, K.-C. Chang, K.-Y. Wu, Y.-L. Tsai, J.-S. Lu, H. Chen, Fabrication of superhydrophobic silica-based surfaces with high transmittance by using tetraethoxysilane precursor and different polymeric species, Appl. Surf. Sci. 255 (2009) 8634–8642.
[99] J.T. Luo, H.C. Wen, Y.M. Chang, W.F. Wu, C.P. Chou, Mesoporous silica reinforced by silica nanoparticles to enhance mechanical performance, J. Colloid Interface Sci. 305 (2007) 275–279.
[100] C.H. Chen, S.Y. Li, A.S.T. Chiang, A.T. Wu, Y.S. Sun, Scratch-resistant zeolite anti-reflective coating on glass for solar applications, Sol. Energy Mater. Sol. Cells. 95 (2011) 1694–1700.
[101] K. Jeevajothi, D. Crossiya, R. Subasri, Non-fluorinated, room temperature curable hydrophobic coatings by sol-gel process, Ceram. Int. 38 (2012) 2971–2976.
[102] R.J.H. Voorhoeve, Organohalosilanes, New York, 1967.
[103] M. Hikita, K. Tanaka, T. Nakamura, T. Kajiyama, A. Takahara, Super-liquid-repellent surfaces prepared by colloidal silica nanoparticles covered with fluoroalkyl groups super-liquid-repellent surfaces prepared by colloidal silica nanoparticles Covered with Fluoroalkyl Groups, Langmuir. 21 (2005) 7299–7302.
[104] A. Nakajima, K. Abe, K. Hashimoto, T. Watanabe, Preparation of hard super-hydrophobic films with visible light transmission, Thin Solid Films. 376 (2000) 140–143.
[105] B.J. Basu, T. Bharathidasan, C. Anandan, Superhydrophobic oleophobic PDMS-silica nanocomposite coating, Surf. Innov. 1 (2013) 40–51.
[106] R.N. Wenzel, Resistance of solid surfaces to wetting by water, Ind. Eng. Chem. 28 (1936) 988–994.
[107] N.K. Adam, The physics and chemistry of surfaces, 3rd edit, Geoffrey Cumberlege, London, 1941.
[108] A.B.D. Cassie, S. Baxter, Wettability of porous surfaces, Trans. Faraday Soc. 40 (1944) 546–551.
[109] J.D. Miller, S. Veeramasuneni, J. Drelich, M.R. Yalamanchili, Effect of roughness as determined by atomic force microscopy on the wetting properties of PTFE thin films, Polym. Eng. Sci. 36 (1996) 1849–1855.

[110] B. van Ginneken, M. Stavridi, J.J. Koenderink, Diffuse and specular reflectance from rough surfaces., Appl. Opt. 37 (1998) 130–9.
[111] M. Mizuhashi, Y. Gotoh, Glass body provided with an alkali diffusion-preventing silicon oxide layer, US4485146, 1984.
[112] G. Helsch, E. R Adlein, G.H. Frischat, On the origin of the aging process of porous SiO_2 antirefection coatings, J. Non. Cryst. Solids. 265 (2000) 193–197.

Chapter 2

Theoretical background of experimental techniques

In this Chapter the techniques and equipment used for the characterization of coatings prepared in this research work are described.
Likewise, the fundamental bases of the measurement and the description of models and methods used for fitting and calculations are also explained.

2.1. Design of AR multi-layer stack assisted by thin layer design software

CODE® software [1] was used for the design of an optimal optical configuration of a GRIN multi-layer stack. This tool, developed by Wolfgang Theiss, allows to obtain the optical spectra of thin layered systems from physical models that are fitted to provide the desired optical performance. It is coupled with SCOUT, which is a Windows NT/2000/XP/Vista software for the analysis of optical spectra by computer simulation.

The main goal of optical spectroscopy is the determination of microscopic features, such as heterogeneity material or thin film thickness from macroscopic experiments, provided that the microscopic phenomena are coupled to the electric fields of the probing radiation. The material property that leads this connection is the dielectric function (ε) or its square root, the complex refractive index ($\tilde{n}$). Those are commonly referred as optical constants.

In the case of layered optical systems, an outstanding technique to assess optical spectra is given by simulation of the experiment (based on a physical model) and adjustment of the model parameters to fit the measured data. The assemblage of simple models using optical constants allows accurate simulations of optical spectra. This enables fast parameter fitting from which the required information of the materials can be attained. The interpretation of optical spectra is the central task of SCOUT.

2.1.1. Effective medium approximation

The effective medium approximation (EMA) is a method for managing a microscopically heterogeneous medium, in which properties such as conductivity (σ), dielectric function, or elastic modulus vary in space [2]. The complex refractive index and the dielectric function are correlated according to equation: $\tilde{n} = n + i\kappa \equiv \sqrt{\varepsilon}$. The real part of $\tilde{n}$, n, is the refractive index and the imaginary part, κ, is the extinction coefficient. EMA models applied in this research work, served to calculate the optical constants of a heterogeneous material, and as a consequence allowed to establish a relationship between the material nano/microstructure and its macroscopic optical response. Clausius and Mossotti [3][4] contributed with the first solution of the EMA theory through the general expression described in Equation 2-1.

$$\frac{\tilde{n}_e^2 - \tilde{n}_a^2}{\tilde{n}_e^2 + 2\tilde{n}_a^2} = c_1 \frac{\tilde{n}_1^2 - \tilde{n}_a^2}{\tilde{n}_1^2 + 2\tilde{n}_a^2} + c_2 \frac{\tilde{n}_2^2 - \tilde{n}_a^2}{\tilde{n}_2^2 + 2\tilde{n}_a^2} + \cdots \quad \text{Equation 2-1}$$

where $\tilde{n}_e$ is the complex refractive index of effective medium, $\tilde{n}_a$ is the complex refractive index of environment, $\tilde{n}_1$, $\tilde{n}_2$ are the complex refractive index of medium 1 and 2; c_1, c_2 are the volume fraction of medium 1 and 2.

The approximation is valid for a grain size of the materials lower than 0.1λ, and implies spherical geometries, and dipolar electromagnetic interactions.

Taking Equation 2-1 as starting point, several researchers developed approximation models by assuming different hypothesis (Sheng, Bruggeman, Landauer, Lorentz-Lorenz, Maxwell-Garnett). One of the most commonly used is the approximation proposed by Bruggeman [5]. If the volume fraction of the implied media is similar, the assignation of environment medium should be interchangeable for the implied materials. For solving that, Bruggeman envisioned that effective medium was the same as environment medium. In this case, $\tilde{n}_a=\tilde{n}_e$, and the Equation 2-1 can be simplified to Equation 2-2.

$$c_1 \frac{\tilde{n}_1^2 - \tilde{n}_e^2}{\tilde{n}_1^2 + 2\tilde{n}_e^2} + c_2 \frac{\tilde{n}_2^2 - \tilde{n}_e^2}{\tilde{n}_2^2 + 2\tilde{n}_e^2} = 0 \quad \text{Equation 2-2}$$

2.1.2. Reflection optimization

The inherent optical losses due to the difference between the refractive indexes of glass and the surrounding medium, typically air, can be reduced by means of AR coating systems [6] designed to minimize Fresnel reflection losses [7–10]. An example of an AR tetra-layer stack is shown in Figure 2-1, in which reflection vectors at each interface are defined by Equation 2-3 to Equation 2-7.

This type of model was used to calculate the characteristics of each layer partaking in the AR multi-layer stacks. The input optical characteristics of the substrate corresponded to transmittance and reflectance spectra of low iron float glass, attained from spectrophotometry as explained in section 2.4. Over the glass substrate, multi-layer stacks were built. Each layer material of the multi-layer stack was defined by Bruggeman effective medium approximation model (BEMA) [5] as a composite formed by SiO_2 matrix in which voids (vacuum) are embedded (Equation 2-2). These calculations permitted to obtain the spectral refractive index, void fraction and thickness of each layer of the multi-layer stack and to select the one that

better fitted the minimization of selected function. Eventually, reflectance value between 300-2000 nm was the function selected for minimization.

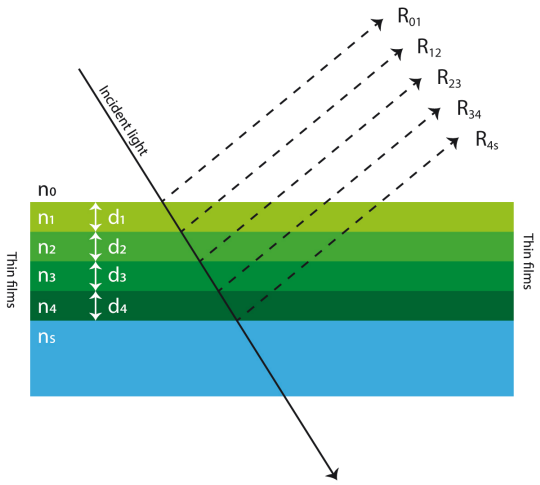

Figure 2-1. Physical description of reflection between interfaces in the multi-layer stack.

In the reflection equations (Equation 2-3-Equation 2-7) of Figure 2-1, medium 0 is air, medium s is the substrate, and media 1 to 4 correspond to each layer. R_{xy} is the reflection at each interface between x and y media; n_n is the real part of the refractive index of each material; and δ_n is the phase angle generated by each layer, defined by Equation 2-8.

$$R_{01}=\frac{n_0-n_1}{n_0+n_1} \qquad \text{Equation 2-3}$$

$$R_{12}=\frac{n_1-n_2}{n_1+n_2}\exp^{-2(\delta_1)} \qquad \text{Equation 2-4}$$

$$R_{23}=\frac{n_2-n_3}{n_2+n_3}\exp^{-2(\delta_1+\delta_2)} \qquad \text{Equation 2-5}$$

$$R_{34}=\frac{n_3-n_4}{n_3+n_4}\exp^{-2(\delta_1+\delta_2+\delta_3)} \qquad \text{Equation 2-6}$$

$$R_{4s}=\frac{n_4-n_s}{n_4+n_s}\exp^{-2(\delta_1+\delta_2+\delta_3+\delta_4)} \qquad \text{Equation 2-7}$$

$$\delta_n=\frac{2\pi n_n \cos\theta_n d_n}{\lambda} \qquad \text{Equation 2-8}$$

where θ_n is reflection angle of each layer; d_n is layer thickness and λ is wavelength.

2.1.3. Mathematical algorithm and calculation method

The physical model was created from the point of view of transmittance maximization in the 300-2000 nm bandwidth. Systems of 1, 2, 3 and 4 BEMA layers were stacked on glass substrate for studying antireflection optimization. As the stacks on both sides of the glass must be symmetric, they were linked as master and slave. Downhill simplex method was the algorithm used for the variation of void fraction and coating thicknesses. This method employs the simplex concept, which is a polytope of N+1 vertex in N dimensions: a line segment in a line, a triangle in a plane, a tetrahedron in the 3D space, etc.

First calculation mode was aimed to give the best idealistic conditions that could offer the highest transmission properties, thus porosity value was not firstly a restriction. However, considering that outstanding mechanical properties are requested to the external surface of AR multi-layer stack, theoretical calculations were also performed restricting the value of the void fraction of each layer to 50%.

The outputs after calculation were the layer properties, refractive index, fraction materials and thicknesses. With this data, the transmittance and reflectance spectra were therefore theoretically attained for each studied case.

2.2. Ellipsometry

Spectroscopic ellipsometry is an optical technique based on the measurement of the polarization state change of a collimated beam formed by polarized monochromatic light when it impacts on a polished surface. The variation of the polarization state of the incident and reflected beams becomes evident through the measurement of the two angles (Δ and Ψ). These angle measurements are related with physical parameters that characterize the illuminated surface (thickness, refractive index, extinction coefficient).

Figure 2-2. Reflected and incident polarization states [11].

Ellipsometric measurements determine the spectral evolution of the ratio between reflected (χ_r) and incident (χ_i) polarization states, also known as complex reflectance ratio (Equation 2-9).

$$\rho = \frac{\chi_i}{\chi_r} = \tan\psi e^{i\Delta} \qquad \text{Equation 2-9}$$

Ellipsometric parameters Ψ and Δ are related with the position of polarizers, and the relationship between them and the optical properties of the sample depends on the experimental setup (incidence angle ϕ_0) and on the model used for describing the structure and materials composing it.

The complex reflectance ratio (ρ) can be obtained by supposing the simplest ambient/material model, of two phases, and using the complex Fresnel reflection coefficients, r_p and r_s, for the parallel, p-polarized light, and perpendicular, s-polarized light, defined by Equation 2-10 and Equation 2-11, respectively.

$$r_p = \frac{\tilde{n}_1 \cos\phi_0 - \tilde{n}_0 \cos\phi_1}{\tilde{n}_1 \cos\phi_0 + \tilde{n}_0 \cos\phi_1} = |r_p| e^{i\delta_p} \qquad \text{Equation 2-10}$$

$$r_s = \frac{\tilde{n}_0 \cos\phi_0 - \tilde{n}_1 \cos\phi_1}{\tilde{n}_0 \cos\phi_0 + \tilde{n}_1 \cos\phi_1} = |r_p| e^{i\delta_s} \qquad \text{Equation 2-11}$$

where $\tilde{n}_1$ is the refractive index of the substrate immersed in a medium of refractive index $\tilde{n}_o$; ϕ_o the incident angle and ϕ_1 the refraction angle; δ_p is the phase change for the p-component upon reflection and similarly for the s-component.

Thus, ellipsometric parameters, Ψ and Δ, are described in the following forms, tan Ψ being the amplitude ratio upon reflection (Equation 2-13) and Δ the phase shift difference (Equation 2-14).

$$\rho = \frac{r_p}{r_i} = \tan\psi e^{i\Delta} \qquad \text{Equation 2-12}$$

$$\tan\psi = \frac{|r_p|}{|r_s|} \qquad \text{Equation 2-13}$$

$$\Delta = \delta_p - \delta_s \qquad \text{Equation 2-14}$$

The complex reflectance ratio is related to the optical properties of the material under investigation, namely, the complex dielectric function, ($\varepsilon=\varepsilon_1+i\varepsilon_2$), the refractive index, n, and the extinction coefficient, κ, by the Equation 2-15.

$$\varepsilon = \sin^2\phi_0 + \sin^2\phi_0\tan^2\phi_0\left(\frac{1-\rho}{1+\rho}\right)^2 = \tilde{n}^2 = (n+i\kappa)^2 \qquad \text{Equation 2-15}$$

The angle of incidence, ϕ_0, should be chosen carefully, depending on the Brewster's angle, of the materials under investigation since it corresponds to vanishing of p-wave reflection, (Brewster's angle $\approx 57^\circ$ for SiO_2 [12]).

The spectra analysis is made by the construction of a model composed by stacking of multiple layers plane-parallel disposed. The Fresnel equations relate electric fields in both sides of each interface. From one to other interface, the relationship between electric fields come from the propagation of a plane wave along the medium defined by the dielectric constant of each material. The experimental spectra are processed through iterative numeric methods with the aim to fit the ρ spectrum of the multi-layer system modelled with the experimentally obtained. The parameters of the model are, apart from number of layers, their thickness and dielectric function.

The models used in the development of this research work consisted in the stacking of one or two layers to the glass substrate, whose optical properties were defined through Cauchy and BEMA equations.

2.2.1. Cauchy model

Among all the parameters of the multi-layered model, one of the most difficult to define is the dielectric function. Unknown dielectric functions are commonly parameterized by analytical functions of the energy, and the selected model depends on the characteristics of the studied material. Thus, for dielectric materials with low absorption, whose dielectric function slightly change with energy, Sellmeier and Cauchy models are used [11].

Cauchy model [13] sets up a simple empirical dispersion law to obtain complex refractive index ($\tilde{n} = n + i\kappa$) parameters (n, Equation 2-16; κ, Equation 2-17). It does not take into account the nature of the material.

$$n(\lambda) = A + \frac{B}{\lambda^2} + \frac{C}{\lambda^4} \qquad \text{Equation 2-16}$$

$$\kappa(\lambda) = D + \frac{E}{\lambda^2} + \frac{F}{\lambda^4} \qquad \text{Equation 2-17}$$

in which A, B, C, D, E, F are the Cauchy model parameters and λ is the wavelength.

2.2.2. Bruggeman effective medium approximation

As explained before, effective medium theory [2] establishes the connection between the microstructure of a heterogeneous thin film and its macroscopic dielectric response. The materials studied here were defined as a composite formed by SiO_2 matrix with embedded voids. Bruggeman [5] proposed the approximation of equalizing the effective medium to surrounding environment (Equation 2-2). By using known dielectric functions of SiO_2 and vacuum, the fitting of ellipsometric parameters allowed to obtain the refractive index, thickness and the volume fraction of each material of the SiO_2-void composite.

2.2.3. Equipment and experimental attainment

Ellipsometric parameters Ψ and Δ were recorded by variable angle spectroscopic ellipsometer (M-2000UTM, J.A. Co., Woollam). Spectra were recorded from 250 to 1000 nm at different angles of incidence taking into account the Brewster's angle (that of vanishing reflection of p-wave, $\approx 57^{\circ}$ for SiO_2 [12]). The measurement performed at incident angles above and below that, ensures a maximum difference in the amplitudes of p- and s-waves thus allowing the fulfilment of all the boundary conditions for a more accurate fitting. The spectra were fitted using both the Cauchy dispersion model [13] and Bruggeman medium effective approximation model [5]. The fitting allowed the calculation of relevant parameters such as refractive index, extinction coefficient, coating thickness and porosity. The apparent porosity was calculated with respect to pure dense silica and a polarization factor of 0.33 was considered. The data analysis was performed with WVase32 software.

2.3. Environmetal ellipsometric porosimetry (EEP)

The characterization of micro- and mesoporous of supported porous thin coatings, can be measured by ellipsometric porosimetry (EP), as first reported by Baklanov et al. [14]. The variations of refractive index provoked by the introduction of a volatile substance in the pores

induced by the change of partial pressure enable the plotting of the adsorption-desorption isotherms.

Pore size distribution of the pores can be directly obtained via porosimetry models usually based on the Kelvin equation (Equation 2-18) for the determination of mesopores sizes.

$$RT\ln\frac{P}{P_0} = \gamma_{lv}V_L\cos\theta_c\frac{dS}{dV} \qquad \text{Equation 2-18}$$

This equation relates the relative pressure (P/P_0) of an adsorbate, the liquid-air surface tension (γ_{lv}) of a curved interface and the adsorbate liquid-interface surface area variation dS when the the volume V_L of adsorbate evolves dV. Where R corresponds to gas constant, T to temperature and θ_c to liquid-solid contact angle.

Boissiere et al. [15] first validated the EEP technique, and designed a device to allow film characterization at ambient pressure and temperature, by using a pulsed air flow with controlled partial pressure of water. Thus, using water as adsorbate. They proposed modification of Kelvin equation. On one side, it usually assumes a perfect pore surface wettability, however, wettability is a crucial factor for the capillarity condensation. The measurement of liquid-solid contact angle is needed to give a correct interpretation of the water adsorption-desorption isotherm. The liquid-air surface tension of a curved interface, was modified according to the Tolman model [16] to take into account the decrease of surface tension due to the high curvature of liquid interfaces in mesoporous networks.

On the other side, they took into account the pore anisotropy and modified Kelvin equation for ellipsoidal pore shapes according to Equation 2-19.

$$RT\ln\frac{P}{P_0} = -\gamma_{lv}V_L\cos\theta\left[1+\frac{C}{2p^2}\right]/b \qquad \text{Equation 2-19}$$

where C parameter was defined as:

$$C = \frac{\ln\left[\frac{1+E}{1-E}\right]}{E} \qquad \text{C parameter}$$

where E is the eccentricity factor:

$$E = \frac{(p^2-1)^{1/2}}{p} \qquad \text{Eccentricity factor}$$

The modified Kelvin relation contains two unknown parameters, b and p. To solve this problem, they proposed the prediction of the anisotropy of the mesopores based on the

contraction model, by measuring the film thickness values before and after calcination. That prediction is based on the hypothesis that the contraction of mesostructured films can be described by an ellipsoidal contraction of pores resulting from the contraction of the mesostructure lattice, plus a simultaneous isotropic contraction of silica walls between mesodomains.

The pore volume, pore anisotropy, pore size and surface area can be determined through the following experimental protocol:

1. Scope: **Pore anisotropy determination**. Method: Preparation of counterpart coatings, one containing structure directing agent (mesostructured coating), and other without it (reference coating). Optical constants of both coatings are characterized by ellipsometry before and after sintering step. The reference coating is used to simulate the contraction behavior of the matrix walls in the mesoporous network. The differences among coatings before and after sintering serve for calculating the contractions and are used for the calculation of pores anisotropy. The contraction model discerns between the contraction contribution of the silica walls and the mesostructure uniaxial shrinking (upon sintering, spherical micelles formed by SDA become ellipsoidal).

2. Scope: **Pore volume (V_P) calculation**. Method: The optical properties of the sintered reference coating are used for determining the properties of the matrix walls in the mesostructured coating. Then, BEMA equation serves for determining the relative volumetric fraction of matrix walls and void (air).

3. Scope: **Adsorption-desorption isotherm**. Method: The evolution of refractive index and thickness as a function of the relative humidity (RH) is measured by ellipsometry. The adsorption-desorption isotherm V_{H_2O}/V_{layer} versus RH or partial pressure (P/P_0) is calculated by BEMA fitting. It serves to calculate the relative volumetric fraction of the water-saturated mesoporous coating (measured at 100% RH) and the empty mesoporous coating (measured at 0% RH), at each RH at which optical constants of the coating is measured. The V_{H_2O}/V_{layer} is assumed to be equal to the product of the pore volume and the volumetric fraction of the water-saturated mesoporous coating.

4. Scope: **Water mono-layer (t-plot)**. The thickness of the water adsorbed on a flat surface of the reference coating is assumed to be equal than that adsorbed on the

mesopores internal surface. Thickness of the water mono-layer (t) is calculated through the fitting of the optical constants of the reference coating at each RH measured.

2.3.1. Equipment and experimental attainment

Water adsorption-desorption was studied in this research work by EEP. Measurements were performed with the above described equipment (M-2000UTM, J.A. Co., Woollam), within a cell with controlled RH. In this case, the spectra were taken at a fixed incident angle of 70º, at different RH values. From the experimental data explained herein, the pore size distribution was calculated from the isotherm using the modified Kelvin's equation, which takes into account Tolman correction and pore anisotropy and the thickness of water mono-layer.

2.4. Spectrophotometry

When electromagnetic radiation arrives to an investigated material, different types of interaction can occur: reflection, propagation, transmission, refraction, adsorption, scattering, luminescence, fluorescence, and others. Transmittance (T) is the ratio between transmitted light and incident light: $T=I/I_0$ or $T\ (\%)=I/I_0 \times 100$ if expressed in percentage. Likewise, transmittance (total) is composed by straight transmitted light and light diffusely scattered in the other angles. On the other hand, reflection (R) is the phenomena of forwarding part of the incident radiation flux without variation in wavelength (if that variation did occur, the phenomena would be fluorescence). Commonly, radiation is forwarded in all the directions, i.e. diffusely scattered (see Figure 2-3). Diffusion is defined as the change in spatial distribution of a light beam when it is deviated in many directions by a surface or an investigated material, without variation of the frequency of monochromatic components [17]. Furthermore, the part of radiation that is forwarded in the similar angle that incident light, it is the specular component (see Figure 2-3).

A spectrophotometer is the equipment designed for the measurement of reflectance, transmittance and absorbance spectra. The objective is to compare the reflected or transmitted radiant flux by the investigated material with the incident radiant flux at each wavelength [17]. This apparatus is able to interpret the electromagnetic radiation beam, and separates it in the integrating components, with the aim to facilitate the identification, qualification and quantification of its energy. The efficiency, resolution, sensitivity and spectral range shall

depend on the design variables and the selection of the optical components that compose it. The indispensable components of the spectrophotometer are light source, monochromator, light detector, so as to the interposed sample.

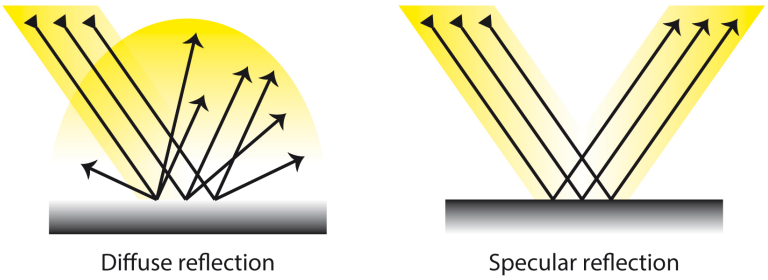

Figure 2-3. Diffuse and specular reflectance.

UV/VIS and UV/VIS/NIR spectrophotometer is an equipment useful only for measuring the direct transmittance of homogeneous samples. When light passes through a homogeneous medium, it propagates straight. However, if the investigated material is not homogeneous or there are irregular boundaries with variations in refractive index, reflection and refraction processes lead to light scattering and only a little part of the light, the direct component, arrives to detector. In that cases, integrator sphere is indispensable to measure total transmittance and total reflectance. This accessory collects the most part of diffused light (transmitted or reflected) by the sample and address it to the detector.

The integrator sphere is composed by a spherical hollow cavity, coated on the inside with a diffusive reflective layer, with the presence of holes that allow incoming flux to enter and to leave towards the detector. Light beam that arrives to any point of the interior surface are equally distributed throughout the entire surface.

The theory of a cubic box for light collecting was first described by W.E. Sumpner in 1892 [18], although the experimental application of the integrator sphere resulted from the work of R. Ulbricht, published in 1900 [19].

2.4.1. Equipment and experimental attainment

Transmittance and reflectance spectra of the coatings and multi-layer stacks investigated in this work supported on different types of glasses, was measured with a Jasco V-670 UV-Vis-NIR spectrophotometer equipped with a 150 mm integrating sphere (ILN-725 model).

Measurements of transmittance (total: direct+diffuse) and reflectance (total and diffuse) were taken in the 300 to 2000 nm wavelength range, with a resolution of 5 nm. The changes in light source and detector were performed at 330 nm and 860 nm, respectively, and the spectra were corrected with two baselines that corresponded to 100% T and 0% T. Reflectance spectra were measured at incident angle of 8º. Diffuse reflectance spectra were taken by removing the specular component port of the integrating sphere. It is important to notice that reflectance is a measurement related to the type of diffusive layer.

2.4.2. Spectra integration

Integration of spectra was calculated by weighting transmittance or reflectance values with solar spectral irradiance. Solar spectra are defined by an air mass (AM) value. Several standard reference spectra have been defined in order to proper compare the performance of photovoltaic devices.

The ASTM E-490 defines the standard solar spectrum for space applications, with and air mass zero, referred as AM0. It has an integrated power of 1366.1 W/m^2. The ASTM G173 defines two solar irradiation spectra for terrestrial use, both with an air mass 1.5. The AM1.5 Global spectrum is used for flat plate modules and has an integrated power of 1000 W/m^2. The AM1.5 direct (+circumsolar) spectrum is used for solar concentrators and has an integrated power of 900 W/m^2. It includes the direct beam from the sun plus the circumsolar component in a disk 2.5 degrees around the sun. In the Figure 2-4 these three standard spectra of solar irradiance are presented.

The integrated transmittance (τ), reflectance (ρ) and diffuse reflectance (ρ_{dif}), were calculated according to Equation 2-20.

$$\tau = \frac{\int_{\lambda_1}^{\lambda_2} T(\lambda)\cdot\varphi_{AM1.5}(\lambda)d\lambda}{\int_{\lambda_1}^{\lambda_2} \varphi_{AM1.5}(\lambda)d\lambda} \qquad \text{Equation 2-20}$$

where $T(\lambda)$ is the transmittance spectrum of the covered glass, $\varphi_{AM1.5}(\lambda)$ is the AM1.5 solar spectrum [20] and λ_1 and λ_2 define the wavelength range where τ is calculated. Integrated reflectance values, ρ or ρ_{dif}, were calculated in a similar way using reflectance spectrum instead of transmittance. Gain value, G, was calculated as the percentage of the increment of τ value

of coated glass over bare glass [$(\tau_{coat}-\tau_{glass})/\tau_{glass}\cdot 100$]. Reduction value, M, was calculated as the percentage of decrement of ρ value of coated glass below bare glass [$(\rho_{glass}-\rho_{coat})/\rho_{glass)}\cdot 100$].

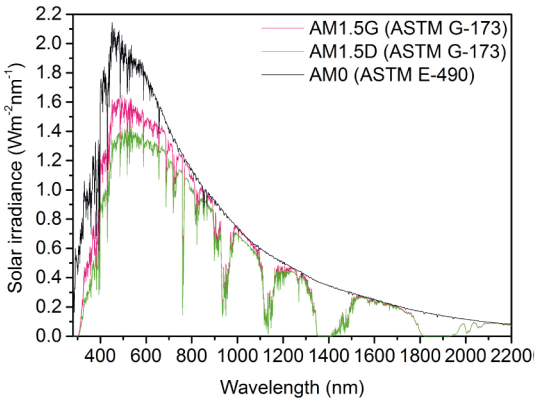

Figure 2-4. Extraterrestrial (AM0) and Earth's surface global (AM1.5G) and direct (AM1.5D) solar spectral irradiance.

2.5. Solar cell current generation

2.5.1. Short-circuit current density calculation

The electrical performance of a PV cell under an incoming irradiance spectrum can be quantified through the calculation of the short-circuit current density (J_{SC}) according to Equation 2-21. J_{SC} corresponds to the maximum current (per area unit) that the cell can reach which is obtained when the voltage across the cell is zero.

$$J_{SC} = q\int_{\lambda_1}^{\lambda_2}\phi(\lambda)EQE(\lambda)d\lambda \qquad \text{Equation 2-21}$$

where q is the elementary electric charge; $\phi(\lambda)$ is the incoming photon flux; $EQE(\lambda)$ is the external quantum efficiency of the cell and λ_1 and λ_2 define the wavelength range where J_{SC} is calculated.

The EQE, is defined as the ratio between the number of electron-hole pairs generated to the number of photons arriving at the cell surface. On the other hand, the internal quantum efficiency (IQE) is defined as the ratio between the number of electron-hole pairs generated to the number of only photons that arrive at the surface and are absorbed by the cell. The dismissed photons are reflected out of the cell. Therefore, IQE corresponds to $EQE/(1-R_{cell})$.

The effect of a cover glass (bare or AR coated) on the electrical performance of the cell can be quantified by considering its optical properties in the incoming photon flux factor. Moreover, the calculation of the incoming flux considers the coupled effect of glass (bare or AR coated) transmittance and reflectance as well as the cell reflectance through Equation 2-22, derived from standard net radiation methods [21][22].

$$\phi(\lambda) = \varphi_{AM1.5}(\lambda)\frac{T_1(\lambda)}{1 - R_{12}(\lambda)R_{cell}(\lambda)} \qquad \text{Equation 2-22}$$

where $\varphi_{AM1.5}$ is the AM1.5 solar spectrum [20]; T_1 is the transmittance of the glass (bare or AR coated), R_{12} is the internal air-coated glass interface reflectance and is R_{cell} the air-cell reflectance.

2.5.2. Silicon solar cell current indoor measurement

The electrical characteristics of a silicon cell, that produce direct current (DC) are commonly assessed through the relationship between the current and the voltage, by means of its I-V characteristic curve. This curve represents the operation of the silicon solar cell, under controlled conditions of irradiance and temperature, and provides information to configure a given solar system in order to operate at its optimal peak power point.

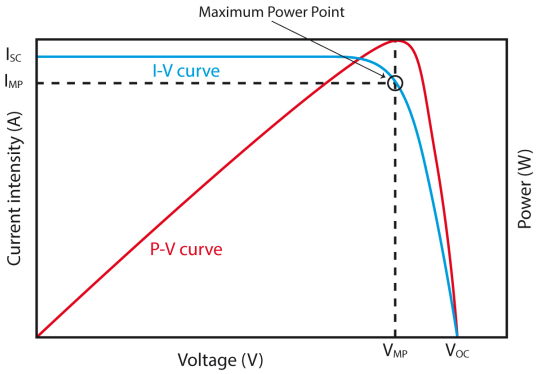

Figure 2-5. Current and voltage (I-V) characteristics of a photovoltaic silicon cell.

Important points on this I-V graph are i) the x-intercept, that corresponds to open circuit voltage (V_{OC}) when the solar cell is open-circuited, thus current being zero; and ii) the y-intercept, that corresponds to the maximum current that the cell can reach, thus the short-circuit current (I_{SC}), which is obtained when the voltage across the cell is zero.

Although neither of these situations generates power, the maximum power is in between, known as maximum power point (MPP), that corresponds to the particular combination from which I x V reaches the maximum power value, thus I_{MP} x V_{MP}. I_{SC} and V_{OC} are directly related with values at MPP.

Therefore, the MPP is the optimum power point for the operation of solar cell, however also being aware of operation temperature, since it affects both voltage and current.

2.5.2.1. Equipment and experimental attainment

The I-V curves of bare and encapsulated monocrystalline silicon cells were measured by PASAN CTSLAB906 cell solar simulator under standard conditions of AM1.5 solar spectrum and 1000 W/m^2 irradiance.

2.5.3. Multi-junction solar cell current indoor measurement

Short-circuit current of MJ solar cells was measured by means of a solar simulator following the description presented by Domínguez et al. [23]. MJ solar cells consist of the stacking of multiple subcells. Each subcell has a different spectral response (SR) and ideally all of them should be matched to generate the same current under an incident spectral distribution (AM1.5D for terrestrial applications), since they are connected in series. Otherwise, total current would be limited by the subcell producing the lowest generation. Therefore, any change in the incoming irradiance spectrum may introduce unbalanced generation and current generated by the MJ cell would be limited by some of the subcells. Because of that, when measuring the MJ cell current under solar simulator, it is crucial the control and monitoring the simulated spectral conditions. To apply this method, it is important to find a sensor that measures the incident light at the different spectral bands corresponding to wavelength range sensitive for each subcell. This is usually approached by means of an isotype, thus single-junction cells with the same SR for each of the subcells within the MJ solar cell.

The Equation 2-23 permits to calculate the current generated by an ith subcell under an incoming irradiance spectrum $\varphi(\lambda)$, using its SR and the active area of the cell (A).

$$I_{SC,i-component} = A\int_{\lambda_1}^{\lambda_2}\varphi(\lambda)SR_i(\lambda)d\lambda \qquad \text{Equation 2-23}$$

Equation 2-23 is similar to Equation 2-21, however the area term is introduced for avoiding the use of the current density, and spectral response of the cell or subcells SR(λ) is used instead of EQE. SR(λ), with the units A/W, is defined as the ratio of the photocurrent generated by a solar cell under monochromatic illumination of a given wavelength to the value of the spectral irradiance at the same wavelength [24]. In fact, SR(λ) is related to quantum efficiency (EQE or IQE) since the number of photons and irradiance are related according to Equation 2-24.

$$SR(\lambda) = \frac{q\lambda}{hc} QE(\lambda) \qquad \text{Equation 2-24}$$

By comparing the short-circuit current under the reference spectrum AM1.5D (then defined as $I^*_{SC,i-component}$) the cell isotype can be used as a sensor to measure the irradiance at the corresponding spectral band. The direct normal irradiance that effectively generates current at the i^{th} subcell is calculated according to Equation 2-25. It is calculated in suns for simplicity, where a sun corresponds to a light intensity of 1000 W/m² with a relative spectral irradiance distribution of AM1.5D.

$$DNI_{i-component} = \frac{I_{SC,i-component}}{I^*_{SC,i-component}\left(1000 \frac{W}{m^2}, AM1.5D, 25\ ^\circ C\right)} \qquad \text{Equation 2-25}$$

- Spectral matching ratio in the solar simulator

Spectral matching ratio (SMR) is used in CPV to define how similar a spectrum (e.g., simulated spectrum) is, compared to the reference spectrum AM1.5D. It is calculated for any pair of subcells as the ratio between the effective irradiances of each of the subcells according to Equation 2-26.

$$SMR^{top}_{middle}(\varphi(\lambda)) = \frac{DNI_{top}}{DNI_{middle}} \qquad \text{Equation 2-26}$$

In the most used MJ solar cells, the bottom subcell usually produces and excess of current, and thereby the current of the whole MJ cell is limited by either top or middle subcells. Therefore, by using the common MJ solar cells, the similarity of a given spectrum to AM1.5D can be merely assessed by comparison of top and middle irradiances. $SMR^{top}_{middle} = 1$ indicates and effective AM1.5D spectrum, $SMR^{top}_{middle} < 1$ indicates a red-rich spectrum and $SMR^{top}_{middle} > 1$ indicates a blue-rich spectrum.

- Limitation diagram

The subcell limitation diagrams are used to determine the optical efficiency corresponding to the wavelength range converted into electricity by the top and middle subcells.

For a studied MJ solar cell, any change in the incoming irradiance produces similar variations on the photocurrent generated in both the studied and the isotype cells. However, if the spectral conditions vary too, the current of the isotype cell varies in a different way, allowing the identification of the limiting subcell of the studied MJ. When using a simulated irradiance spectrum, provided for example by a xenon flash lamp, the current density within the flash bulb decays exponentially throughout the pulse as well as the irradiance. By measuring the photocurrent generated by the studied MJ and the $\mathrm{DNI}_{\mathrm{i-component}}$ of every isotype it is possible to detect which is the limiting subcell at any time of the flash decay. Therefore, different values of SMR are obtained across the flash pulse. Then, for every SMR across the flash pulse, it is possible to obtain the photocurrent normalized by the $\mathrm{DNI}_{\mathrm{i-component}}$ of each subcell according to Equation 2-27.

$$\mathrm{I}_{\mathrm{N,i-component}} = \frac{\mathrm{I}_{\mathrm{SC,MJ}}}{\mathrm{DNI}_{\mathrm{i-component}}} \qquad \text{Equation 2-27}$$

Therefore, $\mathrm{I}_{\mathrm{N,i-component}}$ is the subcell current normalized to its corresponding spectral band (top or middle).

The subcell limitation diagram represents the evolution of the ratio of the short-circuit currents of the MJ solar cell to the isotype cell versus SMR, thus the variation of the spectral distribution through the flash decay. Such diagram allows the determination of the short-circuit current of every subcell within the MJ solar cell. The SMR range in which one of the normalized currents is constant, corresponds to the subcell that is limiting the MJ cell current. The Figure 2-6 represents this situation. In the A zone, the MJ follows the top-component and $\mathrm{I}_{\mathrm{SC,MJ}} = \mathrm{I}_{\mathrm{SC,top}}$, while in the B zone, the MJ follows the middle-component and $\mathrm{I}_{\mathrm{SC,MJ}} = \mathrm{I}_{\mathrm{SC,middle}}$. In the A zone the photocurrent generated by the MJ solar cell is $\mathrm{I}_{\mathrm{SC,MJ}} = \mathrm{DNI}_{\mathrm{top}}\mathrm{I}_{\mathrm{N,top}}$, while in the B zone is $\mathrm{I}_{\mathrm{SC,MJ}} = \mathrm{DNI}_{\mathrm{middle}}\mathrm{I}_{\mathrm{N,middle}}$.

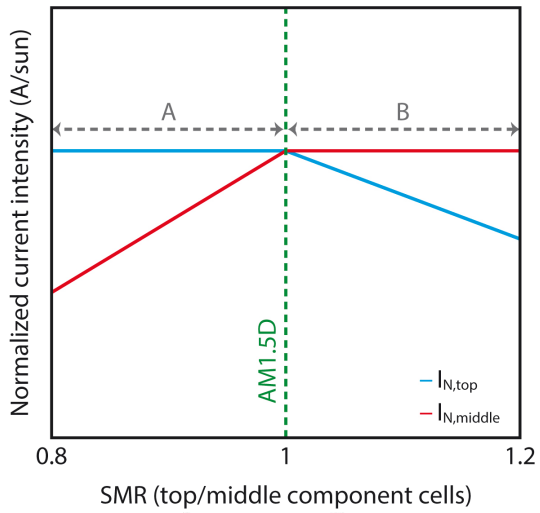

Figure 2-6. Limitation diagram for the top and middle subcells.

2.5.3.1. Equipment and experimental attainment

An indoor setup was set to perform the electrical measurements by creating the spectral sweep. The solar simulator Helios 3198 was used to produce direct light radiation over the CPV systems by means of a xenon flash lamp that generates a 3-ms wide light pulse. This is reflected by a collimator mirror to produce a parallel light beam over the receiver plane with an irradiance of up to 2000 W/m^2.

2.6. Surface energy

For a flat and chemically homogeneous surface its free energy is given by the Young's equation (Equation 2-28).

$$\gamma_{sl} = \gamma_{sv} - \gamma_{lv}\cos\theta_c \qquad \text{Equation 2-28}$$

where γ is the surface tension, subscripts sl, sv, and lv refer to the solid-liquid, solid-air, and liquid–air interfaces and θ_c is the contact angle.

The contact angle value, which is still commonly used as the basis for calculating the surface free energy (SFE) [25], can be affected by further phenomena that may occur in the solid-liquid interface like adsorption, catalysis or wetting. Because of that, some assumptions concerning relation between γ_{sl}, γ_{sv} and γ_{lv} have been theoretical and empirically developed. Anyway, due to the easiness of performing measurements and high accuracy of the results, those based on contact angle measurements remain the most widely used.

Several authors pioneered by Fowkes [26] developed the idea of the partition of the SFE into individual components. The main assumption is that the surface free energy is the sum of independent components, associated with specific interactions like dispersion, polar, hydrogen bonds, induction or acid-base. Owens and Wendt [27] considered only two phenomena by making a distinction between the weak, dispersive van der Waals forces, called dispersion component and the stronger hydrogen-bonding forces, associated with the polar interaction, which derived in the relationship presented in Equation 2-29. For solving equation, the contact angle must be measured using at least two liquids wherein at least one of them must have a polar part > 0.

$$(\gamma_{sv}^{d}\gamma_{lv}^{d})^{0.5} + (\gamma_{sv}^{p}\gamma_{lv}^{p})^{0.5} = 0.5\gamma_{lv}(1 + \cos\theta_c) \qquad \text{Equation 2-29}$$

By calculation and plotting the expressions appearing in the Figure 2-7, obtained for each test liquid, polar and dispersive surface energy components can be easily determined from slope (square root of γ_{sv}^{p}) and y-intercept (square root of γ_{sv}^{d}) of the regression line.

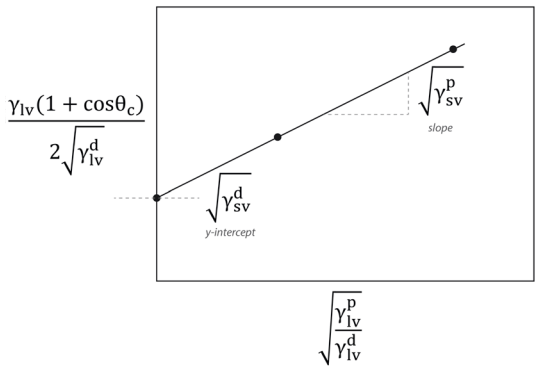

Figure 2-7. Owens-Wendt fitting from three test liquids data.

The SFE in this research work was determined by Owens and Wendt method based on measurements of the contact angle of the surface with water (γ_{lv}^{p}=51 mN/m; γ_{lv}^{d}=21.8 mN/m), ethanol (γ_{lv}^{p}=2.6 mN/m; γ_{lv}^{d}=18.8 mN/m) or methanol (γ_{lv}^{p}=4.3 mN/m; γ_{lv}^{d}=18.2 mN/m) and n-hexadecane (γ_{lv}^{p}=0 mN/m; γ_{lv}^{d}=27.5 mN/m).

2.6.1. Equipment and experimental attainment

The contact angle was determined by the static drop method, using Digidrop Contact Angle Meter (GBX Instruments). Ten measurements of the apparent contact angle were taken for water ($\theta_c^{H_2O}$), methanol (θ_c^{MeOH}), ethanol (θ_c^{EtOH}), and hexadecane ($\theta_c^{C_{16}H_{34}}$) by placing drops of

each liquid on the horizontal and flat coating surface and measuring the angle at the liquid-solid-air boundary.

2.7. Nanoindentation

The nanoindentation technique uses an already established method where an indenter tip with a known geometry is driven into a specific site of the material to be tested, by applying an increasing normal load. When reaching a pre-set maximum value, the normal load is reduced until partial or complete relaxation occurs. This procedure is performed repetitively; at each stage of the experiment the position of the indenter relative to the sample surface is precisely monitored with a differential capacitive sensor.

For each loading/unloading cycle, the applied load value is plotted with respect to the corresponding position of the indenter. The resulting load/displacement curves (see Figure 2-8) provide data specific to the mechanical nature of the material under examination. Established models are used to calculate quantitative hardness and elastic modulus values for such data.

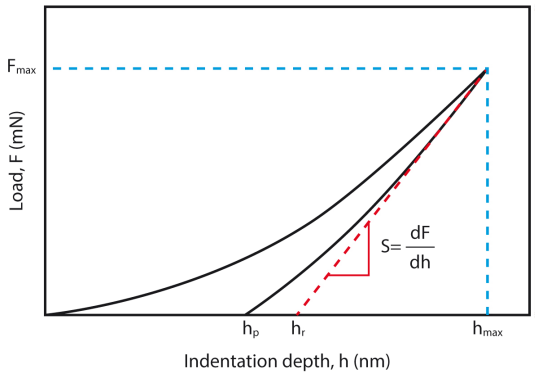

Figure 2-8. Typical load versus displacement curve.

In order to determine hardness and elastic modulus of the investigated material, power law method developed by Oliver and Pharr was used [28][29]. This method describes the upper portion of the unloading curve by the power law relationship of Equation 2-30.

$$F=F_{max}\left(\frac{h-h_p}{h_{max}-h_p}\right)^m \qquad \text{Equation 2-30}$$

where F is the test force; F_{max} is the maximum applied force; h is the indentation depth under applied test force; h_p is the permanent indentation depth after the removal of the test force; h_{max} is the maximum indentation depth at F_{max}; m is a power law constant exponent.

The power law exponent m is determined by least squares fitting procedure and is a function of the indenter geometry.

The contact stiffness (S) is given by the derivative at peak load according to Equation 2-31.

$$S=\left(\frac{dF}{dh}\right)_{max}=m\cdot F_{max}\left(h_{max}-h_p\right)^{-1} \qquad \text{Equation 2-31}$$

and the tangent depth (h_r) is thus given by Equation 2-32.

$$h_r=h_{max}-\frac{F_{max}}{S} \qquad \text{Equation 2-32}$$

where h_r is the point of intersection of the tangent to unloading curve at F_{max} with the indentation depth-axis.

The contact depth of the indenter with the test piece at F_{max}, h_c, corresponds to Equation 2-33.

$$h_c=h_{max}-\varepsilon(h_{max}-h_r) \qquad \text{Equation 2-33}$$

where ε depends on the power law exponent m.

From this data, the calculation of the coating hardness and Young's modulus can be obtained as follows:

- Indentation testing hardness H_{IT}:

The indentation testing hardness is determined from the maximum load F_{max} divided by the projected contact area A_p at the contact depth h_c. A_p is a function of the contact depth h_c and is determined by a calibration of the indenter tip.

$$H_{IT}=\frac{F_{max}}{A_p(h_c)} \qquad \text{Equation 2-34}$$

- Vickers hardness HV:

The Vickers hardness is defined by Equation 2-35.

$$HV=\frac{F_{max}}{9.81\cdot A_c(h_c)} \qquad \text{Equation 2-35}$$

where A_c is the developed contact area and can be calculated from the projected contact area A_p and the indenter geometry as presented in Equation 2-36.

$$A_c = \frac{A_p}{\text{sen } \alpha} \qquad \text{Equation 2-36}$$

where α is the angle between the axis of the diamond pyramid and its faces. $\alpha = 68°$ for a Vickers indenter and $\alpha = 65.27°$ for a modified Berkovich indenter.

For a Vickers indenter: $HV=0.0945 \cdot H_{IT}$

For a modified Berkovich indenter: $HV=0.0926 \cdot H_{IT}$

- Indentation modulus E_{IT}:

The reduced modulus of the indentation contact (E_r) is given by Equation 2-37.

$$E_r = \frac{\sqrt{\pi} S}{2\beta\sqrt{A_p(h_c)}} \qquad \text{Equation 2-37}$$

where β is a geometric factor depending on the diamond shape (circular: $\beta = 1$, triangular: $\beta = 1.034$, square: $\beta = 1.012$).

The Young's modulus of the sample (E_{IT}) can then be obtained from Equation 2-38.

$$\frac{1}{E_r} = \frac{1-\upsilon_s^2}{E_{IT}} + \frac{1-\upsilon_i^2}{E_i} \qquad \text{Equation 2-38}$$

where υ_i is the Poisson's ratio of the indenter; υ_s is the Poisson's ratio of the sample and E_i is the modulus of the indenter.

2.7.1. Equipment and experimental attainment

Nanoindentation measurements were made by ultra nanoindentation tester (UNHT) from Anton Paar. It was equipped with a Berkovich indenter that applied a linear load rate between 60 and 180 μN/min, being the maximum load 10 μN or 20 μN, depending on the sample. Hardness and Young's modulus were calculated, using Oliver-Parr method and a Poisson's ratio (υ_s) of 0.17, for SiO_2 material.

2.8. Nanoscratch

The scratch-test method consists of the generation of scratches with a sphero-conical stylus (generally Rockwell C diamond, cone angle 120° and tip radius 200 μm or other) which is drawn at a constant speed across the coating-substrate system to be tested, under either constant or progressive loading at a fixed rate. When the scratch is made in the constant loading mode, the critical load (Lc) is defined by the load at which a regular appearance of the failure is observed. When the scratch is made in the progressive loading mode, the Lc is the smallest load at which the first recognizable failure occurs. In this case, the stresses produced in the lower load regime, generally result in conformal or tensile cracking of the coating, that however usually remains fully adherent. That phenomena are related with a first critical load. In the higher load regime, a second critical load corresponds to the emergence of another type of failure, usually related to coating detachment from the substrate by spalling, buckling or chipping.

The scratch test is mainly a comparison test. The critical loads depend on the mechanical strength (adhesion, cohesion) of a coating-substrate composite but also on several other parameters some of them are directly related to the test itself, while others are related to the coating-substrate system [30].

The most reliable method to detect coating damage is by microscopic observation. This technique is able to differentiate between cohesive failure within the coating and adhesive failure at the interface of the coating-substrate system.

2.8.1. Equipment and experimental attainment

Cohesion and adhesion properties were examined by scratch test by means of Anton Paar nano scratch tester (NST) with 2 μm radius spheric-conical indenter. Three scratches on each specimen of 0.3 mm or 0.6 mm in length were produced at 1.2 mm/min speed, loading rate of 78.8 mN/min, starting load from 0.5 and final load 20 mN or 40 mN depending on the sample. For the evaluation of the critical loads, panorama image of scratches was taken which enabled the determination of critical points after the tests by recording the image of the scratch track synchronized with the recorded signals of depth, residual depth, friction and normal force.

2.9. Nuclear magnetic resonance

^{29}Si nuclear magnetic resonance (NMR) was used to study kinetics and mechanisms of the hydrolysis-condensation reactions of TEOS prior to gel point [31] and the connectivity of the silicon central atom in the sol was determined, i.e. the number of oxygen atoms shared by a second silicon atom (bridging oxygens) as well as the number of alkoxy groups that have been hydrolyzed.

2.9.1. Equipment and experimental attainment

^{29}Si NMR spectra were obtained at room temperature on a Bruker AVANCE III 500 spectrometer equipped with an 11.7 T magnet (99.36 MHz for ^{29}Si). After preparation, the sol was placed in NMR tubes (5 mm of diameter), where 50 μl of deuterated methanol and 50 μl of trimethyl silane were added before inserted it into the magnet. The experiment was accomplished using a single 60 degrees pulse. The number of data points was 16 K, with a 300 ppm bandwidth, 1024 scans and 5 s relaxation delay. Spectra were processed using a 20 Hz exponential apodization function and the ^{29}Si NMR background signal from the NMR probe and tube was subtracted.

For the presentation of the structure of building units the commonly used Q_n notation was adopted. In this notation, Q represents a silicon atom bonded to four oxygen atoms forming a tetrahedron. The subscript n indicates the connectivity, i.e. the number of oxygen atoms shared by a second silicon atom (bridging oxygens). Thus, Q_0 denotes species with no bridging oxygen, $Si(OH)_x(OEt)_{4-x}$; Q_1 denotes species with one bridging oxygen (end of chain) $(Si\text{-}O)\text{-}Si(OH)_x(OEt)_{3-x}$; Q_2 denotes species with two bridging oxygens (middle groups in chains or rings), $(Si\text{-}O)_2\text{-}Si(OH)_x(OEt)_{2-x}$; Q_3 denotes species with three bridging oxygens (chain branching sites), $(Si\text{-}O)_3\text{-}Si(OH)_x(OEt)_{1-x}$ and Q_4 three-dimensionally cross-linked groups, $(Si\text{-}O)_4\text{-}Si$.

2.10. Viscosity

2.10.1. Equipment and experimental attainment

Kinematic viscosity of sols was measured at 22 ºC by means of Ubbelohde viscometer in which the liquid flows through a capillary tube due to its gravity. Different types of capillary tube

were used depending on viscosity values, thus type 0B was used for sols with kinematic viscosity between 1-5 cSt and type 1C was used for sols with kinematic viscosity between 6-30 cSt. Dynamic viscosity (μ) was obtained by multiplying kinematic viscosity and density that was previously determined with pycnometer/specific gravity bottle. The stability of final liquid sols, which is related to pot-life, was characterized by viscosity measurements along six months after preparation. Viscosity increase was calculated as the percentage of the increment of viscosity after certain aging time over initial value presented for each sol $[(\mu_{aging}-\mu_{initial})/\mu_{initial}\cdot 100]$.

2.11. Profilometry

Contact profilometer was used for coating thickness determination. This equipment served to make linear scans through a pin that touches the surface and detects changes in the topography. The electrical signals are then interpreted in a surface profile. In general, it allows the positioning in the XY plane of the unevenness in the Z axis, what lead to a cartography of the surfaces. In general, these types of equipment offer a higher precision in the Z axis (nanometer) than in the XY plane (tenth or hundredth of centimeter).

2.11.1. Equipment and experimental attainment

The profilometer used in this thesis was Dektak 150 from Veeco, with a precision of ±3 nm in Z axis; ±100 μm in X axis and ±12 μm in Y axis.

Coatings were scratched with a pin before being subjected to thermal treatment. After thermal treatment, scans were taken crossing the scratch along 50 mm. All the measurements were performed using a pin of diameter 2 μm that applied 3 mg of load and Y axis resolution of 1/3 μm. Thickness was determined by calculation of the step height using Dektak V9 software. Mean of five scans on each sample was calculated. In the Figure 2-9 an example of the scan of a scratched coating is shown.

Mapping of the surface was performed with the same equipment to obtain 3D images of the surface. In this case, stacking of 134 linear measurements performed along 400 μm in X axis (3 μm resolution), being 1-2 mm length (1/3 μm resolution) with the 2 μm diameter pin and load of 1 mg. The stacking and analysis of these measurements were used for graphing the 3D surface mapping using Vision advanced analysis software.

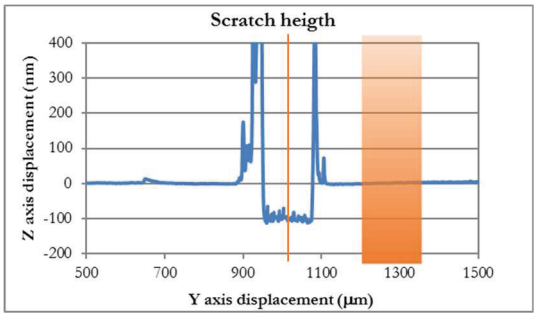

Figure 2-9. Scan over scratched coating for thickness calculation through height difference.

2.12. Atomic force microscopy

2.12.1. Equipment and experimental attainment

The surface of developed coatings was analyzed using atomic force microscopy (AFM). AFM phase and height images were collected by operating in tapping mode with a scanning probe microscope Multimode 8 from Bruker with Nanoscope V controller. The AFM was equipped with an integrated silicon tip/cantilever having a resonance frequency of ~300 kHz and 42 N/m spring constant. Scan rates ranged from 0.7 to 1.2 Hz/s. In order to get repeatable results, different regions of the investigated coatings were scanned to choose representative AFM images. Height and phase AFM images were very similar, thus only AFM phase images are shown here. The roughness of each investigated coating was measured using AFM high images (5 µm x 5µm). Root mean square (R_q) or arithmetic mean (R_a) values were used for roughness specification.

2.13. Thermogravimetric analysis

2.13.1. Equipment and experimental attainment

Thermogravimetric analysis (TGA) was used to study the temperatures at which SDAs are degraded, as well as weight change of sol during heating, in order to stablish the temperature for treat the dried gel after deposition. Experiments were accomplished in TG-DTA92 thermobalance. Organic SDA were subjected to a measurement program from 25 to 1000 ºC at 5 ºC/min heating rate in air. The analyzed sols were subjected to a measurement program from 25 to 350 ºC at 5 ºC/min heating rate, dwelled for 60 min at 350 ºC, and raised up to 1000 ºC at 10 ºC/min heating rate in air.

References

[1] W. Theiss Hard- and software, (n.d.). http://www.mtheiss.com/.

[2] D. Stroud, The effective media approximations: Some recent developments, Superlattice Microst. 23 (1998) 567–573.

[3] R. Clausius, Die Mechanische Behandlung der Elektricität, Vieweg, Braunschweig, 1858.

[4] O.F. Mossotti, Memorie di Matematica e di Fisica della Società Italiana delle Science Residente in Modena 24 (Part2), 1850.

[5] D.A.G. Bruggeman, Berechnung verschiedener physikalischer konstanten von heterogenen substanzen. I. Dielektrizitätskonstanten und leitfähigkeiten der mischkörper aus isotropen substanzen, Ann. Phys. 24 (1935) 636–664.

[6] D. Chen, Anti-reflection (AR) coatings made by sol gel processes : A review, Sol. Energy Mater. Sol. Cells. 68 (2001) 313–336.

[7] A. Gombert, W. Glaubitt, K. Rose, J. Dreibholz, B. Blasi, A. Heinzel, D. Sporn, W. Doll, V. Wittwer, Antireflective transparent covers for solar devices, Sol. Energy. 68 (2000) 357–360.

[8] K. Burrows, V. Fthenakis, Glass needs for a growing photovoltaics industry, Sol. Energy Mater. Sol. Cells. 132 (2015) 455–459.

[9] G. Helsch, J. Deubener, Compatibility of antireflective coatings on glass for solar applications with photocatalytic properties, Sol. Energy. 86 (2012) 831–836.

[10] J. Deubener, G. Helsch, A. Moiseev, H. Bornhöft, Glasses for solar energy conversion systems, J. Eur. Ceram. Soc. 29 (2009) 1203–1210.

[11] M. Garriga, M.I. Alonso, Caracterización estructural mediante elipsometría espectral de multicapas basadas en SiO_2, Bol. Soc. Esp. Ceram. Vidrio. 39 (2000) 729–734.

[12] J.N. Helbert, Handbook of VLSI microlithography: principles, technology, and applications, Noyes Publications, 2001.

[13] A.L. Cauchy, Sur la réfraction et la réflexion de la lumière, Bull. Des Sci. Mathématiques. XIV (1830) 6–10.

[14] M.R. Baklanov, K.P. Mogilnikov, V.G. Polovinkin, F.N. Dultsev, Determination of pore size distribution in thin films by ellipsometric porosimetry, J. Vac. Sci. Technol. B. 18 (2000) 1385.

[15] C. Boissière, D. Grosso, S. Lepoutre, L. Nicole, A.B. Bruneau, C. Sanchez, Porosity and mechanical properties of mesoporous thin films assessed by environmental ellipsometric porosimetry, Langmuir. 21 (2005) 12362–12371.

[16] R.C. Tolman, The effect of droplet size on surface tension, J. Chem. Phys. 17 (1949) 333–337.

[17] E.J. Gilabert, Medida del color, Valencia, 2002.

[18] W.E. Sumpner, The diffusion of ligth, Proc. Phys. Soc. London. 12 (1892) 10–29.

[19] R. Ulbricht, Die bestimmung der mittleren räumlichen Lichtintensität durch nur eine Messung, Elektrotech. Zeit. 21 (1900) 595–597.

[20] ASTM G173-03, Standard tables for reference solar spectral irradiances: direct normal and hemispherical on 37º tilted surface, 2013.

[21] S. van Riesen, M. Neubauer, A. Boos, M.M. Rico, C. Gourdel, S. Wanka, R. Krause, P. Guernard, A. Gombert, New module design with 4-junction solar cells for high efficiencies, AIP Conf. Proc. 1679 (2015).

[22] M. Machado, T. Baenas, N. Yurrita, Optical model for multilayer glazing systems: Experimental validation through the analytical prediction of encapsulation-induced variation of PV modules efficiency, Sol. Energy. 135 (2016) 77–83.

[23] C. Domínguez, I. Antón, G. Sala, S. Askins, Current-matching estimation for multijunction cells within a CPV module by means of component cells, Prog. Photovoltaics Res. Appl. 21 (2013) 1478–1488.

[24] T. Markvart, L. Castañer, Principles of solar cell operation, Elsevier Ltd, 2017. http://dx.doi.org/10.1016/B978-0-12-385934-1.00001-5.

[25] M. Żenkiewicz, Methods for the calculation of surface free energy of solids, J. Achiev. Mater. Manuf. Eng. 24 (2007) 137–145.

[26] F.M. Fowkes, Attractive forces at interfaces, Ind. Eng. Chem. 56 (1964) 40–52.
[27] D.K. Owens, R.C. Wendt, Estimation of the surface free energy of polymers, J. Appl. Polym. Sci. 13 (1969) 1741–1747.
[28] W.C. Oliver, G.M. Pharr, Measurement of hardness and elastic modulus by instrumented indentation: Advances in understanding and refinements to methodology, J. Mater. Res. 19 (2004) 3–20.
[29] W.C. Oliver, G.M. Pharr, An improved technique for determining hardness and elastic modulus using load and displacement sensing indentation experiments, J. Mater. Res. 7 (1992) 1564–1583.
[30] P.A. Steinmann, Y. Tardy, H.E. Hintermann, Adhesion testing by the scratch test method: The influence of intrinsic and extrinsic parameters on the critical load, Thin Solid Films. 154 (1987) 333–349.
[31] J.C. Pouxviel, J.P. Boilot, J.C. Beloeil, J.Y. Lallemand, NMR study of the sol/gel polymerization, J. Non. Cryst. Solids. 89 (1987) 345–360.

Chapter 3

Optimization of the antireflective porous silica coating

In this Chapter the theoretical optical performance of antireflective coating system approached by graded refractive index layer stacks is presented.
Then, the coatings required to build the AR layer stack have been experimentally attained through acid-catalyzed sol-gel method combined with evaporation induced self-assembly during dip coating process. The optimization of the sol-gel formulations has been conducted through the scanning of four types of organic/inorganic phase systems in two conditions of water/alkoxide ratio. The main aim of this research work has been focused on the achievement of the process conditions that allow to grow coatings fulfilling specific thickness, porosity and optical constants (n, κ) with, in parallel, a high stability of the formulated sol. These coating properties have been studied by ellipsometry, environmental ellipsometric porosimetry and atomic force microscopy while optical transmittance and reflectance of AR coated glasses have been characterized by spectrophotometry, under the AM1.5D reference solar spectral irradiance.

The research work presented in this Chapter has resulted in the following publications:

C. Agustín-Sáenz, J.Á. Sánchez-García, M. Machado, M. Brizuela, O. Zubillaga, A. Tercjak, Broadband antireflective coating stack based on mesoporous silica by acid-catalyzed sol-gel method for concentrated photovoltaic application, Sol. Energy Mater. Sol. Cells. 186 (2018) 154–164.

C. Agustín-Sáenz, M. Machado, A. Tercjak, Antireflective mesoporous silica coatings by optimization of water content in acid-catalyzed sol-gel method for application in glass covers of concentrated photovoltaic modules, J. Colloid Interface Sci. 534 (2019) 370–380.

3.1. Introduction

The main objective presented in this Chapter is, on the one hand, the calculation of the features of the coatings partaking in the AR layer system that provides optimized optical transmission for the glass-air interface, in the wavelength range that matches the spectral response of the solar cells. On the other hand, the growth control of the coatings based on SiO_2 material for attaining the thickness, refractive index and porosity required for composing the optimized AR layer stack.

Oxide materials (glass, ceramics) can be fabricated from intermediates that result from the polymerization of organometallic precursors dissolved in an alcoholic solvent during the sol-gel-glass process [1]. The material composition, morphology and texture can be controlled by the proper selection of the followed sol-gel route. The key point relies on the control of the reactivities of the different precursors used in the reaction. In this research work, only one type of inorganic precursor, TEOS, is involved. Still, there are many ways in which TEOS monomers can be polymerized, mainly because the Si atoms, which have fourfold coordinate covalent bond possibilities, are incompletely linked to each other during the polymerization reaction. The polymerization of TEOS is conducted through hydrolysis of the ethoxy groups into silanols, followed by the condensation of the silanols to form the siloxane bridge. By controlling the reaction parameters, one can control the polymer growth, such as long or short chains, highly or poorly branched, etc, to obtain a desired structure, by the grade of compactness (dense or porous structured).

Although highly porous structures are attained by basic-catalysis, the obtained coating exhibits weak bindings between particles and poor abrasion resistance. Compared to acid-catalysis, the hydrolysis kinetics are more strongly affected by other parameters like the concentration of alkoxide and nature of the solvent, and the resulting sols usually present short-term stability, thus leading to low-efficient processes. For PV applications, robust coatings with high mechanical properties derived from an environmental-friendly, cost-effective and up-scalable process are required, and acid-catalyzed synthesis is the best route for it [2]. The mesostructure, pore volume and pore size in these conditions can be managed by the presence of organic phases (amphiphiles) that form micelles serving as template for the inorganic network growth induced by solvent evaporation during coating deposition [3][4]. In the state of the art, acid-catalyzed TEOS as single precursor for the deposition of AR porous SiO_2 coatings has been

successfully combined with amphiphiles as SDA, such as cetyltrimethylammonium chloride [5][6], cetyltrimethylammonium bromide/polypropylene oxide (PPO) mixture [7]. The mixture of acid-catalyzed TEOS and MTES as SiO_2 precursors has been studied assisted by polyethylene oxide (10) octadecyl ether [8], t-octylphenoxypolyethoxyethanol [9–12] and t-octylphenoxypolyethoxyethanol/polyethylene oxide (PEO) mixture [13]. Other research works reported materials composed by several layers either as composite or layer stack with enhanced features such as self-cleaning or photocatalysis of pollutant degradation process. For example, Li et al. [7] have modelled and synthesized bi-layer SiO_2 stack based on sol-gel with several molar ratio of cetyltrimethylammonium bromide/PPO mixture as SDA to obtain coating stacks combining materials with several refractive index and thickness values. Polyethylene oxide-b-polypropylene oxide-b-polyethylene oxide tri-block copolymer (PEO-b-PPO-b-PEO) is also a very commonly used SDA, and it has been reported for deposition of porous SiO_2 as part of multilayer stack with TiO_2 coatings [14–16].

By adjustment and selection of the synthesis parameters and in the presence of amphiphiles as SDA, acid-catalyzed sol-gel approach results in a proper method to control the microstructure, the pore volume and pore size of the coating, while obtaining highly stable sols and materials with robust mechanical properties. Water/alkoxide molar ratio, is another important structure-regulating tool [17], through the control of hydrolysis and condensation of TEOS. Some works have reported acid-hydrolyzation of TEOS for the preparation of AR coatings using a R_w 2 stoichiometric ratio of acidified water [18–20], other studies use R_w between 3-5 [9,11,13,15], while only Xu et al.[6] and Prado et al. [14] prepared silica sols by hydrolyzing TEOS in high R_w conditions of 12 and 16, respectively. They obtained coatings with good antireflective performance, although they did not focus on aging and durability of the prepared sols.

In this Chapter, the optimization of the material synthesis is presented. Particularly, inorganic and organic phases concentration have been optimized, as well as the water/alkoxide molar ratio. The general approach consists on the hydrolysis of TEOS with four or eight equivalents of acidified water in the presence of ethanol as homogenizing agent and five organic SDAs, that are scanned as templates. Particularly, amphiphiles or surfactants of different nature have been scanned in the same conditions and concentration level. Five types of micelle-forming surfactants have been studied. Two amphiphiles consisting of di-block copolymers having a hydrocarbon tail and a hydrophilic head: one of them formed by PEO as the hydrophilic block and n-alkyl-chain as the hydrophobic block; the other one having also PEO chain as the

hydrophilic block and an aromatic hydrocarbon as the hydrophobic group. One amphiphile consisting of a tri-block copolymer arranged in an A-B-A triblock structure, which consists of hydrophilic PEO and hydrophobic PPO. Two amphiphile molecules with charged head groups from the sub-class of ionic surfactants: one cationic surfactant that dissociates in water into an amphiphilic cation, formed by the anion bromide and a positively charged n-alkyl-chain; one anionic surfactant that dissociates in water into an amphiphilic anion, formed by the dissociation of cation sodium and a negatively charged n-alkyl-chain.

In essence, the main aim of research work presented in this Chapter is to experimentally develop durable coatings from stable sols, with controlled thickness, refractive index and porosity, for producing the AR layer stack that theoretically provides the highest reduction of Fresnel reflection losses in the glass-air interface.

3.2. Characterization techniques

The characterization methods used in this Chapter are in the following outline:

- Kinematic and dynamic viscosity (μ) of sols were characterized by Ubbelohde viscometer through 0B and 1C capillary tube. Density was measured with a glass pycnometer bottle.
- ^{29}Si NMR spectra were collected at room temperature on a Bruker AVANCE III 500 spectrometer.
- Ellipsometric parameters Ψ and Δ were recorded by variable angle spectroscopic ellipsometer (M-2000UTM, J.A. Co., Woollam). Spectra were taken from 250 to 1000 nm at three angles of incidence (60º, 65º, 70º) at room temperature conditions. The spectra were fitted using both the Cauchy dispersion model and Bruggeman medium effective approximation model. The data analysis was performed with WVase32 software. The apparent porosity was calculated with respect to pure dense silica and a polarization factor of 0.33 was considered.
- Water adsorption-desorption was studied by EEP. Measurements were performed with the variable angle spectroscopic ellipsometer (M-2000UTM, J.A. Co., Woollam), within a cell with controlled relative humidity (RH). In this case, the spectra were taken at a fixed incident angle of 70º, at different RH values. Pore size distribution were calculated as explained in Chapter 2 section 2.3.

- The surface of the investigated coatings was analyzed using the AFM Multimode 8 from Bruker with a Nanoscope V controller.
- TGA was accomplished in TG-DTA92 thermobalance. Organic SDA were subjected to a measurement program from 25 to 1000 ºC at 5 ºC/min heating rate in air.
- Transmittance and reflectance spectra were measured using a Jasco V-670 UV-Vis-NIR spectrophotometer equipped with a 150 mm integrating sphere. Reflectance was measured at an incident angle of 8º. Spectra were taken in the wavelength range from 300 to 2000 nm wavelength. In this range, integrated transmittance, τ, and reflectance, ρ, were calculated according to Equation 2-20. Gain value (G) was calculated as the percentage of the increment of τ value of coated glass over bare glass $[(\tau_{coat}-\tau_{glass})/\tau_{glass}\cdot 100]$. Reduction value (M) was calculated as the percentage of decrement of ρ value of coated glass below bare glass $[(\rho_{glass}-\rho_{coat})/\rho_{glass}\cdot 100]$.
- The water contact angle ($\theta_c^{H_2O}$) was determined by the static drop method, using Digidrop Contact Angle Meter (GBX Instruments). Ten measurements of the apparent contact angle were taken by placing drops of water on the horizontal and flat coating surface and measuring the angle at the liquid-solid-air boundary.

3.3. Sol preparation and coating deposition

3.3.1. Acid-catalyzed synthesis

Silica sols were prepared via acid catalysis following a two-step procedure. In a first step, TEOS, ethanol, acidified water (0.1 M HCl) and 5 SDAs of different nature with concentration values from 25 to 150 g/L were mixed and stirred for 90 min at 60 ºC. In a second step, a mixture of ethanol and acidified water (in order to obtain R_w equal to 4 and R_w8) was added drop by drop to the solution, that was stirred for 60 min at 40 ºC. Sols with no SDA content were also prepared with R_w4 and R_w8. Ethanol quantity was adjusted in a final stage since depending on final molar ratio between TEOS:ethanol, different equivalent concentrations of SiO_2 were prepared by varying ethanol/TEOS molar ratio (R_{Et}). Sols with R_{Et} 4 were prepared only for NMR study, sols with R_{Et} 8.7 were denoted as H-sols and those with R_{Et} between 22-25 were denoted as L-sols. The resultant sols were aged in sealed glass containers for 2 days. The scanned SDAs were polyethylene oxide (20) hexadecyl ether (SDA1),

cetyltrimethylammonium bromide (SDA2), PEO-b-PPO-b-PEO tri-block copolymer (SDA3), t-octylphenoxypolyethoxyethanol, (SDA4) and sodium dodecyl sulphate (SDA5). Table 3-1, Table 3-2 and Table 3-3 summarize the formulations that were prepared and studied. Table 3-1 collects the conditions of sols prepared with and without SDAs at R_w4 conditions, Table 3-2 collects the conditions of sols prepared with and without SDAs at R_w8 conditions and Table 3-3 collects the conditions of sols prepared to finally optimize the formulation with SDA1 and R_w8 conditions.

Table 3-1**.** Reactants molar ratio, SiO_2 concentration, type and concentration of amphiphiles in the sols formulated with R_w4 conditions.

Molar ratio TEOS:H_2O:EtOH	SiO_2 concentration	Amphiphile	Amphiphile concentration (g/L_{sol})
1:4:4	-	-	0
1:4:4	-	SDA1	75
1:4:8.7	H	-	0
1:4:8.7	H	SDA1	25, 50, 100, 150
1:4:22.5	L	SDA1	50, 75
1:4:8.7	H	SDA2	25, 50, 100, 150
1:4:22.5	L	SDA2	50, 75
1:4:8.7	H	SDA3	25, 50, 100, 150
1:4:22.5	L	SDA3	50, 75
1:4:8.7	H	SDA4	25, 50, 100, 150
1:4:24	L	SDA4	50, 75
1:4:8.7	H	SDA5	25, 50

Table 3-2. Reactants molar ratio, SiO_2 concentration, type and concentration of amphiphiles in the sols formulated with R_w8.

Molar ratio TEOS:H_2O:EtOH	SiO_2 concentration	Amphiphile	Amphiphile concentration (g/L_{sol})
1:8:4	-	-	0
1:8:4	-	SDA1	75
1:8:8.7	H	-	0
1:8:8.7	H	SDA1	25, 50, 100, 150
1:8:23.7	L	SDA1	50, 75
1:8:8.7	H	SDA2	25, 50, 100, 150
1:8:23.7	L	SDA2	50, 75
1:8:8.7	H	SDA3	25, 50, 100, 150
1:8:23.7	L	SDA3	50, 75
1:8:8.7	H	SDA4	25, 50, 100, 150
1:8:25.5	L	SDA4	50, 75
1:8:8.7	H	SDA5	25, 50

Stable and transparent sols were obtained with all the SDA excepting SDA5. Whitish sols were obtained with the latter, and no coatings were prepared with them.

Table 3-3. Reactants, molar ratio, and concentration of SDA1 in the optimized sol formulations at R_w8 conditions.

Molar ratio TEOS:H_2O:EtOH	Amphiphile concentration (g/L_{sol})
1:8:17.4	150
1:8:41	75
1:8:17.4	100
1:8:24.4	78

3.3.2. Acid and basic-catalyzed synthesis

Silica sols were prepared via combined acid and basic catalysis following a two-step procedure. The first acid step was similar to that followed in the acid-catalyzed synthesis explained above. TEOS, ethanol and acidified water (0.1 M HCl) were mixed and stirred for 90 min at 60 ºC to search the pre-hydrolysis of TEOS. In a second step, a solution of water-ammonia and ethanol, was added drop by drop to the solution and was stirred at room temperature. Table 3-4 reports the molar ratio at each step of prepared formulations.

Table 3-4. Reactants molar ratio in the first acid and second basic steps of the basic-catalyzed sol formulations.

Molar ratio in first step $TEOS:H_2O_{(HCl\ 0,1M)}:EtOH$	Molar ratio in second step $H_2O:NH_3:EtOH$	Final molar ratio $TEOS:H_2O:EtOH$
1:0.3:4.4	0.8:0.3:4.4	1:1.1:8.7
1:0.3:4.4	0.7:0.1:4.4	1:1:8.7
1:1.3:4.4	3:0.1:4.4	1:4.3:8.7

The aim of this synthesis route was the attainment of counterparts coatings grown from basic-catalyzed sol-gel approach, in order to compare their optical and mechanical properties with those obtained from acid-catalysis. However, all prepared formulations jellified in a few hours after preparation, and no coatings were grown.

3.3.3. Coating deposition

Silica sols were deposited on 4 mm (thick) low iron float glass specimens after being cleaned in ethanol under sonication for 15 min and then air dried. The coating deposition was performed by dip coating at a controlled withdrawal rate of 5 cm/min on both sides of the low iron float glass. Compared to other deposition procedures, dip coating method allows to obtain extremely thin, uniform and highly homogenous layers. Furthermore, the deposition under a defined atmosphere is easily approachable. In this case, it provides also the possibility of recovering flat specimens on both sides.

After coating deposition, a sintering step is required for i) eliminating the amphiphile from the coating to obtain the porous structure and ii) consolidating inorganic network to obtain the required mechanical stability. Sintering was performed in a conventional furnace at 450 ºC in air atmosphere for 1 h in the study of SDA screening accomplished in the sections 3.6 and 3.7. In the final SDA1 optimization study of the section 3.8, the sintering step was performed in a conventional furnace at 350 or 550 ºC in air atmosphere for 1 h.

3.4. Theoretical optical performance of simulated AR coating stacks

Multi-layer stacks were designed using CODE software [21] by minimizing the total reflection in the 300-2000 nm wavelength range. Table 3-5 shows theoretical optical characteristics of each layer integrated in the mono-, bi-, tri- and tetra-layer stacks on both sides of a 4 mm thick

low iron float glass (experimental $\tau_{300\text{-}2000}$ = 90.1% and $\rho_{300\text{-}2000}$ = 8.5%) as well as its integrated transmittance and reflectance values for both free and restricted up to 50% void fraction.

The highest transmittance value in the whole operation range was achieved for the tri-layer stack with growing void fraction layers of 11, 45 and 77%. Nevertheless, considering that such a high porosity would result in very fragile layers with poor mechanical properties, the void fraction of the external layer was restricted to 50%. In this scenario, integrated transmittance value was similar for bi- and tri-layer stacks. However, as shown in Figure 3-1, spectral differences were found in transmittance and reflectance curves. In the 400-980 nm wavelength range, the integrated transmittance values of the bi-layer stack were higher than the corresponding values of the tri-layer stack while in the 980-2000 nm wavelength range, the integrated transmittance values of the tri-layer stack were higher than those of the bi-layer stack.

In most current multi-junction solar cell configurations, top and middle subcells operate in the range between 350-900 nm, and bottom cell operates between 900-1800 nm. Usually the top and middle subcells generate similar current density while the bottom cell over generates current [22]. Therefore, the latter is not the one which limits the current of the total series connected cells, and the decisive parameters concern the top and middle subcells range. The τ and ρ values independently integrated in the three spectral ranges between 350-650, 650-900 and 900-1800 nm, approximated to spectral response of top, middle and bottom subcells in MJ solar cells are presented in the Table 3-5. Taking the above into consideration, a bi-layer stack composed by an inner layer with 1.41 refractive index at 700 nm and 106 nm thick and outer layer with 1.22 refractive index at 700 nm and 119 nm thick, was selected as target for experimental development as discussed below.

Table 3-5. Theoretical calculation of refractive index (n) at 700 nm, void fraction and thickness (d) of layers in mono-, bi-, tri- and tetra-layer stacks and integrated transmittance (τ) and reflectance (ρ) values in different spectral ranges corresponding to both sides coated 4 mm thick low iron float glass.

	Layer	n	Void fraction (%)	d (nm)	$\tau_{300-2000}$ (%)	$\tau_{350-650}$ (%)	$\tau_{650-900}$ (%)	$\tau_{900-1800}$ (%)	$\rho_{300-2000}$ (%)	$\rho_{350-650}$ (%)	$\rho_{650-900}$ (%)	$\rho_{900-1800}$ (%)
Free void fraction												
Mono-layer	1	1.23	48	117	96.4	98.7	97.0	93.3	2.3	1.1	1.4	4.6
Bi-layer	1	1.14	67	127	97.8	99.3	98.2	96.1	0.8	0.5	0.1	1.7
	2	1.34	24	107								
Tri-layer	1	1.10	77	129	98.3	99.6	98.1	97.2	0.3	0.1	0.2	0.6
	2	1.24	45	114								
	3	1.40	11	100								
Tetra-layer	1	1.10	77	113	98.3	99.6	98.1	97.2	0.3	0.1	0.2	0.7
	2	1.03	93	10								
	3	1.24	45	117								
	4	1.40	11	100								
Restricted void fraction												
Mono-layer	1	1.23	48	117	96.4	98.7	97.0	93.3	2.3	1.1	1.4	4.6
Bi-layer	1	1.22	50	119	97.4	98.9	97.7	95.9	1.4	1.0	0.6	2.5
	2	1.41	10	106								
Tri-layer	1	1.22	50	115	97.4	98.7	97.0	96.6	1.2	1.0	1.3	1.3
	2	1.35	22	100								
	3	1.45	0	80								
Tetra-layer	1	1.22	50	114	97.4	98.9	96.8	96.4	1.3	0.9	1.5	1.4
	2	1.35	21	110								
	3	1.43	5.5	6								
	4	1.44	2.5	96								

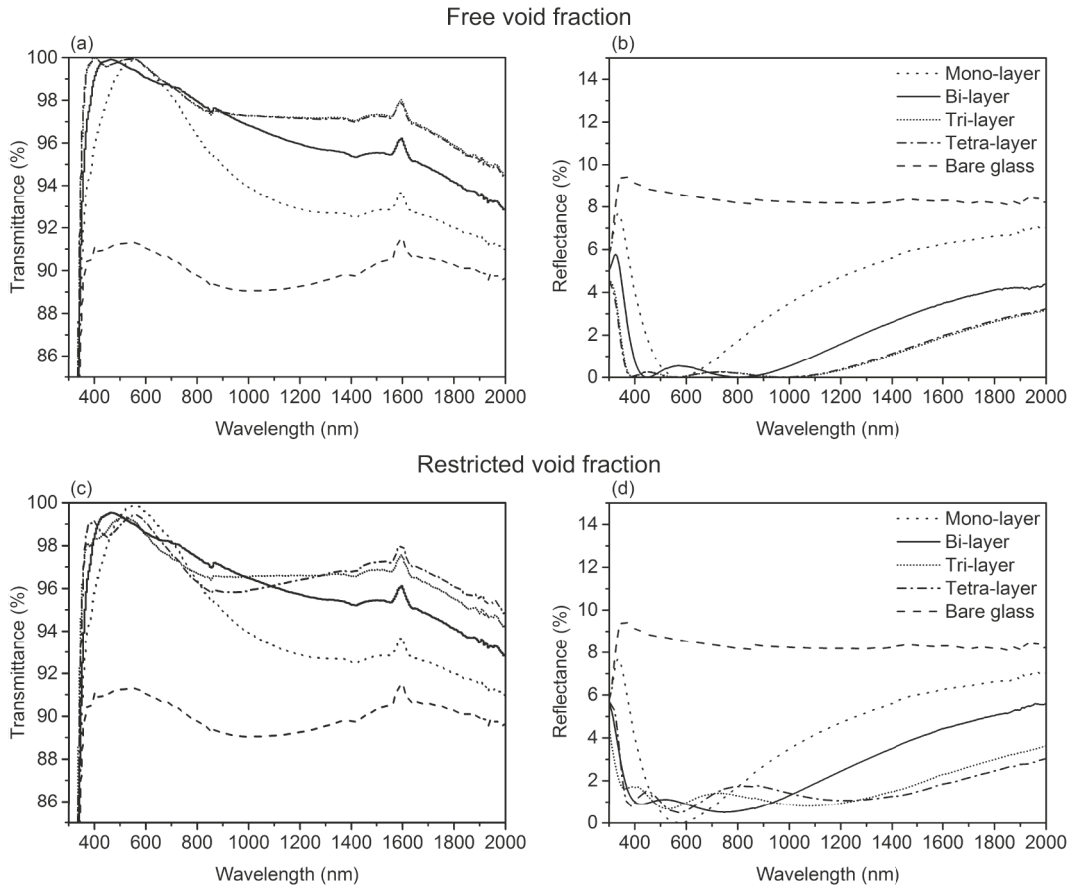

Figure 3-1. Transmittance (a, c) and reflectance (b, d) spectra of different optimized multi-layer stacks calculated with no restrictions (a, b) and with void fraction restricted to 50% (c, d).

3.5. Effect of water and organic SDA type in sol-gel transition

The sol-gel transition in tetra alkoxides-based systems such as TEOS is characterized by a strong increase in sol viscosity [23]. The time evolution of this parameter was registered, due to the direct influence it has in the pot life of sols. The viscosity changes according to the formation and the growth of the polymer-like silica, that may be linear chains, ring-like chains or form branching and interconnected chains, until the formation of the gel structure is reached. Preparing high stable sols is of interest for PV applications since it permits to obtain an efficient, robust and scalable process for AR coating deposition. The viscosity of H-sols registered along one-year period without SDA prepared with R_w4 and 8 at different aging times is presented in Figure 3-2a.

Under acid-catalysis, the role of excess water above four equivalents, R_w4, on gelation time depends also on the experimental conditions such as pH and alcohol content [24]. Several postulations have been studied in terms of a high R_w formulated sol from both theoretical and experimental point of view. It has been shown that a high R_w may shorten gelation time. However, it has also been stated that a minimum gelation time close to R_w4 may be obtained. Depending on the structures that are promoted or inhibited under each particular synthesis, the size of the sol particles changes continuously during the nucleation and growth process [23], due to the direct and the reverse reactions explained in the Figure 1-8 in Chapter 1. For example, if ring-like structure formation is inhibited by some process, it may provoke also a delay in the gelation process [24]. Therefore, it is crucial to analyze the viscosity evolution of each investigated system.

Regarding the systems under study, the initial viscosity of the H-sols with four water equivalents was 2 mPa·s, while the formulation with excess water exhibited 2.6 mPa·s. As observed in Figure 3-2a, both synthesis routes showed a similar evolution of viscosity along a one-year duration, and they exhibited an increase of around 18% and 24%, respectively, after 6 months of aging. Moreover, both doubled the initial value of viscosity after one year. This was an outstanding result from the point of view of sol durability. This evolution showed independence from R_w in this system, since the viscosity evolution of the two sols suffered a parallel increase.

Concerning the silanol and condensed silica species in the sols, Pouxviel et al. [25], who studied the sol-gel polymerization of TEOS with four and ten water equivalents, R_w4 and R_w10 by ^{29}Si NMR in the early stages after preparation, observed that silanol and condensed species were the same in both cases and only differences in peak intensities were found. However, they stablished that only with high R_w hydrolysis and condensations reactions were totally separated, based on the fact that the concentration of Si-OR species disappeared rapidly. In Figure 3-3, the ^{29}Si NMR performed after 2 days did not show silanol groups (peaks around -80 ppm) in none of the sols. The silica oligomers for R_w4 (Figure 3-3a) were mainly formed by condensed linear or ring-like chains and branched silica species, thus Q_2 and Q_3, respectively (localized between -90 ppm and -106 ppm) after 2 days. Totally branched silica, Q_4 species (around -110 ppm) were detected after 7 and 15 days of aging whereas after 35 days only Q_3 species composed the sol. Therefore, in this case, depolymerization and subsequent repolymerization seems not to reach equilibrium. However, the silica oligomers for R_w8 (Figure 3-3b) were linear

or ring-like, Q_2 species, and branched silica, Q_3 species, at all scanned times, thus arriving at an equilibrium in the species formed during depolymerization and subsequent repolymerization along time.

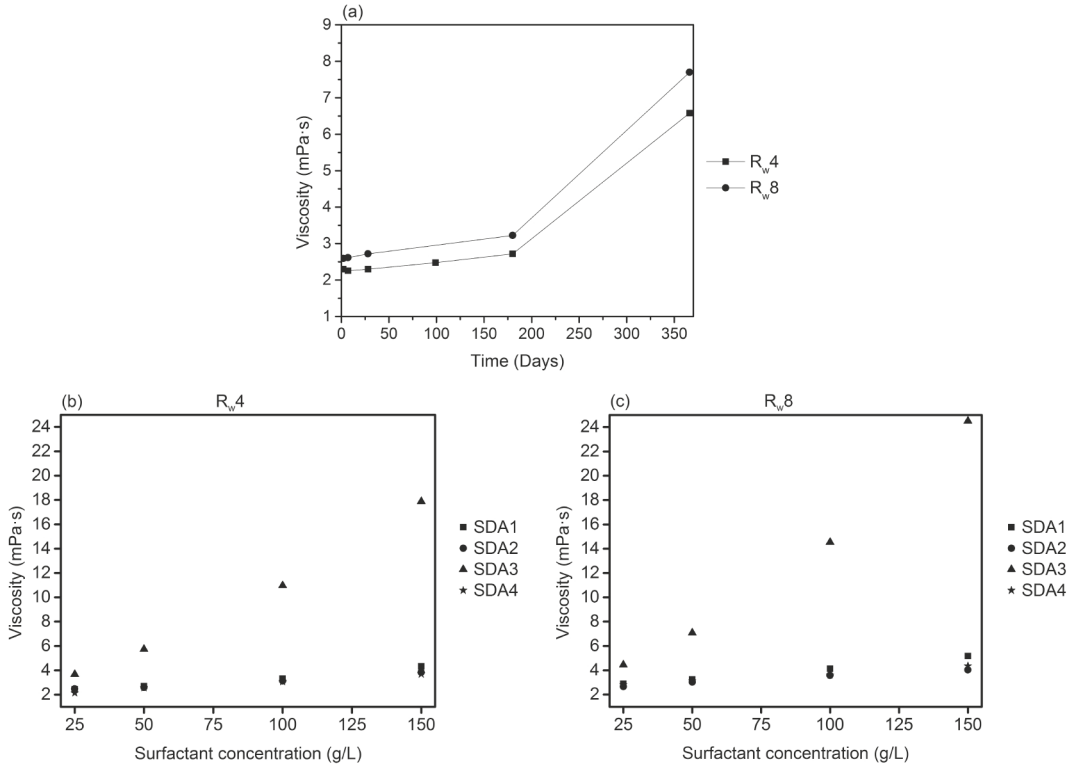

Figure 3-2**.** The dynamic viscosity as a function of time for H-sols prepared with R_w4 and R_w8 (a) and effect of SDA concentration on initial dynamic viscosity of H-sols (b). (Standard deviation < 0.05 mPa·s).

Viscosity of H-sols was also measured as a function of different SDA concentrations, that were scanned to achieve porosity of 50% for R_w4 and R_w8 conditions (see Figure 3-2b and Figure 3-2c, respectively). In this experimental scanning, difference for each surfactant was observed when viscosity value increased with increase of surfactant concentration. Viscosity of H-sols based on $SDA1_{Rw4}$, $SDA2_{Rw4}$ and $SDA4_{Rw4}$ varied from 2.3±0.2 mPa·s for 25 g/L surfactant concentration to 4.0±0.3 mPa·s for 150 g/L surfactant concentration while viscosity of H-sols with $SDA3_{Rw4}$ varied from 3.7 to 17.9 mPa·s for the same surfactant concentration as before. The viscosity of the sols prepared with R_w8 was in all cases slightly higher than the viscosity corresponding to R_w4 and increased as a function of the different amphiphiles in the same way as for R_w4 as long as their concentration did. Viscosity of H-sols

based on SDA1$_{Rw8}$, SDA2$_{Rw8}$ and SDA4$_{Rw8}$ started from 2.8±0.1 mPa·s for 25 g/L of SDA concentration and reached 4.0, 4.4 and 5.2±0.3 mPa·s for 150 g/L of SDA2$_{Rw8}$, SDA4$_{Rw8}$ and SDA1$_{Rw8}$, respectively. The viscosity of H-sols with SDA3$_{Rw8}$ varied from 4.5 to 24.5 mPa·s for the same increasing SDA concentration.

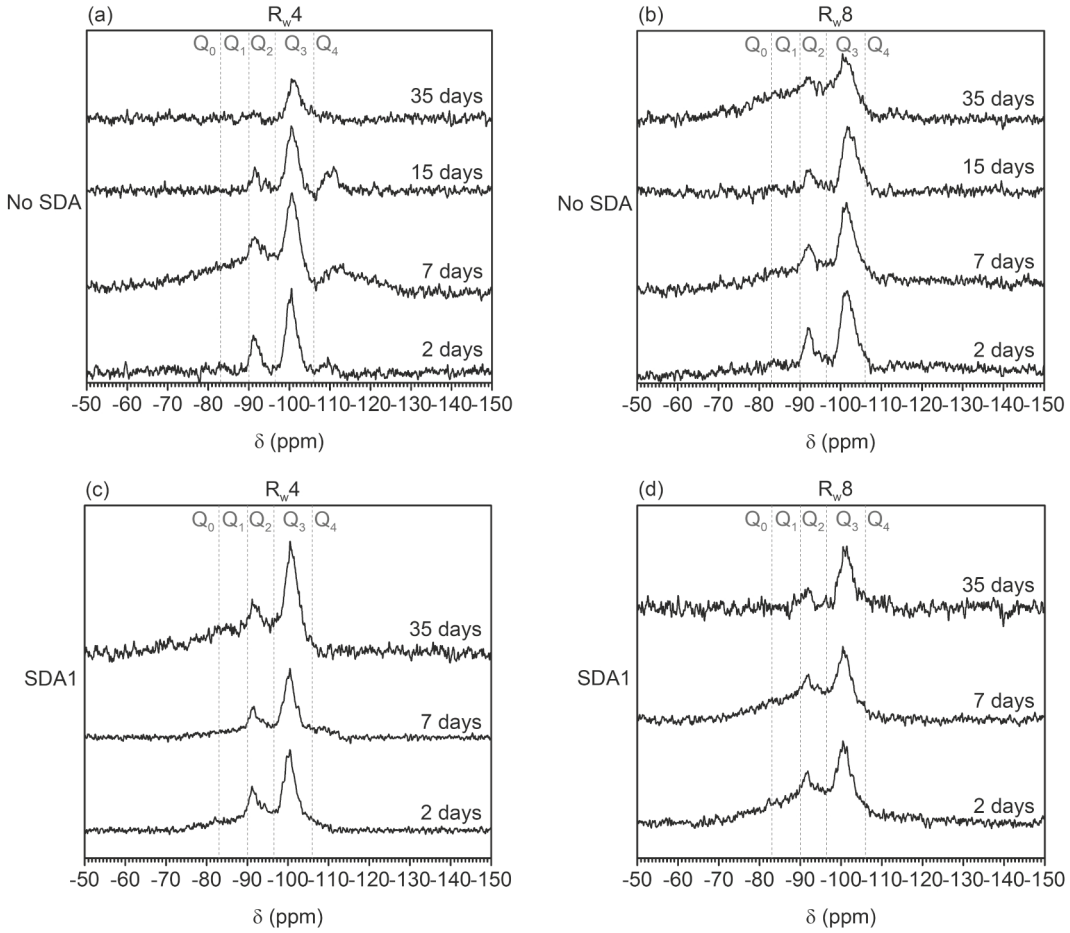

Figure 3-3. ^{29}Si NMR studies of the sols prepared with R_w4 with no SDA (a); R_w8 with no SDA; R_w4 with SDA1 (c); R_w8 with SDA1 (d) measured at several times after preparation.

The silica oligomers were also determined by ^{29}Si NMR after 2, 7 and 35 days in sols prepared with R_w4, R_w8 and 50 g/L of SDA1, given that the degree of condensation of inorganic chains has a crucial influence in the accommodation with organic SDA micellar phases [26]. In view of these results, shown in Figure 3-3c and Figure 3-3d, equilibrium states of linear or ring-like chains Q_2 and branched Q_3 silica species were detected at all times for both R_w tested, revealing an equilibrium between formed species along time in both conditions of R_w. These condensed species are excellent to accommodate around the template formed by organic micelles.

3.5.1. Viscosity evolution of sols with SDA

Evolution of viscosity of H-sols prepared at R_w4 and R_w8 with and without SDA was monitored up to six months of aging. Regarding sols prepared at R_w4, as observed previously, the viscosity increase of H-sol without SDA was around 18% after six months of aging. Only sols prepared with $SDA1_{Rw4}$ and $SDA4_{Rw4}$ were stable after that time in the whole surfactant concentration range tested, understanding as stable sols those which maintained their transparent, fluid, and one-phase status. The viscosity increase for sols with $SDA1_{Rw4}$ after six months was in decrescent order, 15% for sol with 25 g/L, 9% for sol with 50 g/L, 5% for sol with 100% while no increase was detected for sol with 150 g/L. The viscosity of sol with 25 g/L $SDA4_{Rw4}$ doubled its value after six months of aging. However, sols with 50, 100 and 150 g/L of $SDA4_{Rw4}$ maintained their initial value after six months of monitoring. In these cases, the presence of organic phases, contributed to improve the viscosity stability of sols as long as their concentration increased. Among sols prepared with $SDA2_{Rw4}$, only those prepared at 25, 50 and 100 g/L were stable after six months, and their viscosity increased in 2, 10 and 4% respectively while that prepared with 150 g/L was not stable after one week. The viscosity increase after one month of ageing of sols prepared with $SDA3_{Rw4}$ was around 7-8% for 25, 100 and 150 g/L concentrations while no increase was detected for sol prepared with 50 g/L. After one month, they became a two-phase separation and further measurements did not occur.

Regarding sols prepared at R_w8, the most relevant result was that the increase of viscosity for all $SDA1_{Rw8}$-sols, all $SDA4_{Rw8}$-sols and $SDA2_{Rw8}$-sols of 50 and 100 g /L was less than the one experimented by the sol without SDA. Therefore, the presence of organic phases highly contributed to improve the viscosity stability of sols in these R_w conditions. On the other hand, the 25 g/L $SDA2_{Rw8}$-sol experimented an increase close to 50%, while $SDA2_{Rw8}$-sol of 150 g/L was not stable for longer than 2 days. Viscosity of $SDA3_{Rw8}$-sols was measured up to one month since they experimented a two-phase separation.

3.6. Porous silica coating by acid-catalyzed sol-gel method with four water equivalents

3.6.1. Effect of SDA concentration on thickness and refractive index of coatings

It is known that EISA method is a complex approach due to the chemical and physical phenomena involved [26]. Depending on the ratio between inorganic and organic parts, the solvent, and the quantity of water as well as the processing conditions, the structure of prepared coating material can be controlled. For this reason, the four types of organic/inorganic systems of different nature were scanned in order to obtain coatings with 50% of void fraction and thickness around 120 nm. The coatings grown with H-sols, at R_w4 conditions, containing different weight concentration of the four different SDAs were analyzed by ellipsometry. Thickness and refractive index obtained by ellipsometric data and fitted by Cauchy model [27] are represented in Figure 3-4a and Figure 3-4b, respectively. The apparent porosity resulting from Bruggeman fitting [28] is graphed in Figure 3-4c.

Several forces contribute to the coating formation and its derived thickness during withdrawal of substrate from sol, such as dragging force, gravity, forces related to liquid surface tension and to the interaction between solid specimen and liquid [29]. Most of these factors are inherent of the system and other such as the dragging force can be controlled since it is proportional to the viscosity of the sol and the withdrawal rate. This was another reason whereby viscosity of sols was deeply studied as a function of surfactant concentration as presented in section 3.5. The Landau-Levich equation [30] which describes the thickness in terms of the equilibrium between the adhesion of the fluid on the substrate and gravity-induced viscous drag, predicts that the thickness is proportional to the viscosity of the fluid to the power 2/3. Taken this into account, higher viscosity sols will lead to higher coating thickness.

The wide range of obtained sol viscosities led to a broad spread of thickness values for the derived coatings, as shown in Figure 3-4b. As expected, similarly to the trend found for the viscosity, the coating thickness increased as a function of surfactant concentration. Coatings without SDA presented thickness of 121 nm. Thickness of the coatings based on SDA1 and SDA4-sols expanded from around 170 nm for 25 g/L surfactant concentration to around 300 nm for 150 g/L surfactant concentration while thickness of the coatings based on SDA3 sols

expanded from around 200 nm to almost 1000 nm, for the same surfactant concentration as before. The only exception was found for coatings based on SDA2 surfactant, since the coatings formed with these sols at highest concentration did not present the expected increase of thickness. This result is in good agreement with the low porosity values obtained for these coatings.

Refractive index and apparent porosity of these coatings as a function of surfactant concentration are represented in Figure 3-4b and in Figure 3-4c, respectively. It is clearly observed that for H-sols with SDA1, SDA4 and SDA3, the increase of organic phase resulted in coatings with lower refractive index and consequently higher porosity, reaching the targets predicted by the theoretical calculation.

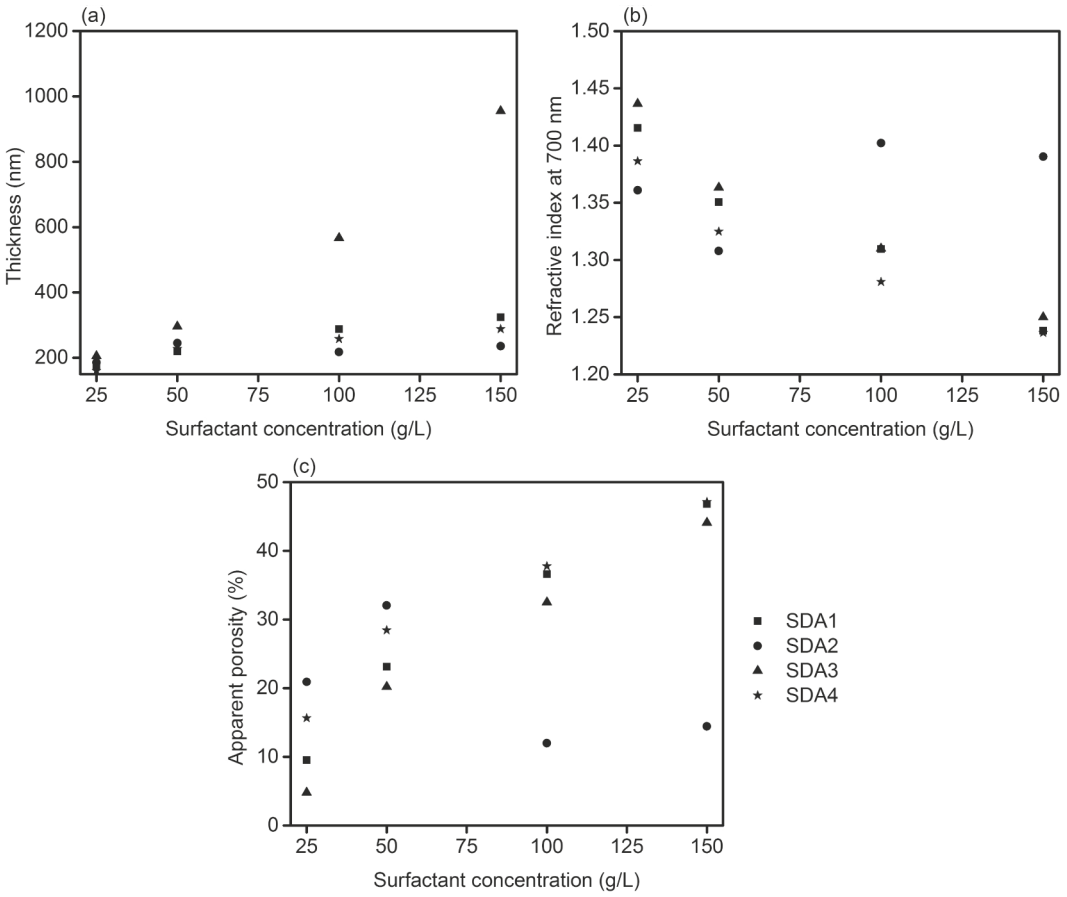

Figure 3-4. Effect of SDA concentration on thickness (a) refractive index (b) apparent and porosity (c) of coatings obtained from H-sols. (d ± 0.5 nm; n ± 0.001; apparent porosity ± 0.2%).

The coatings grown with the SDA2-sols reached a maximum value of porosity at surfactant concentration of 50 g/L, while sols with higher concentration did not form higher porosity in coatings.

It is also noticeable that for lower surfactant concentrations, 25 and 50 g/L, the highest porosity was detected for SDA2-sols, followed by SDA4-sols, SDA1-sols and SDA3-sols, which is in good agreement with the increase of molecular weight of the organic surfactants. Other remarkable result was that for surfactant concentration equal to 150 g/L, SDA2 excluded, the differences between organic surfactants were reduced and porosity merged into a similar value close to 50%, in agreement with the theoretical prediction.

Anyhow, an optimum thickness value should be accompanied by an optimum porosity value to obtain the optimum value of transmittance. Therefore, although H-sols permitted to prepare layers with porosity around 50%, the obtained thickness values did not fit the requirements to be candidate for composing the AR multi-layer stacks.

3.6.2. Textural properties

The porous coatings investigated in this section were analyzed by EEP. Adsorption-desorption curves of the coatings from H-sols at R_w4 based on different amphiphiles at a concentration of 50 g/L and their pore size distribution are showed in Figure 3-5. The amphiphile concentration of sols was selected since this is a common concentration at which derived coatings presented most similar porosity values. The typical behavior of mesoporous materials associated with isotherms type IV was observed for all coatings. The hysteresis loops appear due to the difference of radius of curvature of condensed liquid meniscus during the adsorption and desorption processes in the mesopores [31]. Its shape can be further correlated to the texture (e.g., pore size distribution, pore geometry, and connectivity) of a mesoporous material [32] according to an empirical classification in four types of curves given by IUPAC. Hysteresis loops of all coatings were identified as type H1, which exhibits parallel branches and is associated with porous materials consisting of well-defined cylindrical-like pore channels or agglomerates of approximately uniform spheres. For coatings deposited from sols with the same amphiphile concentration, total volume of pores was 20% for SDA3, 30% for SDA1 and about 35% for both SDA2 and SDA4.

Pore size distribution was determined using modified Kelvin's equation [33] and, as mentioned above, results are showed in Figure 3-5. SDA4, SDA2 and SDA1 coatings showed a narrow pore size distribution with maximum at 6, 7 and 4.5 nm, respectively, while SDA3 coating exhibited a bi-modal distribution with pores around 6.5 and 9 nm.

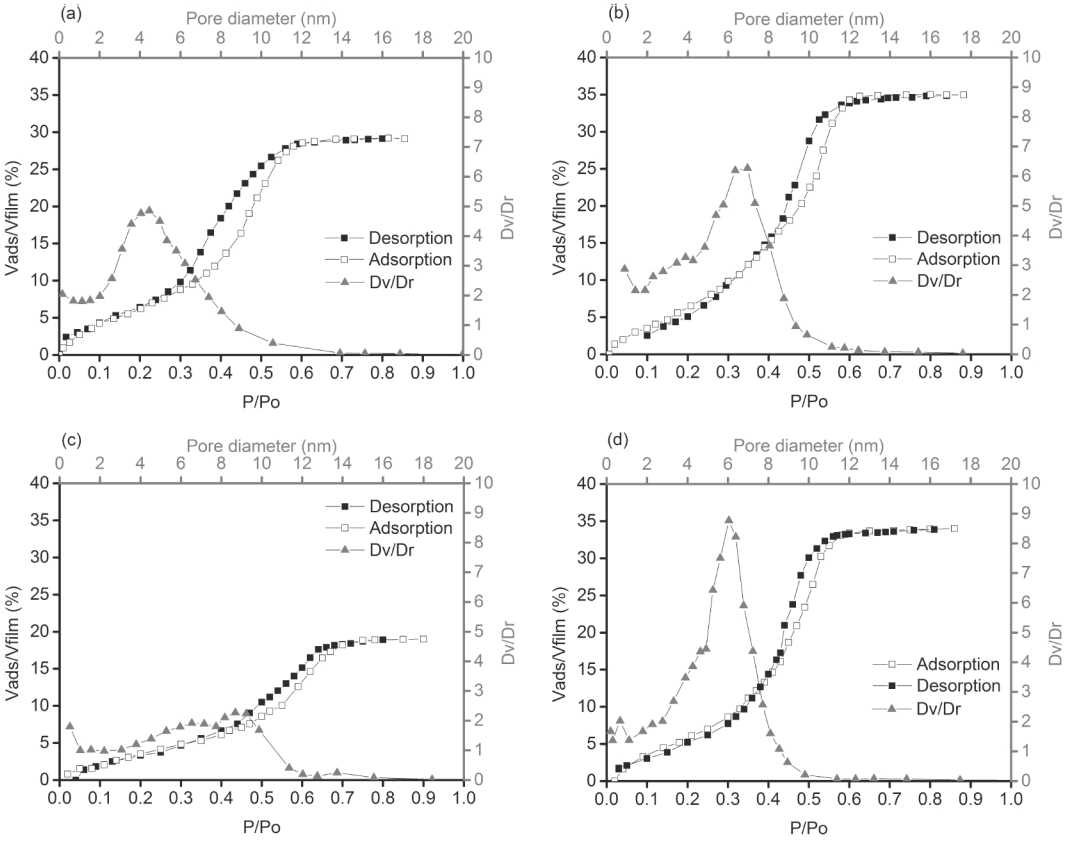

Figure 3-5. Adsorption/desorption isotherms and pore size distribution of coatings obtained from H-sols with 50 g/L of SDA1 (a), SDA2 (b), SDA3 (c) and SDA4 (d).

Figure 3-6 shows the AFM phase images of the coatings obtained from H-sols and R_w4 with 50 g/L of different amphiphile as well as H-sol with no amphiphile content. It can be observed that the surface of investigated coatings was crack free and homogenous. The resulting topography of the porous coatings was composed of small grains apparently without any particular order. Slightly differences in the topography were found between SDA2 and SDA4 coating surfaces, formed by more rounded grains, in comparison to SDA1 and SDA3 coatings, whose surfaces seemed to be defined by the cavities where SDA was accommodated before calcination. The result of the former case was a surface formed by convex shaped particulate matter and the latter was a surface formed by concave cavities. This morphology should be

attributed to the accommodation between inorganic and organic phases that provoked the self-assembly during coating deposition.

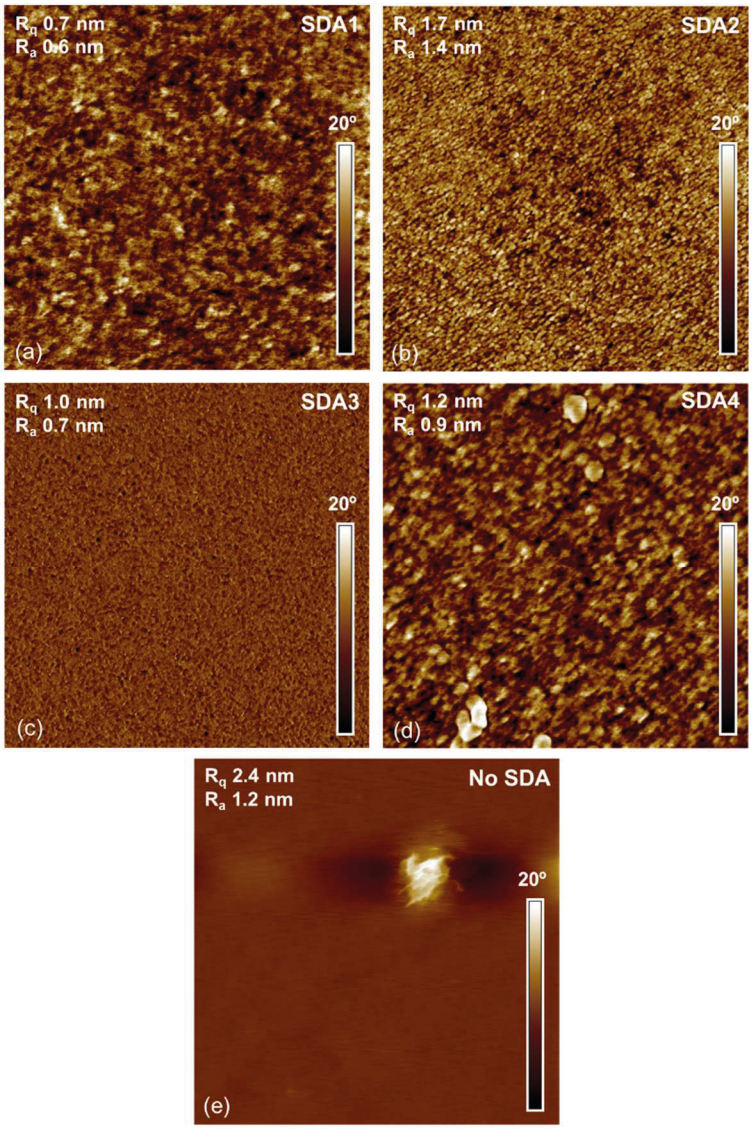

Figure 3-6. AFM phase images (1 μm x 1 μm) of coatings obtained from H-sols with 50 g/L of SDA1 (a), SDA2 (b), SDA3 (c), SDA4 (d) and without SDA (e).

Regarding the particulate matter size, coatings prepared with the same quantity of di-block copolymers SDA1 and SDA4 presented grains of around 12±2 nm, although in the case of SDA4 coating some aggregated can be distinguished on the investigated surface. SDA2 and SDA3 coatings, thus formed by the self-assembly induced by amphiphiles with a marked different nature, cationic surfactant and tri-block copolymer, respectively, were formed by

similar small grains around 5±1 nm. Image root mean square roughness (R_q) of porous coatings was in rising order, 0.7 nm for SDA1 coating, 1 nm for SDA3 coating, 1.2 nm for SDA4 coating and 1.7 nm for SDA2 coating. The topography of dense coating resulted in a smooth surface since it did not present void fraction, although R_q was 2.4 nm, higher than porous coatings roughness. Consequently, there was not a proportional relation between observed grain size and surface roughness. Nevertheless, for all investigated systems the roughness was very low.

3.6.3. Effect of inorganic precursor and SDA concentration on thickness, refractive index and thermal shrinkage of coatings

As explained before, as long as amphiphile concentration increased in the sol formulation both porosity and thickness of the deposited coating followed an increasing tendency. Since the coating structural features such as refractive index and porosity do not vary with the thickness [34], it could have been appropriate to modify withdrawal rate in order to obtain thinner coatings with the same porosity. However, lower withdrawal rate did not provide thinner coatings, what permitted to conclude that operating conditions were near to critical withdrawal speed between draining and capillarity regime, in which at low speeds, the thickness increases when speed decreases [34]. Taken this into account, new formulations with lower concentration of equivalent SiO_2, L-sols, were prepared in order to reach the proper conditions. Theoretical concentration of SiO_2 in these new sols was about 35 g/L, with amphiphile concentration of 50 and 75 g/L however maintaining molar ratio of TEOS:amphiphile as in cases of 100 and 150 g/L of H-sols. Optical constants and porosity of these L-sol coatings were obtained from ellipsometry, as well as their corresponding thickness before and after sintering. The obtained results are shown in Table 3-6. It is observed that thickness increased with SDA concentration from 50 to 75 g/L only for SDA1, SDA2 and SDA3, also accompanied by a decrease of refractive index (and consequently an increase of porosity). Furthermore, the increase of thickness was more pronounced when porosity increase was higher. In the case of SDA4, the concentration increase from 50 to 75 g/L did not result in the formation of a more expanded coating. Indeed, the thickness difference of the coatings before sintering, merged in similar values after sintering, led by a higher contraction of the coatings prepared with 75 g/L of SDA2 over that prepared with 50 g/L. The same behavior was observed for coatings prepared with 50 and 75 g/L of SDA1.

Therefore, the coatings prepared with 75 g/L of di-block copolymers SDA1 or SDA4, shrank double than those prepared with 50 g/L after sintering step. This effect was more levelized for SDA2 and the contrary effect was observed for sols containing SDA3.

The densification of the gel material during the thermal treatment depends strongly on its microstructure, and it is related to different mechanisms arising as temperature increases. The first event is the water loss, then inorganic network stabilization by further condensation of silica, and the decomposition of the organic phase [35]. Indeed, organic phase keeps a fixed volume during the sintering step, at least from ambient up to its decomposition temperature, that is around 200 ºC (see Table 3-7). Table 3-7 shows the temperatures at which a 5% weight loss was detected by TGA, for each SDA. The experimental work revealed that the SDA1 and SDA3 started to decompose at ~180 ºC, followed by SDA4 at ~200 ºC while the cationic surfactant SDA2 started its decomposition at ~220 ºC. Consequently, at temperatures below the decomposition temperature of organic phases (namely ~T_5 in Table 3-7 for each SDA) the coating contraction is governed only by the volumetric contraction of the inorganic silica phase. However, at temperatures above the decomposition temperatures, the thickness decrease is related to the sum of the contraction of silica walls and the thermal decomposition of the organic phase. This thickness reduction is accompanied by a unidirectional contraction of the domain normal to the surface plane [26]. Finally, it can be pointed out that pores get empty through complete organic phase elimination. Depending on the combination of polymer-like silica species such as linear, branched or cyclic and micelles created by the organic phase, the properties of the obtained mesoporous (pore size, wall thickness, specific area) shall be affected. As explained, the shrinkage after sintering coatings from sols with 50 g/L and 75 g/L of SDAs was strongly dependent on the type of amphiphile. In the case of SDA1, SDA2 and SDA4, a higher quantity of SDA induced a higher thickness contraction during the thermal treatment and therefore it did not imply a proportional increase in porosity. The contrary effect was observed on the coatings derived from SDA3, since the coating containing more amphiphile shrank less, and thus allowed to obtain a high difference in their refractive index and porosity values.

Coatings prepared from SDA1- and SDA4-sols presented acceptable thickness, while SDA2-sols formed too thin coatings and SDA3-sols yet generated too high thickness. The coating that best matched thickness and refractive index values corresponded to formulation with 75 g/L of SDA1. Viscosity did not increase in L-sols prepared with SDA1, SDA2 and SDA4 after

six months with the exception for SDA2 and SDA4 both at 75 g/L that became unstable. Viscosity of sols with SDA3 was constant after one month of aging.

Table 3-6. Refractive index (n) at 700 nm, porosity and thickness (d) of coatings obtained from L-sols by spectral ellipsometry.

Coating	n (at 700 nm)	Apparent porosity (%)	d (nm)	d_{raw} (nm)	% shrinkage
L-SDA1-50g/L	1.28	37.3	120	181.7	51.4
L-SDA1-75g/L	1.25	45.3	126	247.7	96.3
L-SDA2-50g/L	1.41	10.9	88	205.1	133.1
L-SDA2-75g/L	1.34	23.7	98	238.9	144.3
L-SDA3-50g/L	1.39	15.1	142	241.8	70.9
L-SDA3-75g/L	1.27	40.4	258	340.8	32.3
L-SDA4-50g/L	1.29	36.3	117	219.5	87.6
L-SDA4-75g/L	1.28	38.8	112	340.8	203.2

Table 3-7. Temperature at which each organic template lost 5% mass (T_5) and 95% mass (T_{95}) determined by TGA.

Amphiphile	T_5 (ºC)	T_{95} (ºC)
SDA1	180	334
SDA2	217	440
SDA3	177	267
SDA4	203	320

Figure 3-7 shows the AFM phase images of the coatings obtained from L-sols with 50 g/L of different surfactants. Coatings deposited from SDA1-, SDA3- and SDA4-sols showed crack free surface and homogeneously distributed voids. The surface of all exhibited the convex shaped particulate matter type according to the above description. Furthermore, the coating derived from SDA3-sol showed mesostructured porosity since grains were ordered showing a fingerprint structure. SDA1 and SDA4 coatings did not show any mesostructure. Regarding the particulate matter size, in this case SDA1 and SDA3 amphiphiles triggered the formation of surface with convex grains of around 8±2 nm, while those formed through SDA4 were slight bigger, around 10±2 nm. The coating obtained with SDA2-sol presented some inhomogeneities, like different grain sized grains and aggregates. The lower roughness was obtained in coatings assisted by SDA1 and SDA4, with R_q 0.9 nm and 1.2 nm, respectively. The highest roughness values arrived up to 3 nm for SDA3 mesostructured coating, and 4.6 nm for SDA2 inhomogeneous coating.

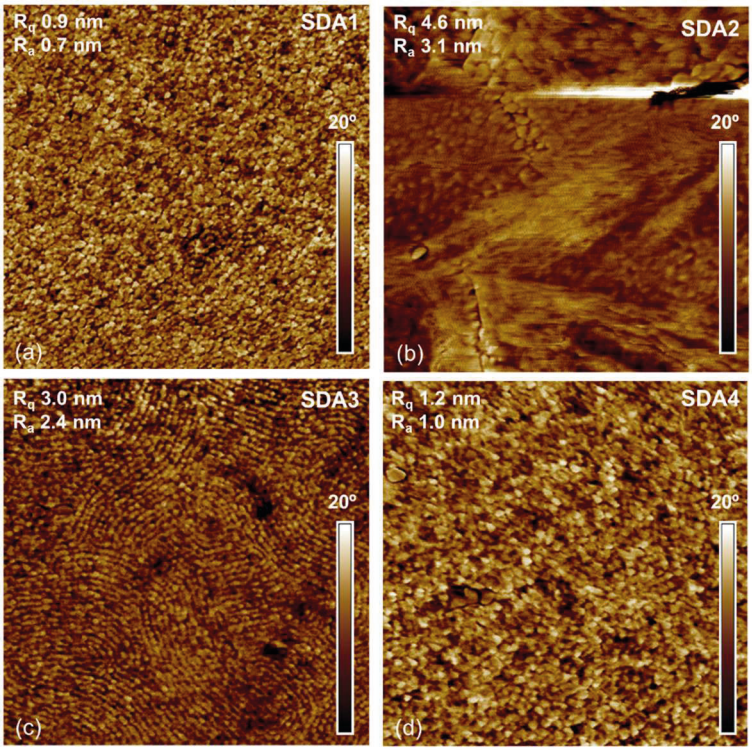

Figure 3-7. AFM phase images (1 μm x 1 μm) of coatings obtained from L-sols with 50 g/L of SDA1 (a), SDA2 (b), SDA3(c) and SDA4 (d).

3.6.4. Antireflective properties

Transmittance and reflectance spectra of bare and double side coated low iron glass with L-sols prepared with surfactant concentration of 50 and 75 g/L are represented in Figure 3-8. It was clearly observed that both spectra were consistent for each coating, showing corresponding maxima and minima at equal wavelengths. Analysis of the spectra showed that maximum values in transmittance spectra were settled in the 550-600 nm range for coatings deposited with SDA1-, SDA2- and SDA4-sols. Within this range, when increasing surfactant concentration from 50 to 75 g/L, the maximum of SDA1- and SDA2-sols derived coatings, was slightly shifted from lower to higher wavelengths, while the maximum in coatings with SDA4-sol did not vary. These results were related to the obtained variation in the coating thickness. In the case of SDA3-sols derived coatings which presented the highest thickness values, the maxima were around 700 and 1370 nm for 50 and 75 g/L of surfactant, respectively.

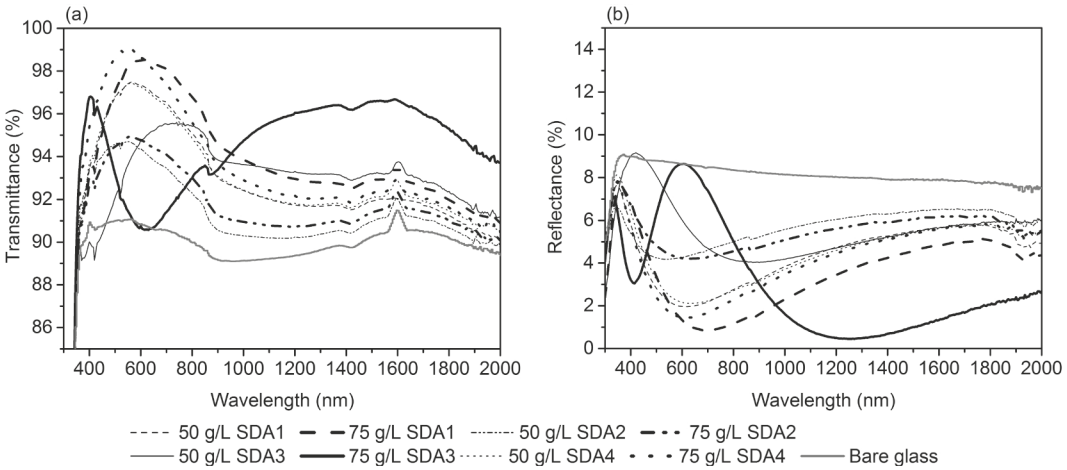

Figure 3-8. Transmittance (a) and reflectance (b) spectra of low iron float glass coated on both sides with R_w4 and L-sols.

Nonetheless, higher transmittance/lower reflectance integrated values along the whole spectrum were clearly obtained for coatings deposited with SDA1- and SDA4-sols. Integrated values calculated in the 300-2000 nm spectral range are compiled in Table 3-8. Attending to these, coatings deposited with both SDA1-sols showed the best results. Particularly, the sol with 75 g/L of SDA1 allowed preparing the porous coating with proper thickness and refractive index which permitted to obtain the highest reflection reduction among the mono-layers studied (as low as 2.7%) being 68% (M) lower than bare low iron float glass. Consequently, the gain in transmittance over bare low iron float glass was 6%.

Table 3-8. Integrated transmittance (τ) and reflectance (ρ) values between 300-2000 nm of coatings obtained from L-sols on both sides of low iron float glass 4 mm thick; gain (G) and reduction (M) over bare glass.

Reference	τ (%)	G (%)	ρ (%)	M (%)
Bare glass	90.1		8.4	
L-SDA1-50g/L	94.5	4.9	3.4	-59.1
L-SDA1-75g/L	95.6	6.0	2.7	-68.1
L-SDA2-50g/L	92.4	2.5	5.1	-39.9
L-SDA2-75g/L	92.7	2.9	5.0	-40.5
L-SDA3-50g/L	93.5	3.7	5.7	-32.1
L-SDA3-75g/L	93.3	3.6	4.7	-44.0
L-SDA4-50g/L	94.5	4.9	3.6	-57.8
L-SDA4-75g/L	95.5	6.0	3.1	-63.4

3.7. Porous silica coating by optimization of water content in acid-catalyzed sol-gel method

3.7.1. Effect of SDA concentration on thickness and refractive index of coatings

Following the same procedure as H-sols prepared with R_w4, sols prepared at R_w8 conditions containing different weight concentration of the four different SDAs were also analyzed by ellipsometry. The four types of organic/inorganic systems were scanned following the porosity-thickness tandem (50% - 120 nm). Thickness and refractive index obtained by ellipsometric data and fitted by Cauchy model [27] are represented in Figure 3-9a and Figure 3-9b, respectively. The apparent porosity resulting from Bruggeman fitting [28] is graphed in Figure 3-9c. The coating obtained from 150 g/L SDA2-sol was not homogeneous and transparent, therefore it was not possible to fit the ellipsometric parameters in this case.

Coating thickness increased as a function of SDA concentration as predicted by viscosity measurements. Coating without SDA presented a 129 nm thickness. The thickness of the coatings based on SDA1- and SDA4-sols expanded from around 170 nm for 25 g/L SDA concentration to around 300 nm for 150 g/L SDA concentration. Additionally, the thickness of the coatings based on SDA3-sols expanded from around 200 nm to almost 1000 nm, for the same increasing SDA concentration. An exception was found for coatings based on SDA2,

since they did not present the expected thickness increase, as it occurred at R_w4 conditions. Regarding the nature of the organic templates, while SDA2 is a low weight cationic surfactant, SDA1, SDA3 and SDA4 are block copolymers. Therefore, since the weight concentration was the same in all the formulations, the molar ratio SDA/TEOS became different. In the case of SDA2, it seems that the molar ratio needed to obtain the highest coating expansion was around the lower concentrations used in the preparation of these sol formulations. According to the surfactant-ethanol-water phase diagram, several nanocomposite architectures [26][4] can be achieved thanks to a successful combination of sol-gel and self-assembly approaches. Each of the obtained micelle architecture, such as lamellar, cubic or hexagonal shall present different packing density and therefore a different film expansion. Some works [36] have compared the self-assembly characteristics of block copolymers and the low weight cationic surfactants, and several differences have been established such as the use of block copolymers allowing to obtain more complex multiscale mesostructures, thicker pore walls and adjustable pore size.

In comparison to similar coatings synthesized with R_w4 (section 3.6), thickness values were similar for the corresponding SDA concentration. Despite the viscosity values of R_w8-sols were higher that with R_w4, this difference did not become detectable in terms of derived coating thickness.

H-sols with SDA1, SDA4 and SDA3 formed coatings with decreasing refractive index, with the exception of the coatings obtained with 100 g/L SDA1 and 50 g/L SDA4, that exhibited higher than expected values for such SDA concentration. The initial differences for low concentration SDA values were reduced as the concentration increased and the refractive index converged towards 1.23 similar value, with porosity being close to 50% for the maximum SDA concentration. For all concentration values tested, only coatings derived from SDA3-sols and R_w8 exhibited a slight increase of porosity with respect to the results corresponding to synthesis at R_w4.

Consistently with the obtained thickness values, coatings grown with the SDA2-sols showed the lowest refractive index values at lower concentration levels in comparison to other SDAs. However, they reached their minimum value at 50 g/L SDA concentration, while the sols with higher concentration did not form porous or homogeneous coatings.

Once again, the use of these coatings in AR multi-layer stacks would not be suitable. They require that the specific pairs of porosity-thickness values are jointly achieved, by finding the

conditions of sol preparation, given that the increase of porosity with SDA concentration was found to lead to thickness values outside the required range.

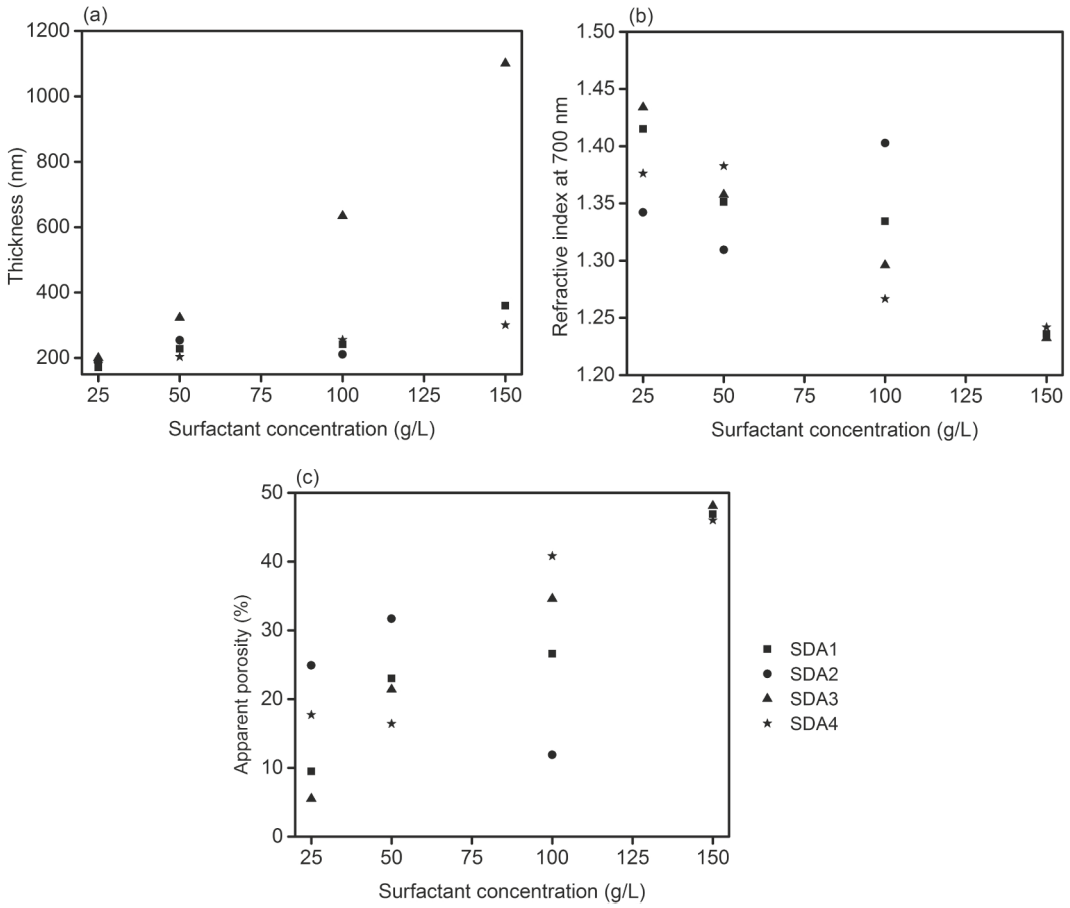

Figure 3-9. Effect of SDA concentration on thickness (a) refractive index (b) apparent and porosity (c) of coatings obtained from H-sols. (d ±0.5 nm; n ±0.001; apparent porosity ±0.2%).

3.7.2. Textural properties

Surfaces of the coatings grown with H-sols prepared at R_w8, with 50 g/L of different amphiphiles as well as H-sol with no surfactant content are presented in Figure 3-10. The surface of the coatings prepared at this R_w condition with SDAs was also crack free, homogenous and composed of small grains without any particular order, formed by convex shaped particulate matter in the case of SDA2, SDA3 and SDA4 coatings, and by concave cavities in the case of SDA1-coating. However, the surface of the coating prepared without SDA was totally different. In this case, the morphology was compact, without grains, holes or pores. Nevertheless, non-smooth surface was found, with white zones throughout the surface

corresponding to differences in height which may come from agglomeration. The reason behind this was likely related to differences in solvent evaporation rates, (co-existence of ethanol and a relatively high quantity of water) during the sintering step due to the high quantity of unreacted water in this sol. However, the roughness R_q exhibited by this surface was as low as 0.4 nm.

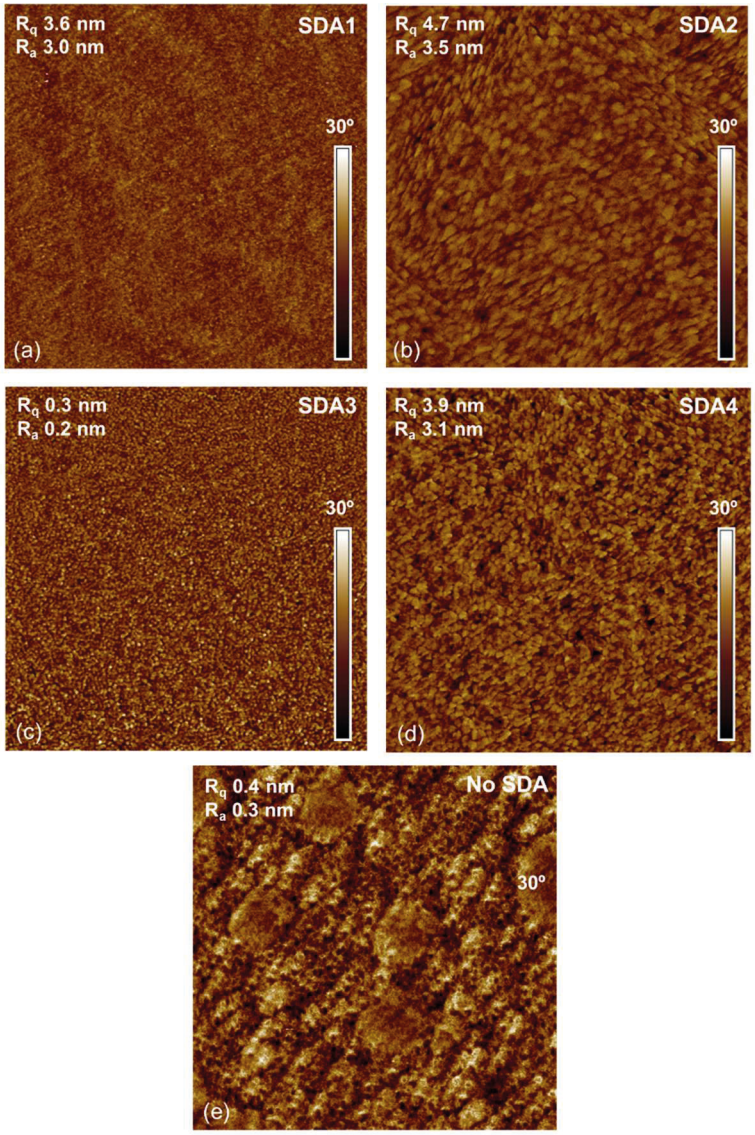

Figure 3-10. AFM phase images (1 μm x 1 μm) of coatings obtained from R_w8 H-sols with 50 g/L of SDA1 (a), SDA2 (b), SDA3 (c), SDA4 (d) and without SDA (e).

Regarding the porous coatings, some differences were found related to grain size and shape with respect to the same coatings prepared at R_w4. The similar appearance between SDA1 and

SDA4-coatings prepared at R_w4 conditions, diverged herein in the case of their counterparts prepared at R_w8 conditions. Specially the grain size of the coating prepared with SDA1-sol was drastically diminished from ~12 nm (at R_w4 conditions) to low values that were not possible to measure (at R_w8 conditions). Furthermore, some white points related to differences in height were eliminated, as well as in the coating with SDA4-sol. In that case, the grain size was maintained in the same order when comparing the same coatings synthesized at R_w4 and R_w8 conditions. In the case of SDA2, the coating prepared at R_w8 conditions, was formed by higher grains around 14±2 nm, and SDA3-coating, although maintained the particulate matter size, the morphology changed from concave cavities at R_w4 to convex grains at R_w8. In general, these ethanol-water-SDA systems gave more homogeneous coatings in morphology, although roughness values were higher than their R_w4 counterparts. An extremely low roughness was exhibited by SDA3-coating, with R_q around 0.3 nm, however, SDA1, SDA4 and SDA2-coatings revealed higher values of R_q 3.6, 3.9 and 4.7 nm, respectively.

3.7.3. Effect of inorganic precursor and SDA concentration on thickness, refractive index and thermal shrinkage of coatings

In order to obtain coatings with proper porosity-thickness tandem values to prepare highly performing AR coatings, the SiO_2 concentration in the sols was adjusted. H-sols prepared with 100 and 150 g/L of SDA were mixed with ethanol in an equal volume ratio to obtain L-sols. The viscosity of sols remained stable at least after 6 months since its preparation. The optical constants of the coatings prepared with these sols were characterized by ellipsometry and their final porosity, together with the corresponding thickness before and after sintering was obtained by BEMA [28] and Cauchy [27] fitting as shown in Table 3-9. These results led to conclude that thickness increased with SDA concentration, also corresponding with a decrease of refractive index (and consequently an increase of porosity). However, the difference in final thickness (after sintering) of the coatings prepared with 50 and 75 g/L of SDAs was only slight in comparison to the thickness difference observed between coatings prepared with 50 and 75 g/L of SDAs before sintering. Therefore, the material contraction of the coatings prepared with 75 g/L of SDA was higher than those prepared with 50 g/L of SDA.

Table 3-9. Refractive index (n) at 700 nm, apparent porosity, thickness of sintered coatings (d) and before sintering (d_{raw}) obtained from L-sols by spectral ellipsometry.

Coating	n (at 700 nm)	Apparent porosity (%)	d (nm)	d_{raw} (nm)	% shrinkage
L-SDA1-50g/L	1.34	25.6	95.3	192.9	102.4
L-SDA1-75g/L	1.24	45.7	111.3	371.7	234.0
L-SDA2-50g/L	1.39	14.0	76.9	151.8	97.4
L-SDA2-75g/L	1.38	16.1	78.5	244.5	211.5
L-SDA3-50g/L	1.31	31.7	178.3	252.8	41.8
L-SDA3-75g/L	1.22	50.3	278.5	417.2	49.8
L-SDA4-50g/L	1.24	44.4	102.4	188.0	83.6
L-SDA4-75g/L	1.28	36.6	104.0	311.6	199.6

The increase of SDA3 and SDA1 concentration (from 50 to 75 g/L) provoked the largest effect on thickness and porosity of the coatings. Sols with increasing SDA3 concentration produced coatings with decreasing refractive index and increasing thickness values. SDA2-sols formed similar coatings in terms of thickness and porosity, while SDA4-sol with higher SDA quantity did not result in higher porosity in the formed coatings. In most cases, sols with R_w8 led to coatings with lower refractive index and lower thickness when compared to sols with R_w4. Therefore, higher R_w values during sol preparation allowed to achieve coatings with higher porosity and lower thickness. Water plays a relevant role in the hydrolysis and condensations steps. Excess water condensates within the sols and contributes to their dilution resulting in growing of thinner coatings.

More balanced joint thickness-porosity values were achieved with L-sol containing 75g/L of SDA1, which made it the most suitable coating to achieve the highest transmittance values.

AFM phase images of the coatings obtained from L-sols at R_w8 conditions with 50 g/L of the tested amphiphiles are shown in Figure 3-11. SDA3 and SDA4 amphiphiles induced the formation of homogenous surfaces formed by convex particulate matter of grain size around 7-9 nm. It can be concluded that SDA3 amphiphile induced the formation of the same grain size independently on sol-gel synthesis conditions proved herein. Once more again, SDA2-sol with high content of ethanol did not formed homogenous coatings.

However, the most startling case was the coating formed with SDA1-sol. At these conditions of water and ethanol content, the coating showed a compact morphology not formed by grains

and voids. This situation was continuously repeated at these synthesis conditions, and consistently supported by ellipsometry results. It was concluded that these conditions of inorganic and micelles concentration and the ratio between solvents promoted a highly packed structure induced by SDA1 self-assembly during coating formation.

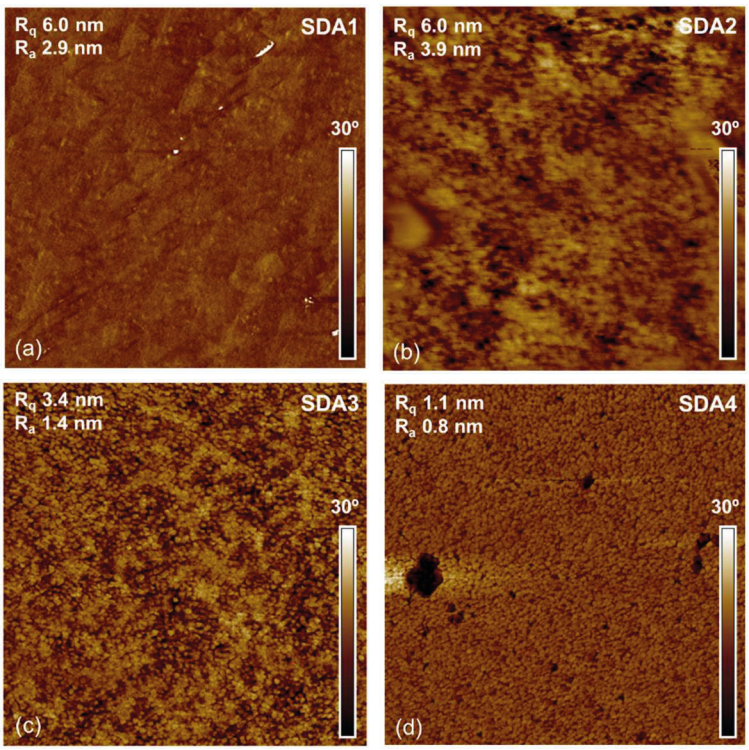

Figure 3-11. AFM phase images (1 μm x 1 μm) of coatings obtained from L-sols with 50 g/L of SDA1 (a), SDA2 (b), SDA3(c) and SDA4 (d).

3.7.4. Antirreflective properties

Transmittance and reflectance spectra of bare and double side coated low iron glass with L-sols prepared at R_w8 and amphiphile concentration of 50 and 75 g/L are showed in Figure 3-12. It was clearly observed that both spectra were consistent for each coating, showing corresponding maxima and minima at equal wavelengths. Analysis of the spectra showed that maximum values in transmittance spectra were settled in the range 505-565 nm for coatings deposited with SDA1-, SDA2- and SDA4-sols, being located displaced towards lower wavelength if compared with same coatings prepared with R_w4. This fact was totally in accordance with the slightly lower values of thickness for coatings grown with sols formulated at R_w8. Given that all coating thickness prepared with R_w8 were slightly higher as amphiphile

concentration increased from 50 to 75 g/l, transmittance maximum location was slightly shifted from lower to higher wavelength.

SDA3-sols gave coatings slightly thicker, and the transmittance maximum were located towards higher wavelengths, around 830 nm and 1380 nm for 50 and 75 g/L of surfactant, respectively.

In parallel to spectrophotometry data obtained for coatings grown at R_w4 conditions, higher transmittance/lower reflectance integrated values along the whole spectrum were obtained for coatings deposited from SDA1- and SDA4-sols, as observed in Table 3-10.

Particularly, the sol with 75 g/L of SDA1 prepared at R_w8 led to an improvement of the optical properties obtained at R_w4 conditions. The proper tandem refractive index-thickness achieved, permitted to obtain the highest optical transmission up to 96%, offering a gain over bare glass of 6.5% over the 6% that was obtained at R_w4 conditions. Consequently, the highest reflection reduction obtained was as low as 2.5% in the 300-2000 nm range, and thus a reduction (M) of bare glass reflectance from 68 to 70.4% for R_w4 and R_w8, respectively.

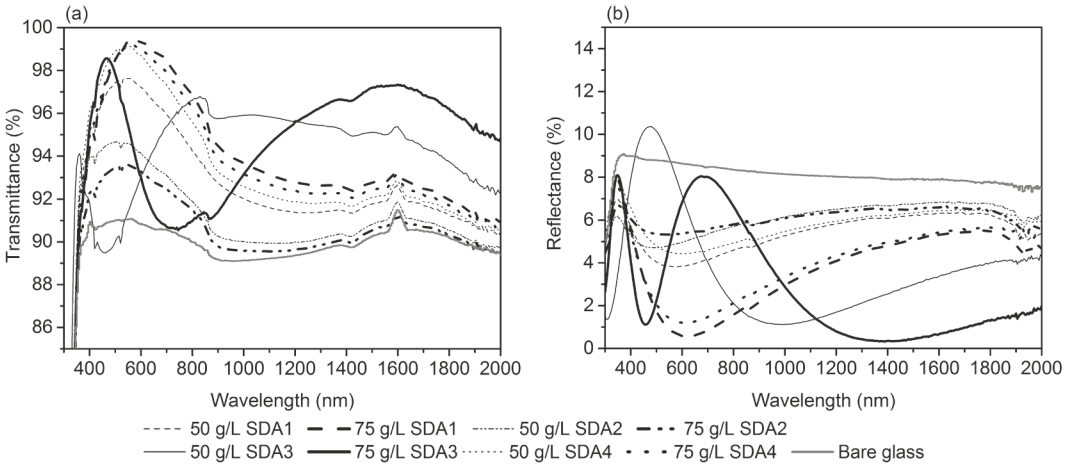

Figure 3-12. Transmittance (a) and reflectance (b) spectra of low iron float glass coated on both sides with R_w8 and L-sols.

Table 3-10. Integrated transmittance (τ) and reflectance (ρ) values between 300-2000 nm of the coatings obtained from L-sols on both sides of low iron float glass 4 mm thick; gain (G) and reduction (M) over bare glass.

Reference	τ (%)	G (%)	ρ (%)	M (%)
Bare glass	90.1		8.4	
L-SDA1-50g/L	94.5	4.8	4.8	-43.0
L-SDA1-75g/L	96.0	6.5	2.5	-70.4
L-SDA2-50g/L	92.2	2.4	5.6	-33.5
L-SDA2-75g/L	91.5	1.5	5.8	-30.8
L-SDA3-50g/L	93.9	4.2	4.8	-42.8
L-SDA3-75g/L	93.8	4.1	4.3	-48.8
L-SDA4-50g/L	95.5	6.0	5.2	-37.6
L-SDA4-75g/L	95.7	6.2	2.9	-65.9

3.8. Optimized process and coating

An ultimate optimization of the formulation was accomplished in which SDA1 and R_{Et} were accurately adjusted to 78 g/L concentration in order to deposit coatings with thickness between 120-130 nm and 50% apparent porosity. The formulations studied at this stage are those corresponding to Table 3-3.

The viscosity of the sols prepared with R_w8 and this optimized R_{Et}, with and without SDA1, was monitored up to one year. The results are represented in Figure 3-13. It was revealed that sols with R_w8 and the corresponding R_{Et} were very stable and independent of the presence of SDA1, which is very promising for the implementation and scaling up of the process.

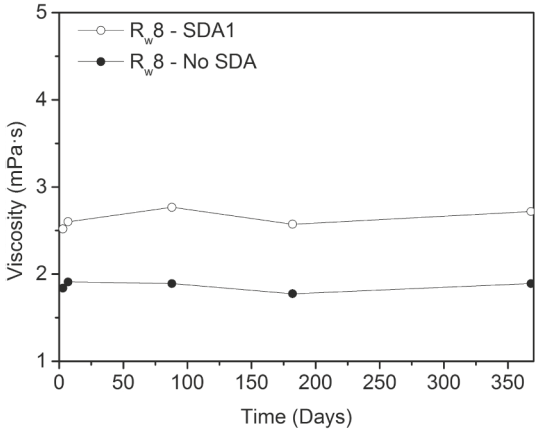

Figure 3-13. Dynamic viscosity in the function of time for final sols prepared with and without SDA1. (Standard deviation < 0.05 mPa·s).

This sol formulation allowed to grow coatings with 50% porosity, refractive index 1.22 at 700 nm and 125-130 nm thick sintered at 350 and 550 ºC during 1 h. Two considerably different temperatures were chosen in order to sinter the coatings, with the purpose of establishing the minimum sintering temperature that ensures compliance with the durability requirements of photovoltaic standards [37]. On the one hand, 350 ºC was chosen as the minimum temperature at which SDA is expected to be totally decomposed. On the other hand, 550 ºC was used as higher temperature since at this temperature the silica network was expected to be a more thermodynamically stable and a relaxed structure can be achieved [38].

The porosimetry of single coatings sintered at 350 and 550 ºC was analyzed by EEP, which provides the amount of adsorptive (water) inside pores from the variation of the optical characteristics of the coatings (thickness and refractive index), measured at several water partial pressures. Adsorption-desorption curves for coatings sintered at 350 and 550 ºC and their respective pore size distribution are displayed in Figure 3-14a and Figure 3-14b, respectively. The coatings showed the typical behavior of mesoporous materials associated with type IV-V isotherms, according to IUPAC classification of adsorption isotherms of porous materials. The main difference between them was the related hysteresis loops, whose shape can be correlated to the texture (e.g., pore size distribution, pore geometry, and connectivity) of the mesoporous material [32]. The adsorption hysteresis of type IV-V isotherms is in turn classified by IUPAC in four types (H1-H4) of curves. The studied coatings may be identified as H1 type, shaped by parallel branches and associated to well-defined cylindrical-like pore channels or agglomerates of approximately uniform spheres as explained in section 3.6.2. Although the volume of pores was similar for coatings sintered at both temperatures, ~47%, several differences were found between their isotherms. With the increasing of RH, little adsorption was observed up to capillary adsorption zone, which is characterized by a steep increase of adsorbed volume, detected at 55 and 66% RH for coatings sintered at 350 and 550 ºC, respectively. During capillary desorption, the decrease of the adsorbed water happened at RH around 53% and around 58% for coatings sintered at 350 and 550 ºC, respectively. The effect of the capillary adsorption taking place at different RH values can be a consequence of different water-on-silica wetting angles. Differences among adsorption-desorption branches are associated to the difference in the radius of curvature of condensed liquid meniscus during the adsorption and desorption processes in the mesopores [31]. Water contact angle measurements confirmed the difference in the relative strength of fluid-wall for coatings

sintered at two temperatures. Coatings sintered at 350 ºC showed 32.3±0.6º if prepared without SDA and 16.6±1.1º if prepared with SDA1. Coatings sintered at 550 ºC showed higher $\theta_c^{H_2O}$, which can be related to the loss of free hydroxy groups being 48.8±1.4º for the coating prepared without SDA, while 19.5±1.4º was found for the coating with SDA1 content.

Pore size distribution was determined using modified Kelvin's equation [33] and the corresponding results are included in Figure 3-14. The coatings showed a narrow pore size distribution with maximum at 8-9 nm for both coatings.

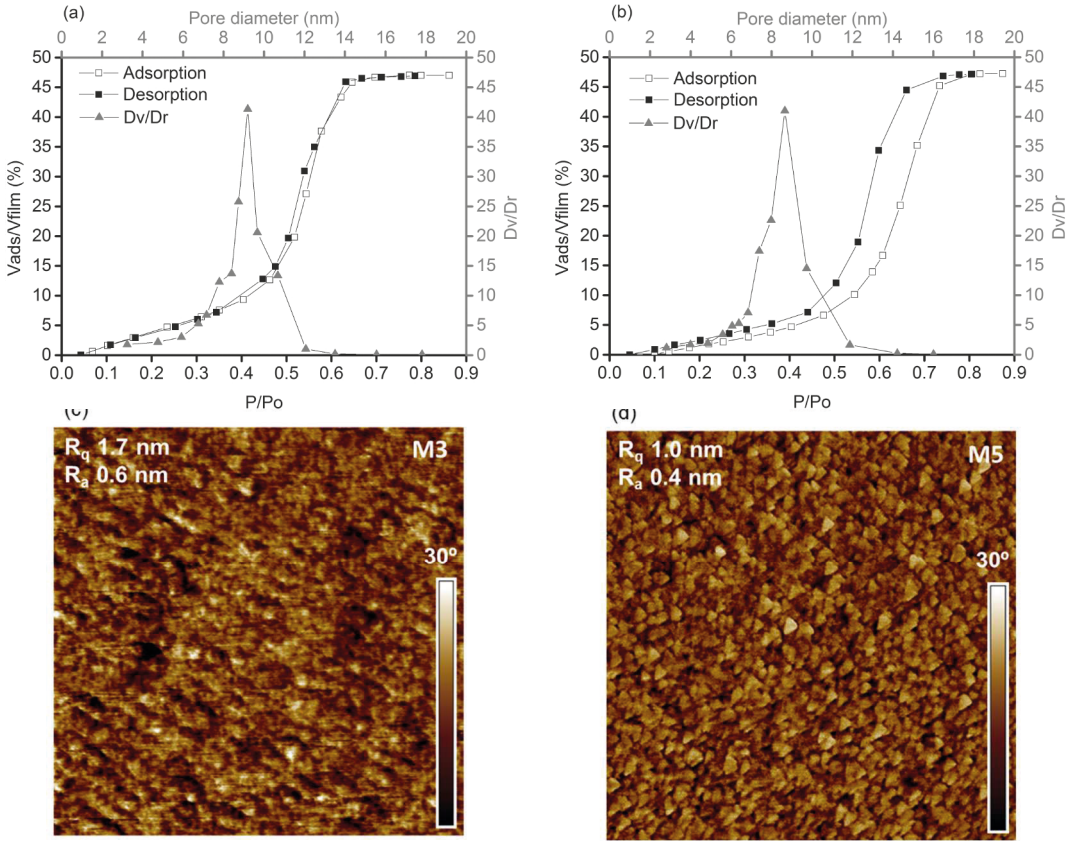

Figure 3-14. Adsorption/desorption isotherm and pore size distribution of optimized coatings sintered at 350 ºC (a) and 550 ºC (b) and AFM phase images (1 μm x 1 μm) of surface coatings sintered at 350 ºC (c) and 550 ºC (d).

The porous structure of the coating was confirmed by AFM measurements, as showed in the surface images of the coatings sintered at 350 and 550 ºC in Figure 3-14. The surfaces of porous coatings sintered at two temperatures were homogeneous and did not present any crack. In both cases, the topography of the porous coatings was composed of small grains of convex particulate matter in which no particular order was detected. The size of these grains

was 12±3 nm for the coating sintered at 350 ºC and 7±2 nm for the coating sintered at 550 ºC, which can be related to the high shrinkage due to the higher temperature. Moreover, these grains were comparable in size to the pore size obtained by EEP. Differences in the topography of the coatings were observed since grains in the coating sintered at 550 ºC were packed closer and even connected to each other if compared with the coating sintered at 350 ºC. This result was also consistent with the pore size obtained by EEP, which was somewhat smaller for the coating sintered at 550 ºC (compare surface images in the Figure 3-14a and Figure 3-14b). The low roughness values indicated that surfaces of both coatings were highly smooth.

These latter coatings deposited from the optimized sol with SDA1, were used to build the AR mono- and the bi-layer stacks, also prepared at two sintering temperatures.

The inner layers of the bi-layer stacks were grown from H-sol and R_w4. In order to prevent degradation of the glass and the external AR porous coating, the inner coating of the stack was designed to exhibit a dense structure, aimed to act as alkali diffusion-preventing-layer, with refractive index at 700 nm between 1.42-1.45 and thickness between 115-130 nm.

Figure 3-15 shows the transmittance and reflectance spectra of an AR mono-layer stack prepared from SDA1-containing sol and an AR bi-layer stack with inner coating obtained from no-SDA sol deposition and R_w4, sequentially followed by outer coating deposition from optimized SDA1-containing sol and R_w8, since this promoted the searched 50% apparent porosity as explained above in this section. The differences in coating morphology, optical constants and porosity between porous coatings grown over the inner dense-structured layer or directly on glass, will be discussed in Chapter 4.

Table 3-11. Integrated transmittance (τ) and reflectance (ρ) values between 300-2000 nm of AR mono- and bi-layer stack deposited on both sides of low iron float glass 4 mm thick and sintered at 350 ºC and 550 ºC; gain (G) and minimization (M) over bare glass.

Reference	τ (%)	G (%)	ρ (%)	M (%)
Bare glass	90.1	-	8.4	-
Mono-layer 350 ºC	96.3	6.8	2.5	70.9
Bi-layer 350 ºC	96.4	7.0	2.0	76.5
Mono-layer 550 ºC	95.6	6.1	2.5	68.3
Bi-layer 550 ºC	96.6	7.2	2.1	75.0

Integrated transmittance in the 300-2000 nm wavelength range gave higher values for the mono-layer treated at 350 ºC than the mono-layer treated at 550 ºC, while and inverse trend was found for bi-layers stacks. The highest value obtained for AR mono-layer was 96.3% while it increased to 96.6% for the bi-layer stack. Thus, a 6.8 and 7.2% increase over bare glass transmittance (90.1%) was respectively achieved, while reflectance values were 2.5% for the mono-layer and 2.0% for the bi-layer stack. The tendency differences among stacks sintered at both temperatures, come from the differences in the external porous coating structure, porosity and grain size, depending on if it is grown on dense-structured coating or directly on glass as it will be explained in the Chapter 4.

The combination of the two layers permitted to obtain higher values in the 1000- 2000 nm NIR spectral range, providing broadband AR properties. This broadband performance ideally matches with the spectral response of the multi-junction solar cells used in CPV modules.

The comparison with previously reported works is not as straightforward as might be expected, since most of them are focused on the design of porous mono-layers, and there is no uniformity in the studied wavelength ranges and the type of glass substrate. Coatings with similar refractive index were obtained by Liu et al. [39], who prepared antireflective porous coatings by base-catalysis instead, and reported transmittance spectra only between 400-800 nm, similarly to other works that used an acid-catalyzed TEOS and cationic amphiphile approach [5][6] and did not report either porosimetry or refractive index data. Therefore, no works based merely on acid-catalyzed TEOS and amphiphile approach producing coatings with a thoroughly tailored porosity have been reported for this application. Among the works that have studied silica multi-layer stacks, several focused on stacks formed by an acid-catalyzed derived inner coating and a base-catalyzed external layer [19][40]. Other works [7] developed two porous layers with different amounts of surfactant, however non comparable, narrower transmittance spectra and different properties to those found herein were reported.

As mentioned before, besides the broadband AR property, the use of a bi-layer stack system could have another benefit related to reliability and durability. The sodium, calcium, potassium, magnesium content in the composition of most float glass products can diffuse out of the glass when it is used for an extended period of time, leading to a decrement of the optical properties [41]. This hypothesis needs to be confirmed under reliability test and research work done on this subject will be discussed in the Chapter 4.

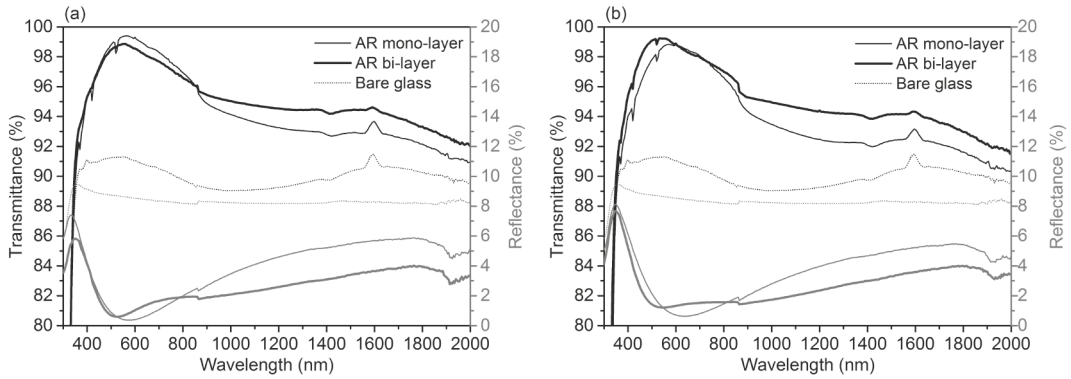

Figure 3-15. Transmittance and reflectance spectra of mono- and bi-layer AR stacks sintered at 350 ºC (a) and 550 ºC (b).

3.9. Conclusions

Sol-gel synthesis via acid catalysis and evaporation-induced self-assembly methods allowed to achieve mesostructured porous coatings with a high control of the void fraction. The scanning of four types of organic/inorganic systems and the optimization of the water/alkoxide ratio were adjusted to correlate the theoretical design with experimental results. Therefore, sol formulations were adapted to fulfill specific thickness, porosity and optical constants (n, κ) and in parallel, a high sol stability was searched.

The final AR layer stack was formed by an inner coating deposited from H-sol and R_w4 that exhibited dense structure, thickness in the 115-130 nm range and refractive index between 1.42-1.45 at 700 nm. The optimized external coating was derived from the L-sol at R_w8 conditions with 78 g/L of di-block copolymer SDA1, showing porous structure, thickness in the 120-130 nm range and 1.22 refractive index at 700 nm. Those values were close to the targets calculated by CODE software as the ideal ones for the achievement of optimal optical configuration of the AR layer stack. The optical transmittance gained up to 7.2% over bare glass in the wavelength range where multi-junction cells are active (300-2000 nm).

The enhancement in the optical performance due to the developed AR coatings can be considered outstanding from the point of view of PV applications and the results are even more promising considering the fact that the coating material was synthesized by acid-catalysis since this process is capable to settle coatings with robust mechanical properties and a very good adhesion. The bi-layer architecture was conceived with the aim to provide both a transmittance enhancement over a wider region of the solar spectrum and the capability to

withstand harsh outdoor conditions (very common in the geographical regions where CPV modules are placed).

In parallel, excellent results on sol stability were attained since the developed sols proved to be stable for at least one year. This fact contributes to provide a simple up-scaling and highly efficient process for implementation of AR layer stacks in PV applications.

References

[1] M. Dubois, B. Cabane, Light-scattering study of the sol-gel transition in silicon tetraethoxide, Macromolecules. 22 (1989) 2526–2533.

[2] J.C. Brinker, Hydrolysis and condensation of silicates: effects on structure, J. Non. Cryst. Solids. 100 (1988) 31–50.

[3] T. Asefa, M.J. MacLachlan, N. Coombs, G.A. Ozin, Periodic mesoporous organosilicas with organic groups inside the channel walls, Nature. 402 (1999) 867–871.

[4] J.C. Brinker, Y. Lu, A. Sellinger, H. Fan, Evaporation-induced self-assembly: nanostructures made easy, Adv. Mater. 11 (1999) 579–585.

[5] X. Meng, Y. Wang, H. Wang, J. Zhong, R. Chen, Preparation of hydrophobic and abrasion-resistant silica antireflective coatings by using a cationic surfactant to regulate surface morphologies, Sol. Energy. 101 (2014) 283–290.

[6] Y. Xu, C. Peng, C. Xin, J. Wu, Preparation of silica antireflective films for solar energy application, Mater. Lett. 94 (2013) 89–91.

[7] Y. Li, H. Lv, L. Ye, L. Yan, Y. Zhang, B. Xia, H. Yan, B. Jiang, Preparation of porous silica films in a binary template system for double-layer broadband antireflective coatings, RSC Adv. 5 (2015) 20365–20370.

[8] T.-J. Ha, H.-H. Park, S.-B. Jung, H. Ryu, B.-G. Yu, Investigation of the effect of calcination temperature on HMDS-treated ordered mesoporous silica film., J. Colloid Interface Sci. 326 (2008) 186–190.

[9] G.S. Vicente, R. Bayón, A. Morales, Effect of additives on the durability and properties of antireflective films for solar glass covers, J. Sol. Energy Eng. 130 (2008) 011007.

[10] G. San Vicente, R. Bayón, N. Germán, A. Morales, Surface modification of porous antireflective coatings for solar glass covers, Sol. Energy. 85 (2011) 676–680.

[11] G. San Vicente, R. Bayón, N. Germán, A. Morales, Long-term durability of sol-gel porous coatings for solar glass covers, Thin Solid Films. 517 (2009) 3157–3160.

[12] H.L. Yang, L. Hao, J.N. Wang, Z.N. Zhang, X.P. Liu, L.J. Jiang, Self-cleaning and antireflective films for all-glass evacuated tube solar collectors, Energy Procedia. (2015) 226–232.

[13] D.B. Mahadik, R.V. Lakshmi, H.C. Barshilia, High performance single layer nano-porous antireflection coatings on glass by sol-gel process for solar energy applications, Sol. Energy Mater. Sol. Cells. 140 (2015) 61–68.

[14] R. Prado, G. Beobide, A. Marcaide, J. Goikoetxea, A. Aranzabe, Development of multifunctional sol-gel coatings: Anti-reflection coatings with enhanced self-cleaning capacity, Sol. Energy Mater. Sol. Cells. 94 (2010) 1081–1088.

[15] M. Faustini, L. Nicole, C. Boissière, P. Innocenzi, C. Sanchez, D. Grosso, Hydrophobic, antireflective, self-cleaning, and antifogging sol-gel coatings: An example of multifunctional nanostructured materials for photovoltaic cells, Chem. Mater. 22 (2010) 4406–4413.

[16] L. Miao, L.F. Su, S. Tanemura, C.A.J. Fisher, L.L. Zhao, Q. Liang, G. Xu, Cost-effective nanoporous SiO_2-TiO_2 coatings on glass substrates with antireflective and self-cleaning properties, Appl. Energy. 112 (2013) 1198–1205.

[17] J.J. van Beek, D. Seykens, J.B.H. Jansen, R.D. Schuiling, Incipient polymerization of SiO_2 in acid-catalyzed TMOS sol-gel systems with molar water/alkoxide ratio between 0.5 and 32, J. Non. Cryst. Solids. 134 (1991) 14–22.

[18] X. Wang, J. Shen, Sol-gel derived durable antireflective coating for solar glass, J. Sol-Gel Sci. Technol. 53 (2010) 322–327.

[19] X. Li, J. Shen, A scratch-resistant and hydrophobic broadband antireflective coating by sol-gel method, Thin Solid Films. 519 (2011) 6236–6240.

[20] H. Ye, X. Zhang, Y. Zhang, L. Ye, B. Xiao, H. Lv, B. Jiang, Preparation of antireflective coatings with high transmittance and enhanced abrasion-resistance by a base/acid two-step catalyzed sol-gel process, Sol. Energy Mater. Sol. Cells. 95 (2011) 2347–2351.

[21] W. Theiss Hard- and software, (n.d.). http://www.mtheiss.com/.

[22] S. Van Riesen, M. Neubauer, A. Boos, M.M. Rico, C. Gourdel, S. Wanka, R. Krause, P. Guernard, A. Gombert, New module design with 4-junction solar cells for high efficiencies, AIP Conf. Proc. 1679 (2015).
[23] W. Vogelsberger, A. Seidel, T. Breyer, Kinetics of sol particle formation as a function of pH studied by viscosity measurements in silica solutions, Langmuir. 18 (2002) 3027–3033.
[24] K.W. Jang, S. Il Pyun, M.S. Jhon, The role of excess water in acidic sol-gel polymerization of tetraethoxysilane (TEOS) using molecular dynamics simulation, Mol. Simul. 29 (2003) 489–494.
[25] J.C. Pouxviel, J.P. Boilot, J.C. Beloeil, J.Y. Lallemand, NMR study of the sol/gel polymerization, J. Non. Cryst. Solids. 89 (1987) 345–360.
[26] D. Grosso, F. Cagnol, G.J.D.A.A. Soler-Illia, E.L. Crepaldi, H. Amenitsch, A. Brunet-Bruneau, A. Bourgeois, C. Sanchez, Fundamentals of mesostructuring through evaporation-induced self-assembly, Adv. Funct. Mater. 14 (2004) 309–322.
[27] A.L. Cauchy, Sur la réfraction et la réflexion de la lumière, Bull. Des Sci. Mathématiques. XIV (1830) 6–10.
[28] D.A.G. Bruggeman, Berechnung verschiedener physikalischer konstanten von heterogenen substanzen. I. Dielektrizitätskonstanten und leitfähigkeiten der mischkörper aus isotropen substanzen, Ann. Der Phys. 24 (1935) 636–664.
[29] L. Scriven, Physics and applications of dip coating and spin coating, MRS Proceedings, 121. (1988).
[30] L.D. Landau, B.G. Levich, Dragging of a liquid by a moving plate, Acta Phisicochim U.R.S.S. 17 (1942) 42–54.
[31] M.R. Baklanov, K.P. Mogilnikov, V.G. Polovinkin, F.N. Dultsev, Determination of pore size distribution in thin films by ellipsometric porosimetry, J. Vac. Sci. Technol. B. 18 (2000) 1385.
[32] Z.A. Alothman, A review: Fundamental aspects of silicate mesoporous materials, Materials (Basel). 5 (2012) 2874–2902.
[33] C. Boissière, D. Grosso, S. Lepoutre, L. Nicole, A.B. Bruneau, C. Sanchez, Porosity and mechanical properties of mesoporous thin films assessed by environmental ellipsometric porosimetry, Langmuir. 21 (2005) 12362–12371.
[34] M. Faustini, B. Louis, P.A. Albouy, M. Kuemmel, D. Grosso, Preparation of sol-gel films by dip-coating in extreme conditions, J. Phys. Chem. C. 114 (2010) 7637–7645.
[35] D. Kundu, H. Zhou, I. Honma, Thermally induced structural changes of lamellar and one-dimensional hexagonal mesoporous silica thin films, J. Mater. Sci. Lett. 17 (1998) 2089–2092.
[36] G.J.D.A.A. Soler-Illia, E.L. Crepaldi, D. Grosso, C. Sanchez, Block copolymer-templated mesoporous oxides, Curr. Opin. Colloid Interface Sci. 8 (2003) 109–126.
[37] IEC 62108 International Standard, Concentrator photovoltaic (CPV) modules and assemblies - Design qualification and type approval, 2016.
[38] J.C. Brinker, E.P. Roth, G.W. Scherer, D.R. Tallant, Structural evolution during the gel to glass conversion, J. Non. Cryst. Solids. 71 (1985) 171–185.
[39] B.T. Liu, W. De Yeh, Antireflective surface fabricated from colloidal silica nanoparticles, Colloids Surf. A Physicochem. Eng. Asp. 356 (2010) 145–149.
[40] Y. Zhang, F. Gao, L. Gao, L. Hou, Y. Jia, Study of tri-layer antireflection coatings prepared by sol-gel method, J. Sol-Gel Sci. Technol. 62 (2012) 134–139.
[41] M. Mizuhashi, Y. Gotoh, Glass body provided with an alkali diffusion-preventing silicon oxide layer, US4485146, 1984.

Chapter 4

Antireflective and hydrophobic layer stacks against soiling adherence

In this Chapter, the optimization of two different methods, i.e. methyl-silylating post-treatment and polyfluoroalkyl functionalization is accomplished to obtain AR coatings with low surface free energy. The main objective is to obtain coatings capable to contribute against soiling adherence of PV modules, without losing the AR properties.
Considering in addition other external factors that may alter the optical properties of the system when operating outdoors, such as harsh climate conditions and alkali diffusion from glass, several AR layer stack configurations have been proposed. The aim is to achieve the most rational design, based on a proper trade-off between cost-efficiency, processability, optical properties and reliability during real life operation. The assessment is based on (i) the analysis of the optical transmittance, reflectance and refractive index (ii) hydrophobicity and effect of water absorption on the external porous coatings (iii) mechanical properties and adhesion (iv) reliability under accelerated aging tests following photovoltaic standards.

The research work presented in this Chapter has resulted in the following publications:

C. Agustín-Sáenz, M. Machado, O. Zubillaga, A. Tercjak, Hydrophobic and spectrally broadband antireflective methyl-silylated silica coatings with high performance stability for concentrated solar applications, Sol. Energy Mater. Sol. Cells. 200 (2019) 109962

C. Agustín-Sáenz, M. Machado, A. Tercjak, Polyfluoroalkyl-silica porous coatings with high antireflection properties and low surface free energy for glass in solar energy application, Applied Surface Science, under revision

4.1. Introduction

Antireflective layer stacks have been prepared in Chapter 3 by an efficient and environment-friendly process, based on acid-catalyzed sol-gel process combined with EISA method, achieving promising optical properties for PV applications. These AR systems operate outdoors and must therefore be designed to assure durability of the high optical performance during their service-life.

As external factors that may alter the optical properties of the system when operating outdoors, mostly soiling, harsh climate conditions and alkali diffusion from glass have been identified. In this Chapter, several strategies to address those factors have been explored. Firstly, low surface energy properties compatible with AR performance have been targeted. This property has been implemented through two different routes: i) methyl-silylating post-treatment of porous coating (two-step process) and ii) formulation modification with low content of polyfluoroalkyl silicon alkoxides of different non-hydrolyzable fluoroalkyl chain lengths (one-step process).

Hexamethyl disilazane is a widely studied methyl-silylating agent that has been incorporated in porous silica coatings either as part of the sol composition [1–5] or as post-treatment of the grown coating by contact with HMDS vapor [6–8], immersion in solution composed by HMDS-hexane [9–12], HMDS-toluene [13–15] or HMDS-alcohol [1]. The best reported results of static water contact angle ($\theta_c^{H_2O}$) values are ~150º [1–4] when the HMDS is part of the sol, ~130º when HMDS is applied as post-treatment on coatings grown from base-catalyzed sols [12] and ~100º when HMDS is applied as post-treatment on coatings grown from acid-catalyzed sols [1,6,9].

On the other hand, there are several works that have combined polyfluoroalkyl alkoxysilanes in a sol-gel matrix with the aim to obtain super-liquid-repellent surfaces. Hikita et al. [16] synthetized a coating based on acid-catalyzed TEOS and (1H,1H,2H,2H-perfluorodecyl triethoxy) silane (FAS17), containing also commercial silica nanoparticles for surface roughness control. Nakajima et al. [17] prepared a bi-layer formed by an inner acid-catalyzed TEOS combined with acrylic polymer and external acid-catalyzed FAS17. In a similar way, Bharathibai et al. [18] prepared an inner layer based on TEOS and polydimethylsiloxane resins (PDMS) that was then sprayed with hydrolyzed and unhydrolyzed (1H,1H,2H,2H-perfluorooctyl) triethoxy silane (FAS13) sols. There are some patented sol formulations that

combine FAS and TEOS compounds with AR applications [19][20], but they do not use amphiphiles to induce the porosity in the coating, and they consider multi-step processes. Another patent [21] relates to a coating formed by metal alkoxide and FAS as a post-treatment of a previously deposited AR porous layer. In summary, to date, there are very limited studies in which the combination of FAS as precursors in sol-gel and EISA synthesis enable the tailoring of a highly antireflective and low surface energy coating for solar energy applications.

Apart from the effect of a methyl-silylating post-treatment on the SiO_2 porous coating and the addition of polyfluoroalkyl silanes to the sol formulation, the presence of the inner layer and the optimization of sintering temperature have been devised here in order to minimize soiling adherence and alkali diffusion from the glass substrate and to assure the required robustness to comply with the durability requirements.

In this Chapter, the optimization of porous and low surface energy SiO_2 through these two routes is presented. These coatings have been combined in different configurations of AR layer stacks. The final aim of this research work is focused on the achievement of the more rational AR design based on a proper trade-off between cost-efficiency, processability, optical properties and reliability during real life operation. The assessment has consisted of (i) an analysis of the optical transmittance, reflectance and refractive index (ii) hydrophobicity and effect of water absorption on the external porous coatings (iii) nanoindentation and nanoscratch analysis in relation to reciprocating abrasion test to assure the required robustness.

4.2. Characterization techniques

The characterization methods used in this Chapter are following outlined:

- The contact angle was determined by the static drop method, using Digidrop Contact Angle Meter (GBX Instruments). Ten measurements of the apparent contact angle were taken for different test liquids (water ($\theta_c^{H_2O}$), methanol (θ_c^{MeOH}), ethanol (θ_c^{EtOH}), and hexadecane ($\theta_c^{C_{16}H_{34}}$) by placing drops of each liquid on the horizontal and flat coating surface and measuring the angle at the liquid-solid-air boundary. Surface free energy was calculated using the averaged contact angle values by Owens-Wendt method [22].
- The surface of the investigated coatings was analyzed using the AFM, Multimode 8 from Bruker with a Nanoscope V controller.

- Ellipsometric parameters Ψ and Δ were recorded by variable angle spectroscopic ellipsometer (M-2000UTM, J.A. Co., Woollam). Spectra were recorded in dry conditions from 250 to 1000 nm at three incidence angles, chosen closely above and below Brewster's angle, (angle of vanishing reflection of p-wave, which is ≈ 57º for SiO_2) 50º, 60º and 70º to ensure a maximum difference in the amplitudes of p- and s-waves, thus assuring fulfilment of all the boundary conditions for a more accurate fitting. The spectra were fitted using both the Cauchy dispersion model and Bruggeman medium effective approximation model. The data analysis was performed with WVase32 software. The apparent porosity was calculated with respect to pure dense silica and a polarization factor of 0.33 was considered.

- TGA was accomplished in TG-DTA92 thermobalance. The analyzed sols were subjected to a measurement program from 25 to 350 ºC at 5 ºC/min heating rate, dwelled for 60 min at 350 ºC, and raised up to 1000 ºC at 10 ºC/min heating rate in air.

- Water adsorption-desorption was studied by EEP. Measurements were performed with the variable angle spectroscopic ellipsometer (M-2000UTM, J.A. Co., Woollam), within a cell with controlled RH. In this case, the spectra were taken at a fixed incident angle of 70º, at different RH values.

- Transmittance, total and diffuse reflectance spectra were measured using a Jasco V-670 UV-Vis-NIR spectrophotometer equipped with a 150 mm integrating sphere. Reflectance was measured at an incident angle of 8º. Diffuse reflectance spectra were taken by removing the specular component port of the integrating sphere. Spectra were taken in the 300 to 2000 nm wavelength range. In this range, integrated transmittance, τ, and reflectance, ρ, were calculated according to Equation 2-20. Gain value (G) was calculated as the percentage of the increment of τ value of coated glass over bare glass $[(\tau_{coat}-\tau_{glass})/\tau_{glass}\cdot 100]$. Reduction value (M) was calculated as the percentage of decrement of ρ value of coated glass below bare glass $[(\rho_{glass}-\rho_{coat})/\rho_{glass}\cdot 100]$. Transmittance change experimented by an AR layer stack was referenced as 'oneself loss τ' and was calculated as the percentage of decrement of τ value after aging test below initial τ value $[(\tau_{before}-\tau_{after})/\tau_{before}\cdot 100]$.

- Coatings thickness was measured using a contact profilometrer Dektak 150. Coatings were scratched with a pin before thermal treatment. After thermal treatment, five scans

were taken crossing the scratch along 50 mm. Thickness was determined by calculation of the step height.

- Kinematic and dynamic viscosity (μ) of sols were characterized by Ubbelohde viscometer through 0B and 1C capillary tubes. Density was measured with a glass pycnometer bottle.
- Cohesion and adhesion properties were examined by scratch test by means of CSM Nano Scratch Tester (NST) with 2 μm radius spheric-conical indenter. Three scratches on each specimen were produced at 1.2 mm/min speed, loading rate of 78.8 mN/min. Starting load was 0.5 and final load arrived up to 20 mN for porous coatings or 40 mN for dense-structured coatings. Therefore, scratches were 0.3 mm length in the case of porous coatings and 0.6 mm length for the dense ones. Panorama image of scratches was taken for the determination of critical points after the test.
- Nanoindentation measurements were made by ultra-nanoindentation tester (UNHT) from CSM. It was equipped with a Berkovich indenter that applied a linear load rate between 60 and 180 μN/min, being the maximum load 10 μN or 20 μN, depending on the sample. Hardness and Young's modulus were calculated, using Oliver-Parr method and a Poisson's ratio (υ_s) of 0.17, for SiO_2 material.
- Damp heat accelerated aging test was performed following the procedure given by IEC 61215 and IEC 62108 PV standards for crystalline silicon modules and concentrated PV modules. The glass specimens were exposed for 1000 h in a climatic chamber at 85 ºC and 85% RH conditions. Spectrophotometry, ellipsometry and $\theta_c^{H_2O}$ measurements were performed at different exposure times to monitor the aging of the coatings. Coating surfaces were analyzed by optical microscopy. Morphology and composition of the coating and deposits were examined by scanning electron microscopy (SEM) using a low-vacuum JEOL JSM 5910 LV equipped with energy dispersive x-ray analyzer (EDX) from Oxford Instrument INCA ACT. Secondary electron images were collected at 20 kV.

4.3. Sol synthesis, coating deposition and post-treatment

4.3.1. Preparation of silica sols

TEOS, polyethylene oxide (20) hexadecyl ether (SDA1), and ethanol were used as precursor, structure-directing agent and solvent for sol-gel formulation, respectively. Two different silica

sols were prepared using acidic water to control hydrolysis and condensation reactions. A sol prepared at R_w4 conditions without SDA (referred in this Chapter as non-SDA silica sol) content served to deposit the inner dense-structured coating. A sol prepared at R_w8 with SDA1 served to deposit the external porous coating (referred in this Chapter as SDA1 silica sol). The molar ratio between inorganic and organic phases, SiO_2:SDA1, their concentrations and water content had been previously adjusted in the Chapter 3, and the synthesis route is defined in the same Chapter, section 3.3.1.

4.3.2. Methyl-silylating post-treatment

The methyl-silylating post-treatment was performed by immersion of porous silica coated glasses in HMDS and n-propanol solutions. The aim was to reduce the number of free silanol groups (Si-OH) on the surface by substituting them with methyl groups ($Si-(CH_3)_3$) and thus converting it into a hydrophobic surface. The post-treatments were applied by immersion of AR coated glass in the solutions held in capped glass bottles. After that, AR coated glasses were dried at different temperatures. Table 4-1 summarizes the studied parameters, i.e., HMDS concentration, time and temperature of immersion and post-treatment temperature.

Table 4-1. Conditions of HMDS post-treatment applied onto porous films.

Post-treatment	HMDS concentration (% vol)	Immersion time (h)	Immersion T (ºC)	Drying T (ºC)
Ha	30	4	20	100
Hb	50	4	20	100
Hc	50	2	60	100
Hd	50	4	60	100
He	50	4	20	250

First, an exploratory study was accomplished in which all the post-treatments collected in Table 4-1 were applied on porous silica single coatings sintered at 350 ºC (M3 defined in Table 4-2). In a second stage, the selected Hb post-treatment was applied on mono- and bi-layers stacks sintered at 350 and 550 ºC (M3, M5, B3, B5 become M3H, M5H, B3H, B5H as defined in Table 4-2 and Table 4-3).

Table 4-2. Deposition sequence for silica AR layer stacks preparation.

Reference	Deposition sequence	AR layer stack
D3	Non-SDA silica sol sintered at 350 ºC	Does not form AR layer stack by itself
D5	Non-SDA silica sol sintered at 550 ºC	Does not form AR layer stack by itself
M3	SDA1 silica sol sintered at 350 ºC	Mono-layer
M5	SDA1 silica sol sintered at 550 ºC	Mono-layer
B3	Non-SDA silica sol sintered at 350 ºC SDA1 silica sol sintered at 350 ºC	Bi-layer
B5	Non-SDA silica sol sintered at 550 ºC SDA1 silica sol sintered at 550 ºC	Bi-layer

Table 4-3. Deposition sequence for methylated-silica AR layer stacks preparation.

Reference	Deposition sequence	AR layer stack
M3H	SDA1 silica sol sintered at 350 ºC Hb post-treatment	Mono-layer
M5H	SDA1 silica sol sintered at 550 ºC Hb post-treatment	Mono-layer
B3H	Non-SDA silica sol sintered at 350 ºC SDA1 silica sol sintered at 350 ºC Hb post-treatment	Bi-layer
B5H	Non-SDA silica sol sintered at 550 ºC SDA1 silica sol treated at 550 ºC Hb post-treatment	Bi-layer

4.3.3. Preparation of polyfluoroalkyl-silica sols

Polyfluoroalkyl-silica sols were prepared via acid catalysis following a two steps procedure. In a first step, TEOS, FAS, ethanol, acidic water and SDA1 were mixed and stirred for 90 min at 80 ºC. Three types of FAS with different chain length $–CH_2CH_2-(CF_2)_n-CF_3$ were used to prepare different sols, with n=0, 5 or 9. More precisely, (3, 3, 3- trifluoropropyl) trimethoxy

silane: $CF_3CH_2CH_2Si(OCH_3)_3$ (FAS3); (1H, 1H, 2H, 2H-perfluorooctyl) triethoxy silane: $CF_3(CF_2)_5CH_2CH_2Si(OC_2H_5)_3$ (FAS13) and (1H,1H,2H,2H-perfluorododec-1-yl) triethoxy silane: $CF_3(CF_2)_9CH_2CH_2Si(OC_2H_5)_3$ (FAS21). Voorhoeve [23] had proved that organohalosilanes with fluorine in the α- and β-carbon positions to silicon hydrolyzed very easily at the –C-Si≡ bond. For that reason, polyfluoroalkyl with hydrogen in α- and β-carbon and fully fluorinated carbon from γ-position to the end of the chain were selected since the aim was to synthesize a covalently bonded organic-inorganic hybrid material.

In a second step, a mixture of ethanol and acidified water (0.1 M HCl) was added drop by drop to the solution and was stirred for 60 min at 40 ºC. The resultant sols were aged in sealed glass containers for 2 days. Different equivalent concentrations of SiO_2 were prepared by varying ethanol/TEOS ratio (R_{Et}). Table 4-4 summarizes all the formulations used in this research work.

Moreover, a polyfluoroalkyl-silica sol without SDA1 content was also prepared for growing polyfluoroalkyl-silica dense coating for comparison. A baseline sol with SDA1 but without FAS content was also prepared for growing silica porous coating used in this study for comparison. Silica sol with neither FAS nor SDA content was prepared for growing pure silica dense coating.

4.3.4. Routes for preparation of coatings and stacks

4.3.4.1. Silica and methyl-silylated silica AR layer stack

The previously defined silica sols were deposited on 4 mm (thick) low iron float glass specimens after being cleaned in ethanol under sonication for 15 min and then air dried. The coating deposition was performed on both sides of the low iron float glass by dip coating at a controlled withdrawal rate of 5 cm/min under controlled environmental conditions of 22 ºC and 60% HR. Compared to other deposition procedures, dip coating method allows to obtain extremely thin, uniform and highly homogenous layers. Furthermore, the deposition under a defined atmosphere is easily approachable. In this case, it provides also the possibility of coating flat specimens on both sides.

After coating deposition, a sintering step is required in order to i) eliminate the amphiphile from the coating to obtain the porous structure and ii) consolidate the inorganic network to obtain the required mechanical stability. Sintering was performed in a conventional furnace at

350 or 550 ºC in air atmosphere for 1 h. The sequence to prepare the studied silica mono- and bi-layer stacks is explained in Table 4-2. In particular, the bi-layer stacks were formed by an inner dense coating derived from non-SDA silica sol dipping at withdrawal rate of 5 cm/min, sintered at 350 or 550 ºC for 1 h, sequentially followed by external porous coating grown from SDA silica sol dipping at withdrawal rate of 5 cm/min, under controlled environmental conditions of 22 ºC and 60% HR.

After external porous coating deposition and sintering, the methyl-silylating post-treatments were performed (see Table 4-1) to obtain the methylated silica AR layer stacks. The sequence of each studied methylated-silica mono- and bi-layer stacks is showed in Table 4-3.

4.3.4.2. Polyfluoroalkyl modified silica AR layer stacks

The previously defined polyfluoroalkyl-silica sols were deposited on 4 mm (thick) low iron float glass specimens after being cleaned in ethanol under sonication for 15 min and then air dried. The coating deposition was performed on both sides of the low iron float glass by dip coating at a controlled withdrawal rate of 5 cm/min under controlled environmental conditions of 22 ºC and 60% RH.

After coating deposition, a thermal treatment was performed in a conventional furnace between 200-350 ºC for 1 h (see Table 4-4) followed by ethanol-water cleaning in ultrasonic bath for extracting surfactant traces.

Table 4-4. Polyfluoroalkyl-silica-SDA1 sol formulations and temperature applied to derived coatings.

Molar ratio TEOS:FAS:SDA1:H_2O:EtOH	SiO_2 concentration	Type of FAS	Applied T (ºC)
1:0.01:0.12:8:24.4	C1	FAS3	200, 240
1:0.01:0.12:8:24.4	C1	FAS13	200, 240
1:0.01:0.12:8:24.4	C1	FAS21	200, 240, 350
1:0.01:0.12:8:34	C2	FAS21	200, 240

The optimized polyfluoroalkyl-silica porous coatings were studied as single AR mono-layers and as external coating in the AR bi-layers stacked on both sides of low iron float glass according to Table 4-5. In particular, the bi-layer stacks were formed by an inner dense coating derived from non-SDA silica sol dipping at withdrawal rate of 5 cm/min, sintered at 550 ºC for 1 h, sequentially followed by external porous coating derived from FAS21-C2 dipping at withdrawal rate of 5 cm/min, under controlled environmental conditions of 22 ºC and 60%

HR. After FAS21-C2 deposition, a thermal treatment was performed in a conventional furnace between 200-240 ºC for 1 h, also followed by ethanol-water extraction.

Table 4-5. Deposition sequence for polyfluoroalkyl-silica AR layer stacks preparation.

Coating	Deposition sequence	AR layer stack
F200	FAS21-C2 sol treated at 200 ºC	Mono-layer
F240	FAS21-C2 sol treated at 240 ºC	Mono-layer
D5F200	Non-SDA silica sol sintered at 550 ºC FAS21-C2 sol treated at 200 ºC	Bi-layer
D5F240	Non-SDA silica sol sintered at 550 ºC FAS21-C2 sol treated at 240 ºC	Bi-layer

4.3.5. Crossed strategies: methyl-silylating agent addition to silica sols and polyfluoroalkyl post-functionalization

Being aware of the intrinsic advantages and disadvantages inherent to a post-treatment or a modification during the sol synthesis, the strategies to obtain hydrophobic silica coatings where intended to be crossed, in order to open the possibilities of obtaining the required properties. That is, an attempt was made to formulate stable silica sols by including HMDS during the sol synthesis. The synthesis was approached in three steps. The first one consisted of a pre-hydrolysis of TEOS through acid catalysis at 60 ºC during 90 min, and in the presence of two di-blocks copolymers, SDA1 or SDA4. Several water:TEOS ratios were tested. In the second step, a mixture of HMDS and ethanol was added to the sol after being cooled up to room temperature. After a 24 h stirring, the third step consisted in the addition of the required acidic water to complete the synthesis. The formulated sols in this stage are collected in Table 4-6.

Table 4-6. Synthesis routes of silica sols formulated with HMDS.

Molar ratio in first step TEOS:$H_2O_{(HCl\ 0,1M)}$:EtOH	Molar ratio in second step HMDS:EtOH	Molar ratio in third step $H_2O_{(HCl\ 0,1M)}$	Final molar ratio TEOS:H_2O:EtOH:HMDS	SDA type and concentration
1:4:8.7	1:8.7	Jellified before ending procedure	1:4:17.4:1	SDA1-150 g/L
1:2.7:8.7	1:8.7	5.3	1:8:17.4:1	SDA1-200 g/L
1:4:8.7	1:8.7	Jellified before ending procedure	1:4:17.4:1	SDA4-150 g/L
1:2.7:8.7	1:8.7	5.3	1:8:17.4:1	SDA4-200 g/L

However, none of these synthesis routes successfully gave stable sols for depositing coatings. When adding HMDS in the second step, NH_3/NH_4OH is formed in the solution, leading to a basic-catalyzed scenario. The sols formulated with the water:TEOS ratio of 4 in the first step, jellified when HMDS was added. The sols formulated with the water:TEOS ratio of 2.7 in the first step, were more stable when HMDS was added, and the completion of the synthesis was approached. However, the sols turned to whitish indicating that colloidal suspensions of large aggregates were formed. These routes were thus discarded.

On the other hand, FAS21 solution in 1-propanol was prepared and used as post-treatment on M3 single porous coating. The conditions of the experiment are collected in Table 4-7.

Table 4-7. Polyfluoroalkyl silane post-treatment applied on single porous silica coating.

FAS21 concentration*	Immersion time (h)	Immersion T (ºC)	Drying
0.012 M	0.5	20	220 ºC/30 min

*in 1-propanol

After applying this treatment, the optical transmittance of M3 coating was drastically reduced, while the water contact angle of the surface grew up only up to 48.7±3.8º. In view that further modification for obtaining higher $\theta_c^{H_2O}$ should be addressed through FAS21 concentration increase, which in turn would lead to an even worse optical performance, this route was also discarded.

4.4. Hydrophobicity obtained in a post-treatment process

4.4.1. Effect of methyl-silylating post-treatment on water contact angle

The external porous coating is susceptible to suffer an irreversible loss of optical transmittance due to weathering during its service life. The cause of deterioration can be attributed to the absorption of soiling and contaminants that are prone to interact with the very reactive Si-OH of the surface (both external and internal) and even collapse the pores. This will result in a change of refractive index and therefore of the antireflection properties. In order to replace the free Si-OH and make the surface less interactive, functionalization with –Si-$(CH_3)_3$ groups was accomplished, and several methyl-silylating post-treatments were optimized for M3 porous coating, which exhibited ~16.6º $\theta_c^{H_2O}$ just after preparation. Five different post-treatments were studied, by varying HMDS concentration, immersion time, immersion temperature and drying temperature as explained in section 4.3.2. The final $\theta_c^{H_2O}$ obtained for the surface after each post-treatment collected in Table 4-1 is showed in Table 4-8. All specimens presented high homogeneity and low dispersion data. Regarding the obtained $\theta_c^{H_2O}$ after each post-treatment, the main found difference was related with the HMDS concentration. Ha post-treatment, composed by 30% HMDS volume, gave $\theta_c^{H_2O}$ around 70º, while Hb-Hd post-treatments, composed by 50% HMDS volume derived in hydrophobic surfaces with $\theta_c^{H_2O}$ between 95-100º. A drying step was considered as final step in order to remove the adsorbed solvent. Two temperatures were studied for this purpose, 100 ºC (Ha-Hd) and 250 ºC (He), in order to study their effect on $\theta_c^{H_2O}$ value achievement. Comparative post-treatments Hb and He showed ~94º after being dried at 100 ºC while ~86º was found after being dried at 250 ºC, revealing that the latter was an excessively high temperature for this step, since some –CH_3 groups can disappear. In fact, Slavov et al. [24] observed that neighbouring trimethylsilyl groups are prone to form Si-O-Si bridges during the reaction of HMDS with silica at 200°C, thus liberating hexamethyldisiloxane.

Eventually, the highest $\theta_c^{H_2O}$ values were around 100º for this type of functionalization of the porous coating. It is known that both surface chemistry and topographical morphologies are essential to achieve superhydrophobicity. The roughness R_a of the mono-layer M3-Hb was as low as 0.4 nm as shown in Figure 4-1.

As previously explained, coatings grown by HMDS-containing sols [1–4] can achieve $\theta_c^{H_2O}$ values as high as 150º. However, if HMDS is added to react with the hydrolyzed TEOS, ammonia is produced and therefore the pH value of the sol increases. Consequently, hydrolysis and condensation of TEOS is led to basic conditions. In these conditions, hydrolysis is produced by nucleophilic attack of hydroxyl anions over the silicon atom. This step gets progressively faster, and all the alkoxide groups are likely hydrolyzed before the first condensation step occurred, then condensation steps result in small, highly branched agglomerates which eventually crosslink to form a colloidal sol. The processed coating will result in a particulate, porous and rough material, presenting, however, weak bindings between particles and poor abrasion resistance. In any case, coatings grown by HMDS-containing sols, are rougher than coatings grown with acid-catalyzed sols. While the highest $\theta_c^{H_2O}$ value obtained was around 100º for post-treatment of an acid-catalyzed derived silica, HMDS-containing sols gave $\theta_c^{H_2O}$ as high as 150º. In parallel, Chen et al. [13], who controlled surface morphology by adding polymers such as PPO in an acid-catalyzed sol, obtained the maximum $\theta_c^{H_2O}$ of 152º for surface with the maximum R_a, namely 76.8 nm.

Finally, Hb was selected as the best methyl-silylating post-treatment considering the trade-off between treatment conditions and the obtained hydrophobicity. Hb methyl-silylating post-treatment was applied on the AR layer stacks under study. The $\theta_c^{H_2O}$ before and after methyl-silylation of all the analysed AR layer stacks are collected in Table 4-9. According to the $\theta_c^{H_2O}$ values exhibited by non-treated layer stacks, it can be mentioned that coatings sintered at higher temperature (550 ºC) exhibited higher contact angles, since increased dehydroxylation of SiO_2 arises as temperature increases. Additionally, the porous mono-layer, when deposited directly on glass, presented slightly lower $\theta_c^{H_2O}$ values in comparison to those of the bi-layer stack, i.e., a porous coating deposited on the dense coating. This performance was attributed to the differences on the formation of the porous layer when directly grown on glass or on the dense-structured coating. The solid-liquid interfacial energy among glass-sol or inner coating-sol, induced differences in the affinities of the sol on each support, thus provoking differences in the formation of the porous coating. Indeed, the AFM images presented in Figure 4-1, allowed to find diverse grain size of the porous layer grown on glass or as external coating in the bi-layer stack. The grain size after Hb methyl-silylation was ~5 nm for M and 10-15 nm for B stacks. Additionally, the ellipsometry data revealed differences in the porosity of the

porous coating depending on where it had been grown, outlined below in section 4.4.2. Although the mean roughness values, R_a, (Figure 4-1) were extremely low for all the studied AR layer stacks (0.3-1.2 nm), the entrapped voids due to the differences in grain size or packing density could lead to such tendency in $\theta_c^{H_2O}$ values.

Table 4-8. Water contact angle ($\theta_c^{H_2O}$) obtained on surface of M3 coating after methyl-silylating post-treatments.

Post-treatment	$\theta_c^{H_2O}$ (º)
Ha	68.6±1.3
Hb	94.4±1.2
Hc	99.3±1.9
Hd	99.1±0.6
He	86.1±0.9

Table 4-9. Water contact angle ($\theta_c^{H_2O}$) obtained on AR layer stacks treated and not treated with Hb methyl-silylation.

Coating	$\theta_c^{H_2O}$ (º)
M3	16.6±1.1
M5	19.5±1.4
B3	20.6±1.7
B5	31.6±1.7
M3-Hb	94.4±1.2
M5-Hb	92.3±1.0
B3-Hb	96.7±1.2
B5-Hb	95.4±1.6

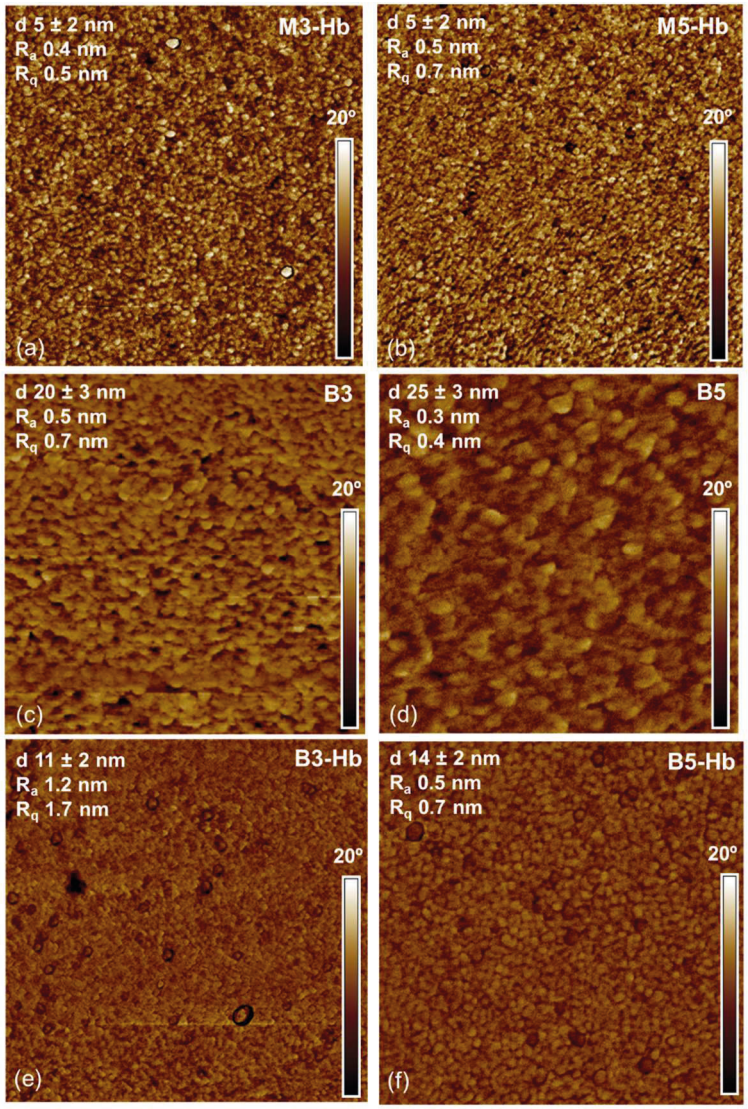

Figure 4-1. AFM phase images (1 μm x 1 μm) of methyl-silylated mono-layers (a, b) and bi-layers before (c, d) and after methyl-silylation (e, f).

Nonetheless, $\theta_c^{H_2O}$ values obtained after Hb methyl-silylation of M and B stacks, revealed hydrophobicity in all cases, being > 90°. However, B stacks exhibited slightly higher values up to ~97°. Besides water (γ_{lv}^p=51 mN/m; γ_{lv}^d=21.8 mN/m), contact angle of Hb methyl-silylated M and B stacks was also measured with ethanol (γ_{lv}^p=2.6 mN/m; γ_{lv}^d=18.8 mN/m) and n-hexadecane (γ_{lv}^p=0 mN/m; γ_{lv}^d=27.5 mN/m), with the aim to calculate surface free energy of these surfaces. The obtained contact angle and the SFE calculated by Owens-Wendt method are shown in Figure 4-2.

Hb methyl-silylated silica porous coating stacks showed SFE values between 23-28 mJ/m². Particularly, M and B stacks sintered at 350 ºC exhibited lower SFE values than their counterparts sintered at 550 ºC. Furthermore, SFE values of the bi-layers were lower compared to the mono-layers. Remarkable outcomes were i) the low contact angle values obtained for the alcohol as liquid test, especially on the mono-layers sintered at both temperatures, and ii) the high data dispersion obtained with n-hexadecane on the bi-layers sintered at both temperatures.

Therefore, the surface demonstrated to be repellent to water and extremely compatible with alcohol. Indeed, the surface polarity was between 10 and 16% of the total surface free energy, which meant that the wetting was driven by the weak dispersive molecular interactions [25].

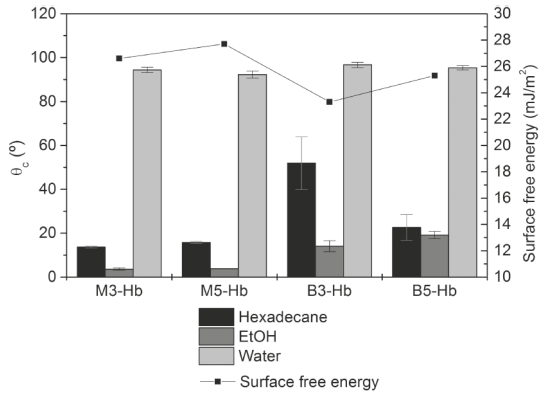

Figure 4-2. Contact angle (θ_c) of AR methyl-silylated mono-layers (M3-Hb, M5-Hb) and bi-layers (B3-Hb, B5-Hb) with three test liquids and surface free energy.

4.4.2. Thickness, refractive index and porosity of the single coatings and bi-layers

The coatings deposited from sol with and without SDA1 that were used to build the mono- and the bi-layer stacks were sintered at two temperatures and characterized by spectral ellipsometry. In addition, coatings deposited from SDA1 silica sol and methyl-silylated with Hb post-treatment, were also characterized.

During the thermal sintering process, the structure of the dried gel gets transformed into a relatively dense glass [26]. The densification of the material is an irreversible process characterized by the decrease of the free energy, whose driving force comes from the high energy of such structure. That structure is strongly dependent on gel microstructure and therefore on the process parameters during sol preparation. The network structure depends

on the degree of hydrolysis and the catalytic conditions employed. Herein, the hydrolysis and condensation of TEOS by acid-catalysis in excess water conditions led to a polymer-like silica network with certain branching in the linear chains as explained in the Chapter 3, section 3.5.

Concerning densification of the inorganic silica network, in the first stage, removal of solvent and water results in additional crosslinking as unreacted hydroxyl and alkoxy groups come in contact. Thus, inorganic network stabilization takes place by subsequent condensation of silica and the pyrolysis of unhydrolyzed alkoxy groups considering that completed organic material combustion takes place between 300 and 400 °C [27]. The physically absorbed water is removed by 427 °C and this leads to further condensation steps. Brinker et al. [26] studied weight loss and thermal transitions of an acid-catalyzed TEOS system. They reported that above 275 °C, the inorganic network densified causing shrinkage and reduction in surface area accompanied by substantial weight loss. However, between 400 and 650 ºC, an appreciable densification of the skeleton was detected, with no increase in the rate of weight loss and accompanied by an exotherm flux. They concluded that the shrinkage observed in this tract did not result from the sintering of open porosity and it was instead attributed to structural relaxation closer to thermodynamically stable structure.

Regarding the organic phase, if SDA1 is present in the desiccated gel, it serves as template for the inorganic network, and the volume during the sintering step is fixed up to its decomposition temperature [28]. The range of decomposition temperature for the SDA1 was between 180-335 ºC, examined by TGA in Chapter 3, section 3.6.3. TGA was also accomplished herein on sols prepared with and without SDA1 in order to observe the effect of the organic template. The resulting curves of mass loss versus temperature are showed in Figure 4-3. In both cases a mass loss > 85% was registered below 130 ºC, this fact being related to ethanol and water evaporation. After this point, the sol without SDA experimented a < 2% mass loss in the 130-350 ºC range, while the sol with SDA1 lost > 10% of mass in this range. As can be observed for SDA1-sol, an inflection point appeared at < 200 ºC, related to the amphiphile decomposition starting point.

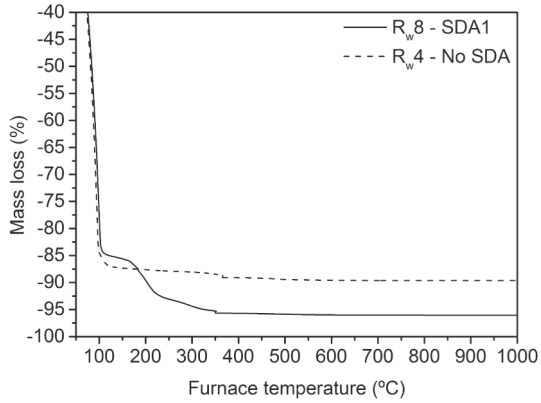

Figure 4-3. Percentage of mass loss during TGA measurement of sols with and without SDA.

Therefore, the objective of the sintering step is the elimination of the SDA and the densification of the inorganic network by the reduction of the skeletal density of the gel to higher crosslinked chains and clusters, which leads to a stable structure. This process conducts to a decrease of surface area, reduction of porosity and elimination of absorbed water as Si-OH groups.

Two considerably different temperatures were chosen in order to sinter the coatings, with the purpose of analyzing the resulting porosity and optical properties together with their durability performance. On the one hand, 350 ºC was chosen as the minimum temperature at which SDA is expected to be totally decomposed. On the other hand, 550 ºC was used as higher temperature since at this temperature the silica network was expected to be closer to thermodynamically stable one and a relaxed structure can be achieved, as explained before.

Thickness, refractive index and porosity of the single coatings as output values after Cauchy [29] and BEMA [30] fitting of ellipsometric parameters Ψ and Δ are compiled in Table 4-10.

As can be seen, the thicknesses of both dense and porous coatings sintered at 350 ºC were slightly higher than their counterparts sintered at 550 ºC.

Therefore, in both cases the differences can be attributed to a slightly higher contraction of the inorganic silica phase inasmuch as sintering temperature increased. Refractive index and the related apparent porosity obtained for dense and porous coatings sintered at both temperatures were similar. As discussed above, the phenomena occurring between these two temperatures are more related to structural relaxation and thermodynamic stability than to sintering of retained porosity in the inorganic silica network.

Regarding the porous coatings treated with Hb methyl-silylation, a porosity reduction was observed from ~50 to ~40% that may be attributed to $–CH_3$ pore-filling, consistent with an increase from 1.22 to 1.27 in the refractive index. Additionally, a slight increase of thickness was also detected. Himcinschi et al. [8] reported similar results for functionalized porous silica layers by exposing them to HMDS vapor for 24 h.

Thickness, refractive index and porosity of the bi-layer stacks as output values after Cauchy [29] and BEMA [30] fitting of ellipsometric parameters Ψ and Δ are compiled also in Table 4-10. While the stacks sintered at 550 ºC displayed consistent thickness values of their stacked coatings, the stacks treated at 350 ºC revealed some unforeseen outcome regarding the coating thickness as single layers or stacked. Given that the material treated at 350 ºC was not completely structurally relaxed, the deposition of the external layer over the inner and the re-sintering process could have provoked further evolution in the material structure and the formation of a non-well-defined interface.

Table 4-10. Thickness (d), refractive index (n) at 700 nm and apparent porosity of D coatings, M and B stacks before and after Hb methyl-silylating post-treatment.

Coating	d_{inner} (nm)	n_{inner} (at 700 nm)	$d_{external}$ (nm)	$n_{external}$ (at 700 nm)	Apparent porosity (%)
D3	-	-	130.3	1.44	-
D5	-	-	111.1	1.45	-
M3	-	-	129.2	1.22	49.9
M5	-	-	124.7	1.22	50.0
M3-Hb	-	-	139.1	1.27	39.3
M5-Hb	-	-	130.9	1.27	39.5
B3	144.5	1.43	105.5	1.21	49.8
B5	115.7	1.44	134.9	1.19	56.4
B3-Hb	142.3	1.43	123.3	1.25	46.6
B5-Hb	111.5	1.44	132.0	1.25	43.4

Refractive index values of the inner coatings were comparable to those obtained as single coating. However, the external porous coatings revealed some differences in its refractive index values and therefore in porosity. In all cases, the refractive index value was lower than the obtained for the single coating, thus related with the increase of porosity, reaching 56.4% for the external coating in the stack sintered at 550 ºC. This result revealed that the growth of

porous coating over the inner dense coating is somehow different than the case of direct deposition on glass, also accompanied by a diverse grain size as explained before. The Hb methyl-silylation induced also a porosity reduction, as observed for the mono-layers.

The surface structure of the bi-layers before and after Hb methyl-silylation and mono-layers after Hb methyl-silylation was investigated by AFM technique and compared with mono-layers before Hb methyl-silylation which are presented in the Chapter 3, section 3.8. Figure 4-1 shows representative AFM phase images of these coatings. The coating surfaces were homogeneous without any particular order and did not show any crack, being their texture very similar. The porosity reduction observed after Hb methyl-silylation, was displayed by a grain downsizing, approximately from 10 to 5 nm in the case of the mono-layers and from 20-25 to 10-15 nm in the case of bi-layers. The roughness measured in a 5 x 5 μm area was extremely low in all cases, being R_a below 1.2 nm.

4.4.3. Transmittance and reflectance of AR layer stacks

Total (direct + diffuse) transmittance and reflectance of AR mono-layer (M) and AR bi-layer (B) stacks deposited on both sides of low iron float glass following the sequence described above were measured by spectrophotometry. Likewise, counterparts of these stacks prepared in the same conditions and methyl-silylated with Hb post-treatment were also measured. The spectra of bare and double side coated low iron float glass are presented in Figure 4-4. Figure 4-4a and Figure 4-4c show total transmittance and reflectance spectra respectively, recorded between 300-2000 nm, of the mono- (M) and bi-layer (B) stacks sintered at 350 ºC (M3 and B3) as well as their corresponding Hb post-treated counterparts (M3-Hb and B3-Hb). In parallel, Figure 4-4b and Figure 4-4d similarly depict transmittance and reflectance spectra for stacks prepared at 550 ºC. Diffuse reflectance spectra recorded between 300-850 nm are represented for stacks sintered at 350 ºC (Figure 4-4e) and 550 ºC (Figure 4-4f).

The integrated total transmittance and reflectance values in the 300-2000 nm spectral range as well as diffuse reflectance values between 300-850 nm are compiled in Table 4-11.

All mono- and bi-layer stacks provided an outstanding transmittance increase in the whole spectral range compared to the bare substrate, achieving an integral transmittance gain in the spectral range 300-2000 nm between 5.6-7.1%. Maximum values were obtained at 565-570 nm in the case of the mono-layers and between 525-560 nm for bi-layers. As discussed in Chapter

3, the combination of the two layers permitted to obtain higher values in the 1000-2000 nm NIR spectral range, providing broadband AR properties. Besides the broadband AR property, the use of a bi-layer stack system has another benefit related to reliability and durability. As mentioned before, the sodium, calcium, potassium, magnesium content in the composition of most float glass products can diffuse out of the glass when it is used for an extended period of time, leading to a decrement of the optical properties [31]. In order to prevent degradation of the glass and the external AR porous coating, the inner coating of the stack was designed to exhibit a dense structure, aimed to act as alkali diffusion-preventing-layer.

Concerning stacks sintered at different temperatures, the optical performance of the mono-layers sintered at low temperature was slightly better, while transmittance of bi-layer stacks was improved for stacks sintered at high temperature. Indeed, in the cases of stacks sintered at 350 ºC, the transmittance in the visible range of the mono-layer surpassed that of the bi-layer, while the transmittance of bi-layer sintered at 550 ºC overtook that of the mono-layer in the whole spectral range.

Table 4-11. Integrated transmittance (τ) and reflectance (ρ) values between 300-2000 nm and diffuse reflectance (ρ_{dif}) values between 300-850 nm of AR layer stacks on both sides of low iron float glass 4 mm thick.

Reference	τ (%)	ρ (%)	ρ_{dif} (%)
Bare glass	90.1	8.5	0.3
M3	96.3	2.5	0.2
M3-Hb	96.0	2.6	0.2
B3	96.4	2.0	0.2
B3-Hb	95.8	2.3	0.4
M5	95.6	2.5	0.2
M5-Hb	95.2	2.7	0.3
B5	96.6	2.1	0.2
B5-Hb	96.2	2.1	0.3

Last analysis was related to the effect of Hb methyl-silylation on the mono- and bi-layer stacks. The change of refractive index and porosity observed in the analysis of ellipsometric parameters, namely a ~10% lower than for untreated stacks, anticipated a detrimental effect on the coated glass transmittance. In fact, as can be observed in Figure 4-4, when comparing

M and B stacks with their counterparts M-Hb and B-Hb, a drop in spectral transmittance was found. However, the loss in the whole spectrum was low, between 0.3-0.6%, depending on the stack. Similar results have been also obtained in other research works [1,9,10,12]. Diffuse reflectance spectra were recorded with the aim to analyze if Hb methyl-silylation induced diffusion scattering which would be detrimental for the electrical production of concentrated photovoltaic systems, which only make use of direct radiation. The integrated value of diffuse reflectance of bare glass was 0.3% and those obtained for the AR layer stacks were under 0.4%, the higher value corresponding to B3-Hb. Although the integrated values were low, the diffusion reflectance spectrum served to explain the slight inconsistency between transmittance and reflectance spectra.

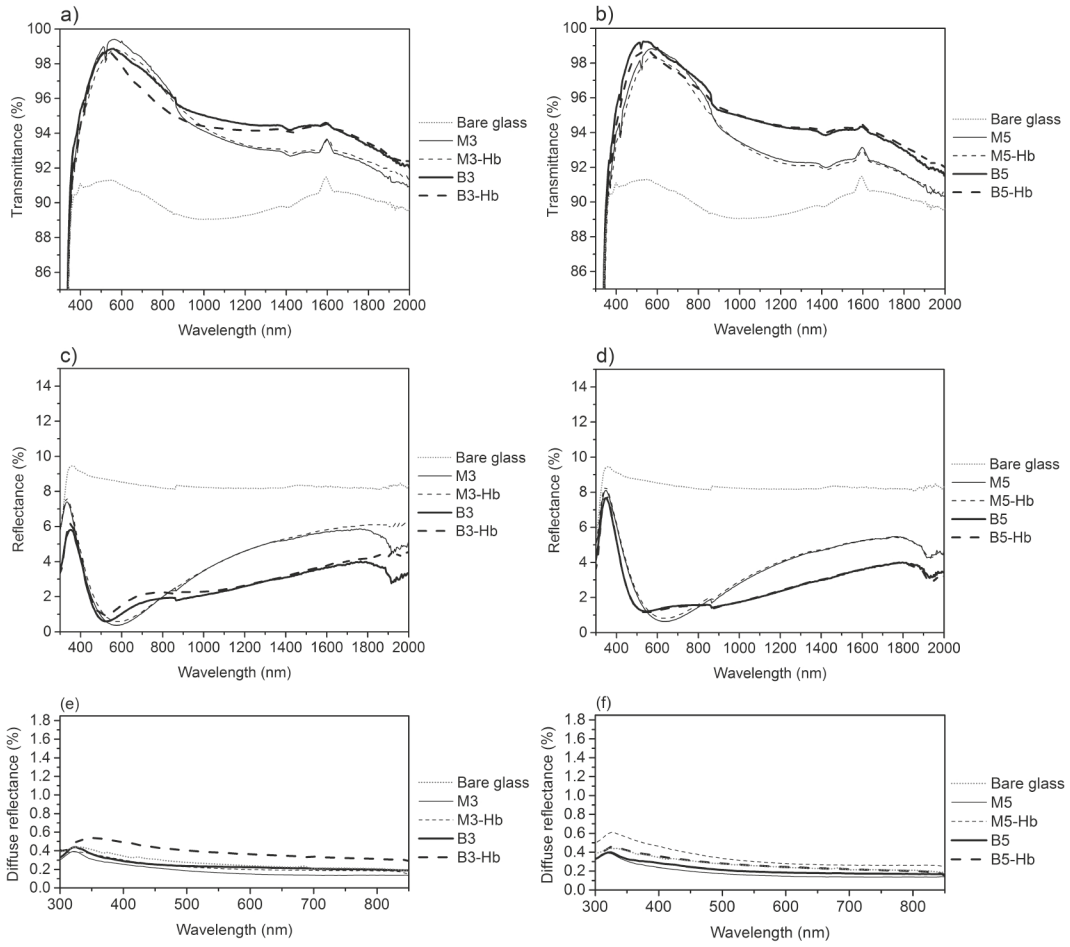

Figure 4-4. Transmittance (a, b), total reflectance (c, d) and diffuse reflectance (e, f) spectra of the mono- and bi-layer stacks sintered at 350 (a, c, e) and 550 ºC (b, d, f).

4.4.4. Optical performance as a function of humidity

Optical constants of the investigated AR mono-layers were analyzed at different RH-conditions by ellipsometry. As long as water partial pressure increases, it is expected to be filling the pores, and this should be reflected in a variation of their optical properties. Refractive index (at 700 nm) obtained from ellipsometric data fitting as a function of RH during adsorption and desorption steps are graphed in Figure 4-5a (M3 and M3-Hb) and Figure 4-5b (M5 and M5-Hb).

M3 and M5 porous AR mono-layers, showed a low refractive index value of 1.22 (at 700 nm) in dry conditions, however, for RH values above 60%, the pores fill in with water, and refractive index values increased up to 1.40 (at 700 nm). Methyl-silylated counterparts M3-Hb and M5-Hb as explained above, showed higher refractive index values (~1.27 at 700 nm) in dry conditions, however they maintained the value independent of RH. Since the CPV modules will be subjected to different environmental conditions during their service life and may be used in different locations, they should show high efficiency independently of their exposure conditions.

Transmittance and reflectance values were calculated by using Cauchy parameters and coating thickness, all obtained from experimental ellipsometric data fitting, using CODE® software.

Spectral transmittance and reflectance of AR mono- and bi-layer stacks were thus calculated for each environmental RH, as shown in Figure 4-5. Figure 4-5b shows integrated transmittance of M3, B3, M3-Hb, B3-Hb simulated stacks at several RH values, Figure 4-5c shows integrated transmittance of M5, B5, M5-Hb, B5-Hb simulated stacks at several RH values, and Figure 4-5d and e graph integrated reflectance values for the mentioned AR layer stacks. In view of obtained refractive index, untreated stacks showed the higher transmittance values at low environmental RH conditions, although these values dropped when relative humidity increased. In contrast, Hb methyl-silylated AR layer stacks, showed lower transmittance values at lower RH, however those values were maintained independently of the RH. Therefore, above 50% RH (stacks sintered at 350 ºC) or 60% RH (stacks sintered at 550 ºC), the integrated transmittance was above their counterpart untreated stacks. Hb treated AR layer stacks showed higher environmental adaptability and they are promising to display a better performance in a variety of locations.

The HMDS functionalization applied as a post-treatment, in comparison to HMDS as a reactant in the sol, presents the advantage that hydrophilic –OH group bonds are replaced by hydrophobic –Si-$(CH_3)_3$ group bonds in the whole specific surface of the porous coating. Therefore, the internal pore surface becomes also hydrophobic, which avoids vapor water to enter, thus preventing the consequent increase in refractive index in case water reached the pores.

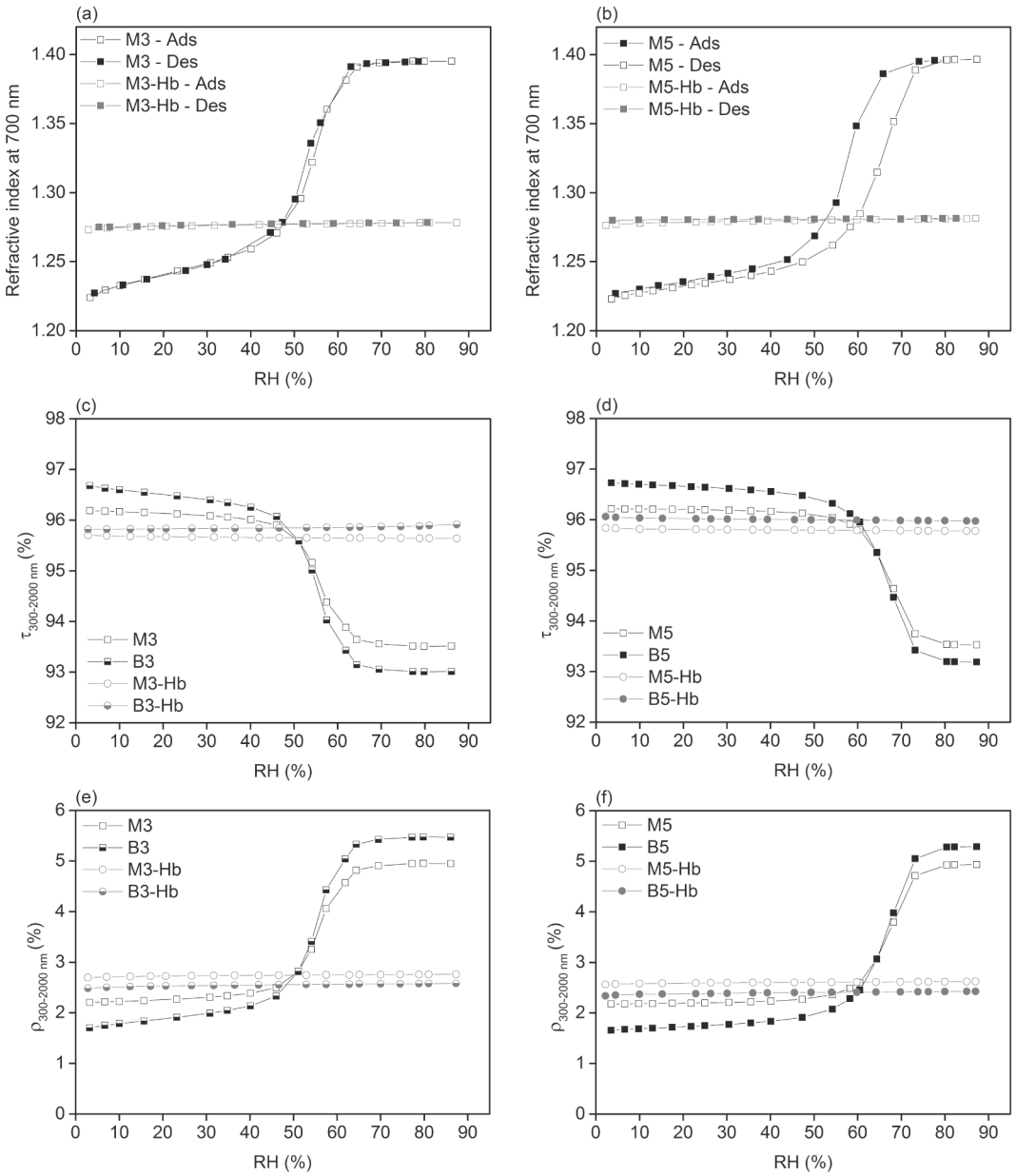

Figure 4-5. Refractive index (at 700 nm) and calculated integrated transmittance and reflectance (300-2000 nm) as function of environmental RH for each investigated layer stack.

4.4.5. Cohesion and adhesion properties determined by nanoscratch testing

Through the analysis of the scratches drawn with sphero-conical stylus at a constant speed across the coating-substrate system, under progressive loading (at constant rate), the load at which recognizable failures occur was calculated. The critical loads at which first failures occurred were identified by microscope analysis of scratches drawn on single coatings and stacks prepared at 350 and 550 ºC. The Figure 4-6 shows the scratch panoramas of the stacks prepared at 550 ºC. The failure emergence depends on the mechanical strength of the coating-substrate system, i.e. cohesion and adhesion, but also on several other parameters related to the test itself [32]. Therefore, the scratch test is mainly a comparison test between the coatings and stacks similarly tested. The driving forces for coating damage in the scratch test are a combination of elastic-plastic indentation stresses, frictional stresses and the residual internal stresses. In the lower load regime, these stresses generally result in conformal or tensile cracking of the coating which still remains fully adherent. The onset of these phenomena defines a first critical load (Lc1) which emerged in porous mono- or bi-layer stacked porous coatings at loads below 20 mN. Dense coating was required to be tested up to 40 mN to coerce Lc1 emergence. In the higher load regime, the onset of failure corresponds to coating detachment from the substrate by spalling, buckling or chipping (Lc2). This failure was only detected on porous single coatings as observed in Figure 4-6.

The calculated critical loads through image analysis are represented in the Figure 4-7 for the dense coating, porous mono-layers, as well as for the bi-layers obtained by their stacking. Lc1, linked to loss of coating cohesion, appeared on M5 coating at 2.8±0.4 mN and on M3 at 2.6±0.1 mN. Lc2, related to adhesive failure of the coating to substrate, appeared on M5 at 4.9±0.6 mN and on M3 at 4.6±0.3 mN. Dense coatings were needed to be damaged with a longer scratch to achieve double test load (40 mN), to finally obtain Lc1 failure at 38.0±0.7 mN and 33.7±0.5 mN for coatings sintered at 550 and 350 ºC, respectively. They did not experimented detachment from the substrate under the tested loads.

Therefore, the porosity, the applied temperature and the resulting coating structure had a crucial influence on the load of failure emergence. By comparing dense and porous coatings, the 50% of porosity provoked a drastic loss of coating cohesion as well as adhesion to the glass substrate.

The critical loads obtained in the analysis of the scratches drawn on the bi-layer stacks differed from those obtained for the mono-layers. The Lc1 emergence in the bi-layer stack prepared at 350 ºC, occurred at 2.6±0.2 mN, similar to the mono-layer. In this case, the porous coating grown on the inner dense-structured coating or directly on glass had shown similar values of porosity. Despite the higher porosity exhibited by porous external coating when deposited on the dense coating, 56.4%, the Lc1 emergence of B5 stack was also similar (2.9±0.1 mN) to that of coating directly grown on glass which had shown 50% of porosity. Therefore, porous coatings exhibited the same cohesion failure independently on where there were grown (on the inner dense-structured coating or directly on glass). However, porous coatings grown on the dense-structured silica coating, did not show adhesion failure below 20 mN. Consequently, adherence of porous coatings can be improved if they are grown as external coating on an inner dense-structure coating.

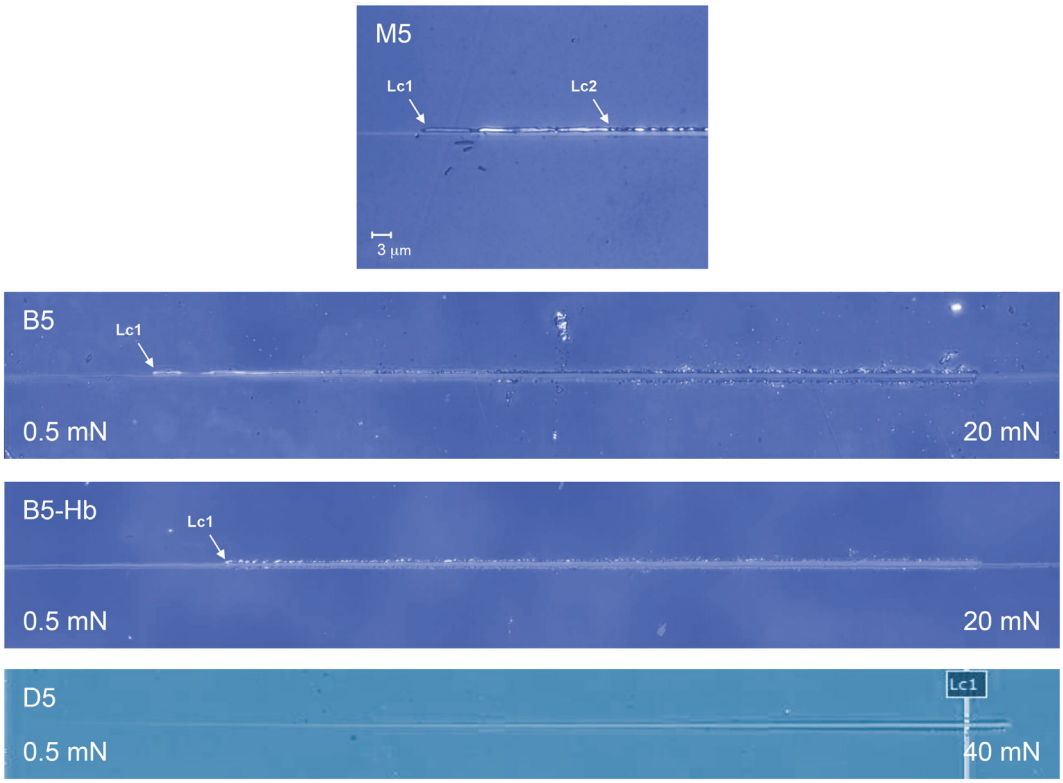

Figure 4-6. Micrographs panoramas of scratches drawn on single coatings and stacks sintered at 550º C and their labeled failures Lc1 and Lc2.

On the other hand, the methyl-silylation of the coating surface provoked a delay on Lc1 emergence in the B5H stack, treated at 550 ºC up to 4.4±0.1 mN, showing a higher coating

cohesion related to its lower porosity that decreased from 56.4 to 43.4%. The B3H stack, treated at 350 ºC showed Lc1 failure at 2.7±0.4 mN, similar to B3. In those cases, the porosity of external coatings presented a slight decrease from 49.8 to 46.6%.

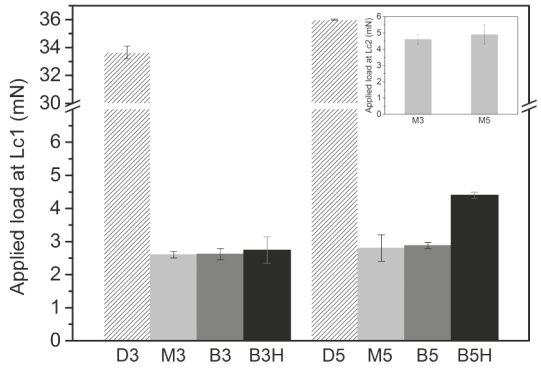

Figure 4-7. Critical load Lc1 and Lc2 obtained from nanoscratch test.

4.4.6. Mechanical properties

Hardness and Young's modulus of coatings materials were expected to be related to coating structure, mainly influenced in this case by porosity and coating consolidation achieved during thermal treatment. The loading-unloading indentation curves of single porous mono-layers M3 and M5 (maximum load 10 μN) are represented in Figure 4-8b. The low roughness exhibited by the coatings allowed to obtain proper measurements since low dispersion (less than 10%) and good repeatability were obtained even for such low load. Indentation depth at 10 μN was ~8 nm for porous silica coating sintered at 550 ºC, while arrived to 13-14 nm for the coating sintered at 350 ºC, which represents ~6 and ~11% of the total coating thickness, respectively. As expected, mechanical properties of coating sintered at 550 ºC were considerably higher than coating treated at 350 ºC. Since the porosity of both samples was 50%, the highest consolidation achieved by coating treated at 550 ºC led to reach higher hardness and elastic modulus as observed in Figure 4-8a. Hardness of M5 was 2.09±0.12 GPa and that of M3 was 1.18±0.08 GPa. Elastic modulus was 38.18±1.88 GPa for M5 and 24.76±2.07 GPa for M3.

Higher maximum forces (up to 20 μN) were applied for measuring the dense coatings and the bi-layer stacks, with the purpose to avoid the influence of indenter tip blunting, which can become significant for very low indentation depths. The hardness of dense-structured silica coating sintered at 550 ºC (represented in Figure 4-8a) was equal to 4.27±0.21 GPa while for

coating sintered at 350 ºC was 3.68±0.20 GPa being more than double than for porous coatings counterparts sintered at the same temperature.

Figure 4-8d displays indentation curves of AR bi-layer sintered at 550 ºC before and after methyl-silylating treatment. The indentation depth at 20 μN load for B5 was 28-32 nm, what implied a decrease in hardness of silica porous coating grown on the dense coating instead of glass up to 0.67±0.03 GPa. As previously discussed, significant differences in the structure, grain size and porosity of silica porous coating were found when grown on glass or on dense coating. Higher grain size, from 7 to 25 nm, and porosity up to 56.4% had a remarkable impact on the decrease of mechanical properties. Herrmann et al. [33] also reported the highly dependence of mechanical properties measured by nanoindentation on the porosity of xerogels (ranged 40-50%).

The effect of methyl-silylating treatment was studied on the AR bi-layer stack B5-Hb. Indentation depth was reduced up to 20-25 nm, and hardness increased up to 1.16±0.08 GPa, therefore almost doubled the B5 value. As explained in section 4.4.2, methyl-silylating treatment drove to a decrease of grain size to 15 nm, and porosity reduction up to 46.6% and this structure allowed to reach higher mechanical properties.

The contrary effect was registered on AR bi-layer sintered at 350 ºC according to the loading-unloading indentation curves represented in Figure 4-8c. In this case, the indentation depth at 20 μN load for B3 was 20-24 nm, what implied a slightly increase in hardness of silica porous coating grown on the dense coating instead of glass up to 1.3±0.1 GPa. This result is linked to the similar porosity values of porous mono-layer and external coating of the bi-layer, being 49.9 and 49.8%, respectively. The effect of methyl-silylating treatment on the AR bi-layer stack B3-Hb was aligned with that observed on stacks sintered at 550 ºC. Indentation depth was reduced up to 20-22 nm, and hardness slightly increased up to 1.5±0.1 GPa. This effect was therefore related with the reduction of porosity from 49.8 to 46.6% after methyl-silylation of bi-layer sintered at 350 ºC.

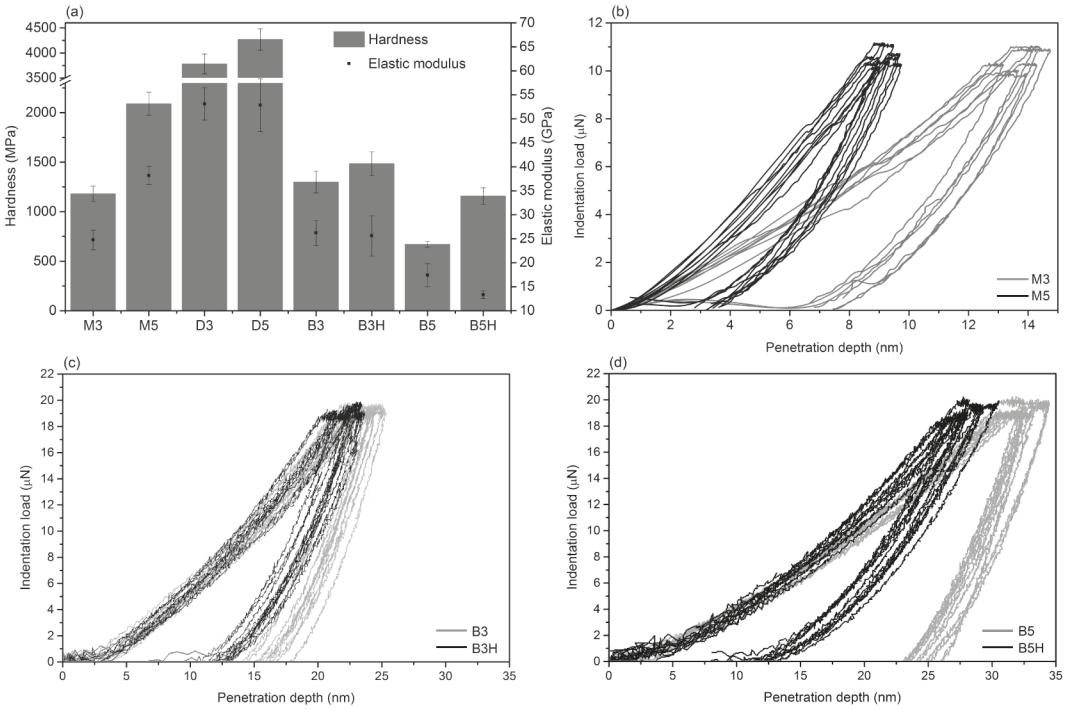

Figure 4-8. Hardness (bars) and elastic modulus (dots) values (a) calculated from nanoindentation curves obtained for the mono-layers (b) and bi-layers (c, d).

4.4.7. Assessment of coating degradation after damp heat aging

The long-term durability of PV modules and their constituents is crucial since they must be capable of withstanding prolonged exposure in harsh environments. The PV industry makes use of IEC 61215 and IEC 62108 standards to validate the performance and reliability of the modules and materials under real operation conditions. Among the reliability tests collected therein, damp heat aging may be considered one of the most critical ones due to the condensation problems caused by the rapid variation of the module temperature [34]. In this Chapter, AR layer stacks were tested under damp heat test conditions with the aim to deeply study the effect of the most aggressive scenario on the developed AR layer stacks. One of the objectives was to establish the contribution of several parameters on the durability of optical properties, namely the presence of the inner dense coating as alkali-diffusion barrier; sintering temperature; and $–Si-(CH_3)_3$ functionalization. Thereupon, the AR layer stacks were characterized again as described above, after their exposure in the chamber at 85 ºC/85% RH for 1000 h.

Spectral transmittance and reflectance of AR layer stacks after damp heat aging are depicted in Figure 4-9. Figure 4-9a and Figure 4-9c show transmittance and reflectance spectra, respectively, recorded between 300-2000 nm for the mono- (M) and the bi-layer (B) stacks sintered at 350 ºC (M3 and B3), together with their corresponding Hb post-treated counterparts (M3-Hb and B3-Hb). In parallel, Figure 4-9b and Figure 4-9d depict the corresponding transmittance and reflectance spectra for stacks prepared at 550 ºC. The loss of transmittance of each stack before and after test and the gain of each over bare aged glass is compiled in Table 4-12. $\theta_c^{H_2O}$ after the test as well as thickness and refractive index from Cauchy fitting of ellipsometric data of AR mono-layers are also presented in Table 4-12.

The obtained results allow a deep analysis of (i) the robustness that higher sintering temperature may provide to the AR layer stacks; (ii) the presence of the inner dense coatings in the bi-layer stacks in comparison to AR mono-layers and (iii) the HMDS resistance and influence on the AR layer stacks.

Spectrophotometric measurements confirmed that the porous AR mono-layer conferred a significant transmittance loss after the test, specially M3, sintered at 350 ºC, which shows a transmittance decrease of almost 9%, with a final transmittance value 2.2% below than bare glass. M5 sintered at 550 ºC showed an almost 2% loss after the aging test. This corroborated the fact that the structural relaxation that occurs during sintering between 350 and 550 ºC can contribute to the achievement of the structure closed to stable one, which plays a crucial role in the durability of the coating performance. The refractive index values related directly to antireflection properties increased after the aging, probably due to mesostructure collapse.

However, attending to the antireflective behavior of the bi-layer stacks, the differences between the two sintering temperatures were less extreme, since B3 coatings lost 1% of their initial transmittance and B5 was almost inalterable. The presence of the inner dense coating in the AR layer stack, apart from contributing to the broadband antireflection properties, displayed a great relevance in the durability-related performance. Whereas all the bi-layers presented a homogeneous and clean surface, the formation of salt deposits embedded in the surface of mono-layers was corroborated through microscopy as observed in the Figure 4-10a and Figure 4-10d. The EDX spectra of the deposits and the smooth surface corresponds to Figure 4-10g and h, respectively. The Ca/Si molar ratio of the smooth surface was around 0.1, which was consistent to the glass composition. The X-ray analysis of the deposits displayed a

highly Ca enrichment showing Ca/Si ratio up to 1, with a higher carbon content, which was attributed to $CaCO_3$ formation, whereas the Si presence corresponded to the bulk glass due to the penetration depth of the X-ray. Consequently, the deposition of the inner dense layer should be considered when designing an AR system, because of its role as a barrier preventing alkali diffusion from glass to the porous coating, which would lead to the formation of salt deposits. The inner dense coating could also have a positive effect on the adherence of porous coatings. The refractive index values obtained after the aging process were also consistent with the obtained antireflection properties. It was as low as 1.23 for external porous coating sintered at 550 ºC while it had increase up to 1.31 for the mono-layer, showing that the inner dense coating acting as a barrier avoided the mesostructure collapse of the external coating.

The HMDS post-treated AR stacks could have an advantage concerning performance in humid conditions, since water vapor does not enter the pores during the damp heat test, and therefore the durability properties would be less affected. However, the antireflection properties for treated and untreated counterparts exhibited similar performance stability. It can be postulated that the resistance under these severe conditions was more related to the achieved inorganic structure than to the ending group bonds of the internal and external surface.

Particularly, the B5-Hb stack presented the best optical performance, showing no transmittance loss after damp heat aging, which corresponded to a gain of 8% over aged bare glass at the end of the test. The thickness and refractive index determined by ellipsometry remained inalterable after the test.

After the damp heat exposure, all the tested AR layer stacks displayed values ranging between 80 and 90º for the $\theta_c^{H_2O}$. As mentioned above, in the case of external porous coatings not treated with HMDS, the ending Si-OH group bonds are prone to interact with any surrounding molecule during the test. At the end of the test, the surface could present unknown uncontrolled ending bond groups, in contrast to the treated stacks, that present controlled – Si-$(CH_3)_3$ group reacted on the surface. A remarkable outcome was that AR layer stacks sintered at 550 ºC presented a higher homogeneity of the $\theta_c^{H_2O}$ throughout the tested surface compared to those sintered at 350 ºC. This outcome was linked with the diffuse reflectance spectra after aging test displayed in Figure 4-9e (stacks sintered at 350 ºC) and Figure 4-9f (stacks sintered at 350 ºC). An important increase of diffuse scattering was observed in

comparison with the values recorded before aging, with the exception of B5 and B5-Hb stacks. The overall diffuse reflectance of stacks was between 0.5-0.8% except for B5 and B5-Hb, which showed 0.2-0.3%, similarly to the values for bare glass.

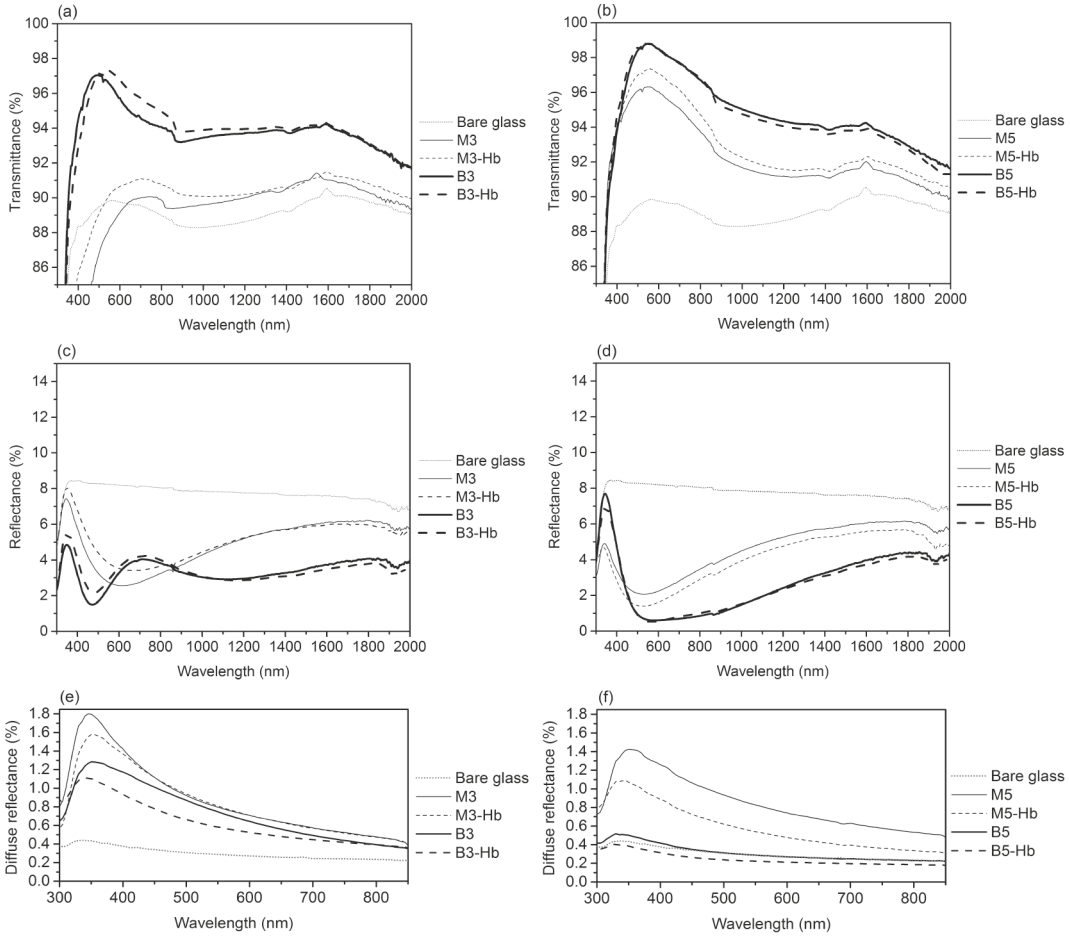

Figure 4-9. Transmittance (a, b) total reflectance (c, d) and diffuse reflectance (e, f) spectra of the mono- and the bi-layer stacks sintered at 350 (a, c, e) and 550 ºC (b, d, f) after 1000 h of damp heat test exposure.

Table 4-12. Thickness (d), refractive index (n) at 700 nm, oneself loss of τ in the 300-2000 nm spectral range, τ gain over aged bare glass in the 300-2000 nm spectral range, diffuse reflectance (ρ_{dif}) values between 300-850 nm and water contact angle ($\theta_c^{H_2O}$) of AR layer stacks after damp heat aging.

Reference	d_{inner} (nm)	n_{inner} (at 700 nm)	$d_{external}$ (nm)	$n_{external}$ (at 700 nm)	Oneself loss τ (%)	τ gain (%)	ρ_{dif} (%)	$\theta_c^{H_2O}$ (º)
M3	-	-	115.3	1.39	9.2	-2.2	0.8	90.0±8.7
M5	-	-	106.0	1.31	1.8	5.4	0.8	86.6±5.2
M3-Hb	-	-	106.2	1.37	10.1	-4.6	0.8	82.4±6.2
M5-Hb	-	-	106.5	1.31	1.6	5.7	0.5	86.6±3.8
B3	156.2	1.43	82.7	1.31	0.8	6.3	0.7	92.78±3.4
B5	120.1	1.45	132.4	1.24	0.1	8.1	0.3	92.02±1.8
B3-Hb	161.1	1.45	106.6	1.29	0.1	6.7	0.6	83.3±4.1
B5-Hb	124.9	1.45	123.7	1.23	0.0	8.2	0.2	82.8±0.9
Bare glass	-	-	-	-	1.3	-	0.3	61.2±3.6

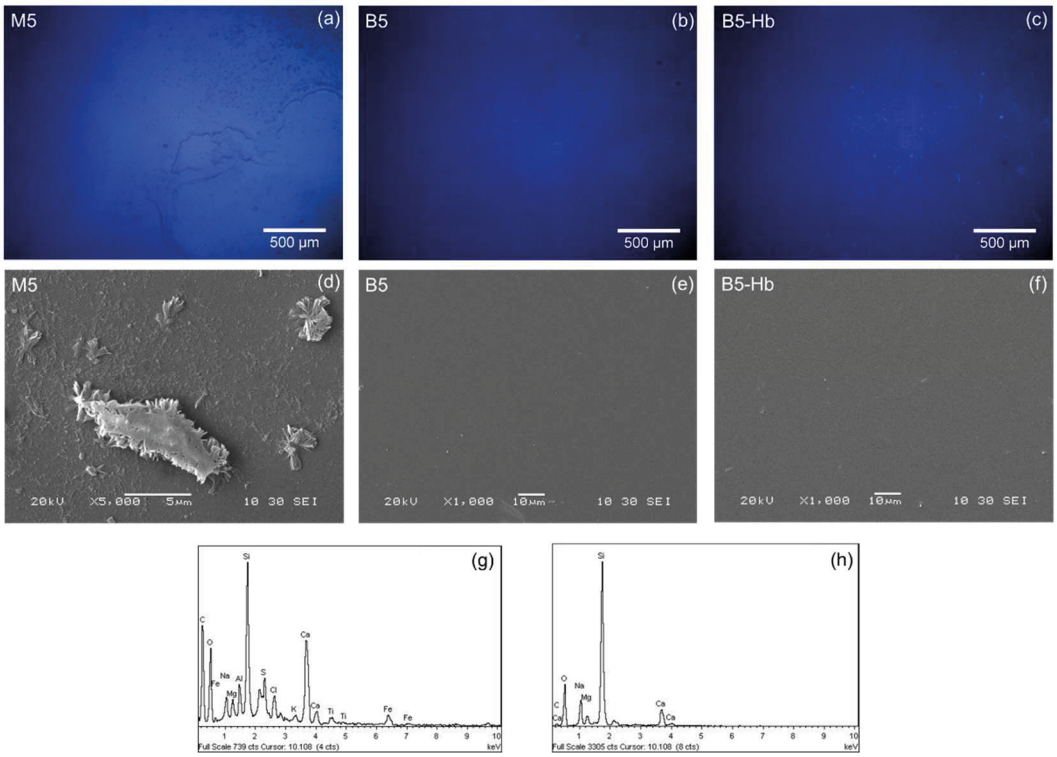

Figure 4-10. Optical (a, b, c) and electron (d, e, f) surface micrographs of mono- and bi-layer stacks sintered at 550 ºC and EDX analysis of deposits (g) and smooth coating (h) after 1000 h of damp heat test exposure.

4.5. Hydrophobicity obtained in a one-step process

4.5.1. Effect of polyfluoroalkyl chain length on wettability, thickness and optical properties

FASs with different polyfluoroalkyl chains length were incorporated during sol preparation to improve final properties of previously studied AR coating materials. The coatings grown from baseline SDA1 silica sol formulation were 125-130 nm thick with refractive index equal to 1.22 at 700 nm (see Table 4-10). With these features, the baseline coating deposited on both sides of low iron float glass revealed $\tau_{300\text{-}2000nm}$ up to 96.3% and $\theta_c^{H_2O} < 20^o$. In order to preserve the high transmittance values provided by the baseline coating, only a low quantity of FAS was introduced into the sol to design AR coatings. As explained before, the three types of polyfluoroalkyl alkoxides were incorporated with the same low molar ratio (1 TEOS:0.01 FAS) during the baseline sol preparation, with the same R_{Et} (concentration C1). Therefore, this permitted the incorporation of the following polyfluoroalkyl chains covalently bonded to porous silica backbone: $–(CH_2)_2\text{-}CF_3$; $–(CH_2)_2\text{-}(CF_2)_5\text{-}CF_3$ and $–(CH_2)_2\text{-}(CF_2)_9\text{-}CF_3$ with the presence of similar concentrations of terminal $-CF_3$ groups in all prepared coating materials. As explained before, Shafrin et al. [35][36] postulated that the non-wettable surface with the lowest surface energy can be ideally comprised by closed packed $–CF_3$ groups. Therefore, wettability appears to be less related to the polyfluoroalkyl chain length itself and more to its proper orientation to yield total exposure of $–CF_3$ moieties. The effect of the introduction of these moieties on the $\theta_c^{H_2O}$ of coatings treated at several temperatures is displayed in Figure 4-11a. One can easily observe that polyfluoroalkyl chain length plays a role in the configuration of investigated coatings, since a higher $\theta_c^{H_2O}$ was exhibited as the chain length increased. In the case of organic surfaces, the wettability is generally given by the nature and packing of the exposed atoms or groups and tends to be independent of the arrangements of the underlaying molecules. In proposed approach, in which FAS compounds were added in a low molar rate, the longer the fluoroalkyl chain embedded in the coating, the more possibilities have the $–CF_3$ moieties to emerge out of the surface. Therefore, in this case, the fluoroalkyl chain length seems to be crucial in order to reach the highest non-wettable surfaces with such low molar rate. It is well known that fluoropolymers composed by perfluoroalkyl chain $–(CF_2)_n\text{-}$ show the best resistance to high temperature, up to 260 ºC, thanks to the strength of the C-F bond. In any case, the rate of decomposition will depend on the particular matrix, as well as the

temperature and the exposure time. As observed in Figure 4-11a, $\theta_c^{H_2O}$ of the coatings treated at 200 and 240 ºC was of the same order for the same coating material. The water contact angle was ~108º and ~105º for $–(CH_2)_2\text{-}(CF_2)_9\text{-}CF_3$ (FAS21), treated at 200 and 240 ºC, respectively, while it diminished to ~70º for the coating treated at 350 ºC.

As long as the polyfluoroalkyl length chain increased, the thickness of the derived coating also did. Figure 4-11b shows the thickness measured by profilometry for coatings treated at 240 ºC. The thickness of coating containing $–(CH_2)_2\text{-}CF_3$ was close to the baseline thickness, while the coating with $–(CH_2)_2\text{-}(CF_2)_9\text{-}CF_3$ reached 260 nm. This modification of coating thickness significantly affected the optical properties. The increase of polyfluoroalkyl length chain acted detrimentally on transmittance as observed in Figure 4-11c, where its integrated value, $\tau_{300\text{-}2000nm}$ is graphed for coatings sintered at 200, 240 and 350 ºC, before and after ethanol-water extraction. On this occasion, the presence of the same molar ratio of TEOS:FAS led to an increase of the weight ratio (FAS3 < FAS13 < FAS21) and the higher quantity of fluorinated moieties in the baseline coating provoked a reduction of the antireflection properties. Indeed, perfluorinated polymers are known to have high reflectance properties, mostly in the diffuse component [37] and therefore, the FAS addition must be rationally designed.

The difference in transmittance between the same coating material when treated at 200 or 240 ºC was notable for measurements before ethanol-water extraction (solid dots), being higher for coatings treated at 240 ºC. This fact was attributed to the higher presence of SDA traces on the coating pores treated at lower temperature. After SDA extraction, coatings treated at 200 and 240 ºC and prepared with the same sol exhibited similar values (hollow dots), being ~96.3% for FAS3-, ~95.0% for FAS13- and ~94.0% for FAS21-coatings. At these temperatures, the fluorinated moiety did not suffer degradation, and the effect of its presence was perceived on the low wettability values. However, the transmittance of FAS21-coating treated at 350 ºC stood out from those treated at lower temperatures, reaching 95.2% against 94.0%, what is also related with the gradual decomposition of fluorinated moiety. This effect was also consistent with the low $\theta_c^{H_2O}$ obtained on this surface. In Figure 4-12, the transmittance spectra between 300-2000 nm of the fluorinated coatings studied in this section together with the baseline coating are displayed. Therein, the similarity among baseline and FAS3-coating spectra evinces that the incorporation of a short polyfluoroalkyl chain does not interfere in the thickness nor in the optical properties. However, FAS13- and FAS21-coatings

spectra evidenced that long polyfluoroalkyl chains had an impact on the thickness and the intrinsic material properties of the baseline coating, thus altering the optimized constructive and destructive interferences of its spectrum. The transmittance of a perfectly smooth coating stacked on glass is described by Fresnel equations, and depends only on its complex refractive index ($\tilde{n} = n + i\kappa$) and thickness. Therefore, the conditions for achieving an optimal tandem must be found. Although only very small amounts of a non-hydrolyzable polyfluoroalkyl chain alkoxysilane were needed to produce the porous silica coatings with low wettability, the coating that displayed the highest $\theta_c^{H_2O}$ value, with the longest fluoroalkyl chain embedded, did not show the required antireflective performance. Fluoroalkyl moiety quantity should henceforth be optimized in order to balance low surface tension and high antireflection properties in a one-step coating.

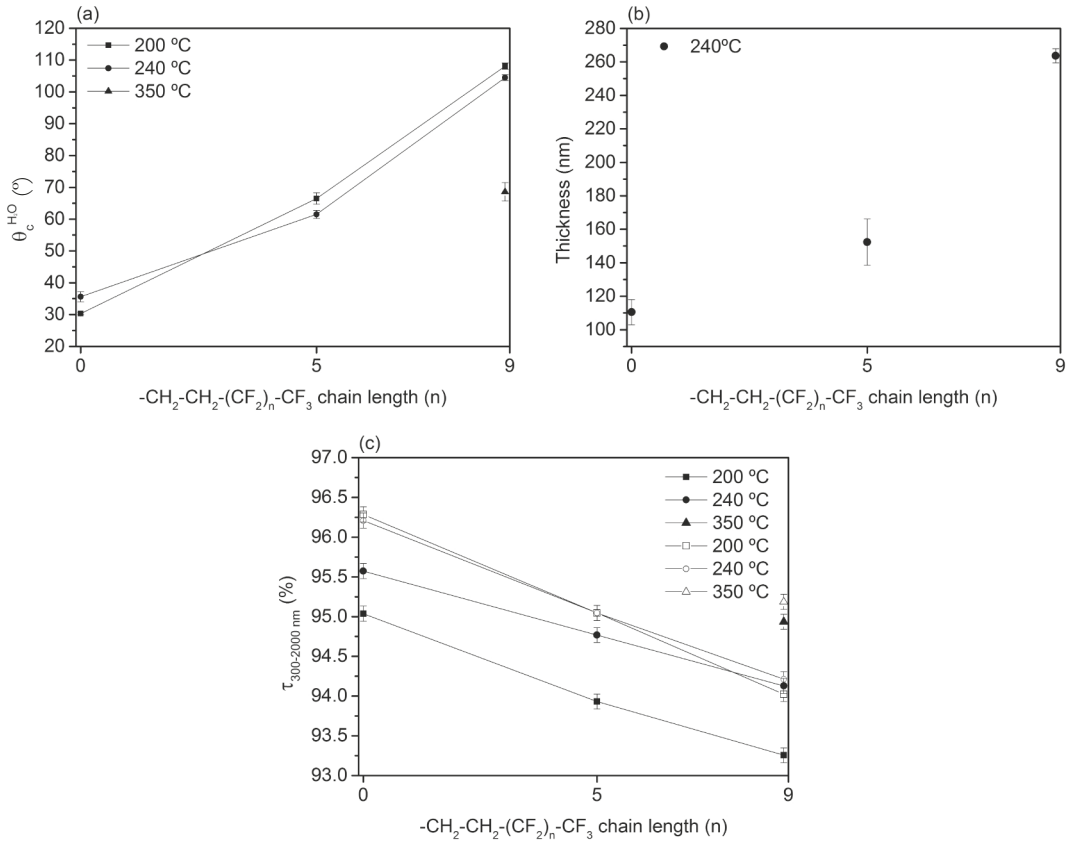

Figure 4-11. Water contact angle ($\theta_c^{H_2O}$) (a), thickness (b) and integrated transmittance (300-2000 nm) (c), of polyfluoroalkyl-silica porous coatings with different chain length.

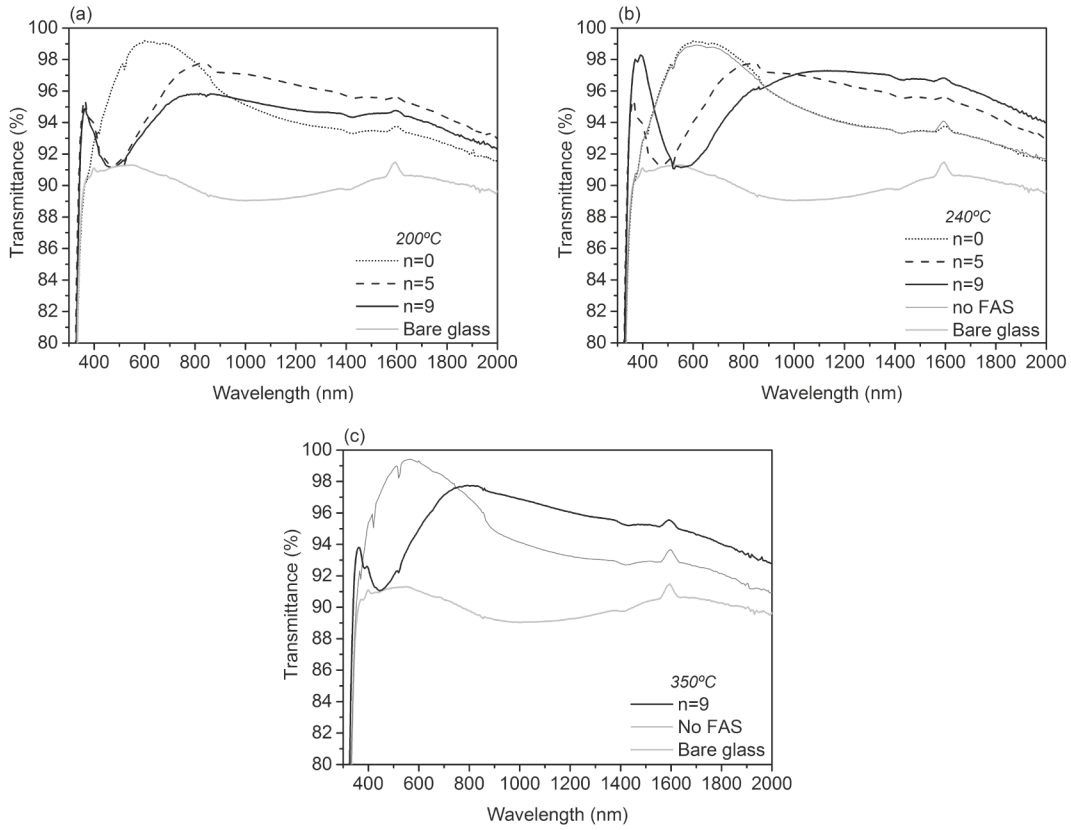

Figure 4-12. Total transmittance spectra of polyfluoroalkyl-silica porous coatings with different chain length, deposited on both sides of low iron float glass treated at 200 (a), 240 (b) and 350 ºC (c).

4.5.2. Structural and textural properties of optimized coating with the longest polyfluoroalkyl chain

Motivated by the high value of water contact angle obtained with coatings containing a low quantity of the longest polyfluoroalkyl chain-modified alkoxysilane, the FAS21-C1 formulation was adjusted to obtain a thinner and highly antireflective coating. The optimization of the formulation was accomplished by R_{Et} adjustment with the purpose to interfere in the sol viscosity. The former addition of FAS21 to baseline formulation supposed a viscosity increase from 2.52±0.05 to 2.81±0.01 cP. This parameter was then fitted to 2.30±0.04 cP after ethanol addition to obtain FAS21-C2 sol. The stability of the latter sol was excellent since the viscosity remained invariable at least after a one year aging. This fact is very promising for the implementation and scaling up of the one-step process. Based on the outcome of the optical optimization performed in Chapter 3 which allowed the calculation of the optimal thickness,

refractive index and porosity of the coatings composing AR layer stacks (from 1 to 4 layers), FAS21-C2 sol served to grow AR mono- and bi-layer architectures.

On one side, FAS21-C2 sol and a similar sol without SDA were used to grow polyfluoroalkyl-silica porous and dense coatings, respectively, on low iron float glass. The coatings were characterized by spectral ellipsometry before and after thermal treatment (Table 4-13).

The purpose of the thermal treatment was the elimination of the SDA and the densification of the network by means of the reduction of the skeletal density of the gel to higher crosslinked chains and clusters, with the aim to achieve a stable structure. The presence of SDA in the formulation led to an expansion of the coating thickness before thermal treatment from 90 nm to 500 nm, as presented in Table 4-13. According to TGA measurements exposed in the Chapter 3, the temperature at which SDA starts decomposing is 180 ºC and it is expected to be totally decomposed at 350 ºC. However, the coatings treated at this temperature showed a significant decrease of $\theta_c^{H_2O}$, as explained in the previous section. On the other hand, cover glasses used for solar modules usually need to be tempered in order to achieve higher mechanical strength. This process consists of heating the glass to temperatures around 700 ºC followed by a forced cooling that creates surface and edge compression by air-quenching. The resulting mechanical properties can be modified if the glass is treated again at high temperatures. In order to avoid this effect, the selected temperature to build the final AR mono- and bi-layer stacks was lower than 240 ºC. Consequently, the SDA was totally removed from coating pores in the further step consisting of extraction with ethanol and water mixture. The resultant thickness of the coating treated at 240 ºC was ~130 nm as presented in Table 4-13. During the thermal treatment, the organic phase keeps a fixed coating volume up to 180 ºC when its decomposition starts. Below that temperature the coating contraction is only due to volumetric contraction of the polyfluoroalkyl-silica material. Above that temperature, the thickness shrinkage is due to the sum of the contraction of polyfluoroalkyl-silica walls and the thermal decomposition of the organic phase. It has been postulated [38] that thickness reduction is accompanied by a unidirectional contraction of the domain normal to the surface plane. The thickness of the coating grown with sol without SDA content shrank from ~90 nm to ~60 nm. This 33% contraction, that can be mostly attributed to the polyfluoroalkyl-silica phase densification, was useful to identify which part of the 74% thickness reduction for the coating with SDA came from the material itself. During the thermal treatment, the removal of solvent and water permits crosslinking to continue as unreacted hydroxyl and alkoxy groups

come in contact. However, the temperature applied herein was not high enough to allow neither the pyrolysis of unhydrolyzed alkoxy groups nor the removal of physically absorbed water. The required temperature for achieving the thermodynamically stable structure is not compatible with the maintenance of fluoroalkyl chains in the final network. Thus, the performance of the material treated at relatively low temperature should be validated under reliability tests in order to verify if the obtained structure is stable enough to endure real operation conditions.

The refractive index after the thermal treatment and ethanol-water extraction of SDA from pores, coincided with the target value, 1.22 (at 700 nm), which permits to achieve the optimized transmittance spectrum. The porosity, which was calculated by BEMA fitting [30] with the assumption that the network was formed by pure dense silica and voids, was close to 50%.

On the other side, after showing its suitability for the AR mono-layer, the FAS21-C2 sol was also used to compose the AR bi-layer stack. A dense silica coating was deposited as inner coating (sintered at 550 ºC) followed by FAS21-C2 deposition to form the external porous coating. The ellipsometric parameters were also measured and the values obtained from Cauchy [29] and BEMA [30] fitting are summarized in Table 4-14. The thickness and refractive index obtained for polyfluoroalkyl-silica porous coating were similar than those obtained for the coating directly grown on glass. The morphology of these coatings is presented in Figure 4-13, where Figure 4-13a is referred to the surface of the FAS21 coating deposited on glass and Figure 4-13b corresponds to FAS21 as external coating deposited on dense silica coating. The structure of both was quite similar and homogeneous, being formed by little grains which differed on size. The coating deposited on glass was formed by grains of 4±2 nm size and the coating deposited on a silica dense coating presented 12±3 nm grains. The roughness, R_q, was as low as 0.6 nm in both cases. The surface of FAS21-silica dense coating grown from the sol without SDA showed a different structure (Figure 4-13c). The morphology of the surface was compact, without grains, holes or pores. However, there are white zones throughout the surface that correspond to differences in height and may come from agglomeration. The roughness R_q of this sample was 4.5 nm, relatively higher than the values obtained for the porous coatings. The presence of SDA, apart from being porogen, also participated in the achievement of homogeneous and smooth surfaces.

The polyfluoroalkyl-silica porous and dense coatings grown on glass were further analyzed by EEP. Refractive index (at 700 nm) was obtained from ellipsometric data fitting recorded at different relative humidity values during adsorption and desorption steps and depicted in Figure 4-14a. This allowed to obtain the amount of adsorptive (water vapor) inside of pores from the change of optical characteristics of the coatings at several water partial pressures. Adsorption-desorption curves of FAS21-silica porous and dense coatings treated at 240 ºC are showed in Figure 4-14b. As expected, differences of water absorption between dense and porous coatings were detected due to their different structure. Optical properties of FAS21 dense coating showed an initial slight increase of the refractive index that was maintained constant from 10% RH up to the highest RH conditions. This slight increase at lower RH conditions may be associated with the formation of a water mono-layer on the top of the surface whereas no water adsorption was observed. On the other hand, the porous coatings displayed the typical behavior of mesoporous materials associated with type IV-V isotherms according to IUPAC classification of porous materials. Therefore, according to these measurements, water vapor enters inside the pores of FAS21-silica coating.

The real volume of pores, calculated for the FAS21-silica porous coating by taking FAS21-silica dense coating as the reference material, resulted in 47.5% and was filled with water vapor at partial pressure > 0.8, as observed in the adsorption-desorption isotherm. Little adsorption was observed at the lower RH conditions, up to capillary adsorption zone, which is characterized by a steep increase of adsorbed volume, detected herein at 60% RH. During capillary desorption, the decrease of the adsorbed water happened at RH values around 55%. The differences among adsorption-desorption branches are associated to the difference in the radius of curvature of condensed liquid meniscus during the adsorption and desorption processes in the mesopores [39]. The shape of these hysteresis loops may be usually correlated according to an empirical classification in four types of curves (H1-H4) given by IUPAC. The studied coating was identified as H1, characterized by shaped by parallel branches, which are associated to well-defined cylindrical-like pore channels or agglomerates of approximately uniform spheres as displayed by the AFM images of Figure 4-13.

Table 4-13. Refractive index at 700 nm (n), thickness before (d_{raw}) and after thermal treatment (d) and apparent porosity of porous and dense FAS21-silica coating treated at 240 ºC.

Coating	n (at 700 nm)	d (nm)	d_{raw} (nm)	Apparent porosity (%)
F240	1.22	128.2	500.5	51.3
F240-no SDA	1.42	60.8	89.4	-

Table 4-14. Refractive index at 700 nm (n) and thickness (d) of inner and external coatings of the AR bi-layer stack and apparent porosity of the external FAS21-silica coating treated at 240 ºC.

Coating	n_{inner} (at 700 nm)	d_{inner} (nm)	$n_{external}$ (at 700 nm)	$d_{external}$ (nm)	Apparent porosity (%)
D5F240	1.46	107.6	1.22	131.1	50.0

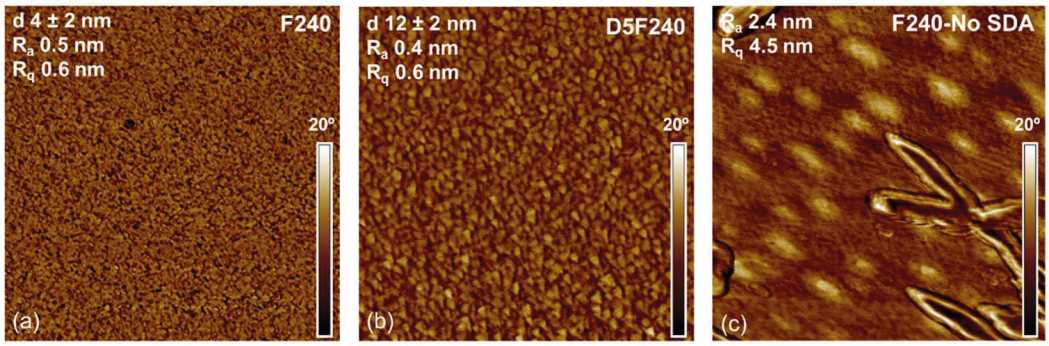

Figure 4-13. AFM phase images (1 μm x 1 μm) of the FAS21-silica porous mono-layer (a), bi-layer (b) and FAS21-silica dense coating (c) all treated at 240 ºC.

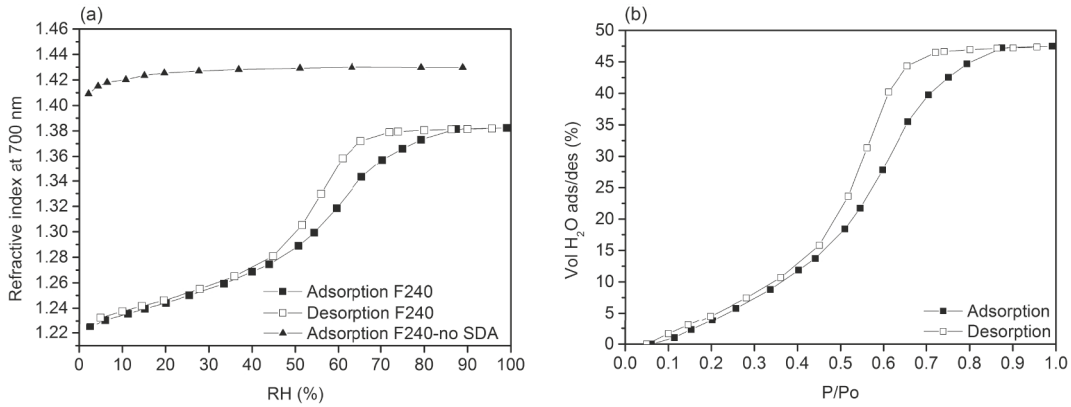

Figure 4-14. Refractive index (at 700 nm) as a function of relative humidity of FAS21-silica porous and dense coatings (a) and adsorption-desorption isotherm (b) of FAS21-silica porous coating treated at 240 ºC.

4.5.3. Surface free energy of optimized coating stacks with the longest polyfluoroalkyl chain

The SFE of optimized polyfluoroalkyl-silica coating stacks was determined by measuring the contact angle of the surface with water (γ_{lv}^{p}=51 mN/m; γ_{lv}^{d}=21.8 mN/m), methanol (γ_{lv}^{p}=4.3 mN/m; γ_{lv}^{d}=18.2 mN/m), and n-hexadecane (γ_{lv}^{p}=0 mN/m; γ_{lv}^{d}=27.5 mN/m). The corresponding contact angle and the surface free energy calculated by Owens-Wendt method are shown in Figure 4-15. The behavior of porous coatings grown from FAS21-C2 sol treated at 200 and 240 ºC and deposited either directly on low iron float glass (AR mono-layer) or on dense silica inner coating (AR bi-layer) was characterized. Polyfluoroalkyl-silica dense coating treated at 240 ºC was also studied for comparison.

All layer stacks exhibited $\theta_c^{H_2O}$ around 100º. Among AR layer stacks, the main differences were found between the coatings treated at 200 or 240 ºC. $\theta_c^{H_2O}$ of the mono-layer treated at 200 ºC was ~105º while the one treated at 240 ºC showed ~99º. The bi-layers exhibited a few grades below the values of their mono-layer counterparts.

Polyfluoroalkyl-silica porous coating stacks showed a very low SFE between 17-20 mJ/m², depending on thermal treatment. Indeed, stacks treated at 200 ºC exhibit lower SFE values than those treated at 240 ºC. However, the polyfluoroalkyl-silica dense coating presented the lowest surface free energy, 15 mJ/m². The surface polarity was in all cases lower than 14% of the total surface free energy, which meant that the wetting was driven by the weak dispersive molecular interactions [25]. The slight change in the FAS21-silica porous coating structure led by the presence of the inner dense coating, provoked a slight increase on the surface polarity. Polar part of F200 increased from 7.5 to 11% when the coating was deposited as the mono-layer or as external layer in the bi-layer, while F240 experimented an increase from 11.8 to 14% for similar stackings. Surface energy properties of pure PFTE, highly inert and non-polar, obtained by Wood III et al. [25] applying Owens-Wendt method on a variety of commercial PFTE, were 18.0 mJ/m² (total SFE) and 0 mJ/m² for the polar component.

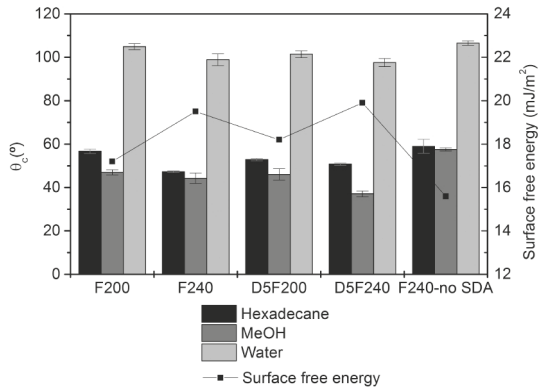

Figure 4-15. Contact angle (θ_c) of AR layer stacks prepared with FAS21-C2 sol treated at 200 and 240 ºC, with three test liquids and surface free energy.

Apart from the low SFE values compared to those obtained for methyl-silylated porous silica coatings presented in section 4.4.1, contact angles obtained for alcohol and n-hexadecane were higher, and displayed low dispersion. The low SFE achieved for the optimized AR coating stacks are considered outstanding taking into account both the low molar quantity of the non-hydrolyzable polyfluoroalkyl alkoxysilane required and the low roughness exhibited by the coatings, compiled in Table 4-15.

Table 4-15. Water contact angle ($\theta_c^{H_2O}$), surface free energy (SFE), their polar and dispersive components and roughness R_q of AR layer stacks.

Coating	$\theta_c^{H_2O}$ (º)	SFE (mJ/m²)	Polar component (mJ/m²)	Dispersive component (mJ/m²)	R_q* (nm)
F200	104.9	17.2	1.3	15.9	3.5
F240	98.9	19.5	2.3	17.2	0.6
D5F200	101.4	18.2	2	16.2	1.4
D5F240	97.6	19.9	2.8	17.1	0.6
F240-no SDA	106.5	15.6	1.2	14.4	4.5

*determined by AFM

It is well known that the wetting of a surface by a liquid is strongly affected by its topography [40][41][42] since surface roughness decreases the spreading of the wetting liquid. Miller et al. [43] prepared PTFE thin films and controlled the roughness R_q at 8 nm and 80 nm (measured by AFM). They observed that roughness strongly influenced the wetting behavior of water at the surface of PTFE thin films. The smother surface permitted to obtain hydrophobic behavior (90-100º) while the roughest surface presented superhydrophobic properties (150º).

Considering the $\theta_c^{H_2O}$ achieved for the films with lowest roughness, formed by such a highly inert and low wettable material, the results obtained herein with such a low polyfluoralkyl content could not have been better with these low roughness values (R_q < 3.5 nm).

However, as exposed above and deeply discussed in section 4.5.4, roughness is a parameter that also affects optical properties, particularly, light diffusion and scattering [44].

4.5.4. Transmittance and reflectance of optimized coating stacks with the longest polyfluoroalkyl chain

The total transmittance and reflectance spectra as well as the diffuse reflectance are represented in Figure 4-16 and Figure 4-17. Figure 4-16 shows the total transmittance and reflectance of AR mono- and bi-layer stacked on both sides of low iron float glass treated at 200 and 240 ºC, before and after ethanol-water extraction. Figure 4-17 shows the diffuse reflectance of AR mono- and bi-layer stacked on two sides of low iron float glass. The integrated values in the 300-2000 nm spectral range are compiled in Table 4-16.

The spectra collected in Figure 4-16 show how the effect of SDA removal from pores on coatings treated at both temperatures affects mainly the visible bandwidth. This effect is consistently stronger for the stacks treated at 200 ºC.

The mono- and bi-layers treated at 240 ºC provided outstanding transmittance properties in the whole spectral range compared to those treated at 200 ºC, achieving an integral transmittance gain of 6.4% for the mono-layer and 7.1% for the bi-layer treated at 240 ºC versus 4.9% and 5.1% for the mono- and bi-layer stacks treated at 200 ºC. Maximum values were obtained at 575 nm for the AR mono-layers and between 530-555 nm for the case of AR bi-layer stacks. The antireflective behavior obtained by the polyfluoroalkyl-silica AR layer stacks treated at 240 ºC were as outstanding as those obtained by the baseline silica mono- and bi-layer stacks. As proven therein, the presence of the inner dense coating in the bi-layer allows to achieve higher values in the NIR bandwidth in comparison to the AR mono-layer.

The reflectance of an ideal smooth surface is described by Fresnel equations, and depends only on the complex refractive index ($\tilde{n} = n + i\kappa$) of the incident and exit media as well as the incidence angle. Ginneken et al. [44] developed a reflection model for isotropic rough surfaces based on the local reflection properties of the material and the topography of the material, i.e., the complex refractive index and the roughness, determining the amount of radiation that is

reflected in the specular direction or diffusely scattered. Surface roughness increases diffuse reflectance, generating a lobe around the specular direction. Additionally, the light transmitted to the bulk of the material and to the external medium after multiple internal reflections produces a diffuse transmittance pattern, which reduces the direct transmittance. Given that concentrated solar systems, in contrast to flat panels [45], only make use of direct solar radiation, the scattering of the incoming solar radiation must be minimized in order to avoid related electrical losses. Consequently, the AR coatings developed herein have been designed to exhibit low roughness, with $\theta_c^{H_2O}$ limited to 100º.

In this case, in which the material is a composite dielectric containing silica, fluorocarbon moiety and voids, diffuse reflectance has been analyzed to discard light scattering coming from differences in phase, especially in view of the high reflectance of pure PFTE [37].

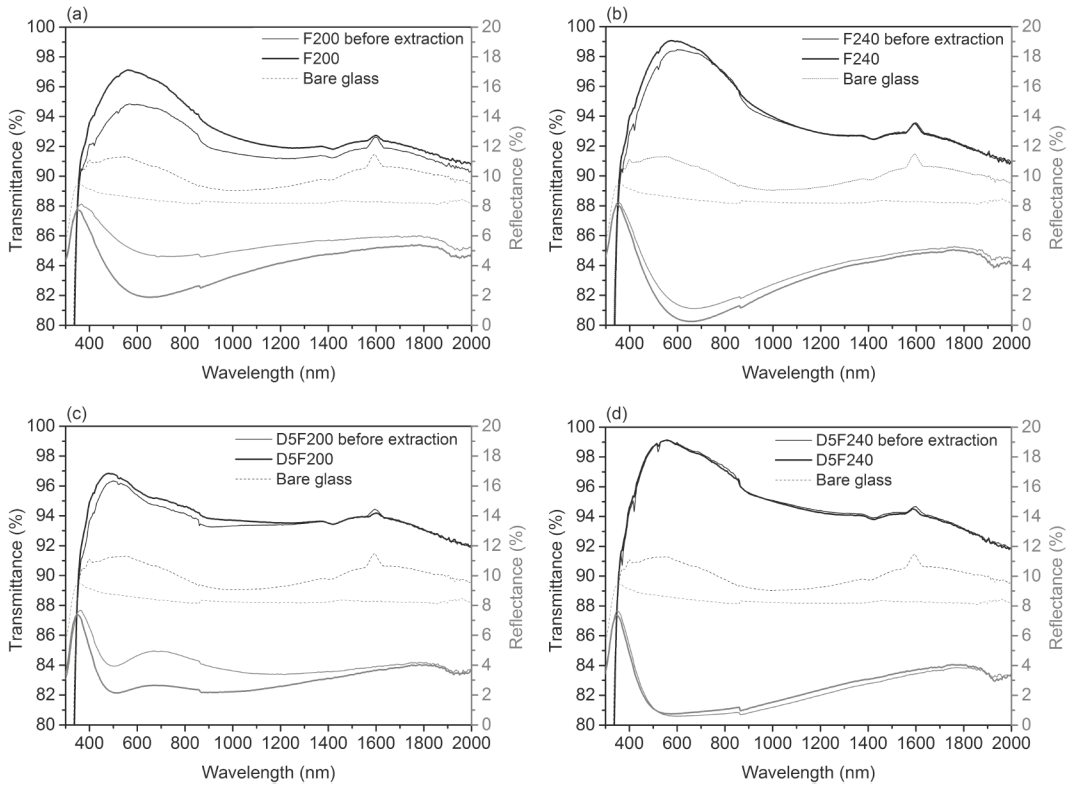

Figure 4-16. Transmittance and reflectance spectra of AR mono-layer (a, b) and bi-layer (c, d) stacks prepared with FAS21-C2 sol treated at 200 and 240 ºC.

The diffuse reflectance spectra of AR mono- and bi-layers stacked on both sides of glass in Figure 4-17 show that most part of the diffuse reflectance is produced in the visible range. Furthermore, stacks treated at 200 ºC exhibit higher values over those treated at 240 ºC.

Diffuse reflectance values in the 380-780 nm range were around 0.5% for stacks treated at 200 ºC versus 0.3% for stacks treated at 240 ºC. As explained before, a higher temperature of the thermal treatment, provide the achievement of the desirable final material, given that removal of solvent and water allows unreacted hydroxyl and alkoxy groups to get in contact.

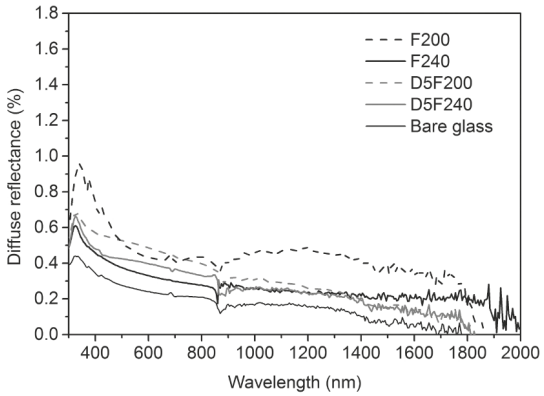

Figure 4-17. Diffuse reflectance spectra of AR mono-layer and bi-layer stacks prepared with FAS21-C2 sol treated at 200 and 240 ºC.

Table 4-16. Total transmittance (τ), total reflectance (ρ) and diffuse reflectance (ρ_{dif}) integrated values in the wavelength range 300-2000 nm of the FAS21-silica AR layers stacked on both sides of low iron float glass.

	τ (%)	ρ (%)	ρ_{dif} (%)
F200	94.5	3.3	0.5
F240	95.9	2.2	0.3
D5F200	94.7	2.8	0.4
D5F240	96.5	1.8	0.3
Bare glass	90.1	8.5	0.2

4.5.5. Optical performance as a function of humidity

Transmittance and reflectance values were calculated by using Cauchy parameters and thickness of the polyfluoroalkyl-silica porous and dense coatings treated at 240 ºC, obtained from experimental ellipsometric data fitting, using CODE® software. Optical constants of the polyfluoroalkyl-silica porous and dense coatings at different RH conditions were analyzed in section 4.5.2.

Despite the low surface free energy achieved, the polyfluoroalkyl-silica porous adsorbed water when they were exposed to high RH as explained before. Refractive index grew from 1.22 (at 700 nm) at low RH conditions to 1.38 at high RH conditions.

Spectral transmittance and reflectance of AR mono- and bi-layer stacks were thus calculated for each environmental RH, as shown in Figure 4-18. Figure 4-18a shows integrated transmittance of F240 and D5F240 stacks at several RH values, and Figure 4-18b shows integrated reflectance.

Both mono- and bi-layer, presented transmittance values between 96.0-97.0% at RH below 50%. Although bi-layer shows 97% at the lowest relative humidity conditions, they equal at RH of 60%. Above this RH value, bi-layer shows integrated transmittance value below that of mono-layer, both exhibiting values between 94.0-94.3% at 100% RH.

Compared to the methyl-silylated mono- and bi-layers, which showed independent transmittance values around 96%, polyfluoroalkyl moieties are not properly positioned in the inside of the pores, since the coating is absorbing water, what consequently changes the optical properties. Once again, the HMDS functionalization applied as a post-treatment, in comparison to FAS21 incorporated in the sol, presents the advantage that hydrophilic –OH group bonds are replaced by hydrophobic –Si-$(CH_3)_3$ group bonds in the whole specific surface of the porous coating.

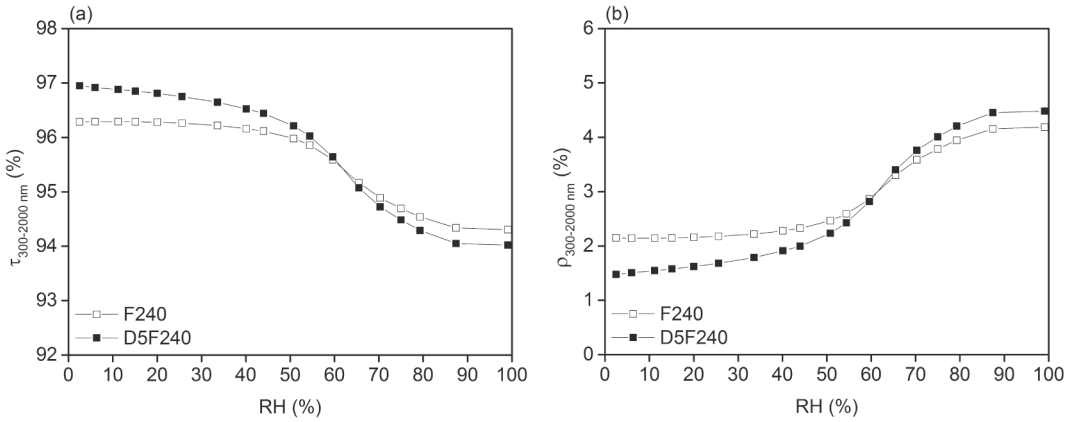

Figure 4-18. Integrated (300-2000 nm) transmittance (a) and reflectance (b) calculated from refractive index (at 700 nm) fitted as function of environmental RH for mono- and bi-layer stack.

4.5.6. Cohesion and adhesion properties determined by nanoscratch testing

The critical loads (Lc) at which first failures occurred were identified by microscope analysis of scratches as presented in Figure 4-19 for polyfluoroalkyl mono- and bi-layers treated at 240 ºC. Loss of cohesion represented by critical load Lc1, appeared on F240 mono-layer at 0.8±0.2 mN, while Lc2, related to adhesive failure of the coating to substrate, appeared at 1.8±0.3 mN. Compared to silica porous coatings (results presented in section 4.4.5), the critical loads at which cohesion and adhesion occurred were drastically reduced since the polyfluoroalkyl functionalized silica coatings were treated at relatively lower temperature.

The cohesion failure Lc1 of polyfluoroalkyl-silica porous coating deposited on the dense coating, bi-layer D5F240, was remarkably improved, reaching 2.6±0.4 mN. In addition, no detachment from the substrate was observed since Lc2 failure was not detected in any case. This fact revealed a substantially improvement of adherence if the porous coating is grown on dense silica coating instead of being grown directly on glass.

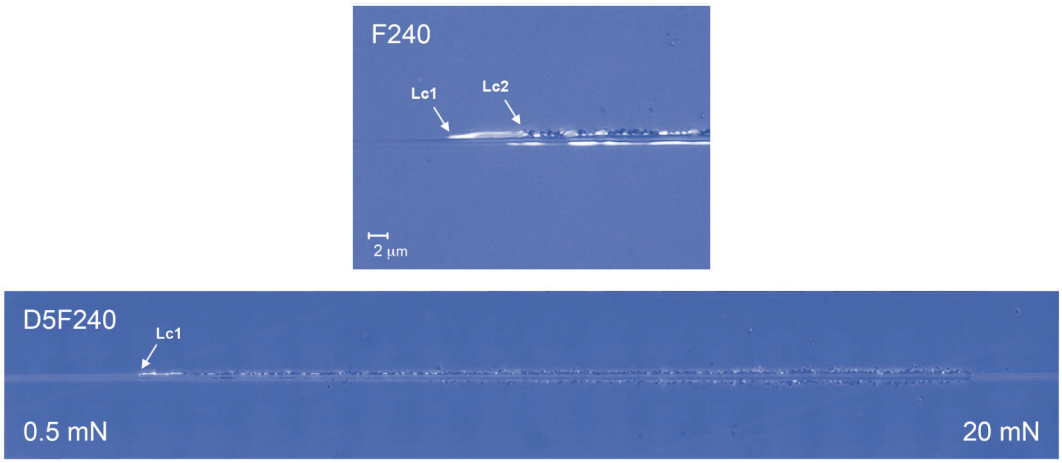

Figure 4-19. Micrographs panoramas of scratches drawn on F240 and D5F240 stacks and their labeled failures Lc1 and Lc2.

4.5.7. Mechanical properties

The loading-unloading indentation curves of single porous mono-layer F240 (maximum load 10 µN) and bi-layer D5F250 (maximum load 20 µN) are represented in Figure 4-20. For F240 coating, indentation depth at 10 µN reached 18-20 nm for polyfluoroalkyl containing coating treated at 240 ºC, which represents ~14% of the total coating thickness. However, the low roughness exhibited by the coating allowed to obtain proper measurements since low

dispersion (less than 10%) and good repeatability were obtained even for a such low load. Calculated from nanoindentation curves, F240 hardness was 0.70±0.05 GPa and elastic modulus was 17.04±1.21 GPa. As expected, the mechanical properties of the coating treated at 240 ºC were considerably lower than those of coatings sintered at 350-550 ºC (section 4.4.6). Although the porosity of both coatings was around 50%, the highest consolidation achieved by the coating treated at 550 ºC led to reach higher hardness and elastic modulus.

In the case of the AR bi-layer stack composed by polyfluoroalkyl-silica as external coating, the effect was opposite to the effect observed between M5 and B5. Whereas the grain size of polyfluoroalkyl-silica porous as mono-layer was 4 and 12 nm as external coating of the bi-layer, the porosity of polyfluoroalkyl-silica porous mono-layer was slightly higher compared to that of the external coating of the bi-layer. The outcome was that polyfluoroalkyl-silica porous deposited on the dense-structured silica coating sintered at 550 ºC, exhibited a slightly increase of hardness from 0.70±0.05 to 0.85±0.05 GPa and elastic modulus from 17.04±1.2 to 22.70±1.1 GPa.

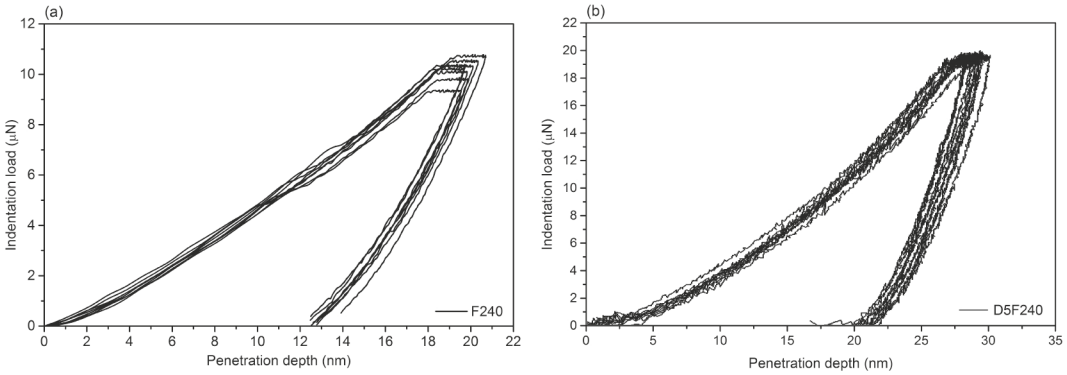

Figure 4-20. Nanoindentation curves obtained for polyfluoroalkyl-silica mono-layer (a) and bi-layer (b) treated at 240 ºC.

4.5.8. Assessment of coating degradation after damp heat aging

Polyfluoroalkyl-silica AR layer stacks with the most balanced and successful features were tested under damp heat conditions according to IEC 61215 and IEC 62108 standards. Having proven that antireflection properties of FAS21-silica porous coatings treated at 240 ºC were as suitable as the ones displayed by the baseline coating, the next step in this work was aimed to ensure the required long-term durability under the most demanding test among those contained in the IEC standards [34]. Acknowledging the importance of the sintering

temperature in the final properties of the coatings, the design of the thermal treatment for these coatings was based on the contact angle and low surface energy properties. The main objective was to assess the durability of the optical properties of the polyfluoroalkyl-silica coating treated at such a low temperature as part of the AR layer stacks. The bi-layer stack, whose configuration contributes to implement the broadband antireflection properties, was then considered due to the role of the inner dense coating as alkali-diffusion barrier.

The evolution of integrated transmittance values in the 300-2000 nm range recorded on mono- and bi-layer stacks with F240 as external coating deposited on both sides of low iron float glass during their exposure in the chamber at 85 ºC/85% RH is presented in Figure 4-21. It is observed therein that the mono-layers displayed a constant deterioration of their optical properties along the exposure time within the chamber. The behavior of the bi-layer stacks, on the other hand, was outstanding, since the transmittance remained constant along the exposure, showing no degradation of the optical properties at the end of the test. Indeed, the mono-layers lost 6% of their initial transmittance while the bi-layers lost a negligible 0.2% which corresponded to an 8.3% gain over aged bare glass as reported in Table 4-17.

The microscope images collected in Figure 4-23 show the appearance of surfaces before and after exposure of AR mono- and bi-layer to damp heat aging. Fresh coatings presented a smooth and homogenous surface that was altered after ageing. The F240 coating performed in a different way to the stress produced along test depending on where it was deposited, directly on glass or on the inner dense silica coating. The mono-layer at the end of the test presented circular cracks of 40-100 μm diameter, showing that forces acting in the coating found the minimization of tension by cracking in a circle shape. However, F240 deposited as external coating on the AR bi-layer stack showed minimum damage after test, which revealed that the cohesion and adhesion forces of polyfluoroalkyl-silica deposited on dense-structured silica where higher and robust enough to withstand the aggressive test conditions.

Coating thickness and refractive index from Cauchy fitting of ellipsometric data as well as $\theta_c^{H_2O}$ after aging are also presented in Table 4-17. These results were perfectly consistent with the obtained antireflection properties and served to explain the behavior of each layer stack. The F240 mono-layer suffered also a thickness reduction and an increase of its refractive index, probably due to the collapse of the mesostructure, since it would not have achieved the thermodynamically stable structure at this temperature. However, the external F240 in the bi-

layer stack maintained indeed their ellipsometric properties, and thus the optical thickness, refractive index and the porosity of the coating. Therefore, the presence of an inner dense-structured coating sintered at high temperature was key to implement a crucial effect on the durability properties of the polyfluoroalkyl-silica porous coating deposited on it. Apart from the broadband antireflection properties displayed by this stack, the incorporation of the inner layer plays an important role on durability which may be caused by the prevention of alkali diffusion from glass to the porous coating and by the positive effect on the adherence of the external polyfluoroalkyl-silica porous coating. After the damp heat exposure, both mono- and bi-layer stacks displayed $\theta_c^{H_2O}$ values of ~113º, slightly higher than initial values.

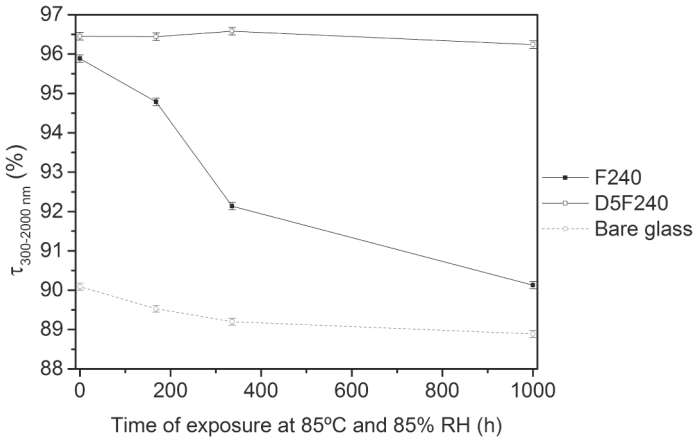

Figure 4-21. Evolution of integrated transmittance (300-2000 nm) of AR mono- and bi-layer stacks at different times of exposure to damp heat test conditions.

Total transmittance and reflectance as well as diffuse reflectance of polyfluoroalkyl-silica AR layer stacks after damp heat aging are depicted in Figure 4-22. Figure 4-22a show transmittance and reflectance spectra, respectively, recorded between 300-2000 nm for mono- (F240) and bi-layer (D5F240) stacks treated at 240 ºC, while Figure 4-22b shows the diffuse reflectance spectra for the same AR layer stacks. As expected, transmittance and reflectance spectra of the bi-layer maintained its broadband AR behavior, while mono-layer spectra revealed a loss of optical performance. Diffuse reflectance spectrum of the bi-layer stack showed no changes from the initial one. However, the damage produced in the mono-layer material after aging increased the diffuse reflectance, which reached 0.6% in the visible wavelength range.

Table 4-17. Thickness (d), refractive index (n) at 700 nm, oneself loss of τ, τ gain over aged bare glass, and diffuse reflectance (ρ_{dif}) in the 300-2000 nm spectral range; and water contact angle ($\theta_c^{H_2O}$) of AR layer stacks after damp heat aging.

Coating	d (nm)	n (at 700 nm)	Oneself loss τ (%)	τ gain (%)	ρ_{dif} (%)	$\theta_c^{H_2O}$ (º)
F240	95.4	1.31	6.0	1.4	0.5	113.0±0.8
D5F240	131.1*	1.22*	0.2	8.3	0.2	112.8±0.8

* External coating in D5F240

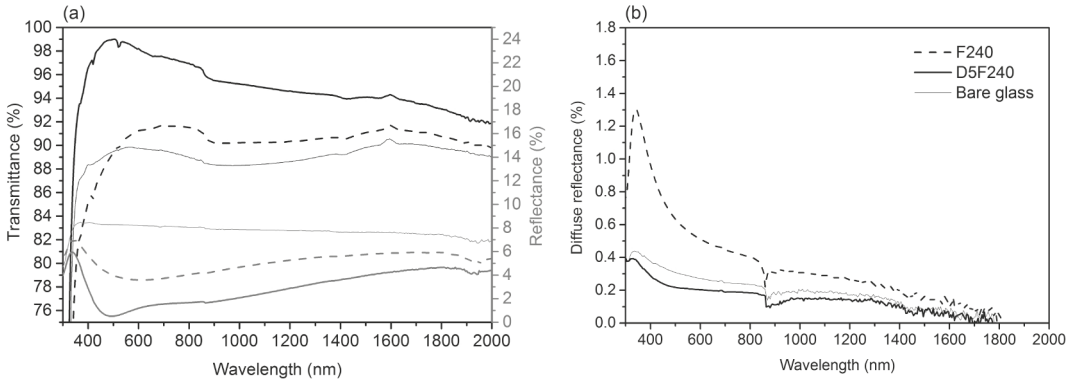

Figure 4-22. Total transmittance and reflectance (a) and diffuse reflectance (b) spectra of AR mono- and bi-layer stacks after 1000 h of exposure to damp heat test.

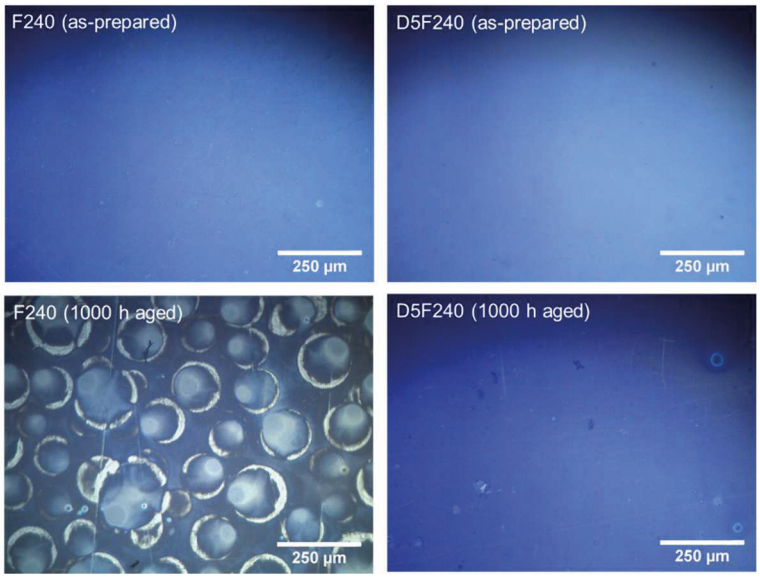

Figure 4-23. Optical microscope images of AR mono- and bi-layer stacks surfaces before (as-prepared) and after 1000 h of exposure to damp heat test.

4.6. Conclusions

To overcome the impact of the soiling, which has a direct impact on operational expenditures in PV plants, the attainment of hydrophobic coatings with low surface free energy was approached by two different routes.

The methyl-silylating post-treatment succeed in replacing Si-OH bond groups by Si-CH_3 both internally and externally. A 10% decrease of the porosity was detected according to ellipsometry measurements, also evidenced by the grain downsizing assessed by the AFM image analysis. The consistent increase of the refractive index was accompanied by a slight decrease of the antireflection properties. However, HMDS treated AR layer stacks showed a high environmental versatility. Optical properties resulted to be inalterable when exposed to high RH conditions, transmittance being around 96% in the range 300-2000 nm.

Through the second route, a low surface energy coating was achieved by the addition of polyfluoroalkyl silanes to the baseline silica sol-gel coating resulting in a covalently bonded polyfluoroalkyl-silica network. The increase of polyfluoroalkyl chain length linked to silicon central atom involved an increase on $\theta_c^{H_2O}$ values, accompanied by an increase of coating thickness and the decrease of integrated transmittance. A final optimized coating with superb transmittance properties treated at 240 ºC was attained. The surface free energy was around 19-20 mJ/m^2, for the desired low roughness values (R_q 0.6 nm) required for obtaining low scattering of the incoming solar radiation. Despite the low surface free energy displayed, the polyfluoroalkyl-silica porous network absorbed water inside the pores when exposed to high RH conditions. The polyfluoroalkyl bi-layer stack showed a transmittance of 97% at low RH conditions and around 94% at high RH conditions.

Concerning differences on the porous coating grown as AR mono-layer or as external coating of the AR bi-layer stack, substantial differences on the coating formation emerged. Porous layer grown on the dense-structured coating showed higher porosity and grain size. In any case, these characteristics led to achieve the best adhesion properties and AR durability performance. The dense structure played an important role regarding durability properties providing a barrier against alkali diffusion and avoiding mesostructure collapse. AR bi-layer stacks subjected to damp heat aging showed a transmittance decrease of only 0.8% if sintered at 350 ºC, and close to 0% if sintered at 550 ºC. Bi-layer stacks sintered at 550 ºC and HMDS treated exhibited a gain of 8.2%, while polyfluoroalkyl-silica bi-layer exhibited a gain of 8.3%

over bare glass after aging test. In the case of polyfluoroalkyl-silica porous coating, the coating appearance after degradation provoked by the aggressive damp heat aging led to the conclusion that the presence of the inner dense-structured layer was particularly mandatory.

References

[1] K. Jeevajothi, D. Crossiya, R. Subasri, Non-fluorinated, room temperature curable hydrophobic coatings by sol-gel process, Ceram. Int. 38 (2012) 2971–2976.

[2] C. Tao, H. Yan, X. Yuan, Q. Yin, J. Zhu, W. Ni, L. Yan, L. Zhang, Sol-gel based antireflective coatings with superhydrophobicity and exceptionally low refractive indices built from trimethylsilanized hollow silica nanoparticles, Colloids Surf. A Physicochem. Eng. Asp. 509 (2016) 307–313.

[3] J. Zhi, L.Z. Zhang, Durable superhydrophobic surface with highly antireflective and self-cleaning properties for the glass covers of solar cells, Appl. Surf. Sci. 454 (2018) 239–248.

[4] S.-D. Wang, S.-S. Luo, Fabrication of transparent superhydrophobic silica-based film on a glass substrate, Appl. Surf. Sci. 258 (2012) 5443–5450.

[5] L. Ye, X. Zhang, Y. Zhang, Y. Li, W. Zheng, B. Jiang, Three-layer tri-wavelength broadband antireflective coatings built from refractive indices controlled silica thin films, J. Sol-Gel Sci. Technol. 80 (2016) 1–9.

[6] T.-J. Ha, H.-H. Park, S.-B. Jung, H. Ryu, B.-G. Yu, Investigation of the effect of calcination temperature on HMDS-treated ordered mesoporous silica film., J. Colloid Interface Sci. 326 (2008) 186–190.

[7] K.C. Hsu, K.J. Chao, S.F. Chen, H.K. Li, P.Y. Wu, The effect of surfactant removal on continuous mesoporous ultra-thin silica films-A study by X-ray reflectivity, X-ray diffraction and Kr adsorption, Thin Solid Films. 517 (2008) 686–690.

[8] C. Himcinschi, M. Friedrich, S. Frühauf, I. Streiter, S.E. Schulz, T. Gessner, M.R. Baklanov, K.P. Mogilnikov, D.R.T. Zahn, Ellipsometric study of the change in the porosity of silica xerogels after chemical modification of the surface with hexamethyldisilazane, Anal. Bioanal. Chem. 374 (2002) 654–657.

[9] G. San Vicente, R. Bayón, N. Germán, A. Morales, Surface modification of porous antireflective coatings for solar glass covers, Sol. Energy. 85 (2011) 676–680.

[10] G. San Vicente, R. Bayón, N. Germán, A. Morales, Long-term durability of sol-gel porous coatings for solar glass covers, Thin Solid Films. 517 (2009) 3157–3160.

[11] H. Ye, X. Zhang, Y. Zhang, L. Ye, B. Xiao, H. Lv, B. Jiang, Preparation of antireflective coatings with high transmittance and enhanced abrasion-resistance by a base/acid two-step catalyzed sol-gel process, Sol. Energy Mater. Sol. Cells. 95 (2011) 2347–2351.

[12] Y. Yuan, Y. Chen, W.L. Chen, R.J. Hong, Preparation, durability and thermostability of hydrophobic antireflective coatings for solar glass covers, Sol. Energy. 118 (2015) 222–231.

[13] Y.-K. Chen, K.-C. Chang, K.-Y. Wu, Y.-L. Tsai, J.-S. Lu, H. Chen, Fabrication of superhydrophobic silica-based surfaces with high transmittance by using tetraethoxysilane precursor and different polymeric species, Appl. Surf. Sci. 255 (2009) 8634–8642.

[14] J.T. Luo, H.C. Wen, Y.M. Chang, W.F. Wu, C.P. Chou, Mesoporous silica reinforced by silica nanoparticles to enhance mechanical performance, J. Colloid Interface Sci. 305 (2007) 275–279.

[15] C.H. Chen, S.Y. Li, A.S.T. Chiang, A.T. Wu, Y.S. Sun, Scratch-resistant zeolite anti-reflective coating on glass for solar applications, Sol. Energy Mater. Sol. Cells. 95 (2011) 1694–1700.

[16] M. Hikita, K. Tanaka, T. Nakamura, T. Kajiyama, A. Takahara, Super-liquid-repellent surfaces prepared by colloidal silica nanoparticles covered with fluoroalkyl groups super-liquid-repellent surfaces prepared by colloidal silica nanoparticles Covered with Fluoroalkyl Groups, Langmuir. 21 (2005) 7299–7302.

[17] A. Nakajima, K. Abe, K. Hashimoto, T. Watanabe, Preparation of hard super-hydrophobic films with visible light transmission, Thin Solid Films. 376 (2000) 140–143.

[18] B.J. Basu, T. Bharathidasan, C. Anandan, Superhydrophobic oleophobic PDMS-silica nanocomposite coating, Surf. Innov. 1 (2013) 40–51.

[19] E. Shmueli, A. Leikovich, Substrate having a self cleaning anti-reflecting coating and method for its preparation, US 20120009429A1, 2012.

[20] S. Mukhopadhyay, D. Nalewajek, Fluorinated antireflective coating, US2012247531A1, 2011.

[21] M. Mitterhuber, Material for coating porous anti-reflection layers, e.g. in solar installations, contains hydrolysable silane and fluorinated organosilane and makes the coated layer more resistant to abrasion, weathering, water and dirt, DE102007057908A1, 2007.
[22] D.K. Owens, R.C. Wendt, Estimation of the surface free energy of polymers, J. Appl. Polym. Sci. 13 (1969) 1741–1747.
[23] R.J.H. Voorhoeve, Organohalosilanes, New York, 1967.
[24] S.V. Stefan, A.R. Sanger, K.T. Chuang, Mechanism of silation of silica with hexamethyldisilazane, J. Phys. Chem. B. 104 (2000) 983–989.
[25] D.L. Wood III, C. Rulison, R.L. Borup, Surface properties of PEMFC gas diffusion layers, J. Electrochem. Soc. 157 (2010) B195–B206.
[26] J.C. Brinker, E.P. Roth, G.W. Scherer, D.R. Tallant, Structural evolution during the gel to glass conversion, J. Non. Cryst. Solids. 71 (1985) 171–185.
[27] F. Orgaz-Orgaz, Gel to glass conversion: densification kinetics and controlling mechanisms, J. Non. Cryst. Solids. 100 (1988) 115–141.
[28] D. Kundu, H. Zhou, I. Honma, Thermally induced structural changes of lamellar and one-dimensional hexagonal mesoporous silica thin films, J. Mater. Sci. Lett. 17 (1998) 2089–2092.
[29] A.L. Cauchy, Sur la réfraction et la réflexion de la lumière, Bull. Des Sci. Mathématiques. XIV (1830) 6–10.
[30] D.A.G. Bruggeman, Berechnung verschiedener physikalischer konstanten von heterogenen substanzen. I. Dielektrizitätskonstanten und leitfähigkeiten der mischkörper aus isotropen substanzen, Ann. Phys. 24 (1935) 636–664.
[31] M. Mizuhashi, Y. Gotoh, Glass body provided with an alkali diffusion-preventing silicon oxide layer, US4485146, 1984.
[32] P.A. Steinmann, Y. Tardy, H.E. Hintermann, Adhesion testing by the scratch test method: The influence of intrinsic and extrinsic parameters on the critical load, Thin Solid Films. 154 (1987) 333–349.
[33] M. Herrmann, F. Richter, S.E. Schulz, Study of nano-mechanical properties for thin porous films through instrumented indentation: SiO_2 low dielectric constant films as an example, Microelectron. Eng. 85 (2008) 2172–2174.
[34] I. Petrina, A.B. Cueli, J. Moracho, A.R. Lagunas, CENER experience testing CPV modules, Energ. Int. 123 (2013) 68–71.
[35] E.G. Shafrin, W.A. Zisman, Constitutive relations in the wetting of low energy surfaces and the theory of the retraction method of preparing monolayers, J Phys Chem. 1046 (1957) 519–524.
[36] D.L. Schmidt, B.M. DeKoven, C.E. Coburn, G.E. Potter, G.F. Meyers, D.A. Fischer, Characterization of a New Family of Nonwettable, Nonstick Surfaces, Langmuir. 12 (1996) 518–529.
[37] A. Springsteen, Standards for the measurement of diffuse reflectance - An overview of available materials and measurement laboratories, Anal. Chim. Acta. 380 (1999) 379–390.
[38] D. Grosso, F. Cagnol, G.J.D.A.A. Soler-Illia, E.L. Crepaldi, H. Amenitsch, A. Brunet-Bruneau, A. Bourgeois, C. Sanchez, Fundamentals of mesostructuring through evaporation-induced self-assembly, Adv. Funct. Mater. 14 (2004) 309–322.
[39] M.R. Baklanov, K.P. Mogilnikov, V.G. Polovinkin, F.N. Dultsev, Determination of pore size distribution in thin films by ellipsometric porosimetry, J. Vac. Sci. Technol. B. 18 (2000) 1385.
[40] R.N. Wenzel, Resistance of solid surfaces to wetting by water, Ind. Eng. Chem. 28 (1936) 988–994.
[41] N.K. Adam, The physics and chemistry of surfaces, 3rd edit, Geoffrey Cumberlege, London, 1941.
[42] A.B.D. Cassie, S. Baxter, Wettability of porous surfaces, Trans. Faraday Soc. 40 (1944) 546–551.
[43] J.D. Miller, S. Veeramasuneni, J. Drelich, M.R. Yalamanchili, Effect of roughness as determined by atomic force microscopy on the wetting properties of PTFE thin films, Polym. Eng. Sci. 36 (1996) 1849–1855.
[44] B. van Ginneken, M. Stavridi, J.J. Koenderink, Diffuse and specular reflectance from rough

surfaces., Appl. Opt. 37 (1998) 130–9.

[45] A. Grosjean, A. Soum-Glaude, P. Neveu, L. Thomas, Comprehensive simulation and optimization of porous SiO_2 antireflective coating to improve glass solar transmittance for solar energy applications, Sol. Energy Mater. Sol. Cells. 182 (2018) 166–177.

Chapter 5

Reliability assessment and performance on photovoltaic and concentrated photovoltaic modules

In this Chapter the reliability and enhancement of electrical response of solar cells provided by promising antireflective layer stacks with low surface free energy developed in Chapters 3 and 4 have been assessed. The differences of the processability of the coatings prepared either by the methyl-silylating post-treatment or by polyfluoroalkyl functionalized silica in one-step consequently led to differences in the properties of the different AR systems which have been evaluated under reliability tests. The final objective was to select the most rational design, by searching the optimal trade-off between cost-efficiency, processability, optical properties and reliability during real life operation.

The antireflective layer stacks have been applied on the glass parts of photovoltaic and concentrated photovoltaic modules in order to assess the effect of the optical properties enhancement on the electrical production of the modules. The increase in short-circuit current of crystalline silicon and multi-junction solar cells related to the antireflective layer stacks has been theoretically calculated and experimentally assessed.

The research work presented in this Chapter has resulted in the following publication:

C. Agustín-Sáenz, M. Machado, J. Nohava, M. Brizuela, N. Yurrita, A. Sanz, O. Zubillaga, A. Tercjak, Mechanical properties of hydrophobic anti-reflective sol-gel coatings and field performance on photovoltaic application, in preparation

5.1. Introduction

In Chapter 4, two different routes were accomplished to attain hydrophobic AR coatings through the involvement of $–(CH_2)_2$-$(CF_2)_n$-CF_3 and $–(CH_3)_3$ moieties in the coating surface. The low surface free energy exhibited by the coatings was expected to contribute against soiling adherence when operating outdoors. The use of antireflective and antisoiling (AS) coatings is highly valued in PV technology, since it contributes to the reduction of LCOE through the modification of both CAPEX and OPEX of PV installations, as explained in Chapter 1.

Route 1 consisted in a methyl-silylating post-treatment of a totally sintered porous silica coating with the aim to reduce the number of free silanol groups (–Si-OH) on the surface by replacing them with methyl groups ($–Si-(CH_3)_3$). Route 2 consisted of the addition of low contents of non-hydrolyzable polyfluoroalkyl alkoxysilane during sol synthesis. Apart from low interfacial free energy surfaces with high optical transmission obtained by both methods, extremely low roughness (R_a < 0.5 nm) was exhibited by all the hydrophobic coatings as well as low diffuse reflectance. In addition, both routes provided an optimized stack capable to withstand the demanding conditions of damp heat aging test.

However, substantial differences exist among both routes from the point of view of production cost, time, and energy consumption, mainly linked to the required production steps and sintering temperatures. Focusing on the cost-effectiveness of the hydrophobic single porous coating processes, it can be first underlined that Route 1 requires two steps. However, Route 2 is a one-step process allowing to achieve the targeted final properties (AR performance and low surface energy). The second relevant aspect of the process is related to the applied temperature in the sintering step needed to consolidate the coating, and therefore the related energy consumption.

The properties displayed by the coating material prepared by each route, are consequently different. Through Route 1, the inorganic nature of the searched pure porous silica coating allows to treat it at the high temperatures required to reach a highly thermodynamic stable and structurally relaxed inorganic network [1]. Thereby the coating treated at 550 ºC exhibited very good mechanical properties, cohesion and adhesion. Further on, the methyl-silylation applied on the totally sintered porous coating, with plenty of hydrophilic –OH group bonds inside and outside the pores, allows to implement hydrophobicity in all the internal and external surface area. The related advantage, as discussed in Chapter 4, section 4.4.4 was that optical constants

(n, κ) and the resulting optical properties (transmittance, reflectance) were independent of environmental RH. Through Route 2, the presence of the polyfluoroalkyl chains in the deposited gel does not allow to reach the relatively high temperatures needed to obtain a coating as consolidated as the former pure inorganic silica network, and therefore cohesion, adhesion and mechanical properties of the single coatings were lower. The dependence between the optical constants (n, κ) and RH revealed that the internal surface area was not hydrophobic, or at least water vapor was capable to enter inside the pores. Furthermore, only the bi-layer stack offered durable AR properties after damp heat ageing test.

Therefore, while single mono-layers prepared by Route 1 are appropriate candidates in terms of AR performance, mechanical properties and durability, bi-layers are strictly required in order to achieve stable coatings by Route 2. The work described in this Chapter is aimed to obtain the most rational design to deposit AR coatings with the minimum process steps that allow to obtain reliability and robustness required for operate outdoors. Therefore, the bi-layer stack configuration with a dense-structure inner coating must be discussed, depending on the Route used for preparation. The inner coating merits are mainly two, a first one related to broadband AR properties enhancement, and a second one related to the prevention of alkali diffusion from glass to porous coating and the formation of salt crystals that would collapse the coating structure. Dense-structured coating has demonstrated its effective role in the adhesion and durability of AR properties after damp heat test. If following Route 2 (porous polyfluoroalkyl-silica), the presence of the inner coating is particularly necessary for adhesion and durability. For Route 1 (methyl-silylated silica), the need of this coating must be discussed, based on the reliability and optical properties required.

With the aim to discriminate among the different options to obtain the most rational design of an AR layer stack, this Chapter is focused on the reliability assessment and the enhancement on the electrical response of different types of solar cells. It is divided in four independent sections. Two of them are related to reliability properties, studied through ageing tests consisting of exposure to different environments and cleaning simulation by reciprocating wear tests. The remaining two sections are related to the application of different AR layer stacks to PV and CPV real components and the related assessment of performance. The assessment consisted on the quantification of the enhancement of the optical properties

and/or the electrical response of different types of solar cells. At the beginning of each section, a specific introduction relates the particular motivation and the followed methodology.

5.2. Routes for AR layer stacks preparation

The AR layer stacks studied in this Chapter were prepared following the procedure explained in Chapter 4. Three types of sols were used in order to grow the different types of AR layer stacks. These are collected in Table 5-1, where the sols and the sintering temperatures are also specified. All coatings were prepared by dipping at withdrawal rate of 5 cm/min, under controlled environmental conditions of 22 ºC and 60% RH. The silica dense coating was grown from non-SDA silica sol, silica porous coating was grown from SDA1 silica sol and polyfluoroalkyl-silica porous coating was grown from FAS21-C2 sol. The methyl-silylating post-treatment was Hb post-treatment, in the conditions defined in Chapter 4. While M3H, M5H, B3H and B5H were fabricated by previously defined Route 1, F240 and D5F250 were fabricated following Route 2. The non-functionalized M3, M5, B3 and M5 were produced for comparison in some cases.

Table 5-1. Deposition sequence for AR layer stacks preparation.

Reference	Deposition sequence	AR layer stack
M3	Silica porous coating sintered at 350 ºC	Mono-layer
M4	Silica porous coating sintered at 450 ºC	Mono-layer
M5	Silica porous coating sintered at 550 ºC	Mono-layer
B3	Silica dense coating sintered at 350 ºC Silica porous coating sintered at 350 ºC	Bi-layer
B5	Silica dense coating sintered at 550 ºC Silica porous coating sintered at 550 ºC	Bi-layer
M3H	Silica porous coating sintered at 350 ºC Methyl-silylating post-treatment	Mono-layer
M5H	Silica porous coating sintered at 550 ºC Methyl-silylating post-treatment	Mono-layer
B3H	Silica dense coating sintered at 350 ºC Silica porous coating sintered at 350 ºC Methyl-silylating post-treatment	Bi-layer
B5H	Silica dense coating sintered at 550 ºC Silica porous coating sintered at 550 ºC Methyl-silylating post-treatment	Bi-layer
F240	Polyfluoroalkyl-silica porous coating treated at 240 ºC	Mono-layer
D5F240	Silica dense coating sintered at 550 ºC Polyfluoroalkyl-silica porous coating treated at 240 ºC	Bi-layer

5.3. Reliability of AR layer stacks on flat glass

The long-term durability of PV modules and their constituents is crucial since they must be capable of withstanding prolonged exposure in harsh climates. The PV industry makes use of IEC 61215 (applicable to crystalline silicon PV modules) and IEC 62108 (applicable to CPV modules) standards to validate the performance and reliability of the modules and materials under real operation conditions. The aim of these standards is to test the mechanical, thermal and electrical characteristics of the PV modules and assemblies in order to assure that the PV components are capable to endure prolonged exposure in the climatic conditions also defined therein. In particular, damp heat accelerated aging test was performed in Chapter 4 as a

discriminating test, since it is among the most aggressive conditions considered in IEC 61215/IEC 62108 standards. A deep assessment on a small coating area allowed to conclude that sintering temperature as well as the presence of the inner dense-structured coating had a crucial influence on the coating degradation. The improvement of adherence of the porous coating when deposited on the inner dense-structured coating instead of directly on glass, together with the highly thermodynamically stable structure of stacks sintered at high temperatures led to keep the outstanding optical transmittance at the end of the aging test.

In this section, up to six replicas of each AR layer stack were subjected to different ageing tests with the aim to obtain reliable statistics. The qualitative pass criteria in the standards refers to no visual evidence of major defects, and quantitative pass criteria refers to electrical losses of the final module. In this case, the degradation was assessed in terms of the initial and final optical transmittance change, which is the most important key performance indicator of the cover glass. Only one bibliographic reference [2] has been found which extrapolate that those pass criteria imply a maximum loss of τ up to 1% relative to the initial value.

The AR layer stacks M3, M3H, M5, M5H, B3, B3H, B5, B5H, F200, F240, D5F240 deposited on both sides of 80x60x4 mm plates of low iron float glass were subjected to damp heat test performed at TECNALIA facilities. This test conducted a preliminary sifting of AR layer stacks to be subjected to other ageing tests. Only the bi-layers (B3, B3H, B5, B5H, D5F240) and the mono-layer sintered at 550 ºC (M5) were selected to follow the test campaign performed at Italian national agency for new technologies, energy and sustainable economic development (ENEA) facilities in the framework of FP7 European project ECOSOLE.

5.3.1. Tests description

- Damp heat test (IEC 61215/IEC 62108): The specimens were exposed for 1000 h in a climatic chamber at 85 ºC and 85% RH conditions.
- UV test (IEC 61345): The specimens were irradiated by UV light at the constant temperature of 60±5 °C by 7.5 kWh/m² in the range 280-320 nm and by 15 kWh/m² in the range 320-400 nm. The total test duration was 96 h.
- Thermal cycling test (IEC 61215/IEC 62108): The specimens were subjected to 400 cycles consisting of 3 h to arrive from -40 to 85 °C, and a dwell time of 10 min at the highest and lowest temperatures.

- Humidity freezing test (IEC 61215/IEC 62108): The specimens underwent a warming cycle at 85 °C and high RH followed by a fast cooling cycle at very low temperature (-40 °C).
- Salt mist corrosion test (IEC 61701): The specimens were held tilted between 15 and 30° for 96 h on a corrosion chamber, where a solution of prepared mixture of NaCl in water, 5% weight, at pH of 3.7 was nebulized. The spray was intermittent with a duty cycle of 5 min in 1 h. Test was performed at room temperature.
- Cyclic tests of corrosion and condensation: after a first pollution phase, realized in salt spray, or by simple immersion, the sample is dried in air; the cycle is concluded with a wet phase condensation.

Transmittance spectra were measured before and after aging tests with a Jasco V-670 UV-Vis-NIR spectrophotometer equipped with a 150 mm integrating sphere. Spectra were taken in the 300 to 2000 nm wavelength range. In this range, integrated transmittance, τ, as well as transmittance loss, τ_{loss}, for a given AR layer stack before and after aging were calculated.

5.3.2. Assessment of optical properties of aged AR layer stacks

Figure 5-1 displays the loss of transmittance, integrated in the wavelength range between 300 to 2000 nm of the silica and methyl-silylated silica layer stacks (Figure 5-1a) as well as the polyfluoroalkyl-silica layer stacks (Figure 5-1b).

In accordance to the assessment performed in Chapter 4, the most remarkable result is related to the better optical performance exhibited by the bi-layer stacks over mono-layers in all cases. Indeed, B3H, B5, B5H and D5F240 bi-layer stacks displayed an almost negligible loss of transmittance while the bi-layer sintered at 350 ºC lost only around 1% transmittance after ageing.

Concerning mono-layers, it was clearly observed that the widest dispersion of the transmission measurements was related to the instability and heterogeneity of aged coatings.

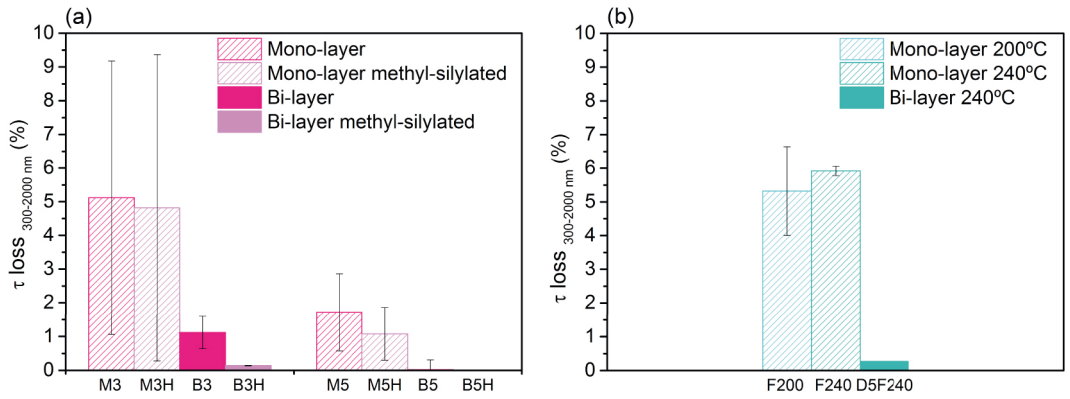

Figure 5-1. Transmittance loss ($\tau_{300\text{-}2000\ nm}$) experimented by AR layer stacks after damp heat aging test.

As explained before, only the bi-layers and the pure silica mono-layer sintered at 550 ºC were selected to follow the ageing test campaign performed at ENEA facilities. In Figure 5-2, the transmittance loss, integrated in the wavelength range between 300 to 2000 nm, obtained after ageing the mentioned AR stacks under ultraviolet, thermal cycling, humidity-freezing, salt mist and corrosion condensation tests is collected.

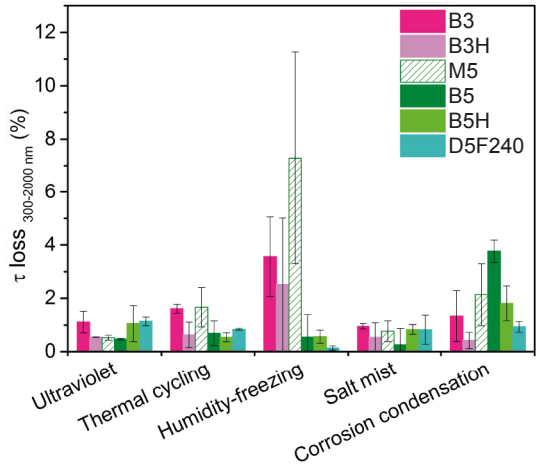

Figure 5-2.Transmittance loss ($\tau_{300\text{-}2000\ nm}$) experimented by AR layer stacks after each aging test.

As observed from damp heat test results, higher transmittance loss values were related with a higher data dispersion, and thus related with a higher instability and heterogeneity of damaged coatings. The transmittance loss induced by ultraviolet, thermal cycling and salt mist tests was below 2% for the tested AR stacks, while humidity-freezing and corrosion condensation led to differences in the performance of AR layer stacks. Particularly, water and temperature were implied in both tests, and the hydrophobic character of the surfaces could have a positive effect on withstanding those aggressive environments.

The detailed effect caused by each test is described hereafter. Ultraviolet ageing induced a milder effect on the pure silica AR stacks sintered at higher temperatures, thus M5 and B5. The optical properties reduction provoked by thermal stress, thus thermal cycling and humidity-freezing tests, was related to the mechanical robustness of the AR stacks. Coatings B3, B3H and M5, which had presented the highest mechanical properties, hardness and elastic modulus, did not withstood the stress associated to thermal changes and showed the highest loss of transmittance, with a high data dispersion related to instability. Indeed, the damages were even more aggressive on non-methyl-silylated AR layer stacks B3 and M5, which can be also related with its capability to absorb water into the pores that can trigger the collapse of the porous structure. Salt mist test was the mildest test or the test that provoked a similar behavior of the aged AR layer stacks. Corrosion condensation test seemed to be mostly related to the hydrophobic character of the AR layer stacks. B3H and B5H transmittance loss was lower than their B3 and B5 counterparts.

To summarize, only D5F240 presented transmittance loss around or below 1% in all the tests, while B5H presented transmittance loss below 1% in all the tests excepting the corrosion condensation aging.

5.4. Cleaning simulation by reciprocating wear test

One of the most important external factors that can change the properties of the surface of a coated cover glass for PV applications is the soiling adherence. The soiling adherence inherently disrupts the intended function of the graded refractive index coatings interposed at the glass-air interface to minimize Fresnel reflection losses, which reduces significantly the power output of the PV plants. The reliability and durability of the AR coating stacks with low surface free energy would lead to a decrease of the cost of solar energy through a reduction of their CAPEX and OPEX. The PV LCOE is calculated according to Equation 5-1.

$$\mathrm{LCOE} = \frac{\mathrm{CAPEX} + \sum_{t=1}^{N} \frac{\mathrm{OPEX}(t) - \mathrm{RV}}{(1+r)^t}}{\sum_{t=1}^{N} Y_0 \cdot \frac{(1-D)^t}{(1+r)^t}} \qquad \text{Equation 5-1}$$

where N are the life years of PV system life, CAPEX is the total investment in €/kWp, OPEX are the annual operation and maintenance expenditures in €/kWp, RV is the residual value in

€/kWp, r is the discount rate (%), Y_0 is the initial yield in kWh and D is the system degradation rate (%).

Then, reduction of the CAPEX will be achieved since the better performing solar power plants accompanied by a negligible rise in the module cost that the long-term service AR layer stacks involve, should reduce their former oversize focused to guarantee a certain amount of energy generation. The reduction of OPEX will be achieved by the reduced cleaning needs of the power plant.

There is an optimum cleaning interval that balances the economic cost of lost revenues due to soiling loss with the cost of cleaning operations [3]. Choosing the right cleaning time interval between each cleaning event is important to minimize the total cost (due to both work/material cost of the cleaning process and the lost revenue due to soiling losses) and thus maximize profitability. The AR coating stacks with low surface free energy should ideally avoid the cleaning events. However, depending on the location or seasonal variations in soiling effect, cleaning can be required anyway. In this case, the AR coating stacks with low surface free energy should help to prolong the interval between cleaning events, thus also minimizing the OPEX and levelized cost of electricity.

In order to ensure the reliability of AR layer stacks with regard to cleaning events on PV plants, the abrasion resistance was studied by a reciprocating wear test. The design of the test was inspired on the most recommended cleaning procedures. Although some parameters can vary depending on the module manufacturer's instructions, site condition, quality of water and cleaning mechanism, the general recommendations are described below.

Quality of water: If available, deionized water is preferred. If using rainwater or tap water, low mineral content (total hardness less than 75 mg/L) is mandatory and chlorides should not exceed 250 mg/ml with water conductivity less than 250 mS/cm. If using hard water with mineral content between 75 to 200 mg/L, the water has to be squeegeed off from the surface to prevent scale build-up. Water with mineral content higher than 200 mg/L must not be used.

Cleaning agent: A mild detergent is recommended with deionized water. Neither acid nor alkali detergents, abrasive cleaners or degreasers must be used.

Water pressure and temperature: Pressure should not exceed 35 bar at the nozzle and water temperature should be the ambient temperature. The modules should be cool to avoid thermal shock.

Rubbing and drying: A soft sponge or non-abrasive brush must be used to remove stubborn soiling, followed by rinsing of the surface with plenty of water. Finally, residual water must be removed from module surface using rubber wiper from top to bottom.

The abrasion resistance of the AR layer stacks was expected to be highly influenced by mechanical properties determined by ultra-nanoindentation in the Chapter 4. Based on the outcome of durability properties studied in the section 5.3, the AR coating stacks selected for this study were the methyl-silylated mono- and bi-layers sintered at the highest temperature (550 ºC) and the polyfluoroalkyl-silica mono- and bi-layers treated at 240 ºC.

5.4.1. Test description

Abrasion resistance of the selected AR layer stacks was carried out simulating the cleaning process by a reciprocating wear test, using a soft sponge soaked with a liquid mixture composed by mild liquid soap and deionized water in a volume ratio 66:33. Specimens were subjected to 25.000 friction cycles on a contact area of 50x50 mm and displacement of 10 mm under 9.8 N load and 1 Hz frequency. The test was performed at room temperature and humidity conditions. After the reciprocating wear test specimens were observed in the optical microscope, and optical properties, wear tracks as well as $\theta_c^{H_2O}$ were characterized as follows:

- Total transmittance, total and diffuse reflectance spectra were measured with a Jasco V-670 UV-Vis-NIR spectrophotometer equipped with a 150 mm integrating sphere. Reflectance was measured at an incident angle of 8º. Diffuse reflectance spectra were taken by removing the specular component port of the integrating sphere. Spectra were taken in the 300 to 2000 nm wavelength range. In this range, integrated transmittance, τ, and reflectance, ρ were calculated.
- Wear tracks were characterized by profilometry (Dektak 150 Surface Profiler). Mapping of the surface was performed to obtain 3D images of the surface. Stacking of 134 linear measurements performed along 400 μm in X axis (3 μm resolution), being 1 mm length (1/3 μm resolution) with the 2 μm diameter pin and load of 1 mg. The stacking and

analysis of these measurements were used for graphing the 3D surface mapping using Vision advanced analysis software.

- The $\theta_c^{H_2O}$ was determined by the static drop method, using Digidrop Contact Angle Meter (GBX Instruments). Ten measurements of the apparent contact angle were taken by placing drops of water on the horizontal and flat coating surface and measuring the angle at the liquid-solid-air boundary.

5.4.2. Assessment of AR layer stacks after 25000 cycles

Optical transmission and $\theta_c^{H_2O}$ of the hydrophobic AR mono- and bi-layer stacks before and after test are compared in Figure 5-3, while total and diffuse reflectance spectra after test are presented in Figure 5-4. The appearance of the coatings surface after the test was analyzed by optical microscopy and contact profilometry. The corresponding images are collected in Figure 5-5 and Figure 5-6.

The tested AR stacks presented different levels of optical loss after the reciprocating wear test. By far, the most damaged one was the polyfluoroalkyl-silica mono-layer, which presented many scratches as observed in Figure 5-5 and a transmittance loss of 1.7±0.1%. Methyl-silylated silica mono-layer presented a reduced number of scratches and a low transmittance loss of 0.4±0.2%. In the case of AR bi-layers, methyl-silylated silica B5H lost 0.6±0.2% of transmittance, while the stack prepared with polyfluoroalkyl-silica treated at 240 ºC (D5F240), showed the same behavior, losing 0.5±0.1% transmittance after the test. Once again, the adherence enhancement provided by the presence of the inner dense-structured coating implemented a considerable improvement of the properties of this coating treated at relatively low temperature.

A clear reduction of scratches of D5F240 stack compared to F240 stack was observed in the image assessment, in Figure 5-5. The surface and geometry of scratches of the tested coatings was also studied by profilometry, as shown in the 2D and 3D images displayed in Figure 5-6. The surface of M5H and B5H coatings did not present any deep scratches, nor remarkable differences between the mono- and the bi-layer stacks. Only some casual defects were observed. Many scratches per millimeter appeared on the scans performed on F240 after test, being up to 105 nm deep and up to 50 μm wide. The number of scans was reduced up to one

or two per millimeter for the coating stacked on the inner dense coating. In this case, each scratch was around 105-110 nm deep and up to 30 μm wide.

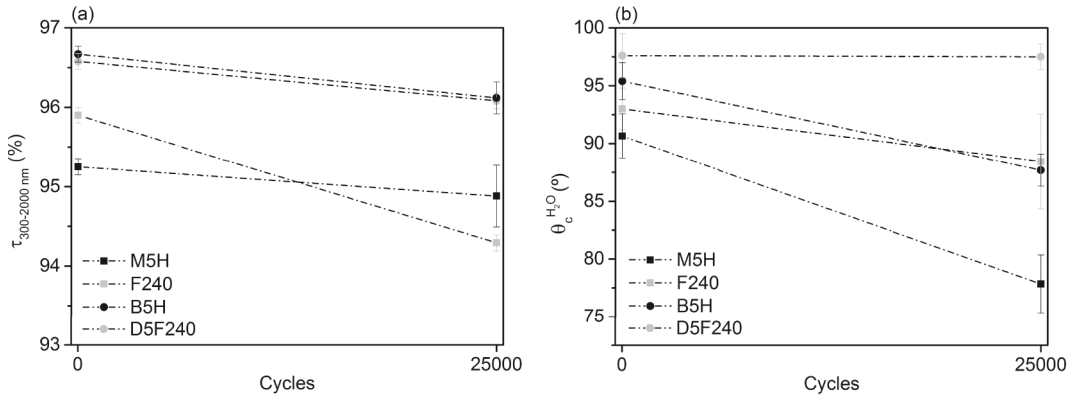

Figure 5-3. Integrated transmittance ($\tau_{300\text{-}2000\ nm}$) (a) and water contact angle (b) variation for hydrophobic AR stacks sintered at 550 ºC and polyfluoroalkyl-silica stacks.

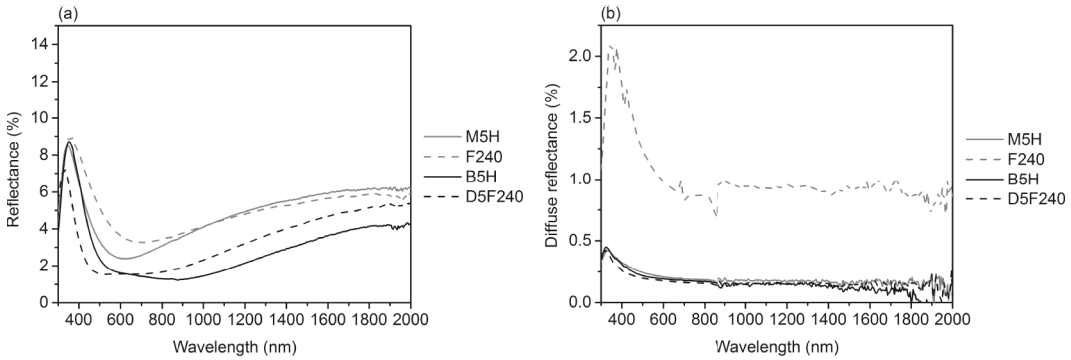

Figure 5-4. Total (a) and diffuse (b) reflectance spectra after 25000 reciprocating cycles for stacks sintered at 550 ºC and fluorocarbon-silica stacks.

Reflectance spectra varied consequently. Integrated reflectance values (300-2000 nm) displayed by the mono-layer of M5H were around 3.7% while F240 presented up to 4.5% integrated reflectance. On the contrary, the bi-layers showed between 2.4-2.6% integrated reflectance values. The most relevant outcome was, however, related to diffuse reflectance. The high number of scratches provoked that light scattering of F240 surface stood out all the other AR stacks, that reached an integrated value (300-2000 nm) of 1.1% over the 0.2% presented by M5H and the bi-layers.

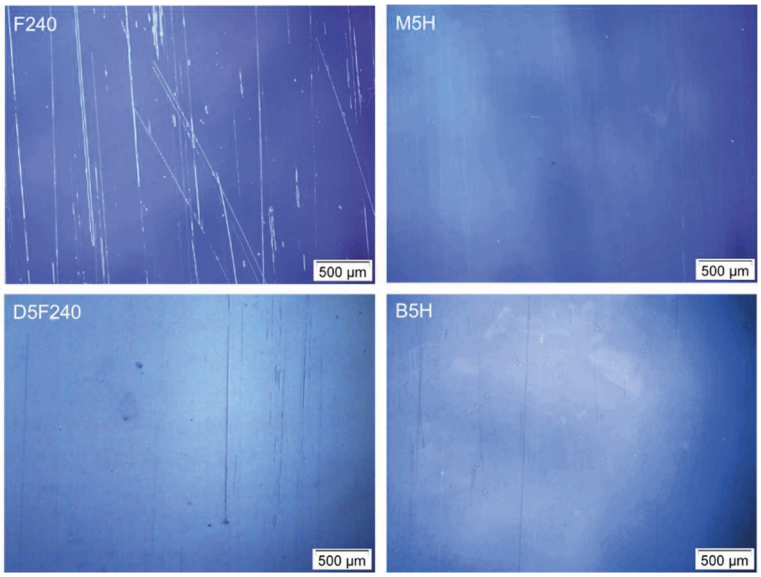

Figure 5-5. Optical micrographs of coatings after abrasion test.

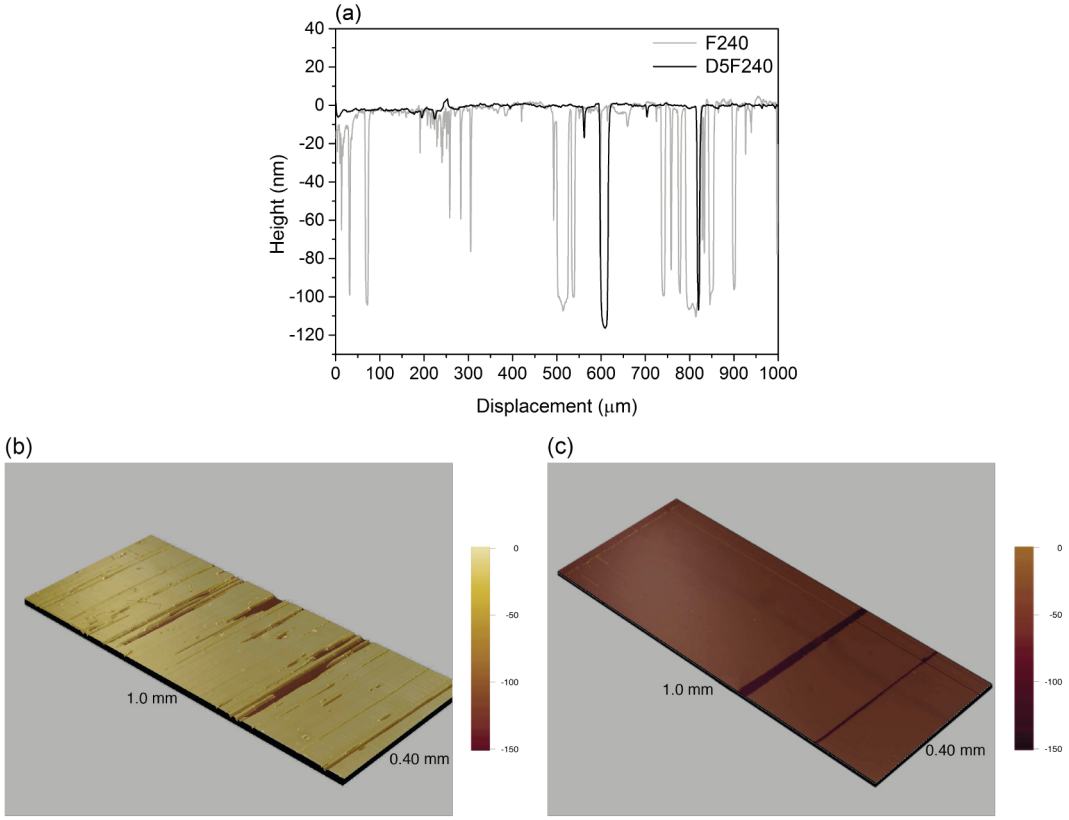

Figure 5-6. 2D scan of AR polyfluoroalkyl-silica layer stacks.

Regarding the hydrophobicity of the surfaces before and after reciprocating, the wear induced a reduction of the $\theta_c^{H_2O}$ in the case of methyl-silylated stacks, that could come from dragging of the methyl groups. However, the polyfluoroalkyl groups chemically bonded to the silica network led to the stability of the hydrophobicity properties.

Concerning abrasion resistance, a comparable behavior was observed between the methyl-silylated silica mono-layer prepared through Route 1, and the polyfluoroalkyl-silica bi-layer stack prepared through of Route 2. Both AR layer stacks require identic steps for preparation although Route 2 requires lower temperature.

5.5. Application on front glass sheet of PV modules

Crystalline silicon is the most mature semiconductor material for PV applications and the long-term market leader [4]. Although large research efforts have been addressed to attain highly effective CPV modules, they are not still cost-competitive. In fact, PV market and production are dominated by c-Si technology that represents 93% of the total. This is due to the conjunction of two factors, (1) the large module production capacity available to provide a significant amount of new energy production plants and (2) the continuously decreasing price of PV electricity. In 2017, industrial c-Si solar modules reached efficiencies between 15 and 18%. The annual PV market in 2018 was 99.9 GW, according to the 2019 Snapshot of Global PV Markets published by the Photovoltaic Power Systems Programme within the International Energy Agency (IEA-PVPS) [5], and will continue to increase, doubling to 200 GW/year in 2022 (data also supported by PV Market Alliance forecast). The cumulated capacity was 500 GWp, or half a TWp, at the end of 2018 [6]. PV electricity is reaching extremely competitive prices, even 0.02 $/kWh in the sunniest regions, like Abu Dhabi. Efforts addressed to improve efficiencies at cell and module level are required to maintain the sector highly competitive, conducting PV systems towards high energy efficiency, long lifetime and low-cost designs.

Dual AR and AS coatings will increase light harvesting of the module over time, leading to an improvement of cell-to-module ratio, i.e., the loss of efficiency induced by an increased absorptance due to cell encapsulation will be reduced.

In order to effectively study the AS effect of the low surface free energy AR coatings developed along this research work, the electrical behavior of PV mono-modules fabricated with AR coated front glass was studied upon outdoor exposure. The electrical behavior of the PV

mono-modules exposed outdoors along a year without being artificially cleaned was analyzed by means of the monitoring of the short-circuit current, I_{SC}.

5.5.1. Module assembly and initial performance

The most promising AR layer stacks prepared by each route were selected and deposited on the front glass sheet of PV mono-modules for subsequent study. Soda-lime float glass (not low-iron) plates sized 210x210 mm and 4 mm thick were one-side coated with M5, M5H and D5F240. Single porous mono-layers sintered at 550 ºC had demonstrated acceptable mechanical properties, in comparison to the bi-layer stacks and therefore the simplest AR stack M5 was prepared in parallel to M5H in order to assess the field performance of methyl-silylation. Concerning FAS-containing layer stacks, the supremacy exhibited by the bi-layer against the mono-layer in ageing tests, its mechanical properties and abrasion resistance seemed clearly-overcoming. Then, given that the deposition sequences leading to hydrophobic AR layer stacks required an identical number of steps, M5H and D5F240 were selected to be compared in real application conditions.

Figure 5-7 shows the transmittance spectra of the selected AR stacks deposited on one side of the soda-lime float glass used for the PV mono-module lamination. Their corresponding transmittance spectra were studied in the wavelength range between 300-1100 nm, which corresponds to the spectral response of c-Si cells. The gain in integrated transmittance over bare glass was between 4.5-5.1%. Despite the broadband antireflection properties that the bi-layer had shown in clear advantage over the mono-layer architecture in low iron float glass in the NIR range from 900 nm, they were not significantly visible when deposited on standard float glass. The spectra of all AR layer stacks are almost overlapped in this region of spectrum, in which soda-lime float glass shows high absorption due to the high iron content, which indeed turns the substrate into a green tinted glass.

The AR coated and uncoated soda-lime glass panels were used as front sheet of the PV mono-modules. Monocrystalline silicon cells sized 127x127 mm with two busbars were used. Electrical connections in monocrystalline silicon cells were prepared by welding ribbons onto the cells using a pilot-scale tabber-stringer. Afterwards, hand-made welding was used for the positive and negative connections to be used for the electrical measurements. 210x210 mm PV mono-modules were manufactured by encapsulation of the monocrystalline silicon cells with polyvinyl fluoride film-based as backsheet; the described glass as front sheet, and

thermoplastic polyurethane (TPU) as encapsulant, using the lab-scale vacuum laminator PEnergy L036LAB. The material stacking that composed the PV the mono-module is schematized in Figure 5-8. Three mono-modules were prepared with each AR layer stack, as well as with uncoated float glass for comparison. Polyisobutylene was used as edge sealant.

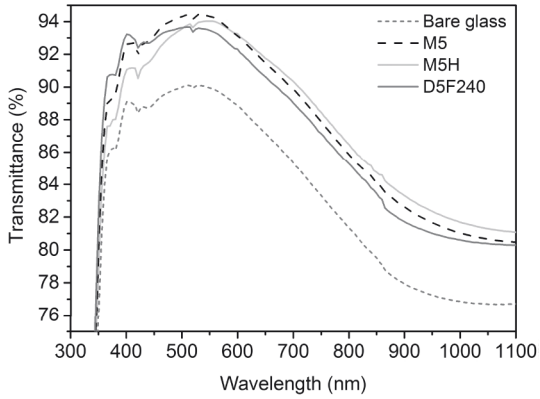

Figure 5-7. Transmittance of bare and coated float glass used for mono-module assembly.

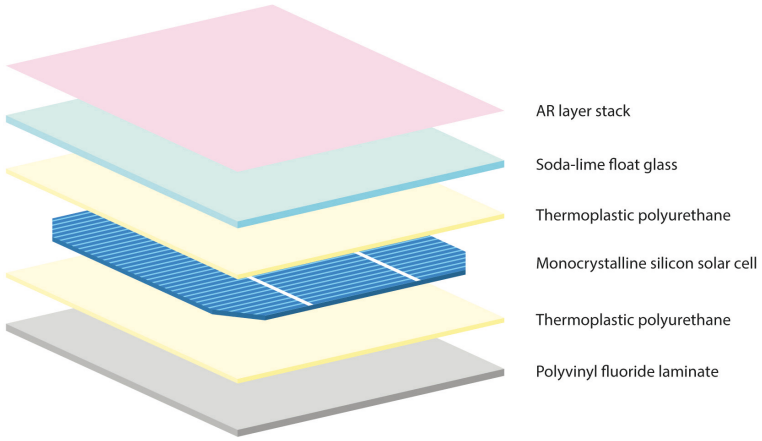

Figure 5-8. Stacking of materials composing the PV mono-module.

The electrical characteristics of the monocrystalline Si cells were assessed by means of their I-V (current-voltage) characteristic curve. The current-voltage curves of bare and encapsulated monocrystalline silicon cells were measured using a PASAN CTSLAB906 cell tester under AM1.5 solar spectrum and 1000 W/m^2 irradiance. This curve represents the operation of the silicon solar cell, under controlled conditions of irradiance and temperature. Since each silicon cell has a particular I-V curve, it is important to perform the comparison of the I-V curve of a particular cell before and after encapsulation. Each Si cell was measured as received and after

encapsulation with bare or AR coated glass. Figure 5-9 collects the I-V curves of each monocrystalline Si cell before and after encapsulation. From these curves, I_{SC}, which is highly related with MMP, was used as the key parameter to study the effect of the coated and uncoated glasses on the electrical performance of the Si cells.

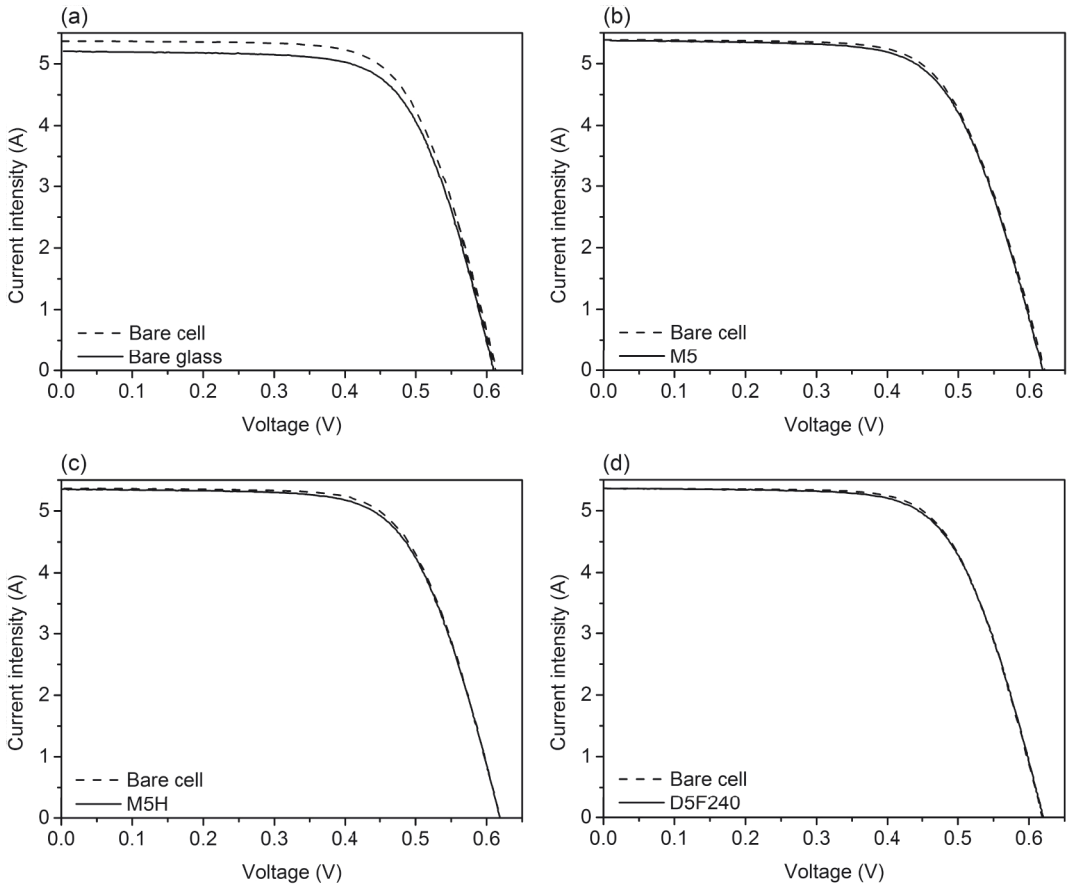

Figure 5-9. I-V curves of silicon cells before and after encapsulation with float glass bare (a) and coated with AR mono-layers M5 (b), M5H (c) and bi-layer D5F250 (d).

The I_{SC} of the Si cell after being encapsulation with bare soda-lime glass was reduced between 2.4-3.1%, because of the Fresnel reflection losses at the air-glass interface and the increased absorption due to the glass and the encapsulation material. However, for the Si cells encapsulated with AR coated glasses, these losses were counterbalanced. D5F240 completely nullified the losses provoked by interposing the glass and the encapsulant, showing similar current generation than bare Si cell. M5 and M5H presented small losses between 0.7-1%. Although the differences in I-V curves of all Si cells after encapsulation are not completely

due to the presence of the AR coatings, since each Si cell has its own imprint, clear differences in the I_{SC} value can be observed at least among bare and AR coated glasses.

5.5.2. Field exposure study

The field exposure study was carried out at TECNALIA facilities in Bilbao (Spain). The modules were south oriented and placed with 26 ºC tilt angle (see Figure 5-10). The current generated by the modules on the roof was continuously monitored. The electric charge (A h) generated by the PV modules was normalized for data analysis. Irradiation, precipitation, moisture and temperature data were provided by Basque Meteorological Agency.

Figure 5-10. PV mono-modules exposed on the roof at TECNALIA's facilities.

After the initial indoor characterization of coated glasses and PV mono-modules, their electrical performance was studied outdoors along a year of exposure. The I_{SC} values were monitored for each type of bare or AR coated glass and then these values were integrated with time. The integrated short circuit value of each AR coated PV module was then weighted with that of the bare glass PV module, in order to obtain an equivalent of the over generation of AR coated PV mono-modules with respect to uncoated ones. This kind of performance assessment was accomplished in order to focus on differences in the behavior among the

different types of AR coatings, since all the mono-modules with AR system performed better than the uncoated ones along the whole experiment, as observed in Figure 5-11a.

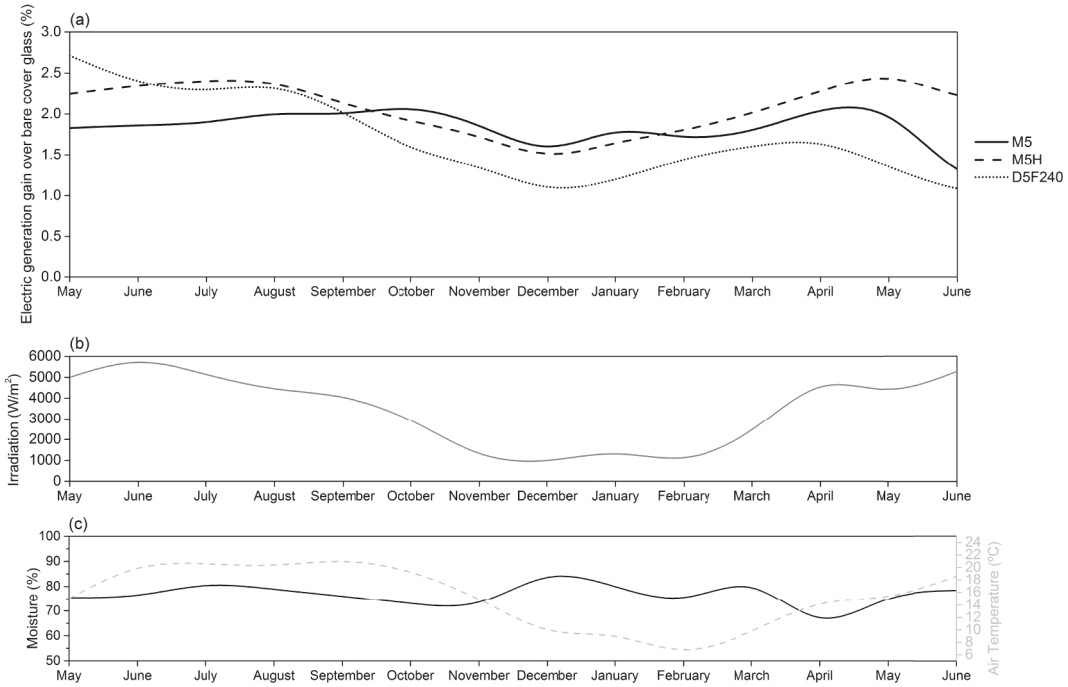

Figure 5-11. Electric generation of AR coated PV mono-modules compared to bare modules and the in situ atmospheric conditions collected along their exposure in Bilbao.

Focusing on the differences among the studied AR coatings, it can be observed that at the beginning of the test the polyfluoroalkyl-silica provided the highest enhancement of the electrical performance of the PV module, followed by the methyl-silylated silica mono-layer. The lowest equivalent overgeneration was exhibited by the single silica mono-layer, probably motivated by the high RH values registered along the whole test (between 60-85%), particularly being 75% at the beginning. Along the one year exposure, the gained electrical response was enhanced at higher irradiation values along the summer months, while on winter the three AR layer systems tested offered lower values of equivalent overgeneration. Furthermore, in low irradiance conditions, the non-functionalized M5 mono-layer offered slightly higher electrical response. The outstanding performance of the polyfluoroalkyl-silica bi-layer coated modules at the beginning of the exposure declined along the test duration, what could be motivated by the degradation of the non-totally consolidated coating, exposed to harsh conditions.

The PV modules covered with M5H resulted in the most stable ones, and overall, during the whole 13 months of exposure, they presented an average equivalent overgeneration of 2.1% over the modules with uncoated glass. The average equivalent overgeneration provided by the polyfluoroalkyl-silica bi-layer was 1.7%. Those results were encouraging taking into account that no cleaning events took place. A singularity observed during the exposure test was that electrical response of M5 and D5F240 mono-modules were dependent to cleaning during precipitation. Their electrical response rebounded after sporadic precipitation episodes which cleaned the accumulated soiling. However, electrical performance of M5H modules was higher, constant and did not need precipitation to rebound, since modules accumulated less soiling independently of the rain episodes.

5.6. Application on CPV primary and secondary optical elements

Currently, most of the commercially available CPV or HCPV modules are based on silicone of glass Fresnel lenses as primary optical element (POE), since the SoG process has proven to be cost effective and highly scalable. It is based on a Fresnel lens structured mold where the silicone is injected and pressed against the cover glass. Finally, the Fresnel lens optical silicone is attached to the cover glass, which provides the require protection and insulation to the module. Therefore, a unique glass-air interface will require the presence of an AR coating. Such AR coating should be applied before manufacturing the Fresnel lens, since its polymeric nature would not withstand the sintering step required for coating consolidation.

The Fresnel-based module configurations are usually equipped with a homogenizer element [7], which is defined as secondary optical element (SOE). The SOE is designed to increase the geometrical concentration, as represented in Figure 5-12. It helps to reduce the area of the solar cell and to increase the tolerance to errors in the module assembly and tracking. The SOE can be reflective or refractive, although the refractive ones allow a higher theoretical maximal concentration [8]. The refractive based optical elements are usually fabricated from quartz or glass, and they can adopt several geometries such as i) refractive truncated pyramid (RTP, Figure 5-12), ii) dielectric-cross compound-parabolic-concentrator (DCCPC), iii) single-lens-optical element (SILO-Pyramid) and iv) trumpet [9].

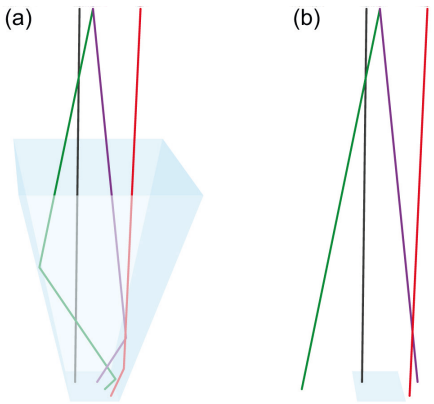

Figure 5-12. Scheme of light ray conveyor accomplished by SOE prism (a) and their absence (b).

However, several factors such as the angular size, the chromatic aberration, and, if the facets have been designed to be flat, their width, are among the main reasons whereby maximum concentration provided by a Fresnel lens is significantly lower than ideal. Among them, chromatic aberration is the most accountable. Therefore, innovative Fresnel lenses are being designed and developed by the community [10]. One of the alternatives are achromatic double Fresnel lenses, which are composed of two coupled materials with different dispersion properties thus allowing the minimization of the chromatic aberration. The attained concentration factor, being three times higher than the equivalent SoG lens, makes possible the elimination of the SOE in the module, thus saving costs, since the manufacturing process is similar to the one employed to fabricate SoG lenses.

In this section, the AR coatings were deposited on glass substrates, that were subsequently used as support for standard and achromatic Fresnel lens manufacturing. The improvement of lens efficiency was determined by measuring their effect on the electrical properties of MJ cells. The main objective was to accurately determine the effect of the broadband antireflective properties provided by the bi-layer on the electrical performance of the cells. Firstly, the theoretical effect of AR coated glass on the short-circuit current density of two different types of MJ solar cells was calculated. Secondly, the experimental effect of such AR coatings was determined by measuring the short-circuit current of a mismatched 3-junction solar cell. Finally, the effect on short-circuit current of the two described types of Fresnel lenses supported on AR coated glass was measured.

AR coating deposition on two refractive truncated pyramids SOEs was also accomplished. The deposition of single porous silica coatings sintered at 350, 450 and 550 ºC and the stacking

on an inner dense-structured layer was studied through spectrophotometry. The reliability of the coated optical elements was also determined by ageing tests.

5.6.1. Short-circuit current generated by multi-junction cells

5.6.1.1. Theoretical calculation

Transmittance and reflectance spectra of hydrophobic AR mono- and bi-layer stacks were used to calculate the effect of the coatings on the electrical properties of two types of multi-junction cells. The short-circuit current density of the subcells was calculated for a simplified module composed by AR coated or uncoated cover glass and the MJ cells. In addition, AR coatings were deposited on one or on both sides of the glass, since depending on the CPV module configuration, one or two glass-air interfaces can be employed. Figure 5-13 displays the transmittance and reflectance spectra of the M5H, F240, B5H, D5F240 mono- and bi-layers deposited on one (a, b) and two (c, d) sides of low iron float glass. The broadband effect of the bi-layers over their mono-layer counterparts is clearly observed on the two scenarios (one and two sides coated).

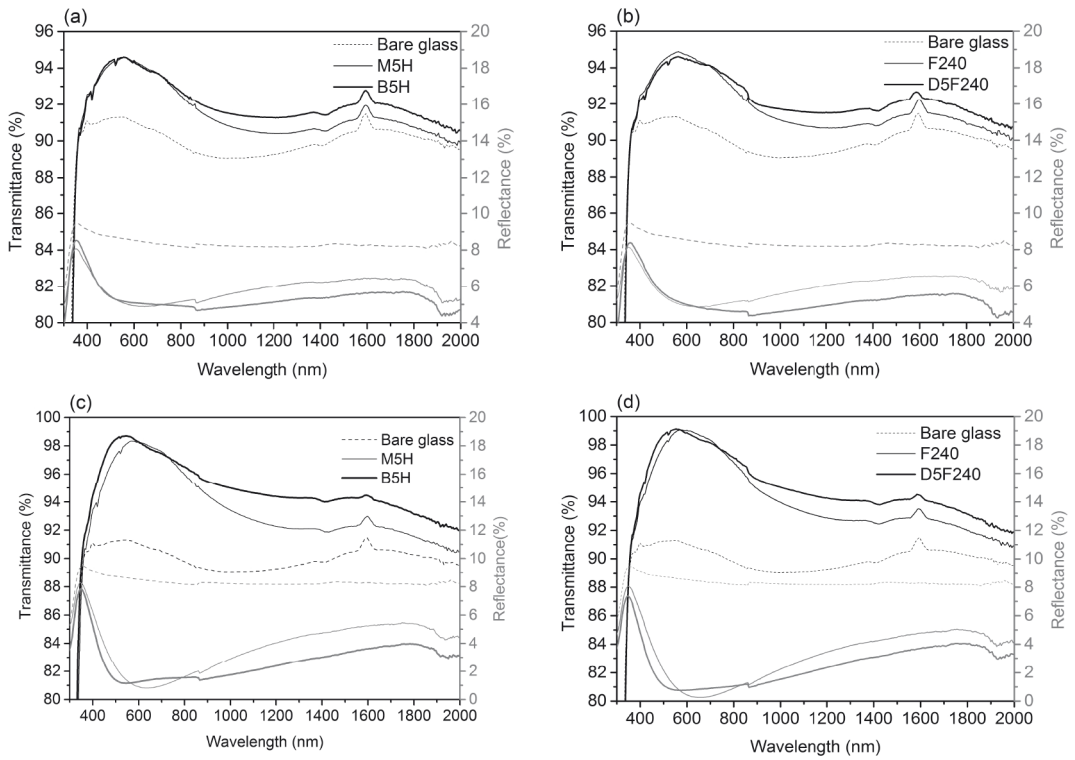

Figure 5-13. Transmittance and reflectance spectra of methyl-silyated silica layer stacks M5H, B5H (a, c) and polyfluoroalkyl-silica layer stacks F240, D5F240 (b, d) deposited on one (a, b) and two (c, d) sides

of low iron float glass.

Two different MJ cells were selected for comparison, an upright metamorphic 3-junction cell, GaInP/GaInAs/Ge (UMM3J from Spectrolab) and an inverted metamorphic 4-junction cell, AlGaInP/AlGaAs/GaInAs/GaInAs (IMM4J from Spectrolab), whose spectral response is comprised in the similar wavelength range, between 350 to 1800 nm. Their EQE curves are presented in the Figure 5-14.

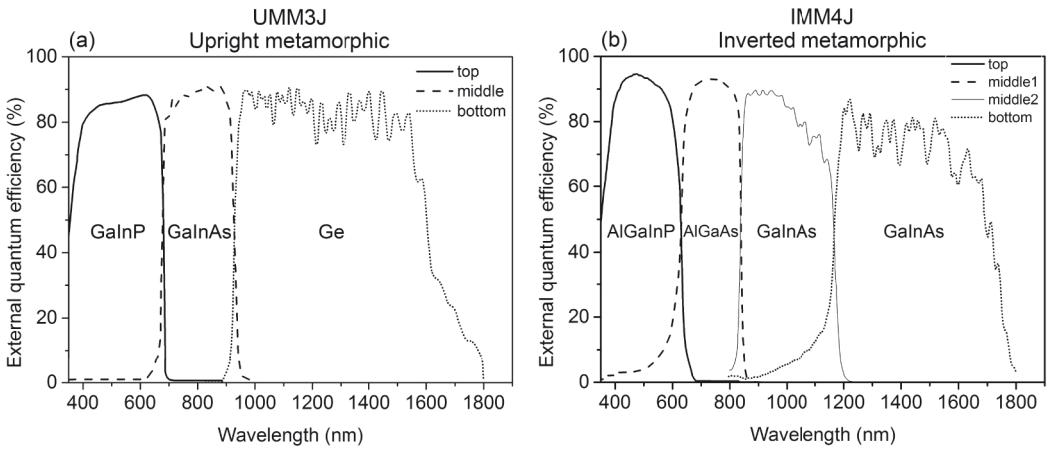

Figure 5-14. External quantum efficiency of the UMM3J (a) and IMM4J solar cells (b).

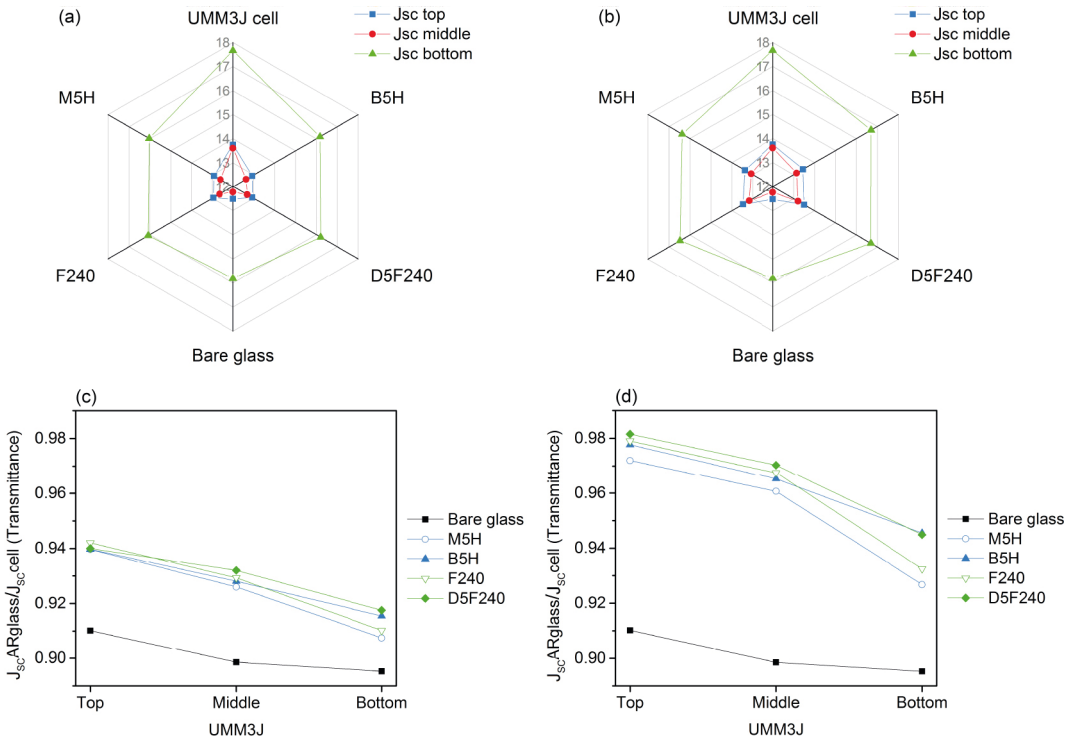

Figure 5-15. Short-circuit current density (mA/cm^2) calculated for each subcell in UMM3J without and with interposed cover glass coated with AR on one side (a) and two sides (b) as well as the transmittance calculated as the ratio of the J_{SC} of the bare cell and the J_{SC} with the interposed cover glass uncoated and AR coated on one (c) or two sides (d).

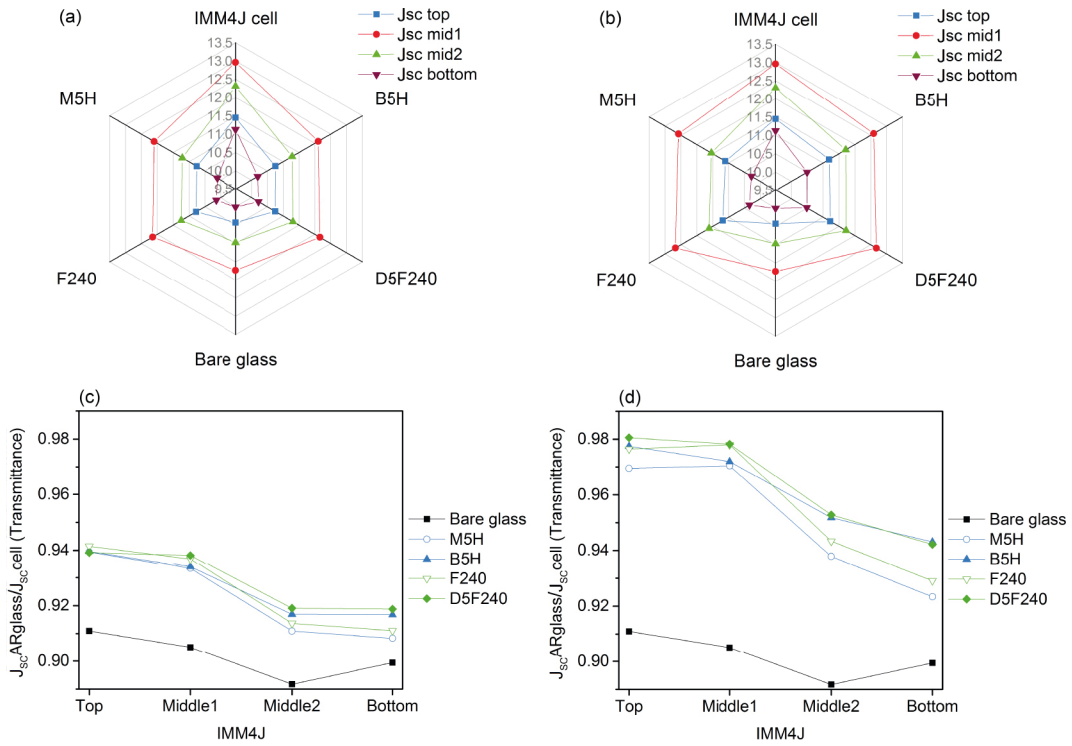

Figure 5-16. Short-circuit current density (mA/cm²) calculated for each subcell in IMM4J without and with interposed cover glass coated with AR on one side (a) and two sides (b) as well as the transmittance calculated as the ratio of the J_{SC} of the bare cell and the J_{SC} with the interposed cover glass uncoated and AR coated on one (c) or two sides (d).

Short-circuit current density was calculated according to Equation 2-21, independently for each of the subcells, by using their corresponding EQE curve in various scenarios. Figure 5-15a represents the short-circuit current density of the bare subcells of UMM3J, uncoated glass + UMM3J cell system, and one side AR coated glass + UMM3J cell system. Two sides AR coated glass + UMM3J cell system is represented in Figure 5-15b. Short-circuit current density of the top and middle subcells was 13.8 and 13.6 mA/cm², respectively, while the bottom subcell's reached 17.7 mA/cm². This constitutes an unbalanced device since the bottom subcell overgenerates current that cannot be used because the subcells are connected in series. The cell producing the lowest current density, which is the middle subcell in this case, will be limiting the whole system. The bare glass interposed between the incoming photon flux and the UMM3J cell provoked a drop in short-circuit current density of subcells which ranged between 12.2 and 15.8 mA/cm². Figure 5-15c and Figure 5-15d represent transmittance calculated as the ratio of the Jsc calculated with and without the interposed glass. The highest loss corresponded to the bottom subcell, although in absolute value the lowest short-circuit

current density was exhibited again by the middle subcell. AR layer stacks deposited on one or two sides of the interposed glass led to an increase in the photogeneration of the subcells compared to uncoated glass. Top and middle subcells generation with AR coated glass experimented a 3-3.7% gain if coating was deposited on one side and 7-8% if coating was deposited on both sides. The bottom subcell experimented the highest loss, even more substantial for the AR mono-layer stacks, if compared to their bi-layer counterparts. This effect can be observed clearly for the one side AR coated glass in Figure 5-15c and for double side coated on the Figure 5-15d. However, in this case in which the bottom subcell is not the one limiting the total current of the system, the improvement provided by the bi-layer would not be the determining factor.

In the case of IMM4J, Figure 5-16a represents the short-circuit current density of the bare subcells of IMM4J, uncoated glass + IMM4J cell system, and one side AR coated glass + IMM4J cell system, while the case of two sides AR coated glass + IMM4J cell system is represented in Figure 5-16b. The short-circuit current density of subcells was comprised between 11 and 13 mA/cm^2, which constitutes a highly balanced device considering that the subcells are connected in series. In this case the subcell producing the lowest current density, and consequently the one limiting the whole system was the bottom one. The bare glass interposed between the incoming photon flux and the IMM4J cell provoked a drop in short-circuit current density of the subcells which ranged between 10 and 11.7 mA/cm^2, 10.8% being the highest loss, which corresponded to the middle 2 subcell as observed in the transmittance graphs (Figure 5-16c and Figure 5-16d). However, in absolute value, the lowest short-circuit current density was generated by the bottom subcell, dropping from 11.1 to 10 mA/cm^2 and being the limiting subcell. The presence of the AR layer stacks on one or two sides of the interposed glass led to an increase in the photogeneration of the subcells compared to uncoated glass. It was easily observed in the transmittance calculations of each subcell tranche in Figure 5-16c (AR coating on one side of glass) and Figure 5-16d (AR coating on two sides of glass). In this case, the highest reduction was again experimented on the bottom subcell tranche, being also more substantial for the AR mono-layer stacks compared to their bi-layer counterparts. In this case the broadband antireflective enhancement provided by the bi-layers concurred with the fact that the limiting subcell was the bottom one and the notable gain in the bottom subcell operational range can be transferred to an improvement of the device. Therefore, the AR bi-layer stacks showed the best complementary performance to IMM4J.

5.6.1.2. Indoor characterization

The effect of the AR coatings on the electrical properties of MJ cells was also determined experimentally. Short-circuit current intensity of the MJ cells with interposed AR coated or uncoated glass was determined through subcell limitation diagrams. The measurements were performed at the Instituto de energía solar (IES-UPM, Madrid, Spain), where the method had been developed in order to measure III-V 3-junction (3J) solar cells with Ge-based bottom subcell [11], as explained in Chapter 2, section 2.5.3. The experimental assembly is shown in the Figure 5-17. The effect of AR coatings on GaInP/GaInAs/Ge solar cell was thus determined.

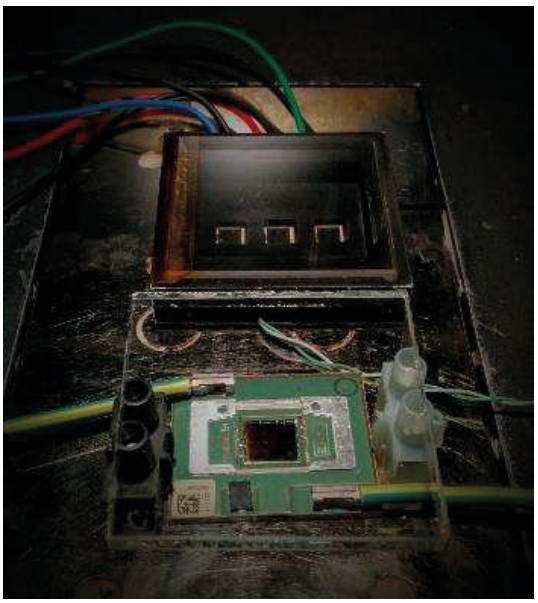

Figure 5-17. 3J-MJ cell with interposed AR coated cover glass.

The M5H and B5H mono- and bi-layer stacks were measured for comparison. Figure 5-18a shows the subcell limitation diagrams corresponding to bare MJ cell, compared to uncoated glass; Figure 5-18b does for uncoated glass compared to M5H coated glass and Figure 5-18c compared to B5H coated glass. Figure 5-18d represents the averaged short-circuit current intensity of bare top and middle subcells and of the cover glass + cell system, with and without the AR mono- and bi-layer stacks. The limiting subcell was the top one in all cases. The presence of the interposed bare glass reduced the Isc of the top subcell to 92.8%, M5H coated glass did to 95.1% and B5H coated glass did to 95.0%. Likewise, the gain provided by mono-layer over uncoated glass was 2.5%, similar to the 2.4% implemented by the bi-layer.

Concerning Isc of the middle subcell, the bare glass implied a reduction of 92.9%, M5H coated glass cut down to 94.8% and B5H did to 95.3%. However, the slightly better behavior of the B5H compared to M5H was useless since the top subcell is limiting the electrical behavior of the device.

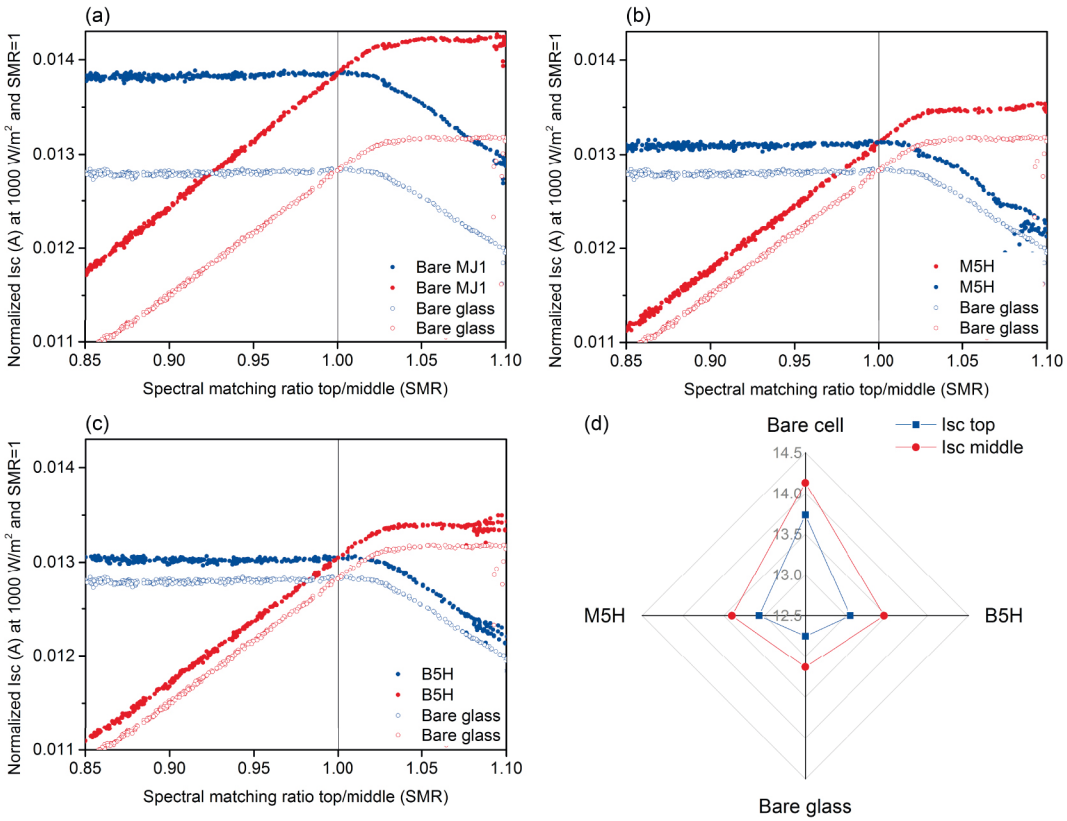

Figure 5-18. Subcell limitation diagrams for a MJ cell, bare and with an interposed uncoated glass (a) AR coated glass with M5H (b) and B5H (c) layer stacks; and short-circuit current intensity (mA) measured for each subcell (d).

5.6.2. Primary optical element (Fresnel lens)

M5H and D5F240 AR stacks were deposited on one side of low iron glass, 150x150 mm² and 4 mm thick. On the other side of the glass, SoG Fresnel lenses sized 92x92 mm² and 192 mm focal distance were manufactured by BECAR Srl (Gruppo Beghelli). Standard validation at BECAR showed up to 4% improvement on lens efficiency due to the AR coatings.

The electrical performance was evaluated at IES-UPM by measuring Isc at different spectral conditions in order to obtain the subcell limitation diagrams. The units were formed by the SoG Fresnel lens (92x92 mm² uncoated and coated with M5H and D5F240) and a refractive

truncated pyramid (26 mm) coupled to the GaInP/GaInAs/Ge MJ cell at 192 mm focal distance (inner side of lens to solar cell). The configuration adopted for performing measurements is presented in Figure 5-19. Figure 5-20 shows the subcell limitation diagrams corresponding with the interposed uncoated glass (a), M5H coated glass (b) and D5F240 coated glass (c), all supporting the SoG on the other side. The normalized Isc of the top subcell was between 0.88 A for uncoated Fresnel lens and 0.95 A for AR coated Fresnel lenses, with a slightly best performance registered for the mono-layer M5H. In the same way, the normalized Isc of the middle subcell was between 0.97 A for uncoated Fresnel lens and 1.05 A for AR coated Fresnel lenses. In this case, the performance of the mono- and the bi-layers was similar when taking the measurement error into account. The presence of the Fresnel lenses provided a geometrical concentration of around 85X (8462 mm^2 lens aperture focused on <100 mm^2 cell) and also in this situation, the limiting subcell was the top one.

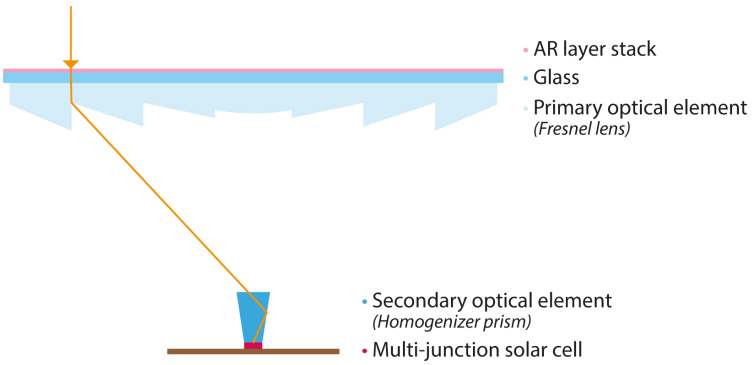

Figure 5-19. Scheme of the configuration used to measure the electrical performance of multi-junction cells with Fresnel lenses as primary optical elements.

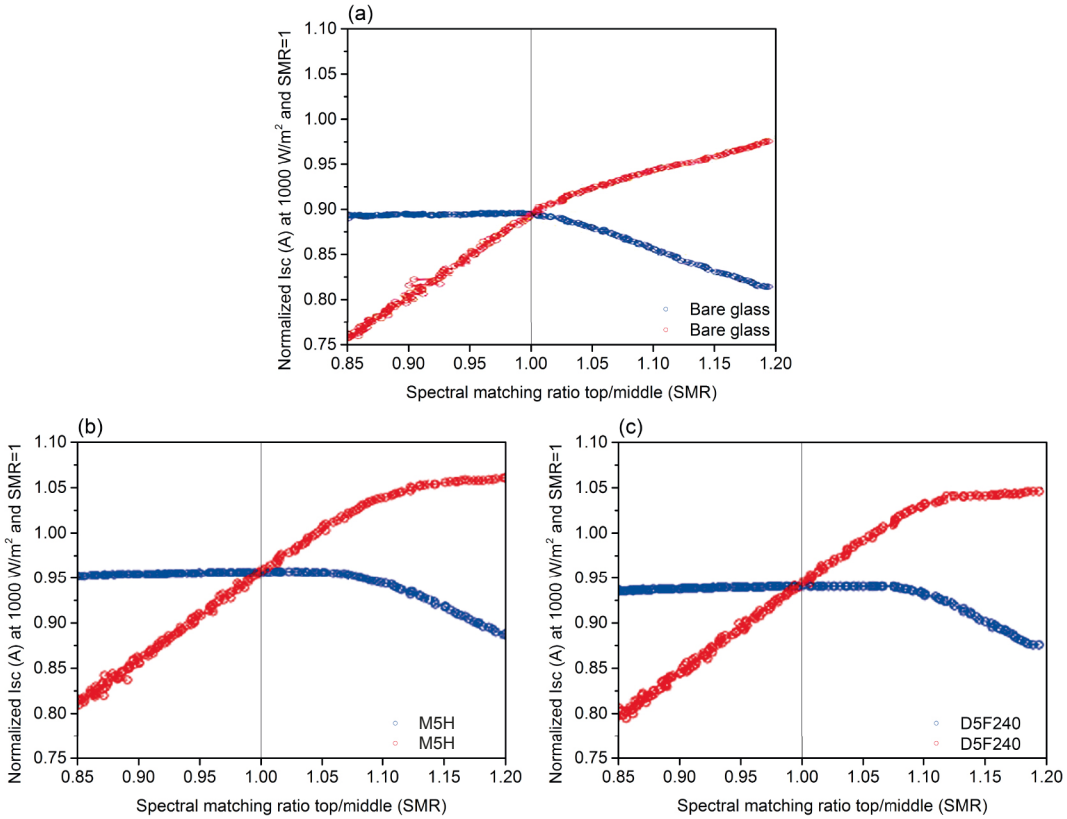

Figure 5-20. Subcell limitation diagrams for a multi-junction cell, bare and with a bare single Fresnel lens (a) and AR coated with M5H (b) and D5F240 (c).

5.6.3. Primary optical element (achromatic double Fresnel lens)

M5H and B5H stacks were deposited on one side of low iron glass, 80x80 mm² and 4 mm thick. On the other side of the glass, achromatic lens with and optical aperture of 40x40 mm² and a theoretical focal distance of 75 mm were laminated at IES-UPM. The innovative achromatic lens patented by IES-UPM (Achromalens) [12] was formed by an elastomer as low-dispersive material and a thermoplastic as high-dispersive material supported on the rigid glass. Manufacture process consisted of laminating glass/elastomer/thermoplastic. Thermoplastic was previously fabricated by plastic injection with designed Fresnel facets on both its sides. Low iron glass was previously coated with AR layer stacks. Elastomer was used as encapsulant between glass and thermoplastic, taking the shape of Fresnel facets in one of its sides.

Ray-tracing simulations were used by IES-UPM to estimate the performance of the achromatic

doublet on glass (ADG) compared to a classic SoG Fresnel lens used as benchmark. A significantly sharper irradiance spot cast and hence a higher concentration had been achieved by the ADG (diameter of 0.84 mm vs 1.77 mm and a concentration of 772X vs 163X).

The electrical performance was evaluated at IES-UPM by measuring Isc at different spectral conditions in order to obtain the subcell limitation diagrams. The units were formed by the ADG (40x40 mm^2 uncoated and coated with M5H and B5H) whose inner side of lens was positioned at a focal distance of 78 mm to the GaInP/GaInAs/Ge MJ cell (10x10 mm^2), with no SOE. The configuration adopted for the measurements is presented in Figure 5-21. Figure 5-22 shows the subcell limitation diagrams corresponding to uncoated glass, compared to mono-layer, M5H coated glass (a) and bi-layer B5H coated glass (b), all supporting achromatic doublet on the other side. The Figure 5-22c represents the averaged short-circuit current density of top and middle subcells obtained for the uncoated ADG, M5H coated ADG and B5H coated ADG.

The normalized Isc of the top subcell was between 0.176 mA for uncoated ADG lens and 0.183 mA for AR coated ADG lenses, with the best performance registered for the bi-layer, which implemented a gain of 3.8% over the uncoated ADG, while M5H provided a 2.8% gain. In the same way, the normalized Isc of the middle subcell was between 0.200 mA for uncoated ADG lens and 0.207 mA for AR coated ADG lenses, with the best performance also registered for B5H bi-layer. In this case, the presence of the ADG lenses provided a geometrical concentration of 16X (1600 mm^2 lens aperture focused on 10x10 mm^2 cell) and the limiting subcell was the top one.

Regardless of the intrinsic optical efficiency of the lenses, the presence of AR layer stacks has demonstrated to effectively contribute to the improvement of efficiency in all the configurations tested. The best AR layer stack from the optical point of view would be the one offering the highest improvement in the electrical performance of the limiting subcell. It has been also demonstrated that the presence of the AR layer on the methamorphic 3-junction solar cell did not correct the unbalanced electrical performance of the top and middle subcells.

Considering the higher industrial processing cost for depositing the AR bi-layer over mono-layer, a deep analysis should be done on each specific case. If the bi-layer stack provides the highest improvement in the electrical performance of the limiting cell, the ratio between the coating processing cost and enhanced efficiency of the photovoltaic system should be taken

into account, as well as reliability and durability properties. If the mono-layer stack provides the highest improvement in the electrical performance of the limiting cell, only the reliability and durability properties should be the key factors to select between AR mono- and bi-layer configurations.

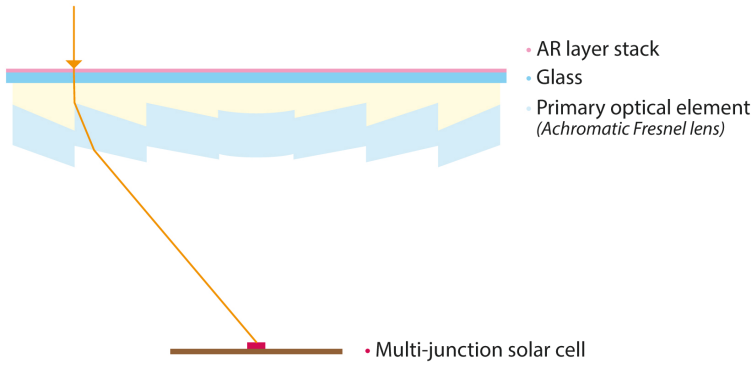

Figure 5-21. Scheme of the configuration used to measure the electrical performance of multi-junction cells with achromatic Fresnel lenses as primary optical elements.

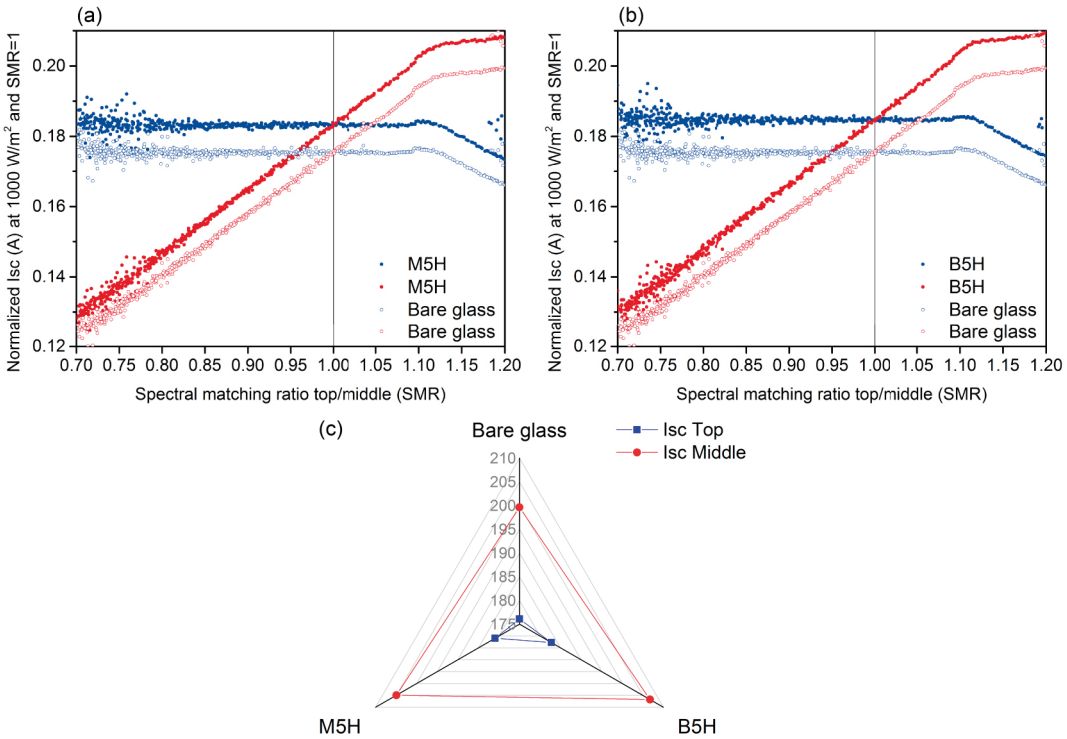

Figure 5-22. Subcell limitation diagrams for the MJ cell with the uncoated ADG lens compared to M5H mono-layer (a) and the B5H bi-layer (b); and short-circuit current intensity (mA) measured for each subcell (c).

5.6.4. Secondary optical element (truncated pyramid)

Silica mono- and bi-layer stacks were applied on the front side of the homogenizer SOE, consisting of refractive truncated pyramids. The truncated pyramids were fabricated at EVONIK (Savosil ®) by an innovative process consisting of sol-gel processing that permits to obtain pure silica material with refractive index around 1.5 [13]. Two different geometries were studied, i) first one, SOE1, with geometry base 1: 12x12 mm ^{2}; base 2: 5.1x5.1 mm^2; height: 30 mm, see Figure 5-23, ii) second one, SOE2, with geometry base 1: 8.45x8.45 mm^2; base 2: 2.85x2.85 mm^2; height: 13.5 mm, see Figure 5-23.

In both cases, AR coatings were applied by dip coating in silica sols (with and without SDA1) under a controlled atmosphere of 60% RH and 22 ºC. Only the front side of the refractive truncated pyramid facing the light was coated. The small base and faces were masked before immersion, and removal of the masking tapes took place before the sintering step. Three sintering temperatures were studied.

Optical transmission was considered the key parameter factor allowing a discrimination among the deposited AR layer stacks. Specific tools were designed and manufactured for the spectrophotometric characterization of the refractive truncated pyramids, one for each geometry. The transmittance measurements were performed with the JASCO V-670 UV-VIS-NIR spectrophotometer equipped with a 150 mm integrating sphere, in the wavelength range from 300 to 2000 nm.

Figure 5-24 collects the transmittance spectra of each truncated pyramid SOE1, both uncoated and coated with porous silica mono-layers sintered at 350 ºC (M3), 450 ºC (M4) and 550 ºC (M5). It can be observed that each truncated pyramid presents its own transmittance spectra. The averaged integrated value in the wavelength range 300-2000 nm of the bare SOE1 was 90.5±0.4%. Up to four truncated pyramid replicas coated and sintered at each temperature were studied. The absolute and averaged integrated transmittance value for coatings treated at 350 ºC on SOE1 was 91.1±0.1%, for coatings treated at 450 ºC it was 92.0±0.3% and for coatings treated at 550 ºC it was 91.4±0.6%. However, the transmittance gain was calculated on each specific truncated pyramid since each of them presented their particularities. The transmittance gain provided by coatings treated at 350 ºC was 1.0±0.5%, by coatings treated at 450 ºC it was 1.8±0.1% and by coatings treated at 550 ºC it was 1.0±0.3%. As the homogenizer is located inside a sealed CPV module, the hydrophobicity property was not

considered for this application. Given that the truncated pyramid was composed of pure SiO_2, the migration of alkali from glass was not a threat and the deposition of an inner dense-structured coating was considered only if the bi-layer stack provided an improvement of the optical properties. Figure 5-25 collects examples of transmittance spectra of traceable truncated pyramids SOE1 when they were uncoated, coated with the inner dense-structured silica coating sintered at 350 ºC (D3) and 550 ºC (D5), and finally coated with porous silica external coating sintered at 350 ºC (B3) and 550 ºC (B5). In this case, the presence of the inner dense-structured coated provoked an undesirable loss of transmittance when applied, what resulted in a lower transmittance gain of the bi-layer stacks compared to mono-layer's values. The deposition of the inner dense-structured coating resulted in a transmittance loss in all cases with respect to uncoated truncated pyramids, ranging between 0.4-0.9%. The further deposition of the porous external coating provided a transmittance gain up to 1.8% over the value exhibited by its precedent inner coating. However, this resulted in a transmittance gain of only 0.9±0.2% of the AR bi-layer stacks over the initial value of the uncoated truncated pyramids. Therefore, for the SOE application, the deposition of the AR bi-layer stacks neither enhanced the optical properties nor was required for the optical durability.

Only the porous silica coating sintered at 450 ºC (M4) was applied on the front side of the truncated pyramid SOE2. Figure 5-26 displays the transmittance spectra of a traceable truncated pyramid SOE2 uncoated and after M4 coating deposition. The averaged integrated transmittance of uncoated SOE2 was 93.3±0.8%. The traceable transmittance gained after M4 deposition presented a high dispersion, ranging from 1 to 2.5%.

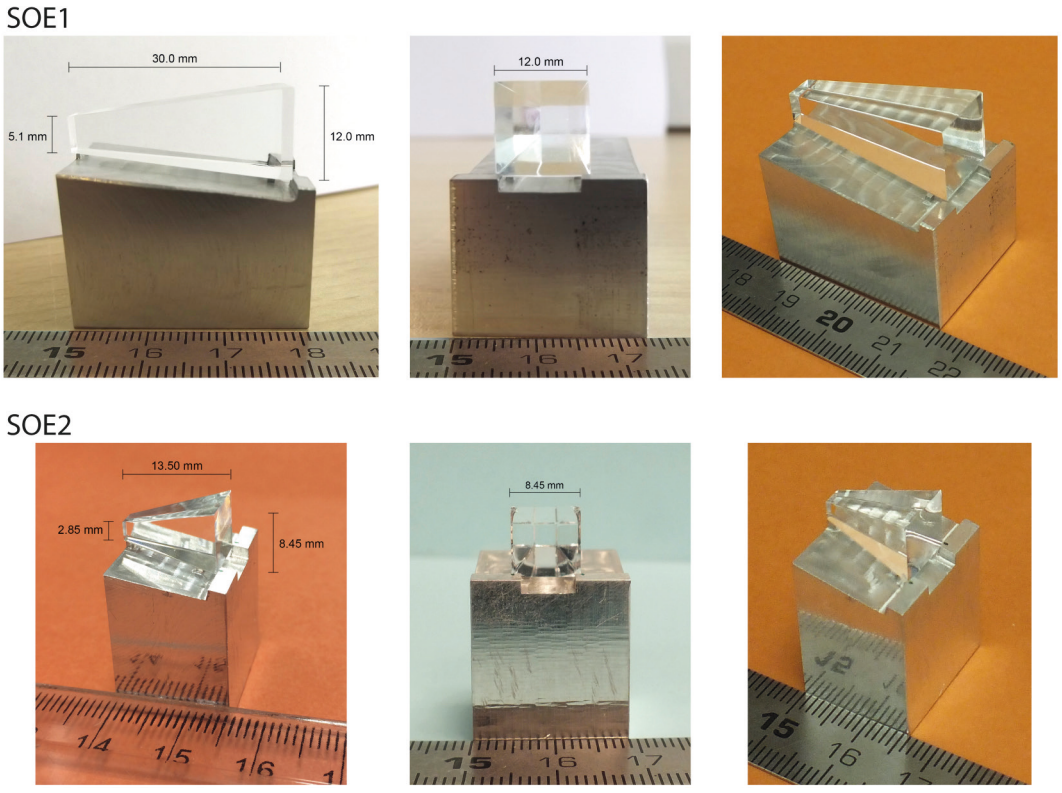

Figure 5-23. Image of the studied SOE prisms and the corresponding tool for optical characterization.

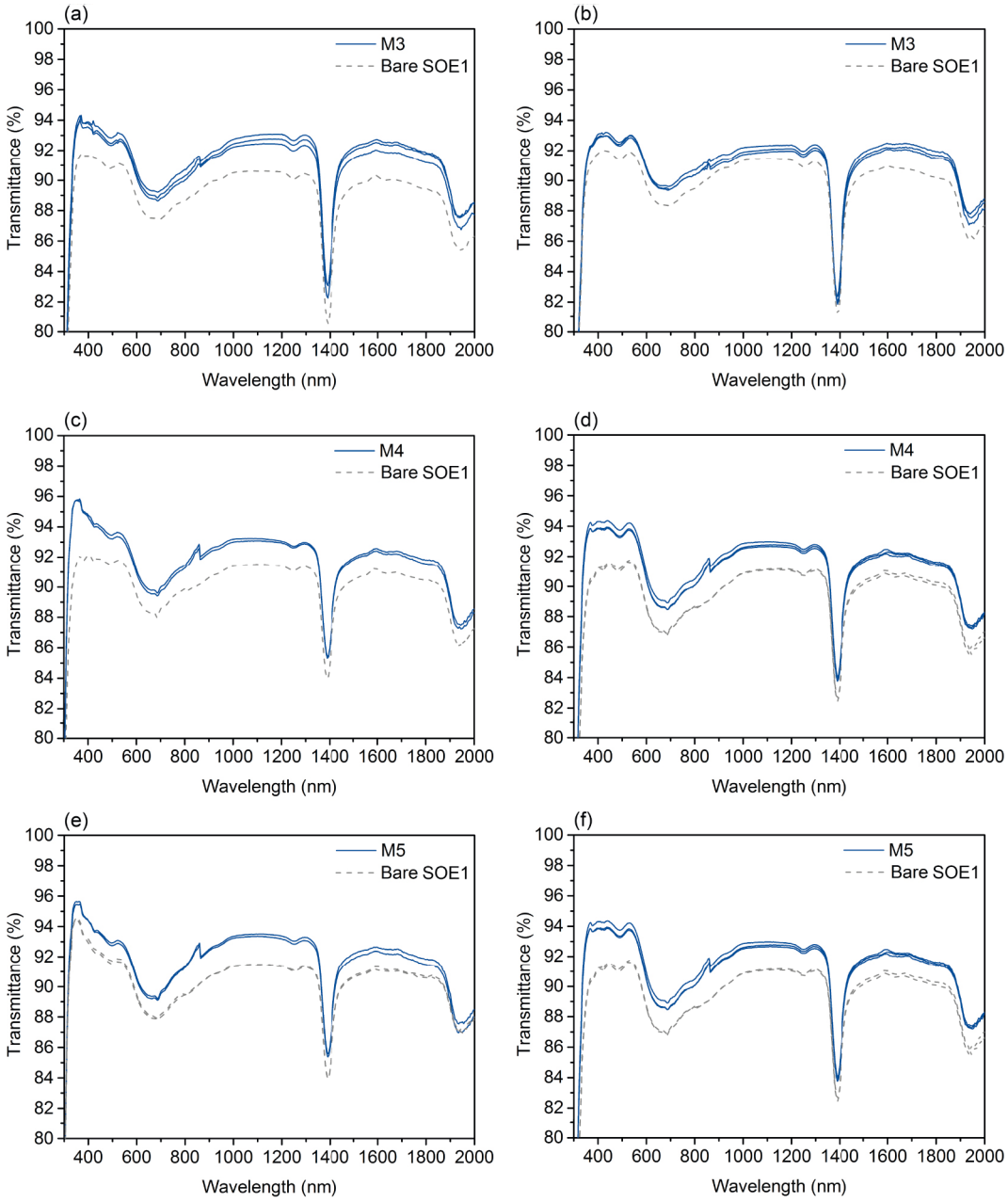

Figure 5-24. Transmittance spectra of each truncated pyramid SOE1 (front side 12x12 mm^2), bare and coated with AR mono-layers sintered at 350 ºC (M3), 450 ºC (M4) and 550 ºC (M5).

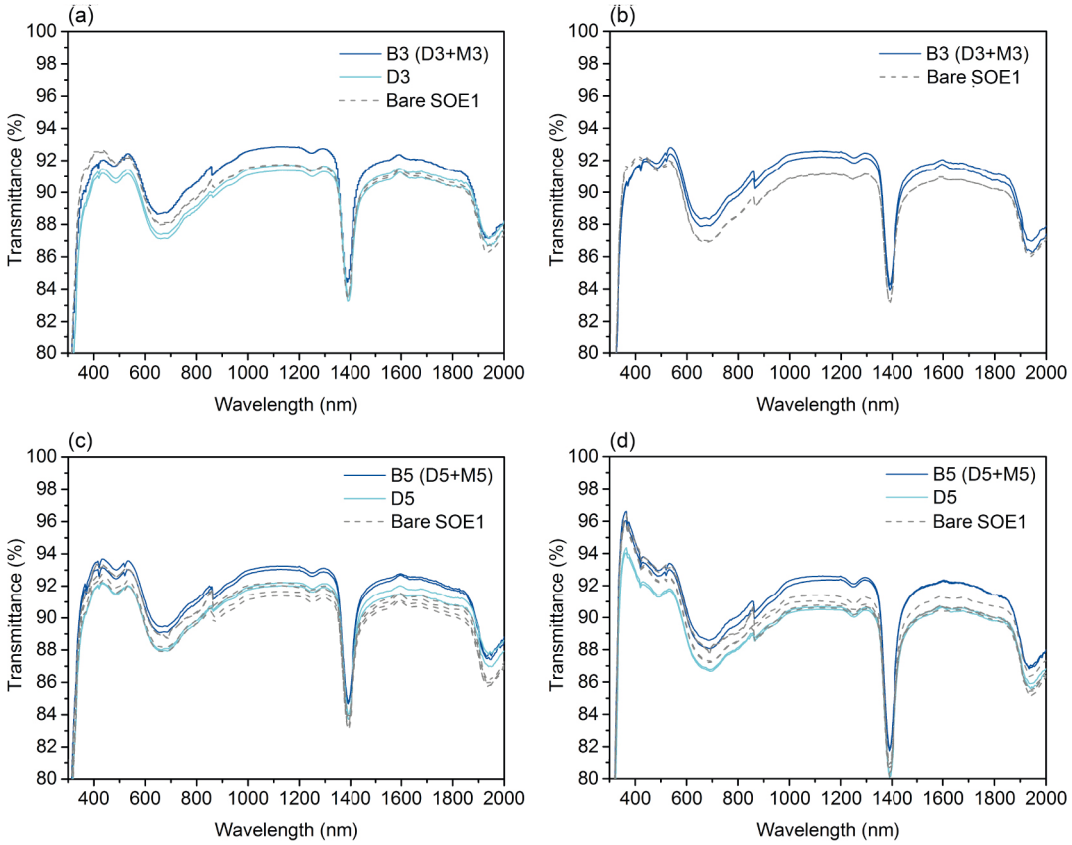

Figure 5-25. Transmittance spectra of each truncated pyramid SOE1 (front side 12x12 mm^2) bare, coated with inner dense-coating (D) and then porous external coating, thus AR bi-layers sintered at 350 ºC (B3), and 550 ºC (B5).

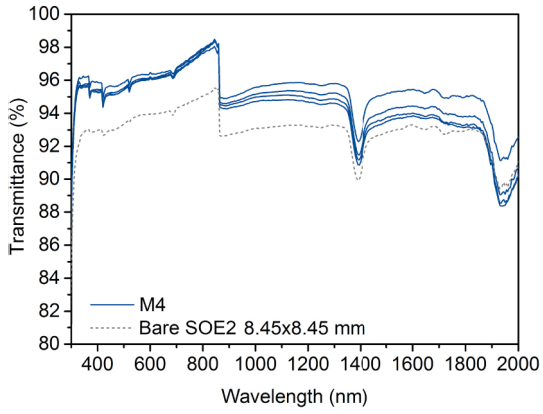

Figure 5-26. Transmittance spectra of truncated pyramid SOE2 (front side 8.45x8.45 mm^2), bare and coated with AR mono-layer sintered at 450 ºC (M4).

5.6.4.1. Reliability testing

Uncoated and mono-layer coated truncated pyramid SOE1 were exposed to damp heat test at TECNALIA facilities as described in the section 5.3.1. The transmittance of the aged specimens was measured at different exposure times. The uncoated truncated pyramids showed an integrated transmittance loss after 1000 h of exposure ranging between 0.6-1.2%. The transmittance loss exhibited by AR coated truncated pyramid SOE1 was lower than 0.6%. Finally, the AR coated truncated pyramids showed a transmittance gain after ageing of 0.8-1.5% related to the initial optical performance before coating them. In addition, the coating sintered at 450 ºC showed the best performance/stability ratio, that arrived to 91.8% after 1000 h of exposure to damp heat test against the 89.8% showed by aged uncoated SOE1.

The M4 coated truncated pyramids SOE2 were exposed to ultraviolet radiation, thermal cycling, humidity freezing, salt mist corrosion and cyclic corrosion-condensation tests at ENEA facilities as described in the section 5.3.1. The Figure 5-27 shows the integrated transmittance measure for each SOE2 before coating deposition and M4 coated before and after being subjected to different ageing tests (two specimens parallelly aged). As observed, the integrated transmittance was diminished after all the tests, however the final transmittance values of the coated truncated pyramids were higher than the one offered by the uncoated in all cases. The AR coated truncated pyramids showed a transmittance gain after ageing of 0.7-1.5% related to the initial optical performance before the coating application. Furthermore, the humidity freezing, and the corrosion condensation tests were the most aggressive for the coated truncated pyramids, showing also an inhomogeneous behavior. This behavior, also observed on flat samples in the section 5.3.2, was argued on the fact that the ageing tests with presence of water can irreversibly affect to porous coatings since they are prone to absorb water into the pores, what can trigger the collapse of porous structure.

The conclusion is that the AR coating on SOE truncated pyramids provides an improvement on both initial optical properties and durability, that however is not particularly outstanding. Additionally, the AR deposition will be feasible depending on the ratio between the coating processing cost and enhanced efficiency of the photovoltaic system.

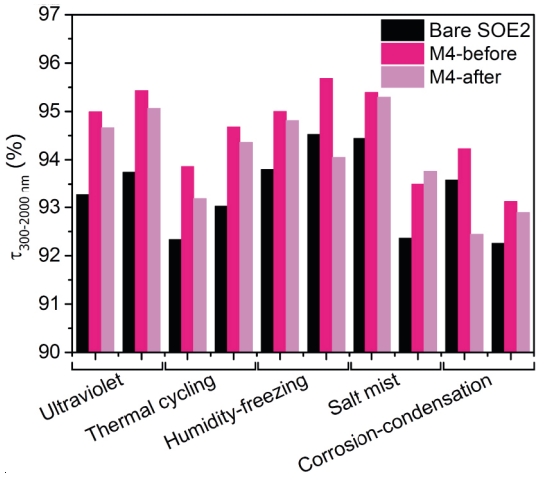

Figure 5-27. Integrated transmittance values of each uncoated truncated pyramid SOE2, and M4 coated before and after reliability tests performed at ENEA.

5.7. Conclusions

The AR layer stacks with low surface free energy with derived antisoiling properties prepared by two different Routes were assessed from the point of reliability and enhancement of the electrical response of solar cells. Summarizing, the AR layer stacks hydrophobized in a post-treatment presented higher mechanical properties, cohesion and adhesion coming from the high consolidation obtained network that was treated up to 550 ºC. Furthermore, the post-treatment allowed to properly functionalize the external and internal specific surface, and thus enabled these coatings to offer optical properties independent from environmental humidity since they did not absorb water into the pores. The polyfluoroalkyl-silica coatings allowed to obtain an AR and hydrophobic surface in one-step process. The $–(CH_2)_2\text{-}(CF_2)_n\text{-}CF_3$ moiety allowed to attain a low surface free energy, more liquid repellent than methyl-silylated one. However, the low required sintering temperature obliged to the presence of the inner dense-structured coating to attain the adhesion, mechanical properties and durability.

Along this Chapter, the differences on the properties of coatings prepared by both Routes have emerged when validated under reliability tests. Damp heat test revealed a better performance of bi-layer over mono-layers. Among the tested mono-layer, M5 and M5H sintered at the highest temperature showed acceptable loss of optical properties. The complementary ageing tests revealed that hydrophobic coatings showed less degradation when subjected to tests that implied the presence of water. However, those purely inorganic AR layer stacks, behaved better under UV ageing. D5F240 bi-layer stack was the unique system that

presented a transmittance loss below 1% in all the tests.

Abrasion resistance tested under reciprocating test was not discriminatory for methyl-silylated layer stacks sintered at 550 ºC while bi-layer was required in the case of polyfluoroalkyl-silica coatings.

The enhancement of electrical response of solar cells was validated according to indoor measurements and validated in the outdoors exposure. The most entitled AR layer stacks M5H and D5F240 tested on the c-Si PV modules showed an equivalent overgeneration of around 2% compared to uncoated mono-modules, although M5H was the most stable and efficient against soiling adherence.

The differences on the electrical response enhancement provided by AR mono-layers and bi-layers were mainly dependent on the spectral response of the different MJ solar cell devices.

References

[1] J.C. Brinker, E.P. Roth, G.W. Scherer, D.R. Tallant, Structural evolution during the gel to glass conversion, J. Non. Cryst. Solids. 71 (1985) 171–185.

[2] J. Li, Y. Lu, P. Lan, X. Zhang, W. Xu, R. Tan, W. Song, K.-L. Choy, Design, preparation, and durability of TiO_2/SiO_2 and ZrO_2/SiO_2 double-layer antireflective coatings in crystalline silicon solar modules, Sol. Energy. 89 (2013) 134–142.

[3] R.K. Jones, A. Baras, A. Al Saeeri, A. Al Qahtani, A.O. Al Amoudi, Y. Al Shaya, M. Alodan, S.A. Al-Hsaien, Optimized cleaning cost and schedule based on observed soiling conditions for photovoltaic plants in central saudi arabia, IEEE J. Photovoltaics. 6 (2016) 730–738.

[4] M.A. Green, High-efficiency silicon solar cell concepts, McEvoy's Handb. Photovoltaics Fundam. Appl. 33 (2017) 95–128.

[5] International Energy Agency - Photovoltaic Power Systems Technology Collaboration Programme, 2019 Snapshot of Global PV Markets, 2019.

[6] European Technology & Innovation Platform PV, PV the cheapest electricity source almost everywhere, 2019.

[7] E.F. Fernández, F. Almonacid, P.M. Rodrigo, P.J. Pérez-higueras, CPV Systems, in: McEvoy's Handb. Photovoltaics, Elsevier Ltd, 2018: pp. 929–986.

[8] P. Pérez-Higueras, E.F. Fernández, High concentrator photovoltaics: fundamentals, engineering and power plants, Springer International Publishing, Heidelberg, Germany, 2015.

[9] J.P. Ferrer-Rodríguez, E.F. Fernández, H. Baig, F. Almonacid, T. Mallick, P. Pérez-Higueras, Development, indoor characterisation and comparison to optical modelling of four Fresnel-based high-CPV units equipped with refractive secondary optics, Sol. Energy Mater. Sol. Cells. 186 (2018) 273–283.

[10] S.P. Philipps, M. Baudrit, K. Hillerich, V. Moreau, R. Parmesani, E. Román, G. Sala, B. Schineller, G. Timò, A.W. Bett, CPVMatch - Concentrating photovoltaic modules using advanced technologies and cells for highest efficiencies, AIP Conf. Proc. 1766 (2016) 060002.

[11] C. Domínguez, I. Antón, G. Sala, S. Askins, Current-matching estimation for multijunction cells within a CPV module by means of component cells, Prog. Photovoltaics Res. Appl. 21 (2013) 1478–1488.

[12] G. Sala Pano, S. Askins, I. Antón Hernández, M. Victoria Pérez, Lens having limited chromatic aberration for photovoltaic concentrators and method for manufacturing said lens, WO2015101626A1, 2015.

[13] C. Algora, I. Rey-Stolle, Handbook of concentrator photovoltaic technology, John Wiley and Sons Ltd., 2016.

Chapter 6

General conclusions, future work and scientific contributions

6.1. Final overview

In the highly competitive energy market, solar energy emerges as the most promising renewable energy source capable to attain competitive prices at large scale due to the reduction of total costs and the improvement of the energy yields during the last years.

To effectively contribute to improve the levelized cost of energy, the efforts focused on the development of highly efficient solar cells must be accompanied by the proper selection of module materials to minimize the optical and electrical losses from cell to module, through cost-competitive solutions.

The front cover sheet required for module insulation is the first surface in receiving irradiation towards solar cell, and the first surface in reducing the photon flux impinging it due to optical losses. The physical calculations presented in the Chapter 3, disclosed that theoretical maximum transmittance value for a GRIN coated glass arrives at 98.3% (in the wavelength range 300 to 2000 nm) for an AR tri-layer stack with growing void fraction silica layers of 11, 45 and 77% interposed on the two glass-air interfaces. Compared to the 90.1% provided by the bare low iron glass, up to 9% of incoming irradiance can be gained in a broadband range of spectrum by depositing an AR coating system on glass. Nevertheless, considering the mechanical properties, and the alkali diffusion from the glass substrate when subjected to thermal loads, the maximum void fraction of external coating was restricted to 50%. In this scenario, the 50% porous coating was able to act as both single AR mono-layer and external layer of an AR bi-layer stack, while an AR tri-layer stack did not further enhance optical properties.

The layer deposition was accomplished by sol-gel method, that was designed considering efficiency, environmental-friendliness, cost-effectiveness and easy up-scaling. Sol-gel via acid catalysis combined with evaporation-induced self-assembly during coating deposition led to tailor mesostructured porous coatings with a high control of the void fraction and thickness. Five types of amphiphiles, water/alkoxide ratio and solvent content were used to correlate the theoretical optical prediction with experimental results. The sols exhibited long-term stability and served to grow coatings with specific optical constants, porosity and thickness. The amphiphile system that allowed to grow the coating with the searched thickness-optical constants tandem under fixed deposition conditions of withdrawal rate and atmosphere was the di-block copolymer formed by PEO and n-alkyl-chain. Optimized process at R_w8

conditions produced 50% porous silica coatings sintered between 350-550 ºC with thickness between 120-130 nm, 1.22 refractive index at 700 nm and pore size around 9 nm. Those coatings were conceived as single AR mono-layer and as external coating of the AR bi-layer, whose inner coating was formed by the dense-structured silica coating prepared at R_w4 conditions. The bi-layer architecture provided a transmittance enhancement over a wider region of the solar spectrum, and the optical transmittance gained up to 7.2% over bare glass in the wavelength range between 300-2000 nm where multi-junction cells are active. Differences on the formation of the porous layer if directly grown on glass or on the dense-structured coating arose along the Chapter 4. The porous coating, which was devised to exhibit same porosity when directly grown on glass or on the dense-structured coating, showed higher porosity and grain size when grown on the latter, also implying a higher water contact angle of the surface.

In the Chapter 4, the external factors that can alter the outstanding AR properties of the coating system developed in the Chapter 3 motivated the design of an effective, durable AR system with envisaged operating expenditures reduction. To deal against soiling adherence, a methyl-silylating post-treatment applied on consolidated porous silica coatings allowed to obtain hydrophobic surfaces in a two-step process. On the other hand, the addition of polyfluoroalkyl silanes to the baseline silica sol-gel coating allowed to obtain hydrophobic surfaces with lower surface free energy, more liquid repellent than methylated ones, in a one-step process. The optical transmittance of coatings prepared by both routes were comparable to the hydrophilic baseline AR layer stacks target. The differences among the two approaches that conferred hydrophobicity were related to the functionalization of the internal surface area of the pores, and the mechanical properties attained depending on the temperature applied during sintering step. Whereas optical transmittance of methyl-silylated silica coating was slightly lower compared to polyfluoroakly-silica coating, their optical constants were inalterable when exposed to high RH conditions due to internal functionalization of the pores, thus repelling water to enter. At the same conditions, the polyfluoroalkyl-silica coating changed the optical constants due to water adsorption into the pores, resulting in a transmittance loss at high RH conditions.

Concerning mechanical properties, the methyl-silylated mono-layers sintered at 550 ºC exhibited better cohesion, adhesion, and hardness properties than polyfluoroalkyl-silica mono-layers treated at 240 ºC. However, the bi-layer configuration led to improve adhesion

properties and to achieve comparable hardness values in stacks prepared by both approaches. The dense structure also played an important role regarding durability properties providing a barrier against alkali diffusion and avoiding mesostructure collapse. The AR bi-layer stacks did not show transmittance decrease after damp heat aging.

In the Chapter 5 the hydrophobized AR layer stacks were subjected to reliability tests according to standards used by PV industry to validate the materials used for solar system components that must withstand exposure in harsh environments during their life cycle. The most aggressive ageing tests were damp heat and humidity freezing, and the mildest were UV and salt mist exposure. The hydrophobic coatings showed less degradation of optical properties when water and temperature participated together in the aging test compared to their hydrophilic counterparts. In general, the higher instability and heterogeneity of damaged coatings after tests, resulted in a higher data dispersion of the optical transmittance. The AR bi-layers hydrophobized by the two routes, presented great behavior under the ageing tests.

Under the ad hoc designed abrasion resistance test, the methyl-silylated silica single mono-layer presented no wear tracks. The polyfluoroalkyl-silane required the bi-layer architecture to show such inalterability due to the adhesion improvement provided by the inner dense-structured coating. Nevertheless, both AR layer stacks required the identic steps for preparation.

The enhancement of electrical response of solar cells was measured according to indoor measurements and validated in outdoor exposure. The presence of AR layer stacks demonstrated to effectively contribute to the improvement of the electrical response assessed under several real configurations. However, from the optical point of view, the bi-layer stack was only required when the limiting subcell matched with the spectral region where transmittance of the bi-layer is higher compared to mono-layer architecture.

Methyl-silylated silica single mono-layer was the most stable and efficient against soiling adherence under outdoor exposure of c-Si PV modules, which exhibited an averaged equivalent overgeneration of around 2% along a year compared to uncoated mono-modules.

Therefore, depending on the type of solar cell, only reliability and durability properties should be the key factors to choose between AR mono- and bi-layer configurations and a feasibility study should balance the coating processing cost, the enhanced efficiency of the PV system, the durability and the antisoiling effect on the operating expenditures reduction.

6.2. General conclusions

The main conclusions extracted along this investigation work are listed below:

- A theoretical model has been obtained with defined layers in terms of material and thickness as outcome. Layer stacking has resulted in an AR system with optimized optical transmittance in the spectral range matched to response of solar cells.
    - Theoretically, up to 9% of optical transmittance can be gained in a broadband range of spectrum by depositing an AR tri-layer stack on glass.
    - In a scenario with restricted void fraction of coatings to 50%, the most efficient system is an AR bi-layer stack. Moreover, in this case the porous coating is able to act as single AR mono-layer, or as external layer of an AR bi-layer stack.
- An environmental-friendly, cost-effective and easy up-scaling process based on acid-catalysis sol-gel approach combined with EISA has allowed to grow coating stacks that exhibit the required enhancement in the optical performance.
    - Sol formulated at R_w8 conditions assisted by polyethylene oxide (20) hexadecyl ether as SDA produces 50% porous silica coatings when sintered between 350-550 ºC with thickness between 120-130 nm, 1.22 refractive index at 700 nm and pore size around 9 nm.
    - A dense-structured silica coating is obtained at R_w4 conditions with thickness between 115-130 nm and refractive index between 1.42-1.45 at 700 nm.
    - The bi-layer architecture provides a transmittance enhancement over a wider region of the solar spectrum, and the optical transmittance gains up to 7.2% over bare glass in the wavelength range between 300-2000 nm where multi-junction cells are active.
    - The porous layer shows a different porosity and structure if directly grown on glass or on the dense-structured coating, which arises up to 56%.
- Low surface free energy surfaces have been obtained through two different approaches without detrimental effect on the optical properties of the AR system.
    - Methyl-silylating post-treatment applied on consolidated porous silica coatings allows to obtain hydrophobic surfaces with $\theta_c^{H_2O}$ up to 99º, in a two-step process.
    - A sol containing polyfluoroalkyl silanes allows to obtain hydrophobic surfaces with low surface free energy, more liquid repellent than methyl-silylated ones, in a one-step process.
    - Methyl-silylating process allows to functionalize internal surface of the pores in contrast to polyfluoroalkyl functionalization.
- Differences in the mechanical, chemical and structural properties of the AR coatings have

been correlated with differences in the behavior under reliability tests.

  - Hardness is strongly dependent on the sintering temperature and coating porosity.
  - Mono-layers sintered at 550 ºC exhibits better cohesion, adhesion, and hardness properties than polyfluoroalkyl-silica mono-layers treated at 240 ºC.
  - The bi-layer configuration leads to an improved adhesion and allows to achieve comparable hardness values for the polyfluoroalkyl-silica stacks prepared at 240 ºC.
  - Abrasion resistance of mono- and bi-layer stacks sintered at 550 ºC is good while polyfluoroalkyl-silica requires the bi-layer architecture to exhibit comparable behavior.
  - The most aggressive ageing tests are damp heat and humidity freezing, and the mildest are UV and salt mist exposure.
  - The inner dense-structured coating plays an important role regarding durability properties since it provides a barrier against alkali diffusion and avoids mesostructure collapse. None the AR bi-layer architectures shows transmittance decrease after damp heat aging.
  - Methyl-silylated silica single mono-layer is the most stable and efficient against soiling adherence.

- Differences in the optical performance of AR coatings have been correlated to electrical response displayed by crystalline silicon and multi-junction solar cells.

  - For the silicon cells, around 3% of improvement on electrical performance is obtained due to the presence of the AR layer stacks.
  - For the silicon cells, an averaged equivalent overgeneration of around 2% along a year of exposure is shown for the methyl-silylated silica mono-layer.
  - For the MJ cells, the bi-layer architecture is required only when the limiting subcell matches with the spectral region where transmittance of the bi-layer is higher compared to mono-layer architecture.

6.3. Prospect

New prospect of future working lines has been identified, mainly related to energy and time consumption and directly implied in processing cost and efficiency of an industrial coating deposition process.

1) Coating deposition method

The coating deposition method has been unquestioned along this dissertation. The deposition method has the decisive influence on the desired properties of the coating like layer thickness and homogeneity. The dip coating method is the most widely technique used for applying sol-

gel technology to create thin films especially in chemical and nanomaterial engineering academic research. Since controlling the thickness of the layer is a key parameter to control for obtaining the desired optical properties of the AR coating, dip coating was selected to create extremely thin, uniform and high-quality layers. Glass plates up to 300x250 mm were successfully scaled-up by dip coating along this work. The glass required for mounting the PV arrays, which is formed by several cells, may be on the range of 2000x1000 m. Focusing on the process transfer to industry, the dip coating presents some drawbacks such as the huge amount of sol that is needed to produce large samples, and the long processing time that the withdrawal of a long plate takes.

Other coating methods can be explored such as spray coating, flow coating, roll coating, spin coating, or wire bar coating, considering the following parameters: viscosity of the sol; volatility and flammability of the solvents; geometry and size of the substrates; flexibility and deformation behavior of the substrate.

Spin coating requires a small quantity of sol to obtain a coating and is used to grow homogenous thin films on flat samples. However, big flat plates cannot be spun at the required high rate to allow the completely spread of the sol by centrifugal sol and the formation of thin film. Spray coating method is widely used in industry for organic lacquers deposition. It requires a small quantity of sol and short production time, therefore with low process cost. It can be adapted to big and complicated substrate geometries. However, the deposition of a thin homogenous coating is a challenge, and still, the structure of the formed coating is different from that obtained by other techniques. Flow coating is a simple, flexible, easy and low-cost process based on the controlled gravity flow of the sol over the substrate. It is commonly used to obtain smooth surface of thick coatings in one step. The required volume of sol is lower than in the case of dip coating technique. The challenge is the deposition of homogenous films through the control of evaporation of the solvent. Wire bar coating is another low-cost procedure to obtain the uniformly of thickness in thin films on flat plates. The difficulties lie in the processing of big plates.

Currently, the deposition of the sol-gel coatings developed in this work is being explored by some these alternative methods at GXC Coatings GmbH facilities in the frame of the H2020 European Project "Global optimization of integrated photovoltaics system for low electricity cost".

2) Methyl-silylating process

The methyl-silylating process optimized along this work can be somehow defined as a chemical conversion process. Therefore, the active reactants needed for converting the free -OH of the surface into $–Si(CH_3)_3$ are progressively depleted from the bath. The effectiveness of the methyl-silylation along time should be studied with the aim to define the life time of the bath.

On the other hand, the process conditions can be balanced to attain the most efficient industrial process. The immersion time can be reduced using higher temperature of reaction and/or higher concentration of methyl-silylating agent. The challenge is to obtain the most efficient combination of time/temperature/concentration.

3) Polyfluoroalkyl silane route

The high strength of the C–F bond which grants high thermal, chemical, photochemical and hydrolytic stability required for outdoor application and weathering resistance offered by the polylfluoroalkyl moiety, has the counterpart of persisting in the atmosphere for thousands of years. Polyfluorcarbon compounds release to the atmosphere are considered greenhouse gases although they not contribute significantly to global warming because of the small amounts released. In spite of the low quantities of fluorocarbon moieties that are needed to provide low surface energy properties to the coatings developed in this work, an alternative for their replacement can be the optimization of the formulations using non-hydrolizable long hydrocarbon chains, that are also good candidates for implementing such property on the coating.

Concerning the constraint that these coatings showed related to the humidity adsorption, the indispensable presence of the inner dense coating and the questionable behavior showed along the field exposure, these coatings could be candidates for space applications. In the cover glass and reflectors of PV and CPV modules required for space applications, there is a necessity related to the repellence of space contaminants that can decrease power output of the solar array if they attach on the functional surfaces. In this case, the highest UV resistance shown by C-F bond bring the polyfluoroalkyl moiety as the best candidate to withstand the aggressiveness of the vacuum UV conditions.

4) Sintering step optimization

Several concepts can be optimized when concerning the industrialization of the AR layer deposition. Particularly considering the energy and time consumption that have directly influence on the processing cost, thermal sintering process of the coating can be adapted. Along this work, a wide broad window of temperatures has been studied ranging from 200 to 550 ºC. The optical, mechanical, adhesion and durability properties depend on the consolidation of the material, which increases as temperature does. However, the sintering time was fixed to 1 h to obtain consistent results when studying different temperatures. The most efficient combination of time/temperature of the sintering step can be studied and adapted in order to find the balance between those parameters that are directly related to processing cost. In addition, concerning the bi-layers stacks prepared under similar sintering treatments applied after each layer deposition, a unique and final co-sintering of all the stacked fresh coatings can be envisaged that would lead to energy and time savings.

On the other side, large glass plates are commonly tempered for safety reasons. The tempered glass is mechanically and thermally stronger than standard glass. Physically, the tempering process consists of creating compression in the out surface of the glass and tension in the interior. That stress gradient is attained by controlled thermal or chemical treatments. Particularly, the thermal tempering process consists of heating the glass at a temperature between 600-700 ºC; and force-cooling the glass obtained in previous step at a temperature between 20-150 ºC to create surface and edge compression by air-quenching. The sintering step required for consolidate the AR coatings can ruin the mechanical and thermal properties of a tempered glass. This fact drives to consider the compatibility of coating sintering and tempering process of glass. It is crucial to evaluate if the properties of developed AR layer stack can be affected by tempering cycle, or even if this thermal treatment can be substitutive of standard thermal sintering of the coating. The latter option is the most promising from the point of view time and energy saving, efficiency and cost. Some exploratory cost calculations have indicated that the thermal sintering has the greatest weight on the processing cost, compared to the reactants price and sol synthesis process.

5) Self-cleaning, thin TiO_2 coatings

Both hydrophobic and hydrophilic properties can be envisaged when designing a repellent or self-cleaning surface. Along this work, hydrophobicity strategy has been pursed with the aim

to obtain low surface free energy dealing against soiling adherence. However, another strategy widely explored by researchers is the so-called self-cleaning property. Self-cleaning is an effect combined by photocatalysis and superhydrophilicity. The photocatalysis property helps decompose organic substances that meet the surface and thus prevents them from building up. The hydrophilicity makes the cleaning more effective as the water spreads over the surface rather than remaining as droplets, which helps collect the dirt better, make the surface dry faster, and moreover, prevent the undesirable water streaking or spotting on the surface. TiO_2 is the most widely used material for self-cleaning application because its thermal stability and photocatalytic properties. In its anatase crystalline state, UV radiation promotes electrons from valence band to conduction band. The free electrons and gaps formed can react with pollutants thus triggering their decomposition. Anatase TiO_2 coatings can be prepared by sol-gel technique, followed by a thermal sintering arising 400-450 ºC, which is required to attain the anatase crystalline phase. If the deposition of TiO_2 as the external layer in the AR interference-type multi-layered configuration is optically feasible, a photocatalytic AR stack with high mechanical properties and robustness is envisaged with the drawback standing on the required multi-step process.

Furthermore, the photocatalytic activity can be enhanced with the increase of effective surface area. Thus, the growth of porous coatings with tailored and controlled porosity, pore size and surface area leads to an increase of the internal contact area with pollutants. However, the intrinsic refractive index of TiO_2, is such high that a single TiO_2 layer would require such a high porosity to obtain the required refractive index that mechanical properties would be ruined. An alternative approach can be the deposition of a very thin TiO_2 on the porous SiO_2 prepared along this work. This strategy would lead to a high surface contact area of the porous structured SiO_2 covered by a few nanometers of TiO_2, which however would be irrevocably accompanied by some loss of optical properties.

6.4. Future work

In the light of these prospects, the following research lines are proposed:

- Optimize the coating deposition by alternative techniques such as spray coating and flow coating.

- Study the methyl-silylating bath depletion.

- Replace polyfluoroalkyl alkoxysilanes by long chain alkyl alkoxysilanes to obtain a more environmentally friendly process.
- Optimize the sintering step time to reach a more efficient process.
- Study of a co-sintering process of the AR bi-layer stacks.
- Study the compatibility of sintering and glass tempering processes, i) study the properties of coatings tempered after standard sintering, ii) study the properties of coatings directly tempered without previous sintering.
- Study the performance of hydrophilic and hydrophobic coatings on modules under real exposure to different climatology conditions.

6.5. Scientific contributions

6.5.1. Publications

Peer reviewed articles published as a result of presented investigation work:

1) C. Agustín-Sáenz, M. Machado, A. Tercjak, Antireflective mesoporous silica coatings by optimization of water content in acid-catalyzed sol-gel method for application in glass covers of concentrated photovoltaic modules, J. Colloid Interface Sci. 534 (2019) 370–380. Impact Factor: 5.091, 33 of 147 in CHEMISTRY, PHYSICAL (JCR 2017), Q1
2) C. Agustín-Sáenz, J.Á. Sánchez-García, M. Machado, M. Brizuela, O. Zubillaga, A. Tercjak, Broadband antireflective coating stack based on mesoporous silica by acid-catalyzed sol-gel method for concentrated photovoltaic application, Sol. Energy Mater. Sol. Cells. 186 (2018) 154–164. Impact Factor: 5.018, 47 of 285 in MATERIALS SCIENCE MULTIDISCIPLINARY (JCR 2017), Q1
3) C. Agustín-Sáenz, M. Machado, O. Zubillaga, A. Tercjak, Hydrophobic and spectrally broadband antireflective methyl-silylated silica coatings with high performance stability for concentrated solar applications, Sol. Energy Mater. Sol. Cells. 200 (2019) 109962, Impact Factor: 5.018, 47 of 285 in MATERIALS SCIENCE MULTIDISCIPLINARY (JCR 2017), Q1

4) C. Agustín-Sáenz, M. Machado, A. Tercjak, Polyfluoroalkyl-silica porous coatings with high antireflection properties and low surface free energy for glass in solar energy application, Applied Surface Science, send for publication Impact Factor: 4.439, 1 of 19 in MATERIALS SCIENCE, COATINGS AND FILMS (JCR 2017), Q1

5) C. Agustín-Sáenz, M. Machado, J. Nohava, M. Brizuela, N. Yurrita, A. Sanz, O. Zubillaga, A. Tercjak, Mechanical properties of hydrophobic anti-reflective sol-gel coatings and field performance on photovoltaic application, under preparation

6.5.2. Contributions in conferences

Contributions in conferences directly related to the investigation work:

1) C. Agustín-Sáenz, M. Machado, A. Tercjak, Antireflective and low surface energy sol-gel coating stack design and field performance on photovoltaic application (accepted abstract), 20th International Sol-Gel Conference, will be held on 25-30 August 2019, St. Petersburg, Russia

2) M. Brizuela, C. Agustín, O. Zubillaga, S. Domínguez-Meister, J. L. Viviente, I. Braceras, P. Corengia, T. C. Rojas, J. C. Sánchez-López, S. Mato, Nanostructured coatings: from lab to application, Nanospain, 7-10 March 2017, San Sebastián, Spain

3) C. Agustín, J. Á. Sánchez-García, N. Yurrita, M. Machado, M. Brizuela, O. Zubillaga, Multilayer broadband anti-reflective and easy-to-clean porous sol-gel coatings for photovoltaics, 18th International Sol-Gel Conference, 6-11 September 2015, Kyoto, Japan

4) C. Agustín, M. Machado, J. Á. Sánchez-García, N. Yurrita, M. Brizuela, O. Zubillaga, Broadband anti-reflective porous sol-gel coatings containing fluorocarbon groups for photovoltaics, E-MRS Spring meeting 2015, 11-15 May 2015, Lille, France

5) J. Nohava, C. Agustín, J. Cech, P. Kempé, M. Brizuela, Nanomechanical characterization and scratch testing of abrasion resistant anti-reflective sol-gel coatings for concentrating photovoltaic applications, 2nd International Surface Treatment Symposium 2014, 25-27 June 2014, Istanbul, Turkey

6) C. Agustín, J.A. Sánchez-García, M. Machado, J. Nohava, J. Cech, M. Brizuela, N. Yurrita, O. Zubillaga, Broadbrand anti-reflective sol-gel coatings with easy-to-clean performance

for concentrating photovoltaics, E-MRS Spring meeting 2014, 26-30 May 2014, Lille, France

7) J. Á. Sánchez-García, M. Machado, C. Prieto, C. Agustín, M. Brizuela, I. Braceras, R. Alonso, F.J. Cano, O. Zubillaga, Reflective multilayer coatings with dielectric barriers for high concentration photovoltaics, EU PVSEC 2013 28th European PV Solar Energy Conference and Exhibition, 30 Sept-4 Oct 2013, Paris, France

8) C. Agustín, J. Á. Sánchez-García, M. Machado, I. Ibáñez, O. Ollo, M. Brizuela, O. Zubillaga, Easy-to-clean abrasion resistant anti-reflective sol-gel coatings for concentrating photovoltaics-CPV, 17th International Sol-Gel Conference, 25-30 August 2013, Madrid, Spain

9) C. Agustín, J. Á. Sánchez, M. Machado, A. Gracia, O. Zubillaga, M. Brizuela, Preparation of anti-reflective silica-based films by sol-gel method, Optocoat 2012, 31 May 2012, Alicante, Spain

6.5.3. Patent applications

1) C. Agustín Sáenz, O. Zubillaga Alcorta, M. Brizuela Parra, A broadband anti-reflective sol-gel coating composition, WO2018130701A1, 2019.

Nomenclature

List of symbols

A	Active area of the cell
A_c	Developed contact area during indentation test
A_p	Projected contact area during indentation test
α	Angle between the axis of the indenter diamond pyramid
AM	Air mass
AM0	Extraterrestrial solar spectral irradiance for an air mass of 0
AM1.5D	Direct solar spectral irradiance for an air mass of 1.5.
AM1.5G	Earth's surface global solar spectral irradiance for an air mass of 1.5.
c_i	Volume fraction of medium i
χ_i	Incident polarization state
χ_r	Reflected polarization state
Δ	Phase shift difference
d_n	Layer thickness
δ_n	Phase angle generated by each layer
δ_p	Phase change for the p-component upon reflection
δ_s	Phase change for the s-component upon reflection
D	System degradation rate
ε	Complex dielectric function
E_i	Young's modulus of the indenter
E_{IT}	Young's modulus of the tested sample
E_r	Reduced modulus of the indentation contact
E	Eccentricity factor
ϕ_o	Incident angle
ϕ_1	Refraction angle
ϕ	Incoming photon flux
F	Nanoindentation test force
F_{max}	Maximum applied force
F_t	Tangential torce
γ	Surface tension
γ_{lv}	Surface tension in the liquid-air interface
γ_{sl}	Surface tension in the solid-liquid interface
γ_{sv}	Surface tension in the solid-vapour interface
G	Transmittance gain of an antireflective coated glass over bare glass
h	Indentation depth under applied test force
h_c	Contact depth of the indenter with the test piece at F_{max}
h_{max}	Maximum indentation depth at F_{max}
h_p	Permanent indentation depth after the removal of the test force

h_r	Intersection of the tangent to unloading curve at F_{max} with the indentation depth-axis
H_{IT}	Indentation testing hardness
I	Intensity
I_{SC}	Short-circuit current
I_{MP}	Intensity at the maximum power value
I	Transmitted light
I_o	Incident light
J_{SC}	Short-circuit current density
φ	Incoming irradiance spectrum
$\varphi_{AM1.5}$	AM1.5 solar irradiance spectrum
κ	Extinction coefficient
λ	Wavelength
Lc	Critical load
M	Metal central atom
M	Reduction of reflectance of an antireflective coated glass over bare glass
m	Power law constant exponent
μ	Dynamic viscosity
n	Refractive index
n_n	Real part of the refractive index of a given material
$\tilde{n}$	Complex refractive index
$\tilde{n}_a$	Complex refractive index of environment
$\tilde{n}_e$	Complex refractive index of effective medium
$\tilde{n}_i$	Complex refractive index of medium i
N	Life years of PV plant
P	Pressure
P_o	Vapour pressure
q	Elementary electric charge
θ_c	Static contact angle
θ_n	Reflection angle
ρ	Complex reflectance ratio
ρ	Integrated total reflectance value
ρ_{dif}	Integrated diffuse reflectance value
R	Generic alkyl group
R	Reflectance, reflection
R_{xy}	Reflection at each interface between x and y media
r_p	Complex Fresnel reflection coefficients for the parallel, p- polarized light
r_s	Complex Fresnel reflection coefficients for the perpendicular, s-polarized light
R	Gas constant
R_a	Arithmetic mean of roughness
R_q	Root mean square of roughness
R_{Et}	Ethanol/alkoxide molar ratio
R_w	Water/alkoxide molar ratio

r	Discount rate
RV	Residual value
σ	Conductivity
S	Contact stiffness
S	Surface
T	Temperature
T	Transmittance, transmission
t	t-plot, thickness of the water monolayer
τ	Intregrated transmittance value
tan Ψ	Amplitude ratio upon reflection
υ_i	Poisson's ratio of the indenter
υ_s	Poisson's ratio of the sample
V	Voltage
V_{OC}	Open circuit voltage
V_{MP}	Voltage at the maximum power value
V	Volume
V_L	Volume of adsorbate
V_P	Pore volume
Wp	Watt-peak
Y_0	Initial yield

List of abbreviations

ADG	Achromatic doublet on glass
AFM	Atomic force microscopy
AR	Antireflective
AS	Antisoiling
BEMA	Bruggeman effective medium approximation model
CAPEX	Capital expenditures
CMC	Critical micellar concentration
CPV	Concentrated photovoltaic
CSP	Concentrated solar power
c-Si	Crystalline silicon
DC	Direct current
DNI	Direct normal irradiance
DCCPC	Dielectric-cross compound-parabolic-concentrator
EEP	Environmetal ellipsometric porosimetry
EISA	Evaporation-induced self-assembly
EMA	Effective medium approximation
ENEA	Italian national agency for new technologies, energy and sustainable economic development
EP	Ellipsometric porosimetry
EQE	External quantum efficiency
EtOH	Ethanol
FAS	Polyfluoroalkyl alkoxysilane
FAS3	(3, 3, 3- trifluoropropyl) trimethoxy silane
FAS13	Triethoxy-1H,1H,2H,2H-perfluorooctyl triethoxy silane silane
FAS17	Triethoxy-1H,1H,2H,2H-perfluorodecyl triethoxy silane
FAS21	(1H,1H,2H,2H-perfluorododec-1-yl) triethoxy silane
GRIN	Graded refractive index structure
HCPV	High concentrated photovoltaic
HMDS	Hexamethyl disilazane
HV	Vickers hardness
H-sol	Sol with high concentration of theoretical SiO_2
IES-UPM	Instituto de Energía Solar - Universidad Politécnica de Madrid
IMM	Inverted metamorphic mismatched
IMM4J	Inverted metamorphic 4-junction solar cell
IMP	Intensity at the maximum power value
IQE	Internal quantum efficiency
IEA PVPS	International Energy Agency Photovoltaic Power Systems Programme
LCOE	Levelized cost of energy
LM	Lattice-matched
L-sol	Sol with low concentration of theoretical SiO_2

MeOH	Methanol
MJ	Multi-junction
MM	Metamorphic-mismatched
MPP	Maximum power point
MTES	Methyl triethoxysilane
NIR	Near infrared region
NMR	Nuclear magnetic resonance
NST	Nano scratch tester
OPEX	Operating expenditures
PDMS	Polydimethylsiloxane
PEO	Polyethylene oxide
POE	Primary optical element
PPO	Polypropylene oxide
PTFE	Polytetrafluroethylene
PV	Photovoltaic
RH	Relative humidity
RTP	Refractive truncated pyramid
SDA	Structure directing agent
SDA1	Polyethylene oxide (20) hexadecyl ether
SDA2	Cetyltrimethylammonium bromide
SDA3	Polyethylene oxide-b-polypropylene oxide-b-polyethylene oxide
SDA4	T-octylphenoxypolyethoxyethanol
SDA5	Sodium dodecyl sulphate
SFE	Surface free energy
SILO	Single-lens-optical element
SMR	Spectral matching ratio
SOE	Secondary optical element
SoG	Silicone on glass
SR	Spectral response
TEOS	Tetraethyl orthosilicate
TGA	Thermogravimetric analysis
TPU	Thermoplastic polyurethane
UV	Ultraviolet region
UMM3J	Upright metamorphic 3-junction solar cell
VIS	Visible region
3J	3-junction solar cell

List of tables

List of figures

Acknowledgements

Me gustaría dar las gracias a Agnieszka y Maider, porque habéis sido mi gran punto de apoyo sobre el que levantar 'el mundo', y me habéis ayudado a ganar la confianza que me faltaba.

A mis compañeros del Grupo de Ingeniería de Superficies y de Solar, por su participación en la realización de este trabajo, Oihana, Naiara, Marta, Pablo, Paco, Eduardo, Iñigo B., Iñigo I., Asier, en especial a José Ángel, por su implicación incondicional cuando yo era una *baby* en esto de la ciencia, y por transmitirme su entusiasmo por este trabajo, y a Eider, por saber entenderme y aconsejarme en lo profesional y por las profundas conversaciones de lo emocional. A las compañeras de WET y a mis compañeros, los que son más amigos que *colleagues* de TECNALIA por su apoyo y preocupación.

A Alicia y Yolanda del ICV, gracias por compartir su conocimiento con nosotros, su colaboración me ha ayudado a sentar las bases de este trabajo, y por su puesto gracias por los buenos momentos compartidos en los congresos de sol-gel.

Me gustaría agradecer a mamá (cómo le gusta esta palabra) y papá, porque soy lo que soy gracias a ellos, gracias por transmitirme con vuestro ejemplo que la constancia, el esfuerzo, el compromiso y el entusiasmo son la clave en la mayoría de los aspectos de la vida. Con el tiempo voy descubriendo muchas cosas que me habéis dicho para mejorar como persona a lo largo de la vida y que en su día no entendía. Y a mis hermanos José Antonio y Javier por apoyar incondicionalmente cada nuevo camino elegido, sin sorprenderse ni ponerme en duda, ya me conocen, y además ayudarme, yo también estoy muy orgullosa de vosotros. También a Bárbara, por todos los momentos buenos que nos esperan, y perdón a todos por haceros tan partícipes de mis adversidades.

Quiero agradecer también a mis tíos Conchi, Tere, Fernando y a David, Ana, Pedro y Marta porque también siempre están sin condiciones. A mi tía Mari por preocuparse por mí. A Jose y Miguel, mis cuñados y sobris por tener 'una casa' tan grande en la que me hacen sentir uno más. A mis amigos de Arnedo, Pamplona, Donosti, mis chicas de la resi, mis compis del CPS, las loquis de calle La Salle y los bologneses, a todos ellos por tantos momentos buenos, apoyo, confidencias, cánticos, festivales, complicidad, en fin...sois lo que ponéis la 'música'.

Y gracias a todos por permitirme decir que sin duda este trabajo ha llegado a su fin gracias al apoyo de Miguel. Desde que el 'destino' nos ofreció encontrarnos hace más de media vida,

hemos crecido juntos como pareja, amigos, equipo. A parte de por su ayuda con las ilustraciones de los artículos y de la tesis, sino hubiera sido por su implicación 'detrás de las cámaras' puedo asegurar que este trabajo no hubiera salido adelante. No exagero si digo que con lo que me ha demostrado, hay que inventar una nueva palabra, porque la palabra amor se queda corta. Gracias por esforzarte en querer ver las cosas a través de mis ojos para comprenderme, por tu innata habilidad para hospedar en tu corazón, por ofrecer todo lo que tienes, por hacer sentir que lo me pasa a mi te pasa a ti y al revés. Creo que tengo que dar gracias a la vida por haberte encontrado, porque no creo que esta forma de sentir esté al alcance de todos. Lo celebraremos este verano en algún festival…just you and me dance forever.

Arnedo, junio 2019